The climate impacts of atmospheric aerosols using in-situ measurements, satellite retrievals and global climate model simulations

Nicholas William Davies

Supervised by
Professor James M. Haywood
Dr Justin M. Langridge

Submitted by Nicholas William Davies
to the University of Exeter
as a thesis for the degree of
Doctor of Philosophy in Mathematics
in September 2018

University of Exeter
United Kingdom

I certify that all material in this thesis which is not my own work has been identified and that no material has previously been submitted and approved for the award of a degree by this or any other University.

Signature: ……..

Abstract

Aerosols contribute the largest uncertainty to estimates of radiative forcing of the Earth's atmosphere, which are thought to exert a net negative radiative forcing, offsetting a potentially significant but poorly constrained fraction of the positive radiative forcing associated with greenhouse gases. Aerosols perturb the Earth's radiative balance directly by absorbing and scattering radiation and indirectly by acting as cloud condensation nuclei, altering cloud albedo and potentially cloud lifetime. One of the major factors governing the uncertainty in estimates of aerosol direct radiative forcing is the poorly constrained aerosol single scattering albedo, which is the ratio of the aerosol scattering to extinction.

In this thesis, I describe a new instrument for the measurement of aerosol optical properties using photoacoustic and cavity ring-down spectroscopy. Characterisation is performed by assessing the instrument minimum sensitivity and accuracy as well as verifying the accuracy of its calibration procedure. The instrument and calibration accuracies are assessed by comparing modelled to measured optical properties of well-characterised laboratory-generated aerosol.

I then examine biases in traditional, filter-based absorption measurements by comparing to photoacoustic spectrometer absorption measurements for a range of aerosol sources at multiple wavelengths. Filter-based measurements consistently overestimate absorption although the bias magnitude is strongly source-dependent. Biases are consistently lowest when an advanced correction scheme is applied, irrespective of wavelength or aerosol source.

Lastly, I assess the sensitivity of the direct radiative effect of biomass burning aerosols to aerosol and cloud optical properties over the Southeast Atlantic Ocean using a combination of offline radiative transfer modelling, satellite observations and global climate model simulations. Although the direct radiative effect depends on aerosol and cloud optical properties in a non-linear way, it appears to be only weakly dependent on sub-grid variability.

Acknowledgements

Firstly I thank Jim and Justin for your guidance, support and patience over the last four years. Thank you for the opportunities you have given me, which allowed me to explore the full spectrum of aerosol research and to develop as a researcher. In particular, I thank you for the unique opportunities to perform airborne fieldwork over India and Ascension Island. These are memories I will cherish forever.

Thanks also goes to Fanny Peers, who has given me much advice and helped me solve many computer-related issues. I thank Ben Johnson for your time spent setting up ever more complicated climate model runs and for our many useful discussions. I thank Kate Szpek, Cathryn Fox, Michael Cotterell and Jamie Trembath for our discussions and for your input and feedback at various stages along the way.

Thanks to Mum and Dad for your continued support and willingness to listen. Thanks to my friends for your support along the way and staging interventions, often involving beer, when required.

My final thank you is to Kirsty. Your love, care and positivity kept me going when I needed it most.

This work was supported by a Met Office/NERC Industrial CASE PhD Studentship (ref. 640052003).

Cite as:

Davies N. W. (2018) The climate impacts of atmospheric aerosols using in-situ measurements, satellite retrievals and global climate model simulations, PhD thesis, University of Exeter, Exeter.

For the journal-published chapters, components of which feature in Chapters 2,3 and 4, it is customary to cite the journal articles.

Table of Contents

List of figures

List of tables

List of abbreviations

AAE	Absorption Ångström exponent
AAOD	Absorbing aerosol optical depth
ACAOD	Above cloud aerosol optical depth
ACCMIP	Atmospheric Chemistry and Climate Model Intercomparison Project
ACDRE	Above-cloud direct radiative effect
ACSSA	Above cloud single scattering albedo
AeroCom	Aerosol Comparisons between Observations and Models
AERONET	AErosol RObotic NETwork
AMS	Aerosol mass spectrometer
AOD	Aerosol optical depth
AR5	Fifth assessment report
AR6	Sixth assessment report
ARA	Atmospheric Research Aircraft
B1999	Bond et al. (1999) correction scheme
BBA	Biomass burning aerosol
BC	Black carbon
BrC	Brown carbon
BVOC	Biogenic volatile organic compound
CALIOP	Cloud-Aerosol Lidar with Orthogonal Polarization
CCN	Cloud condensation nuclei
CH_4	Methane
CLARIFY	CLoud-Aerosol-Radiation Interactions and Forcing: Year 2017
CLASSIC	Coupled Large-scale Aerosol Simulator for Studies In Climate
CMIP5	Coupled Model Intercomparison Project Phase 5
CO	Carbon monoxide
CO_2	Carbon dioxide
COD	Cloud optical depth
CPC	Condensation particle counter
CRDS	Cavity ring-down spectroscopy
CTS	Constrained two-stream
DMA	Differential mobility analyser
DMS	Dimethyl sulphide
DRE	Direct radiative effect
DRF	Direct radiative forcing
EXSCALABAR	EXtinction, SCattering and Absorption of Light for AirBorne Aerosol Research
FAAM	Facility for Airborne Atmospheric Measurements
FSR	Free spectral range
GFED	Global Fire Emissions Database

GFED3	Global Fire Emissions Database 3
GFED4s	Global Fire Emissions Database 4 with small fires
GLOMAP	Global Model of Aerosol Processes
HadGEM2	Hadley Centre Global Environment Model version 2
HadGEM3	Hadley Centre Global Environment Model version 3
IA	Integrated area
IPCC	Intergovernmental Panel on Climate Change
LAC	Light absorbing carbon
LWC	Liquid water content
M2014	Müller et al. (2014) correction scheme
MAC	Mass absorption coefficient
MFC	Mass flow controller
MODIS	Moderate Resolution Imaging Spectroradiometer
N_2	Nitrogen
N_2O	Nitrous oxide
NO_2	Nitrogen dioxide
O_2	Oxygen
O_3	Ozone
OA	Organic aerosol
OMI	Ozone monitoring instrument
OPC	Optical particle counter
PARASOL	Polarization and Anisotropy of Reflectances for Atmospheric Sciences coupled with Observations from a Lidar
PAS	Photoacoustic spectroscopy
PBAB	Primary biological aerosol particle
PCASP	Passive Cavity Aerosol Spectrometer Probe
PMT	Photomultiplier tube
POA	Primary organic aerosol
POLDER	Polarization and Directionality of Earth Reflectances
PSAP	Particle Soot Absorption Photometer
RCP	Representation Concentration Pathway
RF	Radiative forcing
RI	Refractive index
SAFARI	Southern African Fire-Atmosphere Research Initiative
SCHIAMACHY	Scanning Imaging Absorption Spectrometer for Atmospheric Chartography
SMPS	Scanning mobility particle sizer
SO_2	Sulphur dioxide
SO_4	Sulphate
SOA	Secondary organic aerosol
SOCRATES	Suite Of Community RAdiative Transfer codes based on Edwards and Slingo
SSA	Single scattering albedo

SWS	Short Wave Spectrometer
SZA	Solar zenith angle
TAP	Tricolor absorption photometer
TEM	Transverse-electromagnetic
TOA	Top of atmosphere
TOF-AMS	Time-Of-Flight Aerosol Mass Spectrometer
USA	United States of America
UV	Ultraviolet
V2010	Virkkula (2010) correction scheme
VOC	Volatile organic compound

1 Introduction

1.1 Motivation

Climate change is defined as a change in the Earth's mean climate properties that typically occur over time scales of at least decades including, for example, temperature, precipitation and wind (Cubasch *et al.*, 2013). Paleoclimate records indicate that there have been significant climate changes in the past due to changes in the Earth's orbital motion around the sun, changes in solar irradiance, and internal climate variability (Masson-Delmotte *et al.*, 2013). Despite this natural variability, there is robust evidence showing that these effects do not account for the recent observed climate changes; it is extremely unlikely (0–5 % certainty) that the global mean surface temperature increase during 1951–2010 was due to solar variability and virtually certain (99–100 % certainty) that it cannot be explained by internal climate variability alone (Bindoff *et al.*, 2013; Stocker *et al.*, 2013).

Much of the present-day climate change is caused by external perturbations to the Earth's planetary radiation balance due primarily to changes in the atmospheric constituents from human activities, namely increased concentrations of greenhouse gases and atmospheric aerosols (a gaseous suspension of nanometre to micrometre liquid or solid particles) (Seinfeld and Pandis, 2006; Stocker *et al.*, 2013). Since the start of the industrial revolution (often taken as the year 1750), the rate of increase of anthropogenic atmospheric greenhouse gas emissions, including CO_2, CH_4 and N_2O, has been unprecedented, the highest rate for at least 22000 years. Increases in greenhouse gas concentrations modify the Earth's energy balance by absorbing outgoing terrestrial radiation leading to atmospheric heating. It is extremely likely (95–100 % certainty) that over half of the warming during 1951–2010 was caused by human activities (Stocker *et al.*, 2013).

One of the key uncertainties in the drivers of climate change is due to the poorly understood impact that aerosols have on the climate system (Stocker *et al.*, 2013). Aerosols can perturb the Earth's radiative balance by directly absorbing and scattering radiation incident upon them, termed 'aerosol-radiation interactions', or indirectly by modifying the brightness and potentially the lifetime of clouds, termed 'aerosol-cloud interactions' (Boucher *et al.*, 2013). On a global

mean basis, both the aerosol-radiation and aerosol-cloud interactions tend to cool the planet thus offsetting the warming by greenhouse gases by a potentially significant but poorly constrained extent (Stocker *et al.*, 2013). Quantification of the impact that aerosols have on the climate system is uncertain due to their spatial and temporal inhomogeneity, varied chemical, physical and optical properties, and uncertainty surrounding their interaction with clouds (Boucher *et al.*, 2013). Figure 1.1 summarises the estimated radiative impacts of greenhouse gases and aerosols, highlighting the extent with which their mean radiative forcings cancel out; see below for a discussion of the radiative forcing concept.

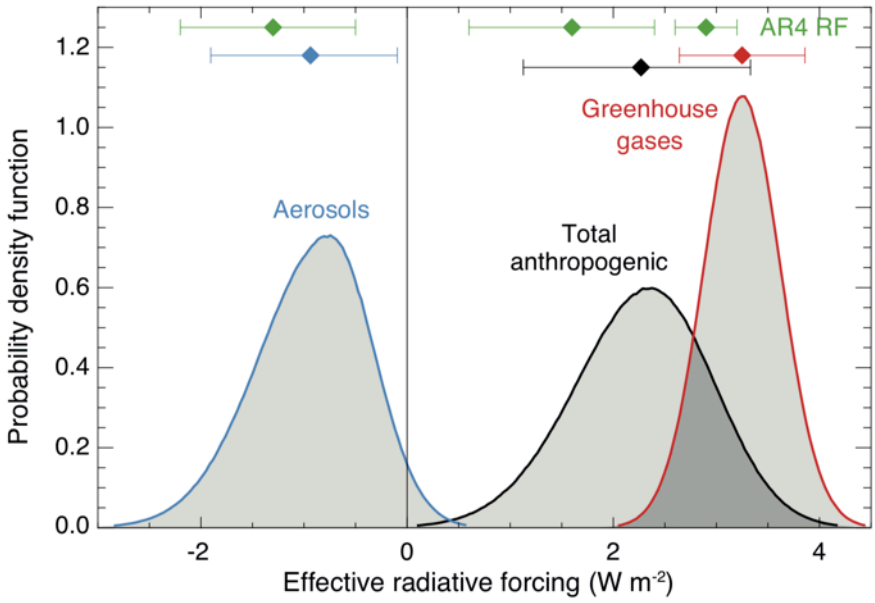

Figure 1.1 *Probability density functions of effective radiative forcing for aerosols and greenhouse gases. Figure from Myhre et al. (2013a).*

Radiative forcing (units $W\ m^{-2}$) is a quantitative measure of the impact that a perturbation to atmospheric constituents such as greenhouse gases or aerosols has on the Earth's radiative balance and is a useful quantity when comparing climate models' responses to a range of climate forcing agents (Gregory *et al.*, 2004). Adjusted radiative forcing (units $W\ m^{-2}$), hereafter referred to as *radiative forcing*, is defined as the change in net downward radiative flux (shortwave plus longwave) at the tropopause after allowing for stratospheric temperatures to adjust to radiative equilibrium relative to pre-industrial conditions, taken as the year 1750 (Stocker *et al.*, 2013). A key benefit of using the radiative forcing concept is that it predicts the equilibrium climate response to an external perturbation accurately due to the relationship between radiative forcing and

global mean surface temperature (e.g. Hansen *et al.*, 1997; Gregory *et al.*, 2004). It follows that the resultant temperature change due to sustained radiative forcing can be approximated by $\Delta T \approx \lambda RF$, where λ is the equilibrium climate sensitivity parameter and RF is the radiative forcing, such that a positive RF leads to warming of the atmosphere-surface and negative RF a cooling (Shine *et al.*, 2003; Myhre *et al.*, 2013a). Similarly, to account for tropospheric adjustments, which ultimately improve climate models' predictions of the global mean temperature response and other climate changes, one must use the 'effective radiative forcing' (units *W m*$^{-2}$) (Shine *et al.*, 2003; Myhre *et al.*, 2013a). Effective radiative forcing is defined similarly to radiative forcing except that tropospheric temperatures are allowed to readjust to radiative equilibrium, i.e. before significant changes in global and annual mean surface temperatures occur (Gregory *et al.*, 2004; Seinfeld and Pandis, 2006; Stocker *et al.*, 2013).

Figure 1.2 details the radiative forcing of the major radiative forcing agents including contributions from greenhouse gases and aerosols. The Intergovernmental Panel on Climate Change's (IPCC's) latest estimate of the total aerosol effective radiative forcing, based on the most recent modelling and observational studies available, was −0.9 [−1.9 to −0.1] W m^{-2} (Stocker *et al.*, 2013). Aerosol-radiation interactions were estimated to contribute −0.45 [−0.95 to +0.05] W m^{-2} and aerosol-cloud interactions −0.45 [−1.20 to 0.00] W m^{-2} (Myhre *et al.*, 2013a). Examination of two decades worth of IPCC assessment reports reveals that the uncertainty associated with aerosol radiative forcing remains persistently high compared to the relatively well defined, positive radiative forcing associated with greenhouse gases. Importantly, aerosols likely offset the warming by greenhouse gases by a potentially significant but poorly quantified amount. Details regarding some of the sources of this uncertainty will be covered in Section 1.4.

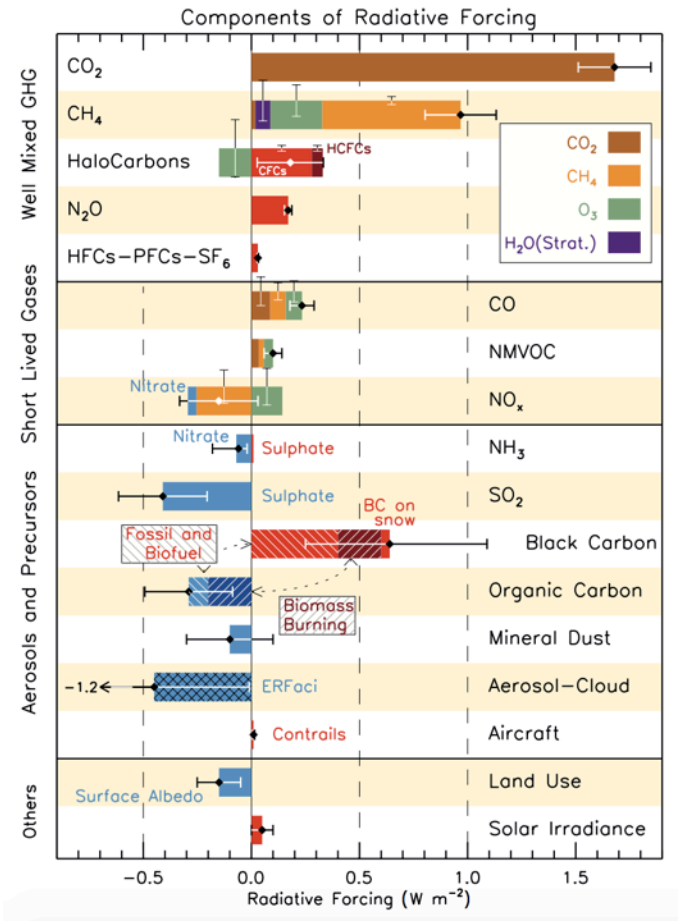

Figure 1.2: *Radiative forcing of atmospheric greenhouse gases and aerosols and other radiative forcing agents. Figure from Myhre et al. (2013a).*

Assessing the impact of a forcing agent globally requires the use of state-of-the-art climate models. These are essential for predicting the future state of the Earth's climate both globally and regionally, thus providing us with the opportunity to mitigate and adapt to the ensuing climate changes in both the near-term (~2050) and long-term (≥ 2100) (Stocker *et al.*, 2013). The IPCC evaluated future climate change scenarios using a suite of climate models (Collins *et al.*, 2013), via the Coupled Model Intercomparison Project Phase 5 (CMIP5) (Taylor *et al.*, 2012). These models were driven by a series of Representation Concentration Pathways (RCPs), which account for a range of future scenarios including estimates for concentrations of atmospheric greenhouse gases, aerosols and ozone (Moss *et al.*, 2010). Under RCP8.5, the estimated total radiative forcing was estimated to be 8.5 W m^{-2} by year 2100 (Stocker *et al.*, 2013). This scenario does not include any specific mitigation strategy and is based on high population growth (12 billion by 2100), little convergence between high and low-income countries and moderate rates of technological advance (Riahi *et al.*, 2011). On the contrary, RCP2.6 aims to limit

total radiative forcing to 2.6 W m^{-2} by 2100, which incorporates significant increases in renewable and nuclear energy sources, the use of carbon capture storage and new technologies, for example in transport (van Vuuren *et al.*, 2011). Figure 1.3 shows the observed temperature change during 1986–2012 and the modelled temperature change during 1986–2050 relative to 1986–2005, indicating increased temperatures globally in all simulations (Stocker *et al.*, 2013). By the year 2050, temperatures are estimated to have risen by between 0.5–2.5 °C relative to 1986–2005, which will clearly have very different and substantial impacts on other variables in the Earth's climate, including, and certainty not limited to, ice sheet extent, sea level rise and changes in precipitation.

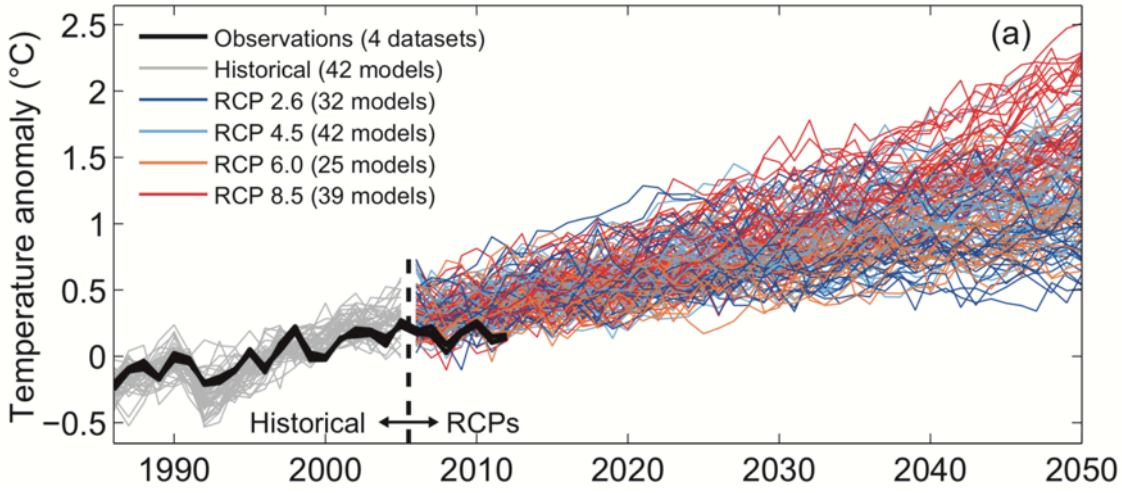

Figure 1.3: *Global mean surface temperature 1986–2050 for all RCP scenarios using the CMIP5 suite of models including observations 1986–2012 relative to 1986–2005. The global mean surface temperature is assessed to have increased by 0.61°C prior to 1986–2005, relative to 1850–1900. Figure from Stocker et al. (2013).*

These human-induced climate changes pose major risks including potential for substantial species extinction, risks to global food security and increases in extreme weather events (IPCC, 2014). It is therefore essential to understand and be able to predict the state of the Earth's future climate to allow us to mitigate and adapt to the ensuing climate changes.

Whilst the RCP scenarios will have the most important effect on how future temperature will evolve, understanding the uncertainty in the underlying climate drivers (i.e. radiative forcing) also plays an important role.

1.2 An introduction to atmospheric aerosols

1.2.1 Overview

Aerosols can be natural or anthropogenic in origin (Haywood and Boucher, 2000). Primary aerosols refer to those emitted directly at source, such as desert dust, sea spray and black carbon from fossil fuel and biomass burning, and secondary aerosols refer to those produced via chemical reactions or condensation of low volatility compounds from the gas phase. An example of a secondary aerosol is ammonium sulphate derived from dimethyl sulphide phytoplankton emissions that form sulphur dioxide gas, which is oxidised to sulphuric acid aerosol and subsequently neutralised by ammonia (Haywood and Boucher, 2000; Andreae and Rosenfeld, 2008; Boucher *et al.*, 2013). Aerosol residence times within the troposphere are typically of the order of minutes to several weeks before removal by wet deposition, sedimentation or impaction (Haywood and Boucher, 2000; Seinfeld and Pandis, 2006). Aerosol processes that are of importance in the atmosphere include coagulation, condensation and nucleation, which have been shown to depend on particle size (Williams *et al.*, 2002). Due to the relatively short atmospheric lifetime of aerosols and geographically localised aerosol sources, there is a wide spatial variability in aerosol mass, type and composition; see Figure 1.4 (Jimenez *et al.*, 2009; Boucher *et al.*, 2013).

1.2.2 Aerosol sources and species

The largest natural emissions sources are from sea spray (~4100 Tg yr^{-1}), mineral dust (~2500 Tg yr^{-1}) and biological matter, for example primary biological aerosol particles (50–1000 Tg yr^{-1}) and biological volatile organic compounds (440–720 Tg yr^{-1}). The largest anthropogenic sources of aerosols and aerosol precursors are non-methane volatile organic compounds (~127 Tg yr^{-1}), SO_2 (55 TgS yr^{-1}) and biomass burning aerosols (49 Tg yr^{-1}) (Boucher *et al.*, 2013).

Sea spray results from bubble bursting at the sea surface due mostly to breaking waves, which depend on the surface wind speed (Boucher *et al.*, 2013). Sea spray consists of sea salt and primary organic aerosol (Russell *et al.*, 2010; Boucher *et al.*, 2013). There exists significant uncertainty in the emission rate of sea spray, which is estimated to be in the range 1400 to 6800

Tg yr^{-1} (Boucher *et al.*, 2013). The emission rate of the organic aerosol component of sea spray is estimated to be in the range 2 to 20 Tg yr^{-1} and is governed by biological activity (Facchini *et al.*, 2008; Gantt *et al.*, 2011; Boucher *et al.*, 2013). The atmospheric lifetime of sea spray lies in the range of seconds to days and is governed by gravitational sedimentation and, for smaller particles, precipitation (de Leeuw *et al.*, 2011). Sea spray can play a major role in governing the number concentration and size distribution of marine cloud droplets due to its hygroscopic nature (Andreae and Rosenfeld, 2008). Sea spray can therefore lead to both a negative direct radiative forcing via increasing the amount of upwelling scattered radiation and an indirect radiative forcing by acting as cloud condensation nuclei, as well as decreasing the amount of radiation absorbed by the oceans (de Leeuw *et al.*, 2011).

Mineral dust is primarily produced during disintegration of soil aggregates through processes such as saltation whereby relatively large dust particles (70–500 μm) can eject smaller dust particles (0.1–10 μm) upon impaction with an arid surface (Alfaro *et al.*, 1997; Kok, 2011; Boucher *et al.*, 2013). The mineral dust emission rate is estimated to be 1000 to 4000 Tg yr^{-1} and is dependent upon wind speed, vegetation cover and soil properties (Huneeus *et al.*, 2012; Boucher *et al.*, 2013). Whilst the Sahara is the world's largest dust source (Shao *et al.*, 2011; Ryder *et al.*, 2013), an estimated 20–25 % of mineral dust is anthropogenic in nature owing to land use change (Ginoux *et al.*, 2012; Boucher *et al.*, 2013). The atmospheric lifetime of dust is typically hours to weeks with dominant removal processes including gravitational settling and wet deposition (Jickells *et al.*, 2005). Mineral dust plays a key role in the biogeochemical cycle by providing essential iron ocean fertilisation for phytoplankton growth. This ocean fertilisation increases CO_2 sequestration and subsequent organic carbon export to the ocean floor as well as increasing dimethyl sulphide concentrations, a precursor to ammonium sulphate (Jickells *et al.*, 2005). Importantly, dust impacts the radiative balance directly at both solar and terrestrial radiation wavelengths (e.g. Ryder *et al.*, 2013), tending to cool the planet at solar wavelengths and warm the planet at terrestrial wavelengths (e.g. Haywood and Boucher, 2000; Myhre *et al.*, 2013a). Although dust can be hydrophobic (Herich *et al.*, 2009), it can become hydrophilic upon atmospheric processing by gaining coatings with soluble material, thereby

altering the planetary radiative balance by acting as cloud condensation nuclei (CCN) (e.g. Andreae and Rosenfeld, 2008).

Light-absorbing carbonaceous aerosol refers to a range of species including black carbon (BC) and organic carbon. BC is formed during flaming combustion and is defined by its unique characteristics including that it consists of elemental carbon which is a strong light-absorber at visible wavelengths, refractory and insoluble in water (Bond *et al.*, 2013). Organic carbon refers to a complex mix of compounds containing carbon, emitted directly as primary organic aerosol (POA) or indirectly as secondary organic aerosol (SOA), forming from gaseous precursors (Zaveri *et al.*, 2012; Bond *et al.*, 2013). A subset of organic aerosol known as 'brown carbon' (BrC) refers to organic compounds that absorb short-visible wavelengths strongly (Kirchstetter *et al.*, 2004; Andreae and Gelencsér, 2006; Bond *et al.*, 2013). Primary sources include fossil fuel and biomass burning whereas secondary sources include condensation from a complex range of biogenic and anthropogenic gaseous precursors (Zaveri *et al.*, 2012). Major sources of carbonaceous aerosols are through heating and cooking using coal and biomass, which contribute 50 % and 70 % to the total black and organic carbon emissions globally, respectively (Amann *et al.*, 2013; Bond *et al.*, 2013). Diesel vehicles are the next largest BC emissions source, which contribute 25 % of BC emissions globally. Africa is the largest source of biomass burning aerosol (BBA), accounting for over half of global carbon emissions (van der Werf *et al.*, 2010). BBAs are predominantly produced through burning of agricultural waste, savannah fires and deforestation (van der Werf *et al.*, 2010). Although BC emissions have been declining in the more economically developed countries, with emissions in the USA falling by 25 % between 1990 and 2004 (Murphy *et al.*, 2011; Bond *et al.*, 2013), emissions have been rising in Asia, by an estimated 40 % in China and India between 1996–2010 (Lu *et al.*, 2011; Bond *et al.*, 2013). Whilst it is anticipated that clean technology will lead to reductions in BC emissions, which may be associated with short-term reductions in aerosol radiative forcing (Bond *et al.*, 2013), increases in global temperatures can lead to increased forest fires and hence increased BC emissions (Westerling *et al.*, 2006).

Other sources of organic carbon include those emitted from natural sources such as those from the sea or terrestrial biological POA particles (Facchini *et al.*, 2008; Burrows *et al.*, 2009) whilst anthropogenic sources include those emitted during fossil fuel burning (Jimenez *et al.*, 2009). Volatile organic compounds (VOCs) such as isoprene and mono-terpenes are a group of chemical species that undergo a range of complex chemical reactions to form SOA (Hallquist *et al.*, 2009; Boucher *et al.*, 2013). Natural VOCs, or biogenic volatile organic compounds (BVOCs), are emitted from marine and terrestrial environments with sources including those emitted from plant foliage and from microbial decomposition of organic matter (Guenther *et al.*, 1995). Anthropogenic sources include those produced from vehicle emissions, landfill sites and industrial activities (Atkinson and Arey, 2003). SOA emissions are estimated to be 20–380 Tg yr^{-1} (Boucher *et al.*, 2013). The large uncertainty in emissions arises in part due to limitations in our knowledge of VOC sources, lack of understanding of the processes leading to SOA formation and lack of detailed in-situ measurements to assess these issues (Hallquist *et al.*, 2009).

Ammonium sulphate is another radiatively important atmospheric species that alters the planetary radiative balance by directly scattering radiation incident upon it and indirectly scattering radiation by acting as CCN due to its highly hygroscopic nature (Boucher *et al.*, 2013). Gaseous precursors to ammonium sulphate include sulphur dioxide (SO_2), dimethyl sulphide (DMS) and ammonia, which are estimated to be emitted at rates of 43–78 TgS yr^{-1}, 10–40 TgS yr^{-1} and 35–50 Tg yr^{-1}, respectively. Anthropogenic sources of SO_2 include fossil fuel burning due to industrial activities, power generation and transport (Klimont *et al.*, 2013) whereas natural sources include volcano emissions (Haywood and Boucher, 2000). Oxidation of SO_2 leads to SO_4 through a range of reaction pathways (Seinfeld and Pandis, 2006). DMS is a compound originating from the decomposition of marine organisms such as phytoplankton, which is subsequently oxidised through a sequence of chemical reactions to form ammonium sulphate (Koga and Tanaka, 1999; Carslaw *et al.*, 2010). Ammonia is emitted to the atmosphere from a range of sources including volatilisation from animal waste and fertilisers, fossil fuel burning, and biomass burning (Behera *et al.*, 2013 and references therein).

Nitrate aerosols are light scattering and hygroscopic with an estimated emission rate of 18 Tg yr^{-1} (Andreae and Rosenfeld, 2008). They are estimated to be the next largest anthropogenic cooling agent after ammonium sulphate (Bellouin *et al.*, 2011; Boucher *et al.*, 2013).

Primary biological aerosol particles (PBAPs) are another significant source of atmospheric aerosols, consisting of microorganisms such as bacteria and fungal spores with an estimated emission rate of 50–1000 Tg yr^{-1} (Burrows *et al.*, 2009).

The aerosol species discussed here relate to those that have the most significant radiative forcing and this list is certainly not exhaustive (Boucher *et al.*, 2013). The constituent components of aerosol vary very widely with geographic location as evidenced by detailed chemical composition analysis using, for example, an Aerodyne aerosol mass spectrometer (AMS) (Jimenez *et al.*, 2009); see Figure 1.4.

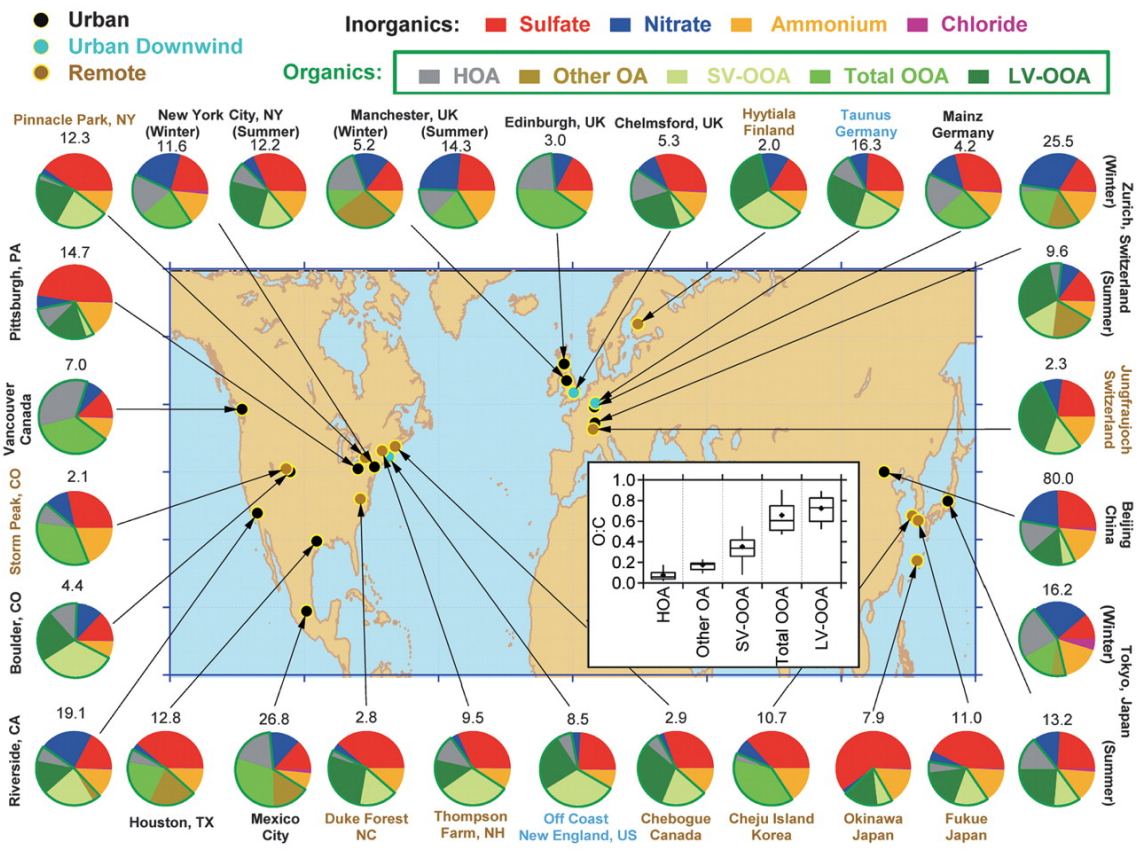

Figure 1.4: *Total mass concentration (μg m^{-3}) and mass fractions of non-refractory inorganic and organic species measured using an aerosol mass*

spectrometer at a range of locations (surface measurements). The inset shows ratios of O:C for the organic aerosol species. Figure from Jimenez et al. (2009).

1.2.3 Aerosol size distributions

Aerosol size distributions are well approximated by lognormal distributions, often with multiple modes present that are typically classed as the nucleation mode (< 0.1 μm), accumulation mode (0.1–2.0 μm) and coarse mode (> 2 μm) (Seinfeld and Pandis, 2006). The lognormal distribution function is

$$\frac{dN}{dD_p} = \frac{N_t}{(2\pi)^{\frac{1}{2}} D_p ln(\sigma_g)} exp\left(-\frac{\left(ln(D_p) - ln(\overline{D_p})\right)^2}{2ln^2(\sigma_g)}\right), \qquad (1.1)$$

where N_t is the particle concentration (units m^{-3}), D_p is the particle diameter (units m), σ_g is the geometric standard deviation and $\overline{D_p}$ is the mean particle diameter (units m).

1.2.4 Aerosol-radiation interactions

Aerosols interact with radiation through absorption and elastic scattering of light, governed by particle size, composition, morphology and mixing state (Alexander *et al.*, 2008; Cappa *et al.*, 2008; Bond *et al.*, 2013; Liu *et al.*, 2015a). Aerosol optical properties pertinent to assessing their impact on Earth's radiative balance include the aerosol (i) single scattering albedo (SSA), (ii) scattering phase function and (iii) specific extinction coefficient (Haywood *et al.*, 1997b). For spherical particles, these properties can be described using Mie-Debye-Lorenz theory (hereafter referred to as *Mie* theory), with inputs including aerosol diameter, refractive index and the wavelength of light (e.g. Bohren and Huffman, 1998). Rayleigh scattering can be used to approximate scattering at particle diameters smaller than approximately 0.1 μm for visible light wavelengths (Seinfeld and Pandis, 2006).

When discussing aerosol optical properties, one must first define the absorption and scattering efficiencies, $Q_{abs}(\lambda)$ and $Q_{sca}(\lambda)$, which govern the amount of light that is absorbed or scattered when incident upon a particle (Seinfeld and Pandis, 2006). Figure 1.5 shows how the absorption, scattering and extinction efficiencies vary with particle radius and refractive index at the wavelength 0.55 μm. The refractive index 1.95 −0.71i corresponding to black carbon was chosen

with three additional lower imaginary refractive indices, corresponding to lower light-absorption (Bond and Bergstrom, 2006).

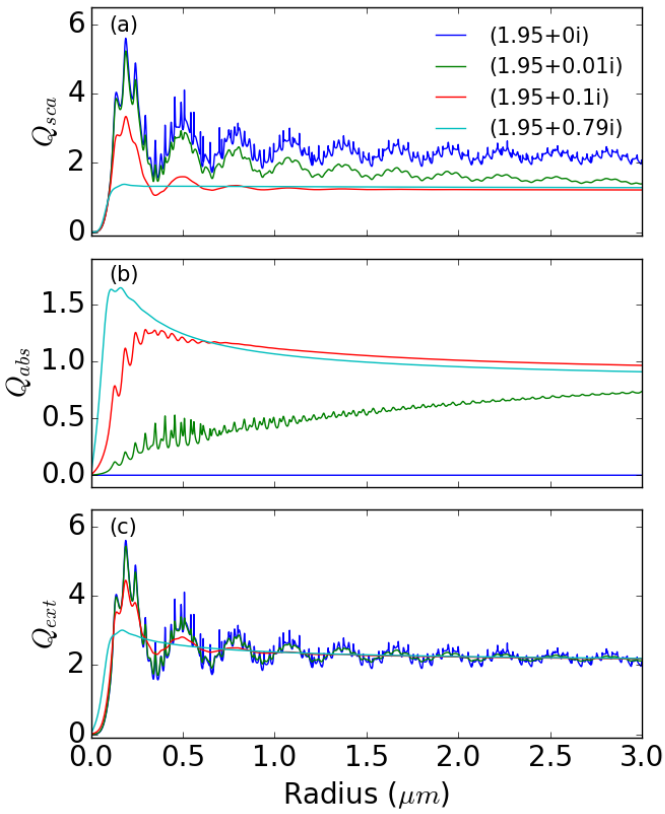

Figure 1.5: *The dependence of the (a) scattering efficiency, (b) absorption efficiency and (c) extinction efficiency with radius for a spherical particle at wavelength 0.55 μm.*

Conservation of energy means that any absorbed light is either re-radiated as scattered light or converted into thermal energy, leading to particle heating (Seinfeld and Pandis, 2006). The aerosol extinction efficiency is the sum of the absorption and scattering efficiencies, defined as

$$Q_{ext}(\lambda) = Q_{abs}(\lambda) + Q_{sca}(\lambda). \qquad (1.2)$$

It follows that the SSA, a measure of the degree of light-absorption such that a value of zero indicates total absorption of light and a value of unity indicates total scattering of light, can be defined as (e.g. Seinfeld and Pandis, 2006)

$$\omega(\lambda) = \frac{Q_{sca}(\lambda)}{Q_{abs}(\lambda) + Q_{sca}(\lambda)}. \qquad (1.3)$$

The second parameter required when assessing the radiative impact of aerosols is the scattering phase function, $P(\theta)$, which describes the direction

and intensity with which light is scattered by a particle (e.g. Haywood and Shine, 1997). The scattering phase function simplifies under the two-stream approximation, whereby light is restricted to either moving away or towards the Earth's surface, which can be approximated using the asymmetry parameter, defined as

$$g = \frac{1}{2}\int_0^{\pi} P(\theta)sin(\theta)cos(\theta)d\theta, \quad (1.4)$$

where θ is the light-scattering angle. The asymmetry parameter assumes a value between −1 to 1 such that a value of zero refers to equal scattering in the forward and backwards directions, a value of 1 refers to forward scattering only and −1 backward scattering only (Seinfeld and Pandis, 2006). Similarly, the hemispheric backscatter ratio, a measure of the light scattered into the backward hemisphere, can be defined as

$$\beta = \frac{\int_{\frac{\pi}{2}}^{\pi} P(\theta)sin(\theta)d\theta}{\int_0^{\pi} P(\theta)sin(\theta)d\theta}, \quad (1.5)$$

such that a value of zero indicates no backscattered light and a value of 1 indicates that all light is backscattered (Seinfeld and Pandis, 2006).

The third key aerosol optical parameter is the aerosol specific extinction coefficient (units $m^2\ kg^{-1}$), which provides the link between aerosol mass concentrations modelled using chemical transport models and the impact that they have on radiative transfer (Bond *et al.*, 2013) defined as

$$k_e(\lambda) = \frac{Q_{ext}(\lambda)\pi r^2}{\rho\frac{4\pi r^3}{3}} = \frac{3Q_{ext}(\lambda)}{4\rho r}, \quad (1.6)$$

where r is the aerosol radius (units *m*) and ρ (units $kg\ m^{-3}$) is the aerosol density (Jennings and Pinnick, 1980). It follows that the aerosol optical depth can be defined as

$$\tau = \int_0^z k_e(\lambda)mdz, \quad (1.7)$$

where m is the mass concentration (units $g\ m^{-3}$) *and* z is the altitude (units *m*) within the atmosphere.

The Ångström exponent is a measure of the dependence of aerosol optical properties with wavelength (Ångström, 1929). The absorption Ångström exponent describes how the strength of absorption changes with wavelength and is often used to differentiate between different aerosol components (e.g. Kirchstetter *et al.*, 2004; Clarke *et al.*, 2007; Yang *et al.*, 2009; Bahadur *et al.*, 2012; Chung *et al.*, 2012; Zhu *et al.*, 2017). The extinction Ångström exponent is defined as (Ångström, 1929)

$$\text{Å} = -\frac{log\left(\frac{b_{ext}(\lambda_1)}{b_{ext}(\lambda_2)}\right)}{log\left(\frac{\lambda_1}{\lambda_2}\right)}, \qquad (1.8)$$

where $b_{ext}(\lambda)$ represents the extinction coefficient. The absorption and scattering Ångström exponents are defined similarly, where $b_{ext}(\lambda)$ is replaced with $b_{abs}(\lambda)$ or $b_{sca}(\lambda)$, respectively. The wavelength dependence of absorption can vary significantly between aerosols. Figure 1.6 shows measurements of the absorptance derived from airborne Particle Soot Absorption Photometer (PSAP) filter samples made with the FAAM aircraft in the laboratory using the Short Wave Spectrometer (SWS) radiometer without the telescope (Haywood *et al.*, 2003a). Absorptance was derived by dividing the reflected radiance of a clean area of the filter by the reflected radiance of the aerosol spot for each wavelength in the range 0.40–0.95 μm with a pixel separation of ~0.003 μm. Fresh biomass burning aerosol emissions show absorption across the full visible spectrum, whereas Saharan dust shows strong wavelength dependence, absorbing strongly at blue-visible wavelengths. This range of aerosols only represents a sub-sample of aerosol sources – in reality, there is a complex range of absorptive properties, which need to be accounted for in climate models (Boucher *et al.*, 2013).

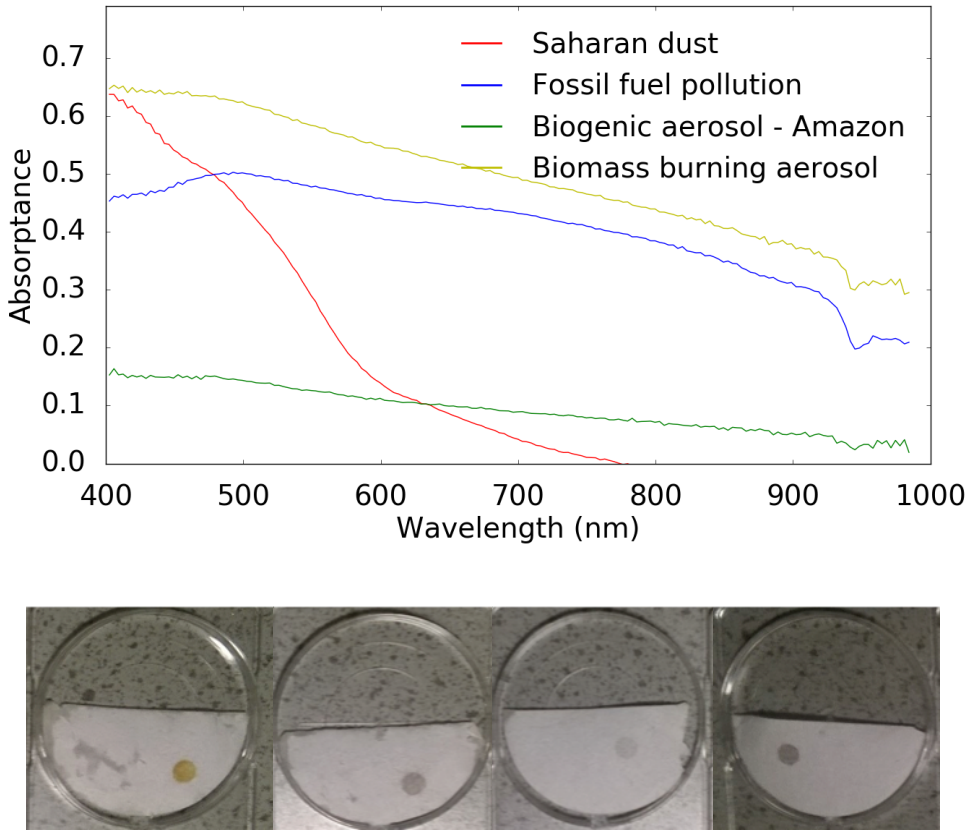

Figure 1.6: *The wavelength dependence of aerosol absorption for four aerosol sources deposited onto filters. From left to right: Saharan dust, fossil fuel burning aerosol, biogenic emissions and biomass burning aerosol.*

1.2.5 Aerosol-cloud interactions

Aerosols can act as cloud condensation nuclei and can thus modify the microphysical and radiative properties of clouds, leading to changes in cloud albedo and lifetime, known as aerosol-cloud interactions (Boucher *et al.*, 2013). Hence, the 'first indirect effect' describes how the cloud albedo depends on aerosol concentration for a fixed liquid water content such that increased concentrations of aerosols lead to smaller cloud droplets and thus higher cloud reflectivity (Twomey, 1974). It follows that the cloud optical depth can be defined as

$$\tau_c = h\left(\frac{9\pi L^2 N}{2\rho_w^2}\right)^{\frac{1}{3}}, \qquad (1.9)$$

where h is the cloud thickness (units m), L is the liquid water content (units g_{H20} $m^{-3}{}_{\text{air}}$), N is the number concentration (units m^{-3}) and ρ_w is the density of water (units g_{H20} m^{-3}) (Seinfeld and Pandis, 2006).

As a result of the reduced cloud droplet radius, the collision efficiency between cloud droplets is reduced and the autoconversion process whereby the droplets grow to sufficient size to precipitate is inhibited. Thus, the 'second indirect effect' has been postulated to decrease the precipitation efficiency reducing the liquid water sink and thus increase the cloud lifetime and thickness (Albrecht, 1989). Recent observations using degassing volcanic eruptions have shown clear evidence of the aerosol first indirect effect, but indicate a negligible second indirect effect suggesting that thermodynamic factors rather than aerosol number concentrations are more important in controlling cloud liquid water path (Malavelle *et al.*, 2017; Toll *et al.*, 2017). Although aerosol-cloud interactions are responsible for significant uncertainty when modelling future climate change as highlighted in Figure 1.2, they are beyond the scope of this thesis and therefore will not be discussed at length.

1.3 A simple radiative transfer model of the effects of aerosols

One can derive a simple radiative transfer model assessing how aerosols impact the Earth's radiative balance due to aerosol-radiation interactions. The change in planetary albedo upon adding a layer of aerosol into the atmosphere (see Figure 1.7), can be approximated by

$$\Delta\mathcal{R}_p = \left(\mathcal{R}_a + \frac{\mathcal{T}^2\mathcal{R}_p}{1-\mathcal{R}_p\mathcal{R}_a}\right) - \mathcal{R}_p, \qquad (1.10)$$

where $\mathcal{R}_a$ is the aerosol reflectance, $\mathcal{R}_p$ is underlying surface reflectance and $\mathcal{T}$ is the aerosol transmittance, which depends on the aerosol optical properties and atmospheric loading (Charlson *et al.*, 1991). The aerosol reflectance and transmittance are defined as

$$\mathcal{R}_a = (1-e^{-\tau})\omega\beta \qquad (1.11)$$

$$\mathcal{T} = e^{-\tau} + (1-\beta)(1-e^{-\tau}), \qquad (1.12)$$

where τ is the aerosol optical depth, ω is the SSA and β is the backscatter fraction.

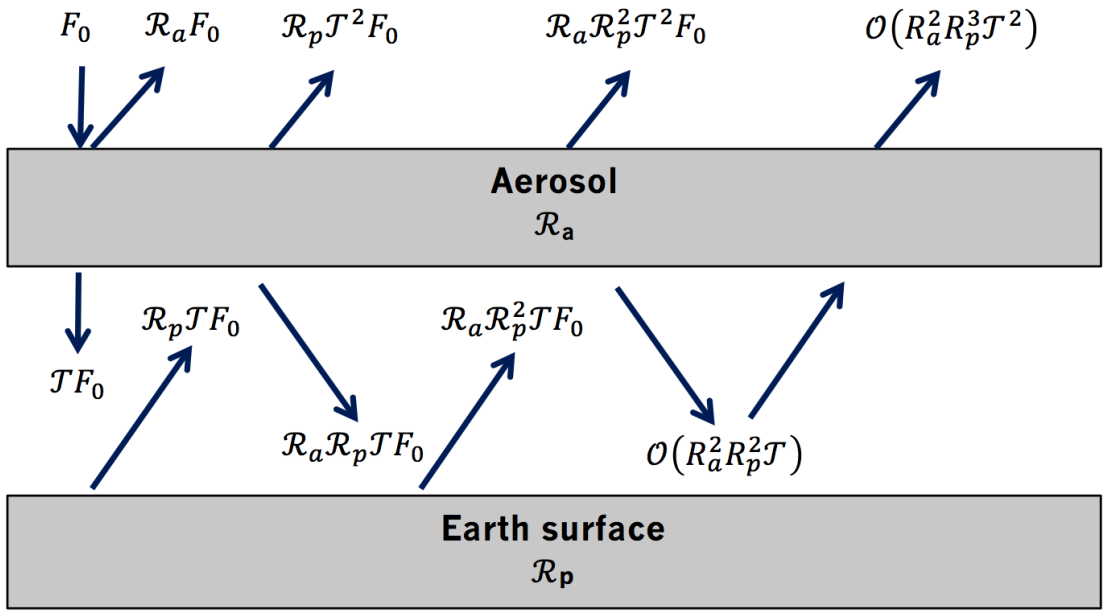

Figure 1.7: *Radiative fluxes in the Earth's atmosphere with a layer of aerosol. Figure adapted from Seinfeld and Pandis (2006).*

Hence, if an aerosol layer is relatively absorbing compared to the underlying surface, i.e. if the aerosol results in more light being scattered back into space, the aerosol will have a cooling influence on the atmosphere. On the contrary, if the aerosol leads to increased absorption, i.e. if the aerosol results in less light being scattered back into space, the aerosol will have a warming influence on the atmosphere. It follows that the 'critical single scattering albedo', the aerosol SSA at which aerosols lead to an atmospheric warming rather than a cooling, i.e. when $\Delta\mathcal{R}_p = 0$, can be defined as (Haywood and Shine, 1995)

$$\omega_{critical} = \frac{2\mathcal{R}_p}{2\mathcal{R}_p + \beta\left(1 - \mathcal{R}_p\right)^2}. \qquad (1.13)$$

Figure 1.8 demonstrates the critical single scattering albedo concept.

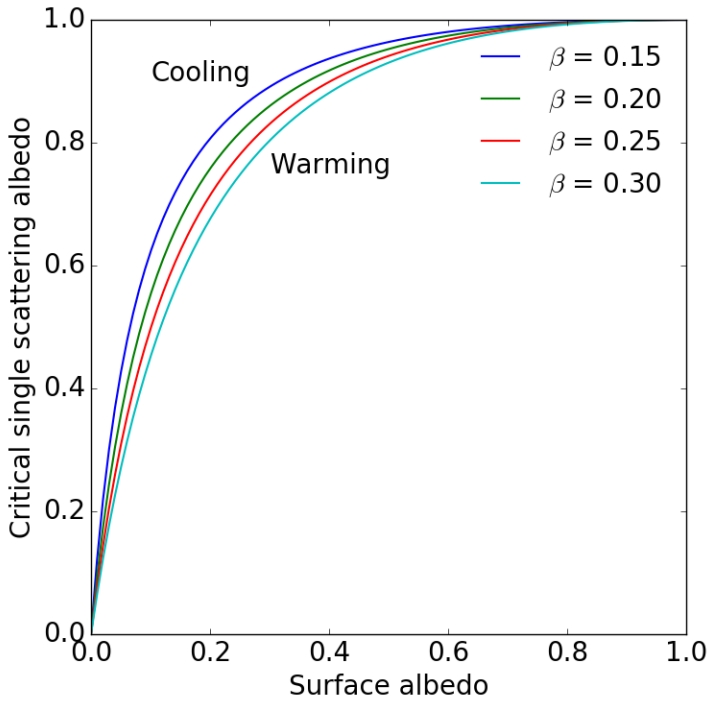

Figure 1.8: *Critical single scattering albedo as a function of the underlying surface albedo. Figure adapted from* Haywood and Shine (1995).

To illustrate the aerosol critical SSA concept, it is helpful to examine a satellite image of partially absorbing biomass burning aerosol. Figure 1.9 demonstrates that biomass burning aerosol overlying ocean increases the planetary albedo, $\mathcal{R}_p$, whereas over bright cloud it decreases $\mathcal{R}_p$.

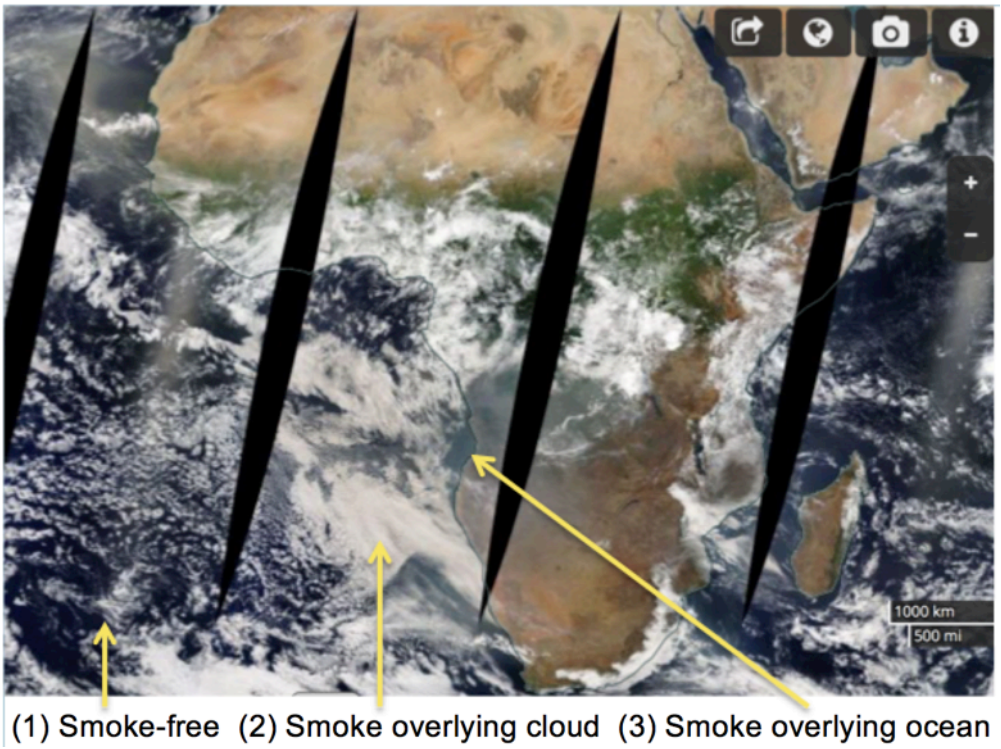

Figure 1.9: *Satellite image of biomass burning aerosol over Southern Africa and the Southeast Atlantic Ocean in September 2017. Screenshot taken from https://worldview.earthdata.nasa.gov - accessed on 23/02/18.*

Although more complex models exist for the assessment of radiative transfer through a layer of aerosols suspended within the atmosphere, this simple model succinctly highlights how the Earth's radiative balance depends on the aerosol albedo relative to the underlying surface albedo. It is beyond the scope of this introductory section to evaluate more complex radiative transfer schemes, which will be presented in greater detail in Chapter 5.

1.4 Assessing the radiative impact of carbonaceous aerosols

1.4.1 Overview

Carbonaceous aerosols contribute one of the largest uncertainties to aerosol direct radiative forcing (Myhre *et al.*, 2013a). In the following section, I aim to elucidate the factors underlying this uncertainty. While the simple conceptual model detailed in section 1.3 provides a physical insight into the impacts of aerosols on aerosol-radiation and aerosol-cloud interactions, the advent of massively parallel computing systems has enabled the development of complex global general circulation models that represent a full range of processes governing aerosol production, transport and deposition. Climate models have been used to assess the impact of carbonaceous aerosols on the climate

system globally (Bond *et al.*, 2013; Stocker *et al.*, 2013). Shindell *et al*. (2013) found that although climate models generally reproduce aerosol optical depth accurately, they underestimate the absorbing aerosol optical depth (AAOD) by ~50 % due to uncertainties in their optical properties and emission inventories; see Figure 1.10. Shindell *et al*. (2013) evaluated model AAOD bias by comparing the modelled AAOD to the Ozone Monitoring Instrument (OMI), AErosol RObotic NETwork (AERONET) and ground-based lidars. Specifically, the modelled black carbon radiative forcing, with sources including fossil fuels and biofuel, was estimated as 0.24 ± 0.09 W m^{-2} (relative standard deviation of 38%), although this value may be underestimated due to the AAOD bias (Shindell *et al.*, 2013). Similarly, Myhre *et al*. (2013b) assessed the direct radiative forcing of black carbon in 16 climate models (AeroCom Phase II) and found a mean radiative forcing of 0.18 ± 0.07 W m^{-2} (relative standard deviation 39%). This spread was attributed in equal measure to diversities in aerosol burden, mass extinction coefficient and the normalised radiative forcing; the latter depends on the aerosol SSA, underlying surface albedo, solar zenith angle and aerosol vertical distribution (Boucher and Anderson, 1995; Zhou *et al.*, 2005; Seinfeld and Pandis, 2006; Myhre and Samset, 2015). It is interesting to compare these results to the AeroCom Phase I simulations whereby 9 climate models predicted the BC radiative forcing to be 0.25 ± 0.08 W m^{-2} (relative standard deviation 32%) (Schulz *et al.*, 2006). Thus the more highly developed AeroCom Phase II models exhibited stronger BC radiative forcing diversity than the AeroCom Phase I models. In the following discussion I will examine the key factors driving the uncertainty in BC radiative forcing.

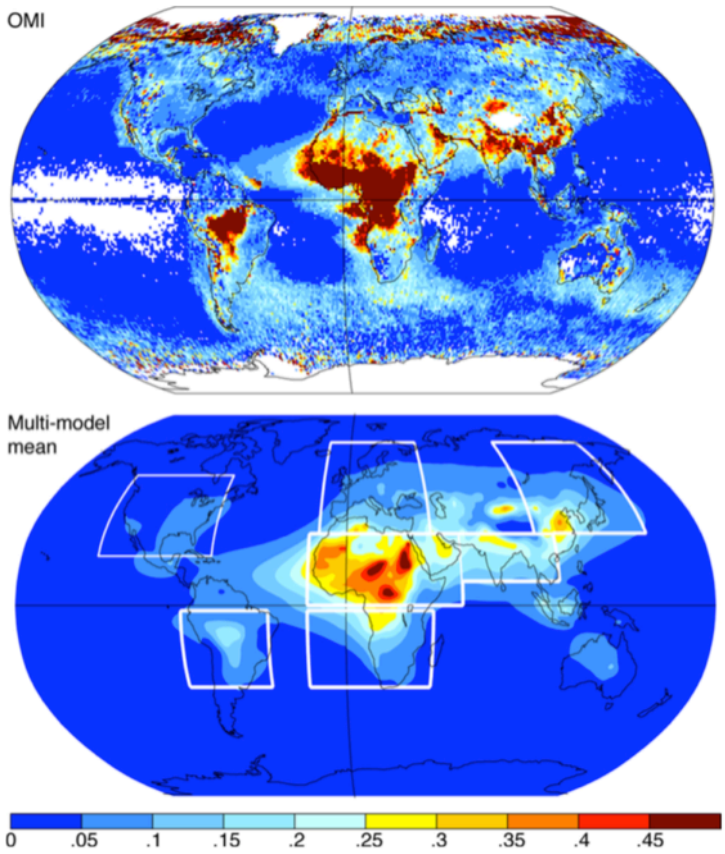

Figure 1.10: *Annual mean absorbing aerosol optical depth measured by the OMI satellite instrument (top) and modelled using the ACCMIP models (bottom) for the period 2005–2007. Figure from Shindell et al. (2013).*

1.4.2 Factors that influence the radiative forcing of carbonaceous aerosols: intrinsic properties

In this section, I will evaluate some of the key factors controlling the uncertainty in aerosol radiative forcing associated with intrinsic properties of carbonaceous aerosols. Intrinsic properties depend only on the type of aerosol and not on the number or concentration of aerosols (e.g. Vaughan *et al.*, 2004). The aerosol SSA dominates the uncertainty in direct radiative forcing (McComiskey *et al.*, 2008; Loeb and Su, 2010; Sherman and McComiskey, 2018), which is a key input into radiative transfer models as highlighted in section 1.3. The aerosol SSA is governed by the relative strength of aerosol absorption and scattering (see equation 1.3) and is influenced by a number of factors including aerosol refractive index, size distribution, mixing state and shape, which will be discussed in turn in sections 1.4.2.1–1.4.2.4.

1.4.2.1 Refractive index

The aerosol refractive index (RI) is a wavelength-dependent variable related to aerosol composition and has real and imaginary parts, which represent the scattering and absorbing components of aerosols, respectively (Seinfeld and Pandis, 2006). Accurate refractive indices are required to quantify the aerosol direct radiative effect, which controls the relative magnitudes of scattering and absorption and hence SSA (Zarzana *et al.*, 2014). The RI of carbonaceous aerosol depends on the fuel type and burn conditions, which can be strongly source-dependent (e.g. Kirchstetter *et al.*, 2004; Chakrabarty *et al.*, 2010; Chen and Bond, 2010; Lack *et al.*, 2012; Saleh *et al.*, 2014; Liu *et al.*, 2015b). Literature values of the real and imaginary parts of BC's refractive index vary between 1.35 to 1.90 and 0.08i to 0.79i at 550 nm, respectively (Hungershoefer *et al.*, 2008; Moteki *et al.*, 2010; Bond *et al.*, 2013), although a central value of 1.95 −0.79i is recommended for void-free carbon (Bond *et al.*, 2006, 2013).

Uncertainties in the RI of organic aerosol (OA), another key component of carbonaceous aerosol that is typically co-emitted alongside BC, are large (Boucher *et al.*, 2013; Myhre *et al.*, 2013b; Wang *et al.*, 2016). OA originating from biomass or biofuel burning is made up of a complex mix of organic compounds with varying optical properties, which are also dependent on the fuel type and burn conditions (e.g. Saleh *et al.*, 2014, 2015). BrC is the light-absorbing fraction of OA (e.g. Kirchstetter *et al*., 2004). Wang *et al.* (2014) summarised the imaginary part of the BrC RI based on a number of field and laboratory studies, which ranged between ~0.01i to 0.20i at wavelength 400 nm. Thus significant uncertainty surrounds the BrC contribution to total absorption of carbonaceous aerosol, which Chung *et al.* (2012b) estimated as 20 % at 550 nm, Feng *et al.* (2013) estimated as up to 20 % over the solar spectrum and Lin *et al.* (2014) as 27 to 70 %. Modelling studies aimed at evaluating the direct radiative forcing of BrC are in the range 0.03–0.60 W m^{-2} and are uncertain due to BrC's poorly constrained optical properties, governed by refractive index, which depend on the source, atmospheric processing and mixing state (Park *et al.*, 2010; Feng *et al.*, 2013; Lin *et al.*, 2014; Wang *et al.*, 2014, 2018; Saleh *et al.*, 2015; Jo *et al.*, 2016). As highlighted in Wang *et al*. (2018), to reduce the uncertainty associated with the direct radiative forcing of BrC, the general paucity of data must be addressed; specifically, (i) evaluation of how BrC's

optical properties change globally due to source influences and (ii) how the optical properties of BrC change with photochemical aging.

1.4.2.2 Size distribution

The aerosol size distribution is a key parameter governing aerosols' optical properties (Boucher *et al.*, 2013). The treatment of the aerosol size distribution within a climate modelling framework is critically important for accounting for aging of aerosol components as aerosols undergo atmospheric processing to become internally mixed to varying degrees (see section 1.4.2.3). In the best case scenario, individual particle sizes and mixing states would be tracked from a range of sources and atmospheric processes such as condensation, evaporation and coagulation accounted for, although implementing this particle evolution within a global climate model framework would be prohibitively computationally expensive (Zaveri *et al.*, 2010). In practice, aerosol size distributions are represented by either modal or sectional schemes (Myhre *et al.*, 2013b and references therein; Matsui and Mahowald, 2017). Modal schemes represent aerosol size distributions using functions, typically log-normal distributions, and assume that all particles within each mode have the same chemical composition, with multiple modes corresponding to a range of aerosol types (Matsui and Mahowald, 2017). Sectional aerosol schemes are relatively sophisticated, which represent aerosol composition and optical properties within discrete size ranges corresponding to a range of aerosol types. Disadvantages of both these schemes is due to grouping aerosol composition and mixing state together, which can lead to biases in ensemble aerosol optical properties (Zaveri *et al.*, 2010).

1.4.2.3 Aerosol mixing state

BC's optical properties depend on its mixing state (Bond *et al.*, 2006), which is often described as being either externally or internally mixed. Although externally mixed BC is initially hydrophobic, BC can grow via condensation and coagulation with semi-volatile gases and hygroscopic organic aerosols, which can coat the BC cores leading to attraction of water and inorganic material (Andrews and Larson, 1993; Jacobson, 2002; Zaveri *et al.*, 2010). External mixtures refer to a 'heterogeneous population of homogeneous particles' that are physically separated from each other (Bond and Bergstrom, 2006) (Figure 1.11a). An internal mixture refers to particles that are either a 'homogeneous

population of homogeneous particles' (Figure 1.11b) or 'internally heterogeneous' (Figure 1.11c) in which an absorbing core (in the case of BC) is encapsulated by material (Fuller *et al.*, 1999; Bond and Bergstrom, 2006; Bond *et al.*, 2006). In-situ measurements have verified that BC is almost always internally mixed within hours of emission (e.g. Murphy *et al.*, 2006; Moffet and Prather, 2009). Well-internally-mixed treatments (Figure 1.11b) whereby the refractive indices of the aerosol components are volume averaged to obtain a single RI for the composite aerosol are not physically plausible (Jacobson, 2000). The Maxwell-Garnett mixing rule is a relatively complex approximation used to estimate the RI of internally mixed aerosols by accounting for small inclusions within a homogeneous matrix, which has been found to be more accurate than the volume averaging method (e.g. Riziq *et al.*, 2007). However, the core-shell model (Figure 1.11c) best represents internal mixing of BC and other gaseous and aerosol components (Bond *et al.*, 2006).

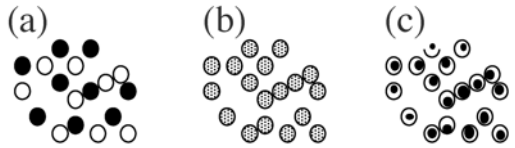

Figure 1.11: *Aerosol mixing state where (a) refers to an external mixture, (b) refers to a homogeneous population of internally homogeneous particles and (c) an internally heterogeneous mixture, whereby a core aerosol is encapsulated by a shell. Figure from* Bond and Bergstrom (2006).

Absorption of light by a BC core (Figure 1.11c) is enhanced due to the presence of a non-absorbing shell, which acts as a lens by focussing radiation onto the absorbing core (Fuller *et al.*, 1999). This enhanced absorption, hereafter referred to as the 'lensing effect' can enhance absorption by up to a factor 2 (Bond *et al.*, 2006; Lack and Cappa, 2010). As pointed out by Lack and Cappa (2010), the absorption enhancement can lead to a change in the aerosol SSA. For certain combinations of BC core diameter and non-absorbing shell thickness (diameter > 50 nm, e.g. ~400 nm core and 400 nm shell), the SSA can decrease by up to 0.3 for an internal mixture relative to an external mixture. However, the absorption enhancement depends strongly on the core particle size, coating thickness and refractive index of the coating (Bond *et al.*, 2006; Lack *et al.*, 2012b). The magnitude of the absorption enhancement varies in a non-linear way with the core and shell diameters even for idealised concentric

core-shell models (Bond *et al.*, 2006). Absorption enhancements may be significantly lower when internally mixed particles are positioned within a non-concentric arrangement, which could be the case for originally hydrophobic BC particles (Fuller *et al.*, 1999; Bond *et al.*, 2006). Absorption is similarly over-predicted for fractal, chain-like aggregates (see section 1.4.2.4) (Adachi *et al.*, 2010). Cappa *et al.* (2012) suggested that the absorption enhancement for BC derived from fossil fuel emissions is only 6 % at 532 nm and increased weakly with photochemical aging, in contrast to laboratory and theoretical calculations that suggested absorption enhancements potentially > 2. This finding suggests that the enhanced absorption may be a function of the BC source and thus needs to be explicitly accounted for in climate models (Cappa *et al.*, 2012). To confound this, Lack and Cappa (2010) found that the enhanced absorption due to the lensing effect for BC cores encapsulated by BrC could be 25–50 % lower compared to BC cores with clear coatings (non-absorbing OA), dependent on wavelength (380–750 nm). This dependence of enhanced absorption on coating optical properties could lead to inaccuracies in estimates of radiative forcing due to the misrepresentation of the BC lensing effect.

In addition to the uncertainty surrounding the fundamental magnitude of the absorption enhancement of internally mixed BC, there is also uncertainty relating to its implementation within climate models (Zaveri *et al.*, 2010). Climate models account for the time-evolution of aerosol mixing state with a range of complexity, which is linked closely to the treatment of aerosol size. Many climate models use modal or sectional aerosol microphysical schemes to represent aerosol size distributions (Myhre *et al.*, 2013b and references therein), which assume that all particles in a given mode or size range have the same mixing state (Zaveri *et al.*, 2010) (see section 1.4.2.2). Zaveri *et al.* (2010) developed a particle-resolved model that explicitly evaluated individual particle mixing states and found that BC absorption was over-estimated by up to 30 % and SSA under-estimated by up to 0.07 under a sectional size distribution framework. This bias was due to artificial aging whereby all particles within a given size bin were assumed to be internally mixed to some degree.

Moreover, climate models only account for BrC in a limited way due to uncertainties surrounding its sources, optical properties and mixing state (Wang

et al., 2018 and references therein). To account for internal aerosol mixing of BC and BrC components, modelling studies (e.g. Wang *et al.*, 2014) typically apply a constant scaling factor for the lensing absorption enhancement, which therefore does not account for the suppression of lensing due to an absorbing BrC shell and likely leads to an overestimation of total absorption (Wang *et al.*, 2016). Saleh *et al.* (2015) further highlighted the importance of treating BrC absorption and mixing state simultaneously as they have a non-linear effect on absorption compared to externally mixed BC and BrC, which can lead to an overestimation of absorption.

1.4.2.4 Aerosol morphology

Atmospheric BC has a complex morphology that affects its optical properties (Bond *et al.*, 2006; Radney *et al.*, 2014). Freshly emitted black carbon is emitted as a chain aggregate (Martins *et al.*, 1998; Bond and Bergstrom, 2006) consisting of a series of spherical particles, typically a few tens of nanometres in diameter (Mikhailov *et al.*, 2006). These aggregates can collapse to form densely packed, spherical-like structures upon aging with organic aerosol, inorganic species and water (Hallett *et al.*, 1989; Abel *et al.*, 2003; Schnaiter *et al.*, 2003; van Poppel *et al.*, 2005). Interactions between adjacent spherules within BC aggregates can lead to a 30 % enhancement in absorption relative to their equivalent collapsed structures (Fuller, 1995; Bond and Bergstrom, 2006). Upon aging, enhanced absorption due to internally mixed black carbon is estimated to increase BC's optical properties by a factor 1.5; this factor represents the net effect of a decrease in absorption due to a collapsed BC structure relative to a chain aggregate and the absorption enhancement due to BC coating (see section 1.4.2.3) (Bond *et al.*, 2006).

Core-shell model treatments accounting for enhanced absorption are commonly used in global climate models but may overestimate BC absorption by up to 30 % due to the shape of BC particles and the position of BC within a coating (Adachi *et al.*, 2010). This overestimation is in-line with Cappa *et al*. (2012), who found that the in-situ-measured absorption enhancement of black carbon was overestimated by up to a factor of 2 when compared to core-shell Mie theory.

1.4.3 Factors that influence the radiative forcing of carbonaceous aerosols: extrinsic properties

I will now evaluate some of the key factors controlling the uncertainty in aerosol radiative forcing associated with extrinsic properties of carbonaceous aerosols. Extrinsic properties depend on the aerosol concentration (e.g. Vaughan *et al.*, 2004) and the geographic distribution of the aerosol in the horizontal and vertical (as demonstrated by Figure 1.9).

1.4.3.1 Emissions inventories

In order to assess the impact that carbonaceous aerosols have on the climate system, climate models must be supplied with emissions data, which depend on source emissions factors such as the amount of fossil fuel used in power-generation plants and the amount of aerosol emitted during specific technological processes or biomass burning conditions (Lamarque *et al.*, 2010). For example, the Global Fire Emissions Database 3 (GFED3) emissions dataset was used to account for biomass burning aerosol emissions in the Coupled Model Intercomparison Project Phase 5 (CMIP5) models for the IPCC AR5 assessment reports (Lamarque *et al.*, 2010; Giglio *et al.*, 2013). To derive the GFED emissions database, burned areas were identified using satellite observations (Giglio *et al.*, 2010) combined with emission factors based on the dataset compiled by Andreae and Merlet (2001). The latest GFED emissions database (GFED4s) is based on an updated burned area product (Giglio *et al.*, 2013), which was able to account for small fires (i.e. with spatial scales < 500 m satellite pixels) as well as an updated aerosol emissions inventory based on extensive smoke measurements that had not undergone significant photochemical processing (Akagi *et al.*, 2011). GFED4s global fire emissions were estimated to be 2.2 Pg C yr^{-1} between 1997–2016 with significant interannual variability (van der Werf *et al.*, 2017). GFED4s carbon emissions estimates were 11 % higher compared to GFED3 during 1997–2016, likely due to the inclusion of small fires. The impact of this uncertainty on aerosol radiative forcing will become apparent in the CMIP6 simulations and the forthcoming IPCC AR6 assessments. Assessing the uncertainties of emissions estimates are difficult to quantify, although were estimated as 50 % for the GFED3 database (van der Werf *et al.*, 2017).

Carbonaceous aerosols are also emitted to the atmosphere from energy-related sources including industrial coal burning and transport (Bond *et al.*, 2013). Emissions inventories representing energy-related sources are often estimated using a 'bottom-up' approach whereby emissions are calculated as the product of activity (for example, the mass of fuel burned) and emission factors (for example, grams of BC emitted per mass of fuel burned) (Bond *et al.*, 2013). Global bottom-up emissions of energy-related BC (i.e. excluding biomass burning) are estimated to be 4800 Gg yr^{-1} with uncertainty bounds 1200 to 15000 Gg yr^{-1}. This range is due to a plethora of poorly-characterised BC sources and factors pertaining to energy-related combustion, which can be highly variable between countries (Bond *et al.*, 2004, 2007, 2013; Junker and Liousse, 2008).

1.4.3.2 Dependence of aerosol vertical structure

The relative vertical positions of clouds and absorbing aerosols can enhance radiative forcing significantly (Haywood and Shine, 1997) and has been found to contribute to diversity in radiative forcing estimates (Zarzycki and Bond, 2010; Samset and Myhre, 2011). Using 12 climate models (AeroCom), Samset *et al*. (2013) estimated that up to 50 % of the diversity in BC radiative forcing is attributable to differences in the BC vertical profile. Schwarz *et al*. (2013) found that model BC concentrations (AeroCom) can be biased high by a factor of 11 (above 500 hPa) and by a factor of 3 (below 500 hPa) when compared to observations, independent of geographical location or season. This overestimation of BC concentration can be explained in part due to an overestimation in BC's atmospheric lifetime (Hodnebrog *et al.*, 2014).

1.4.3.3 Sub-grid variability

Climate models used for estimating aerosol radiative forcing typically have a minimum spatial resolution of ~120 km (Myhre *et al.*, 2013b). These coarse model resolutions do not account for the significant sub-grid variability in, for example, aerosol optical depth and thus represent averages over those areas (Anderson *et al.*, 2003; Weigum *et al.*, 2016). Aerosol optical depths can vary significantly over scales as small as hundreds of metres (Redemann *et al.*, 2005). Weigum *et al*. (2016) found that monthly mean aerosol optical depths could be biased low by up to 30 % when using a climate model with spatial resolution of 10 km compared to 160 km. Biases in aerosol loadings propagate

to biases in radiative forcing, where Gustafson Jr. *et al.* (2011) found a 30 % bias in the daytime aerosol top of atmosphere (TOA) direct radiative forcing for a large percentage of central Mexico when running a climate model at 3 km and 75 km. Neglect of variability in relative humidity, which governs the hygroscopic growth and subsequent aerosol light scattering properties, led to underestimates of the top of atmosphere direct radiative forcing of sulphate aerosol by as much as 73 % in a general circulation model with spatial resolution 160 km compared to a model with spatial resolution 2 km (Haywood *et al.*, 1997a). In terms of black carbon, Weigum *et al*. (2012) quantified the scales of variability of BC plumes over the Pacific Ocean, finding that typical plume scales are between 80 to 100 km. This finding indicates that BC plumes far away from sources are approximately half of the size of current climate model resolutions and whilst still too small to be resolvable, they are certainly within reach as higher resolution models become available.

1.4.4 Measurements for constraining aerosol representation in general circulation models

In this section I will provide an overview of remote sensing and in-situ measurement techniques for determining aerosol optical and microphysical properties that can be used to constrain global climate model representation of aerosols and their associated aerosol-radiation interactions.

1.4.4.1 Surface observation sites

The Global Atmospheric Watch programme takes long-term, ground-based aerosol optical and microphysical measurements including aerosol optical depth (AOD), aerosol vertical profiles, aerosol absorption, scattering and backscattering coefficients, number concentrations, size distributions and chemical composition measurements (Global Atmospheric Watch, 2016). This measurement network quantifies the spatial and temporal variability of aerosol optical properties, which can be used to constrain long-term global climate model simulations (Asmi *et al.*, 2013). Clear limitations of this measurement network is the density of such sites globally, which does not allow trends in aerosol properties to be extrapolated even to regional levels, as well as the financial and human effort required to maintain these sites (Asmi *et al.*, 2013; Collaud Coen *et al.*, 2013). To achieve statistically significant trends, multi-year

records of greater than ~8 years are typically required (Collaud Coen *et al.*, 2013).

1.4.4.2 Passive satellite retrievals of aerosol optical depth and optical properties

AOD is a key property retrieved by passive satellite sensors (Li *et al.*, 2009) and has been used to evaluate and constrain global climate models (e.g. Bellouin *et al.*, 2013). While major advantages of satellite-based observations include that they are global in coverage and have records going as far back as 25 years, uncertainties and biases are introduced to these type of observations due to (i) uncertainties in their calibrations (typically 0.5–5.0 %), (ii) their account of cloud screening, (iii) their assumed aerosol microphysical and optical models and (iv) their treatment of surface albedo (Li *et al.*, 2009). A further drawback of passive observations is that information regarding the vertical profile, mixing state and size distribution of aerosols is limited. Passive remote sensing is generally unable to retrieve aerosol optical depth or aerosol properties when aerosol overlies cloud, which has typically been screened out, although significant research is on-going to allow accurate retrievals in these conditions (Meyer *et al.*, 2015; Peers *et al.*, 2015; Zhang *et al.*, 2016).

1.4.4.3 Ground-based remote sensing

The AERONET program is a ground-based remote sensing network of over 300 well calibrated sun photometers (Holben *et al.*, 1998; Yu *et al.*, 2006). AERONET determines the AOD as well as column integrated size distribution, SSA and Ångström exponent. AERONET has been extensively used to constrain satellite observations and climate model simulations (e.g. Yu *et al.*, 2006; Chung *et al.*, 2012b; Ridley *et al.*, 2016). Limitations of AERONET include that aerosol properties cannot be determined in cloudy conditions or when the AOD is not high enough for almucantar scans, the network has limited spatial coverage and the columnar nature of the retrievals cannot distinguish between aerosols with variable optical properties in different layers in the vertical.

1.4.4.4 Active lidar sensing

The Cloud-Aerosol Lidar with Orthogonal Polarization (CALIOP) satellite instrument can be used to address the issue of uncertainty in aerosol vertical

distribution, which provides global, high resolution vertically resolved aerosol and cloud backscatter observations with a swath width ~ 30 m at wavelength 532 nm (Winker *et al.*, 2007; Kacenelenbogen *et al.*, 2011). Although a number of studies have used CALIOP to determine aerosol vertical profiles and AOD, there exists uncertainty within the retrieval of these properties, which require validation (Kacenelenbogen *et al.*, 2011 and references therein; Winker *et al.*, 2013; Young *et al.*, 2013). A further drawback of this type of measurement is the small swath width of the retrieval, which only provides a snapshot of aerosol and cloud properties for any given overpass.

1.4.4.5 In-situ measurements of aerosol optical properties

Traditionally, during both long-term ground-based monitoring (Collaud Coen *et al.*, 2013 and references therein) and during dedicated airborne measurement campaigns (e.g. Haywood *et al.*, 2003b; Osborne *et al.*, 2008; Johnson *et al.*, 2016), aerosol absorption coefficients have been retrieved using filter-based absorption photometry. This technique relies on determining the change in light transmittance across a particle-laden filter. This technique is subject to biases and, although a range of correction schemes have been proposed (Bond *et al.*, 1999; Weingartner *et al.*, 2003; Arnott *et al.*, 2005; Virkkula *et al.*, 2005; Schmid *et al.*, 2006; Collaud Coen *et al.*, 2010; Virkkula, 2010; Müller *et al.*, 2014), aerosol absorption biases in the range of 20–200 % can remain (Cappa *et al.*, 2008; Lack *et al.*, 2008; Backman *et al.*, 2014; Müller *et al.*, 2014). See Chapter 4 for more details regarding biases in filter-based absorption measurements.

Similarly, nephelometry has typically been used to measure the aerosol scattering coefficient with uncertainties in the range 5–50 % (Anderson *et al.*, 1996; Heintzenberg and Charlson, 1996). Upon combination of these absorption and scattering coefficient measurements, Massoli *et al*. (2009) showed large uncertainties in the aerosol SSA can arise in the range 3 % (SSA=1) rising to 30 % (SSA=0.4). Massoli *et al*. (2009) further showed that deriving the SSA from independent measurements of the absorption coefficient using photoacoustic spectroscopy and extinction coefficient using cavity ring-down spectroscopy leads to significantly lower uncertainties in the range < 1 % at SSA=1 rising to 8 % at SSA=0.4.

While advancements in aerosol optical measurements through airborne photoacoustic spectroscopy and cavity ring-down spectroscopy have proved successful and provide sensitive and accurate absorption and extinction coefficients, their spatial representativeness is a major disadvantage (Langridge *et al.*, 2011; Lack *et al.*, 2012a).

1.5 Summary and aims of this thesis

The overarching aim of this thesis is to reduce the uncertainty surrounding aerosol radiative forcing and hence the uncertainty that aerosols introduce to future climate change scenarios. The three main research areas covered throughout this thesis include:

1. Developing state-of-the-art instrumentation for the measurement of aerosol optical properties and quantifying the accuracy of these measurements whilst simultaneously verifying the accuracy of the instrument calibration procedure.
2. Evaluating biases in filter-based absorption photometry measurements by comparison to state-of-the-art instrumentation for a range of aerosol sources.
3. Evaluating the sensitivity of the direct radiative effect to aerosol and cloud optical depths using a combination of offline radiative transfer modelling, satellite observations and global climate models simulations. The focus is on biomass burning aerosols over the Southeast Atlantic Ocean.

2 EXSCALABAR (EXtinction, SCattering and Absorption of Light for AirBorne Aerosol Research)

Components of this chapter are based on the following publication, a copy of which is provided in Appendix D: Davies, N. W. *et al.* (2018) 'On the accuracy of aerosol photoacoustic spectrometer calibrations using absorption by ozone', *Atmospheric Measurement Techniques*, 11(4), pp. 2313–2324. doi: 10.5194/amt-11-2313-2018.

Table of contents

2.1 Chapter overview

In this chapter I will introduce EXSCALABAR, a state-of-the-art suite of instruments used for the measurement of aerosol optical and physical properties. This chapter begins with an overview of EXSCALABAR's measurement capabilities followed by detailed descriptions of each instrument, namely the photoacoustic and cavity ring-down spectrometers, including details of the relevant underlying physics. I then assess the performance of these instruments.

2.2 Instrument description

2.2.1 Overview

EXSCALABAR measures a range of aerosol optical and physical properties as summarised in Table 2.1. The general instrument design was based on the design by Langridge *et al.* (2011) and Lack *et al.* (2012a) although there have been various modifications to the mechanical layout of the optical enclosure, optical cell designs, number of cells and the flow system.

Aerosol absorption and extinction coefficients are measured using photoacoustic spectroscopy (PAS) and cavity ring-down spectroscopy (CRDS) respectively at fixed visible wavelengths within the range 405 to 658 nm. Absorption coefficients are measured for ambient and thermally denuded aerosols, enabling evaluation of the enhanced absorption due to the lensing effect as well as attribution of absorption to black and brown carbon. Aerosol extinction coefficients are measured under dry conditions (< 30 % relative humidity) and at elevated relative humidity (70 % and 90 %), enabling evaluation of the dependence of aerosol extinction on hygroscopic growth at 405 nm. Ambient aerosol absorption coefficients are also measured using filter-based absorption photometry, namely a commercially available Tricolor Absorption Photometer (TAP) (Brechtel, 2901), facilitating direct comparison between PAS and filter-based absorption photometry. A detailed description of the TAP and an assessment of its performance in terms of measurement accuracy and minimum sensitivity will be provided in Chapter 4. Aerosol size distributions are measured using an optical particle counter, namely a commercially available Passive Cavity Aerosol Spectrometer Probe (PCASP) (DMT, PCASP-100X). The PCASP-100X has been used for measuring the size distributions of aerosols including from airborne platforms for many years (e.g. Haywood *et al.*, 2003, 2008; Ryder *et al.*, 2013; Johnson *et al.*, 2016) and its performance will not be documented here.

Instrument	**Measurement**	**Wavelengths (nm)**	**Conditioning**
Photoacoustic spectrometers	Absorption coefficient	405, 514, 658	Dry (< 30 %), thermally denuded

Cavity ring-down spectrometers	Extinction coefficient	405, 658	Dry (< 30 %), elevated relative humidity (70 %, 90 %)
Tricolor Absorption Photometer	Absorption coefficient	467, 528, 652	Dry (< 30 %)
Passive Cavity Aerosol Spectrometer Probe – 100X	Aerosol size distribution	632.8	Dry (< 30 %)

Table 2.1: *EXSCALABAR optical and physical measurements.*

The EXSCALABAR instrument is fitted to two aircraft racks as shown in Figure 2.1. The photoacoustic and cavity ring-down spectrometers are located within an optical enclosure (the black box in Figure 2.1; Figure 2.2), which is in turn mounted to an aircraft rack using anti-vibrational mounts. This rack also contains the TAP, PCASP, flow conditioning (including thermal denuder, particle filter and mass flow controllers), water cooling system (used to remove the heat from the lasers and thermoelectric coolers used for temperature regulation throughout the instrument), humidification system and computer systems. The second aircraft rack contains a sample pump, ozone generation equipment, power supplies, further flow system components and oxygen and zero-air cylinders.

Figure 2.1: *The EXSCALABAR instrument fitted to the Facility for Airborne Atmospheric Measurements (FAAM) research aircraft.*

Figure 2.2: *Inside the EXSCALABAR instrument's optical enclosure. The instruments on the left are the photoacoustic spectrometers and those on the right are the cavity ring-down spectrometers.*

2.2.2 Flow system

Ambient aerosol is sampled from a common inlet at a volumetric flow rate of 8 litres per minute (L min^{-1}) where it is dried to < 30 % relative humidity (Permapure, PD100T-12MSS), stripped of absorbing gaseous species including ozone and nitrogen dioxide (MAST Carbon) and passed through a 1.3 μm aerodynamic diameter impactor (Brechtel, custom design) to remove super-micron particles. A series of flow splits (Brechtel, 1110 and 1104) evenly distribute the aerosol-laden stream between the suite of instruments, which

each sample the aerosol at a volumetric flow rate of 1 L min^{-1}, as shown in Figure 2.3. For the thermally denuded PAS measurements, the aerosol-laden stream flows first through a catalytic stripper (Catalytic Instruments, CS015) which is heated to 350 °C to remove volatile species from the aerosol. The thermal denuder can be optionally bypassed during sampling by using a pair of automated ball valves (Hanbay, MDM-060DT). For the humidified extinction measurements, the aerosol-laden stream flows first through a custom-built humidifying system whereby deionised water is circulated around a Nafion membrane (Permapure, MD-100), which permeates through the membrane as the sample flows through it. Varying the temperature of the water controls the relative humidity. The gas-phase extinction coefficient is measured at 405 nm. Given the use of an inlet scrubber, this channel serves as nothing more than a check to ensure full removal of absorbing gaseous species. The PCASP uses an isokinetic pickoff with a volumetric flow rate of 0.06 L min^{-1}. Sample flow can be optionally diverted through a particle filter to characterise the background, i.e. particle-free, signal in all cells. Filtered zero-air flows across the mirrors in the cavity ring-down spectrometers at a flow rate of 0.01 L min^{-1} per mirror to prevent particle contamination. A diagram of the full flow system is provided in Appendix A.

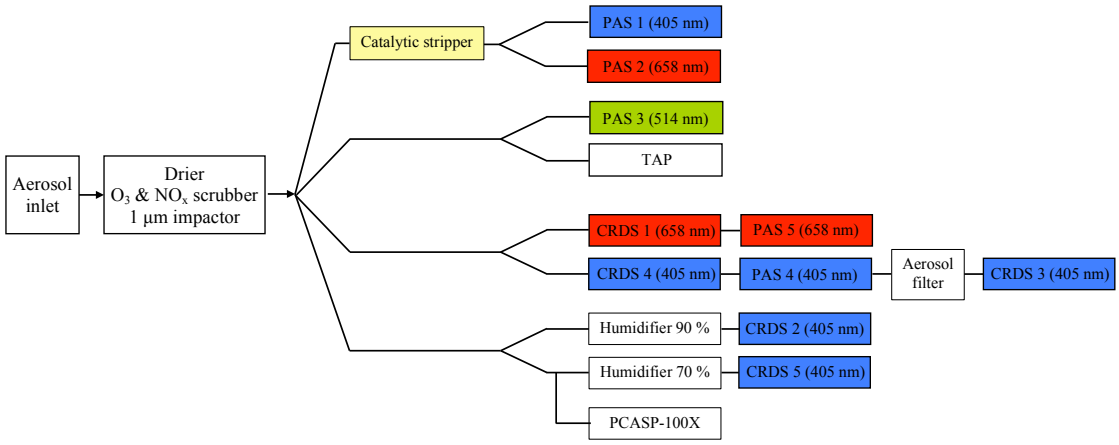

Figure 2.3: *EXSCALABAR flow diagram indicating the relative positions of the PAS and CRDS cells, optical particle counter (OPC) and TAP. Figure adapted from Fox et al. (2017).*

Ozone is used to calibrate the PAS cells and full details relating to this calibration procedure can be found in Chapter 3. For calibration of the PAS cells, ozone is generated using a coronal discharge ozone generator (Longevity Resources, EXT120-T) from high purity oxygen (99.999 %, BOC, grade N5.0). The ozone-laden stream is split approximately evenly between the PAS and

CRDS cells using a manifold equipped with 300 µm diameter orifices, as shown in Figure 2.4. Teflon tubing is used throughout the ozone flow system to minimise contamination and to reduce ozone losses. During calibration, sample flow is passed first through a pressure controller (Alicat Scientific, PC series), which can be used to lower the pressure in the entire instrument. This functionality allows the pressure dependence of the PAS calibrations to be evaluated, which is useful if taking measurements at altitudes other than ground-level, for example when on board the Facility for Airborne Atmospheric Measurements (FAAM) research aircraft.

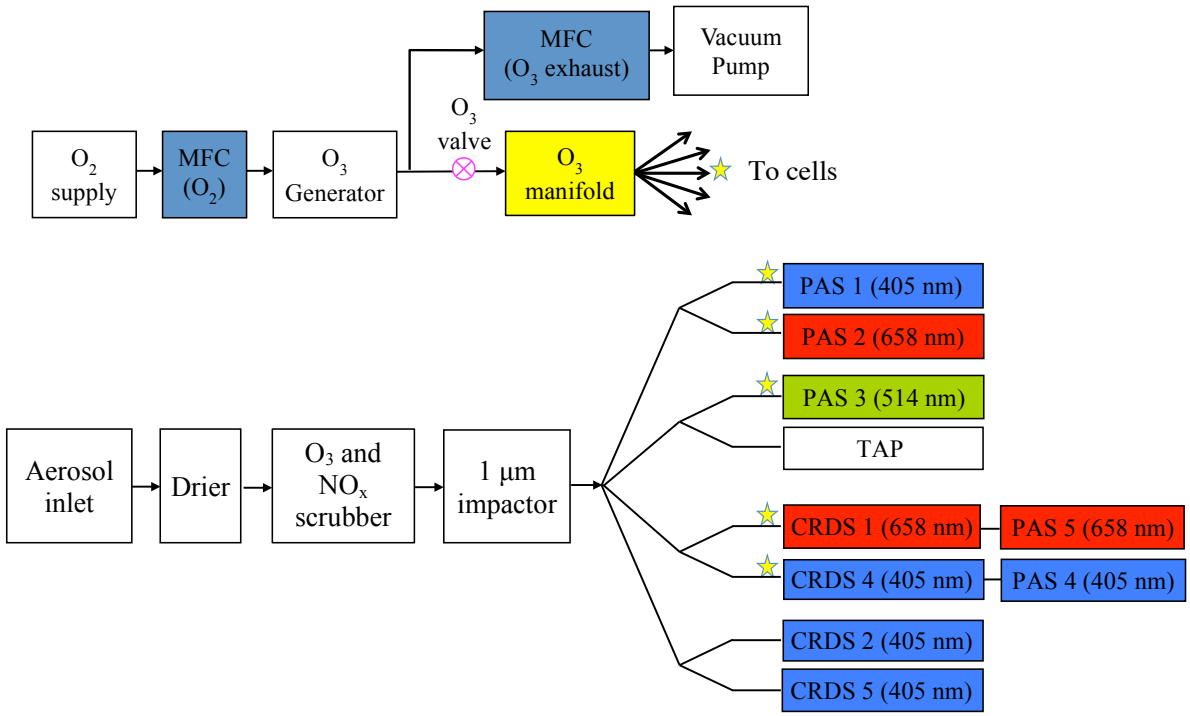

Figure 2.4: *Schematic diagram of the ozone generation system. The stars indicate the ozone flow path, which enters the cells through different ports to the main aerosol flow. The PAS/CRDS wavelengths are centred at 405, 514 and 658 nm respectively. Abbreviations: 'MFC': mass flow controller.*

All flow rates are controlled using mass flow controllers (Alicat Scientific, MC series), which are pumped using a Varian scroll pump (IDP-3). The exhaust stream is dried using silica gel and scrubbed for ozone before leaving the instrument.

2.3 Cavity ring-down spectroscopy (CRDS)

2.3.1 Principles of CRDS

Cavity ring-down spectroscopy (CRDS) is a highly sensitive technique used to measure the optical extinction coefficients of gases and particulate matter (O'Keefe and Deacon, 1988; Romanini *et al.*, 1997) without the need for instrument calibration (e.g. Miles *et al.*, 2011). Although a number of variants of CRDS exist (Brown, 2003), this description will focus on continuous-wave CRDS pertinent to the EXSCALABAR instrument. A central component of CRDS is a cavity bounded by two highly reflective mirrors. Laser light incident on the front mirror (closest to the laser) leads to a build up of light intensity within the cavity that, upon reaching a threshold value, is rapidly switched off. The relative light intensity exiting the cavity through the back mirror (furthest from the laser) is measured using a photomultiplier tube (PMT). The PMT signal decays exponentially with time as light is attenuated due to absorption and scattering by gaseous and aerosol species within the cavity, mirror transmittance loss and diffraction loss. Measuring the decay rate of light intensity exiting the cavity as opposed to the absolute change in intensity ensures independence from any fluctuations in laser power thus avoiding the need for a stable laser source and the uncertainty associated with shot-to-shot variability (Meijer *et al.*, 1994). Ensuring that the laser is turned off rapidly (order < 10 nanoseconds) relative to ring-down events (order several hundred microseconds) avoids the need for fast external optical switching devices for the attenuation of laser light (Langridge *et al.*, 2011). Figure 2.5 describes the key components of a cavity ring-down spectrometer. An optical isolator (Faraday rotator) prevents back-reflections re-entering the laser, which can cause damage. A purge gas flow prevents aerosol deposition onto the mirrors, which would lead to loss of sensitivity and potentially multi-exponential ring-down events.

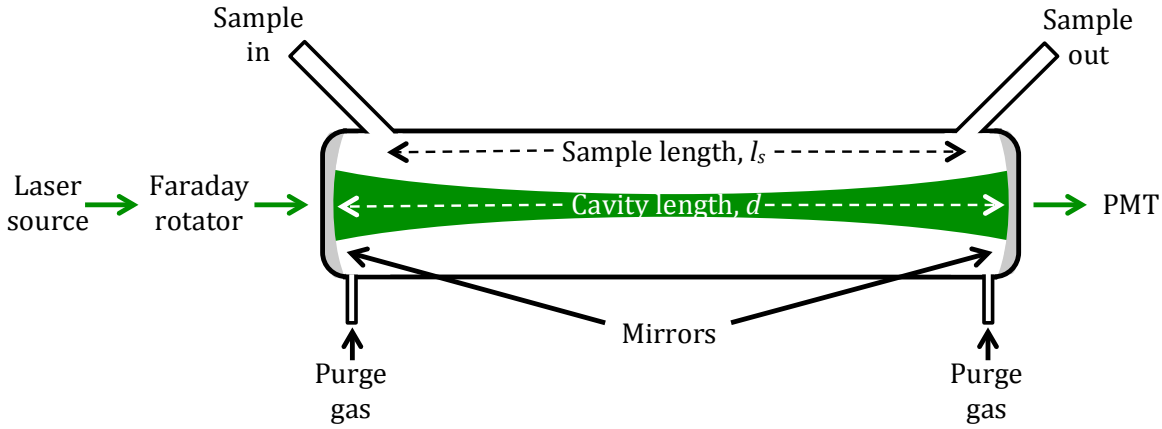

Figure 2.5: *Key components of a cavity ring-down spectrometer.*

2.3.1.1 Ring-down time

The Beer-Lambert law describes how the light intensity, I, changes as it propagates through an optically active species, i.e. one that absorbs and/or scatters light, and can be expressed as

$$I(z,\lambda) = I_0 \exp(-\sigma_{ext} N z), \tag{2.1}$$

where σ_{ext} is the extinction cross section (units m^2), N is the particle number density (units m^{-3}) or molecular density (units *molecules* m^{-3}) and z (units *m*) is the path length through the sample (Seinfeld and Pandis, 2006). The light intensity exiting a cavity ring-down spectrometer can be expressed as

$$I(t,\lambda) = I_0 exp\left(\frac{-t}{\tau(\lambda)}\right), \tag{2.2}$$

where I_0 is the light intensity exiting the cavity immediately after the laser has been switched off, *t* is the time since the laser has been switched off, $\tau(\lambda)$ is the 'ring-down' time, defined as the time taken for the transmitted light intensity to fall by a factor 1/e, and λ is the wavelength of light (e.g. Romanini and Lehmann, 1993; Zalicki and Zare, 1995; Wheeler *et al.*, 1998; Brown, 2003). For a cavity containing an optically active species, the ring-down time can be expressed as

$$\tau(\lambda) = \frac{d}{c(\mathcal{T}(\lambda) + \mathcal{L}(\lambda) + b_{ext}(\lambda) l_s + \alpha_R(\lambda) d)} \tag{2.3}$$

and for a cavity without an optically active species this reduces to the 'empty cavity ring-down time' (Brown, 2003), given by

$$\tau_0(\lambda) = \frac{d}{c(\mathcal{T}(\lambda) + \mathcal{L}(\lambda) + \alpha_R(\lambda)d)} \tag{2.4}$$

where d is the distance between the mirrors, c is the speed of light, $\mathcal{T}(\lambda)$ is the mirror transmittance, $\mathcal{L}(\lambda)$ is the mirror diffraction loss, $b_{ext}(\lambda)$ is the extinction coefficient (units m^{-1}) of the optically active gaseous or aerosol species, l_s is the cavity length occupied by the optically active species (units m) and $\alpha_R(\lambda)$ is the Rayleigh scattering coefficient (units m^{-1}).

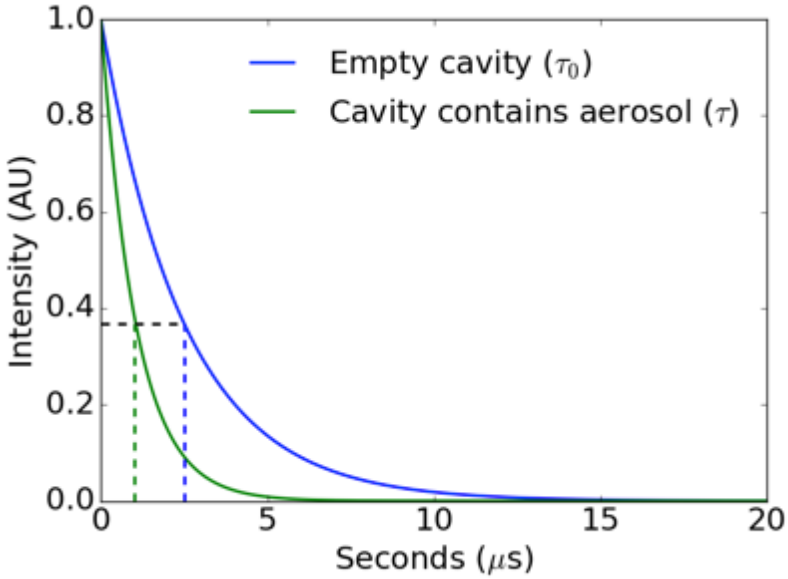

Figure 2.6: *Modelled exponential decay of light intensity within a cavity ring-down spectrometer with and without an optically active species.*

Manipulating equations 2.3 and 2.4 leads to an expression for the extinction coefficient,

$$b_{ext}(\lambda) = \frac{d}{l_s c}\left(\frac{1}{\tau(\lambda)} - \frac{1}{\tau_0(\lambda)}\right), \tag{2.5}$$

where the two ring-down times τ and τ_0 are determined by fitting an exponential decay to the associated ring-down events using equation 2.2. Figure 2.6 demonstrates how the light intensity within a cavity ring-down spectrometer decays exponentially for an empty cavity and for a cavity containing an optically active species.

2.3.1.2 The stability criterion

A stable resonant optical cavity is needed to perform sensitive CRDS measurements, and is readily achieved by trapping a laser beam between

focusing spherical concave mirrors. The focal length, f, for a curved mirror is defined as (Kogelnik and Li, 1966)

$$f = \frac{R}{2} \tag{2.6}$$

where R is the mirror radius of curvature. A cavity is stable if the mirror foci lengths are both greater than half of the mirror separation, as Figure 2.7 shows. The stability criterion for a resonant cavity is thus defined as

$$0 < g_1 g_2 < 1 \tag{2.7}$$

where g_1 and g_2 are the stability parameters, defined as

$$g_{1,2} = \frac{d}{R_{1,2}}, \tag{2.8}$$

where R_1 and R_2 are the mirror radii of curvature corresponding to g_1 and g_2 respectively and d is the mirror spacing (Kogelnik and Li, 1966).

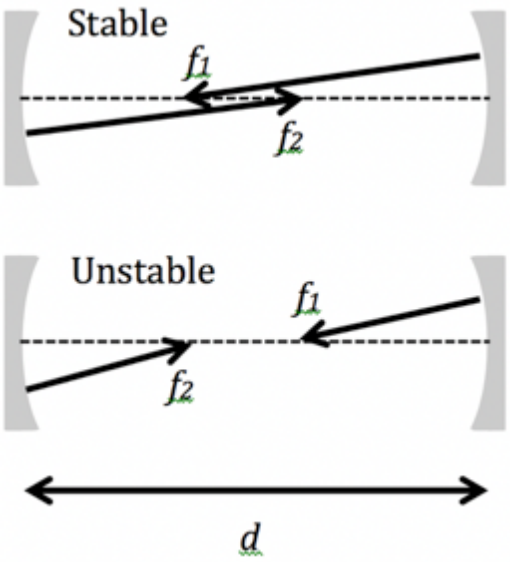

Figure 2.7: *Stability conditions for a resonant cavity with mirror spacing, d, and mirror curvature radii, $R_{1,2}$, leading to mirror foci points, $f_{1,2}$.*

2.3.1.3 Cavity mode structure

Resonant optical cavities are inherently frequency selective independent of the laser pulse bandwidth such that only a discrete number of frequencies are supported, known as the 'transverse' and 'longitudinal' modes of propagation or more formally as the transverse-electromagnetic (TEM) modes (Hodges *et al.*, 1996; Lehmann and Romanini, 1996; Martin *et al.*, 1996). Transverse modes

arise due to interference in a plane perpendicular to the direction of light propagation due to self-reproducing amplitude and phase distributions (Siegman, 1986). Figure 2.8 shows the spatial intensity patterns associated with several low-order transverse modes in a plane perpendicular to the direction of light propagation.

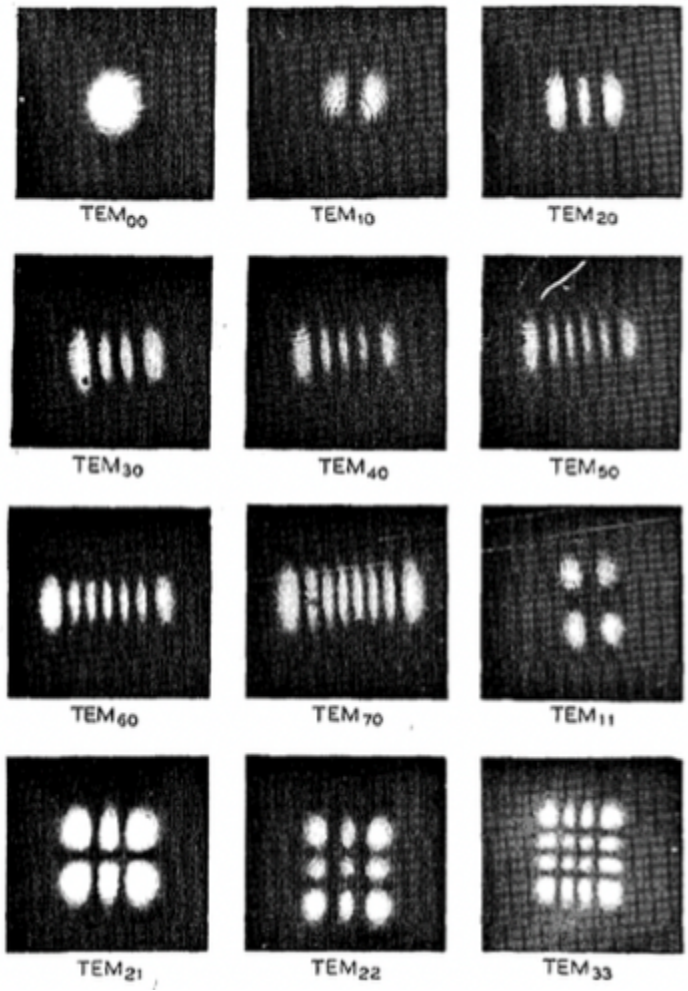

Figure 2.8: *Spatial intensity patterns of light exiting a rectangular cavity associated with some of the low-order transverse-electromagnetic (TEM) modes looking in a plane perpendicular to the axis of light propagation. Figure from Kogelnik and Li (1966).*

It follows that interference in frequency space described by Fabry-Perot theory leads to longitudinal modes of propagation along the axis of light propagation (Zalicki and Zare, 1995). These TEM modes satisfy the round-trip phase shift condition such that,

$$q\pi = \frac{2dv\pi}{c} - (m+n+1)arccos\left(\sqrt{g_1 g_2}\right), \qquad (2.9)$$

where q, m and n are integers, leading to constructive and destructive

interference of frequency components, and ν is the laser light frequency; the right hand term accounts for the additional phase shift induced by the spherical mirrors (Kogelnik and Li, 1966). Figure 2.9 describes four possible longitudinal modes associated with a particular transverse mode along the axis of light propagation between the two mirrors. These longitudinal modes were generated using equation 2.9 for $q = 1$, 2, 3 and 4 such that the phase change over the length of the cavity equals $q\pi$ (Hodges *et al.*, 1996). The black line corresponds to the fundamental longitudinal mode ($q = 1$). The blue, green and red lines correspond to q=2,3 and 4, respectively.

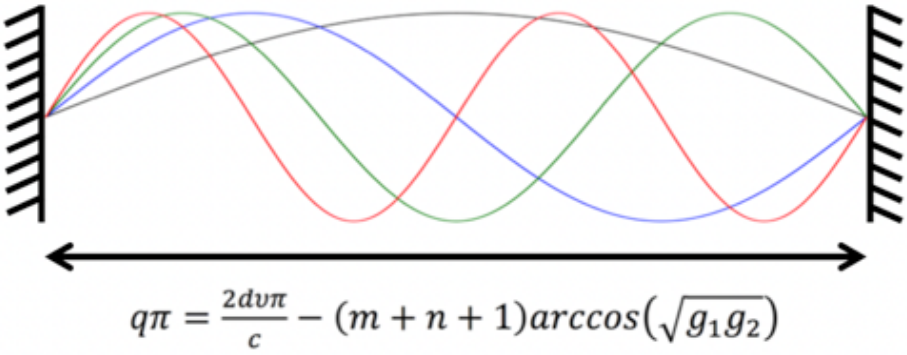

Figure 2.9: *An example of four possible cavity longitudinal modes associated with a particular transverse mode.*

It follows that the resonant frequencies supported by a cylindrical cavity are

$$\nu_{qmn} = \frac{c}{2d}\left[q + \frac{(m+n+1)}{\pi} arccos\sqrt{g_1 g_2}\right], \qquad (2.10)$$

where ν_{qmn} are the resonant frequencies. The widths of the resonant modes are defined as

$$\Delta\nu_{FWHM} = \frac{c(1-\mathcal{R})}{2d\pi\sqrt{\mathcal{R}}}, \qquad (2.11)$$

from which the finesse of the cavity, $\mathcal{F}$ can be defined as

$$\mathcal{F} = \frac{FSR}{\Delta\nu_{FWHM}} = \frac{\pi\sqrt{\mathcal{R}}}{(1-\mathcal{R})}, \qquad (2.12)$$

where $\mathcal{R}$ is the reflectivity of the mirrors and FSR (free spectral range) is the frequency separation between adjacent longitudinal modes, equal to c/2d

(Lehmann and Romanini, 1996). A high finesse cavity is characterised by both a high resolving power and low losses/high recirculating power (Siegman, 1986).

To observe an absorption feature, or similarly extinction due to scattering particulate matter, there must be an overlap in frequency space between the absorption feature, the laser frequency and at least one resonant cavity mode. Absorption features can be missing altogether if the absorption frequency falls between adjacent cavity modes. Therefore it is important to assess the relative sizes and overlaps of the laser bandwidth, $I(\nu)$, the absorption feature linewidth, $b_{ext}(\nu)$, and the cavity resonant frequencies, ν_{qmn}. The absorption linewidth must be at least a factor two larger than the laser bandwidth to ensure a first order rate constant such that Beer's law is valid and a purely exponential decay of light intensity ensues, dependent on the strength of absorption of the sample (Zalicki and Zare, 1995). Figure 2.10 succinctly describes the overlap condition between the three components, where ω is equivalent to ν_{qmn} in equation 2.10, and where $\alpha(\omega)$ is equivalent to $b_{ext}(\nu)$. Overlap of the three components ensures that the absorption feature will be observed. The absorption feature is broad relative to the laser bandwidth, hence Beer's law is valid and a purely exponential decay of light intensity ensues (Zalicki and Zare, 1995).

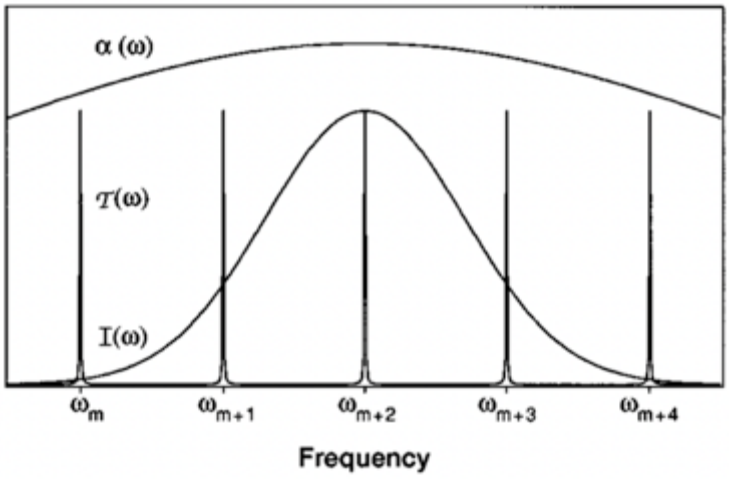

Figure 2.10: *The frequency overlap condition for the laser bandwidth, absorption feature and cavity resonant modes. The absorption feature is represented by* $\boldsymbol{\alpha(\omega)}$*, the laser profile by* $\boldsymbol{I(\omega)}$ *and the position of cavity longitudinal modes by* $\boldsymbol{\omega}$*. Figure from* Zalicki and Zare (1995).

Using a pulsed or multi-mode diode laser source with a broad bandwidth

ensures overlap of many cavity resonant modes. Assuming that only a single transverse mode is excited, each of the associated longitudinal modes that overlap the laser pulse frequency will contribute to the transmitted intensity. A broad absorption feature, $b_{ext}(\nu)$ >> $I(\nu)$, can be considered constant over the pulse bandwidth such that the coupling into each cavity mode is equal; this condition ensures that all modes decay equally leading to a single exponential decay of the transmitted intensity. Significant deviation from an exponential decay occurs if the width of the absorption feature approaches the laser bandwidth due to the variable coupling strength in to each resonant mode; in this case the intensity decay would be non-exponential (Zalicki and Zare, 1995; Hodges *et al.*, 1996).

Thus far it has been assumed that only the fundamental transverse mode, TEM_{00}, is active within the cavity. This condition can be achieved by spatially shaping the laser pulse using a pinhole iris and ensuring accurate on-axis injection into the cavity, i.e. perpendicular to the mirror surface (Scherer *et al.*, 1997). There also exist laser sources which emit specific TEM_{mn} modes. Figure 2.8 provides examples of several low-order transverse modes. However, multiple transverse mode excitation can lead to multi-exponential ring-down decays, even in the absence of absorbing or/and scattering species; this multi-exponential behaviour is caused by mode-dependent attenuation due to variable mirror diffraction loss and imperfect mirror reflectance. Each transverse mode experiences a varying level of diffraction as it travels through the cavity leading to different mirror 'spill over' in which energy is lost due to the finite extent of the mirror (Siegman, 1986). Furthermore, the varying spatial profiles of each transverse mode can interact with different areas of the mirror leading to loss of energy due to non-uniformity in the mirror reflectance due to imperfect coating and particle deposition on the mirror surface (Lehmann and Romanini, 1996).

Aerosol absorption features, $b_{ext}(\nu)$, are broad relative to, for example, molecular absorption features and thus overlap with many cavity resonance modes, which avoids the requirement for careful cavity design to ensure that the absorption features do not fall between cavity modes, as is possible for molecular absorption lines (Berden *et al.*, 2000).

2.3.2 EXSCALABAR CRDS design

2.3.2.1 Mechanical layout

The CRDS cells, including the cavities, lasers, optical detectors and mirrors, are mounted to a carbon fibre cage located within the optical enclosure as shown in Figures 2.2, 2.11 and 2.12. The cage is split into two layers to ensure that all five CRDS cells fit physically into the optical enclosure. All lasers (Toptica, iBeam Smart-S) are continuous wave diode lasers and are protected from back-reflections using Faraday isolators (Thorlabs, IO-5-405-LP and IO-3D-660-VLP). A 658 nm laser (130 mW) pumps the red cell, a 405 nm laser (120 mW) pumps an elevated relative humidity blue cell and a second 405 nm laser (300 mW) pumps the three remaining blue cells as shown in Figures 2.11 and 2.12. Laser wavelengths and line widths were measured using an Avantes spectrometer (CompactLine) for the blue wavelengths and a Hamamatsu spectrometer (C11697MB) for red wavelengths. The high-reflectivity CRDS mirrors are located within an optical mount that is anchored directly to the carbon fibre cage. Actuators allow the positions of the mirror mounts to be moved forwards or backwards, one corner at a time, to adjust the angle of the mirrors. Optimisation of the mirror alignment maximises the path length of the laser beam through the CRDS cells.

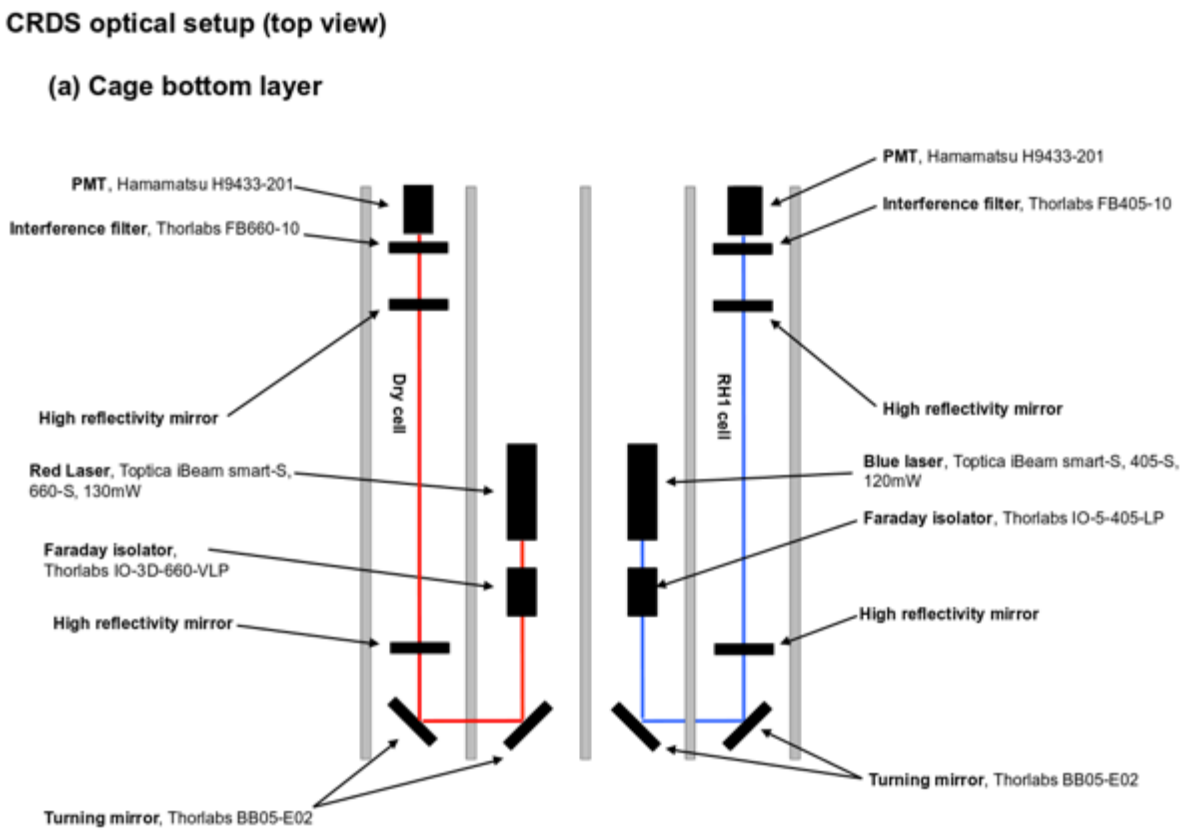

Figure 2.11: *Layout of CRDS components and their positions within the carbon fibre cage (bottom layer).*

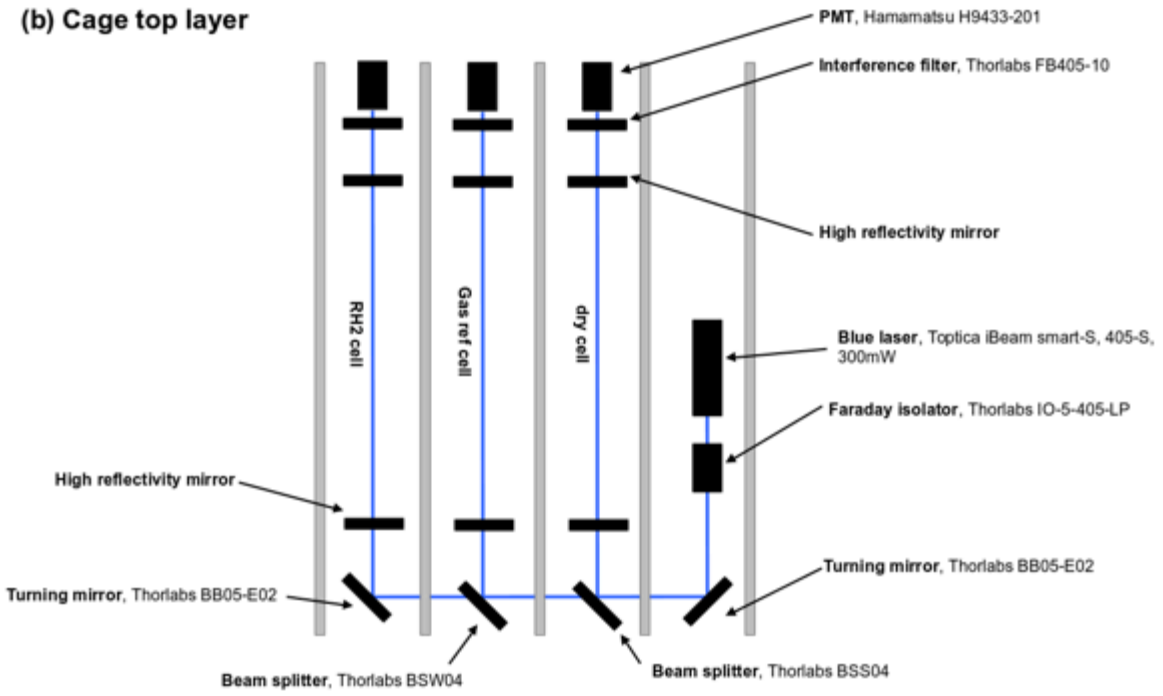

Figure 2.12: *Layout of CRDS components and their positions within the carbon fibre cage (top layer).*

A computer-aided design drawing highlighting the key features of the EXSCALABAR CRDS cells is shown in Figure 2.13. All cells are located within a carbon fibre cage, as shown in Figures 2.11 and 2.12.

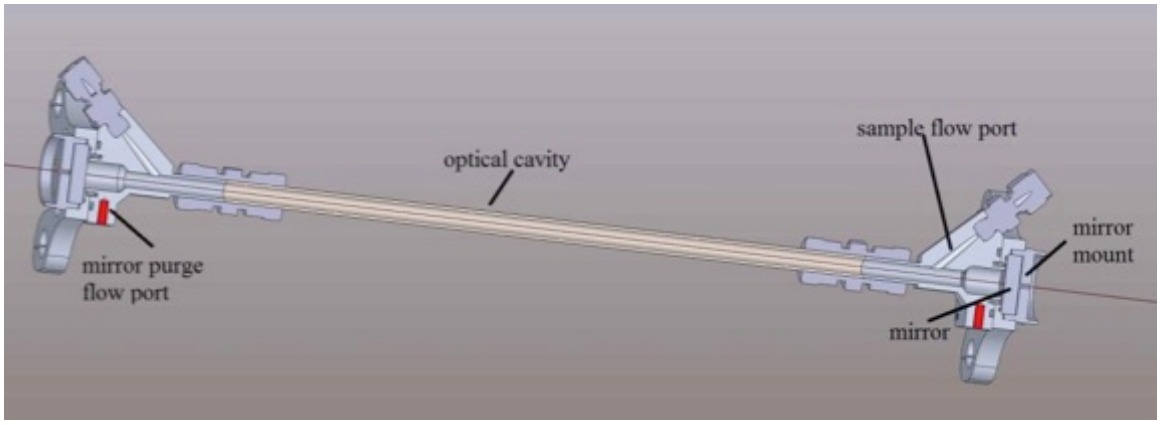

Figure 2.13: *CRDS cell design in the EXSCALABAR instrument.*

Cavity mirrors are manufactured from fused silica with wavelength-specific coatings, 25 mm diameter, radii of curvature of 1 m and reflectivities in excess of 99.99 % (Layertec GmbH, red 660 nm; CVI Laser Optics, blue 405 nm). A high purity zero-air flow (BOC, 270028-L) set to 10 cm^3 min^{-1} per mirror is introduced across the mirrors to prevent particle contamination. The CRDS cells are manufactured out of aluminium. Lasers are operated with square wave modulation at a frequency of 2000 Hz. The laser spectral widths are > 100 GHz and much larger than the free spectral range of the optical cavities (~ 350–400 MHz). These broad laser spectral widths allow passive coupling to occur rather than relying on an active mechanism to match the laser frequency to a cavity mode. Photomultiplier tubes detect light exiting the cavity (Hamamatsu, H9433-201) at a rate of 2.5–4.0 MHz, dependent on the CRDS cell, and were protected from stray light using narrow band interference filters (Thorlabs, FB405-10 and FB660-10). Each time the laser is turned off, the digitised PMT voltage signal decays exponentially. Each ring-down event is recorded for 250 µs. The signal is fitted to a single exponential function to extract the cavity ring-down time using a Fast Fourier Transform fitting algorithm, which enables significantly faster exponential function fitting compared to, for example, the Levenberg-Marquardt algorithm (Everest and Atkinson, 2008). Cavity mirror-to-mirror lengths range from 371 to 423 mm yielding geometric R_L factors in the range 1.150 to 1.173. The R_L factors appropriate for aerosol measurements were determined from the geometric dimensions of the detection cells. As highlighted by Fuchs *et al.* (2008), the R_L factor for detection of gaseous species can be

different from this value, due to the ability of gaseous samples to diffuse. The gaseous R_L factors were evaluated by measuring the change in the ring-down times for filtered air plus ozone in (i) standard operation whereby ozone partially diffuses into the volume between the sample inlet and mirror and (ii) non-standard operation whereby ozone filled the entire mirror-to-mirror length of the cavity. This procedure resulted in R_L factors 1.05 (658 nm) and 1.04 (405 nm).

2.4 Photoacoustic spectroscopy

2.4.1 Principles of photoacoustic spectroscopy

The PAS principle relies on converting energy from a light source into sound, as highlighted in Figure 2.14 (Moosmüller *et al.*, 2009). Light-absorbing media, such as aerosol, transfer electromagnetic energy into thermal energy that heats the surrounding air. This gaseous heating generates a pressure wave that propagates radially away from the heated aerosol particle (Moosmüller *et al.*, 2009).

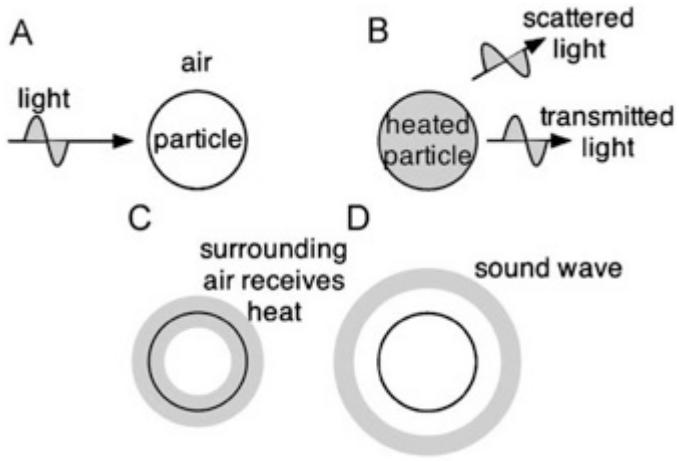

Figure 2.14: *The photoacoustic effect where (A) light is incident upon an aerosol, (B) the aerosol absorbs part of the incident light leading to heating, (C) the air surrounding the aerosol increases in temperature and (D) the surrounding air expands leading to a pressure wave. Figure from Moosmüller et al. (2009).*

The acoustic signal generated when a particle absorbs light can be amplified using an acoustic resonator such that the periodic heating of the sample, driven by an intensity-modulated light beam, is performed at the same frequency as a standing acoustic (pressure) wave eigenmode of the acoustic resonator (Miklós *et al.*, 2001). The eigenmode structure within a cylindrical acoustic resonator

can be described using standing wave theory, such that the resonant frequencies occur at

$$F_{jmq} = \frac{c}{2}\left[\left(\frac{\alpha_{jm}}{R}\right)^2 + \left(\frac{q}{L}\right)^2\right]^{\frac{1}{2}}, \qquad (2.13)$$

where c is the speed of sound, α_{jm} is the jth zero of the mth Bessel function divided by π (where j and m are integers representing the radial and azimuthal resonant modes, respectively), q is an integer number representing the longitudinal resonant modes, R is the resonator radius and L is the resonator length. For the acoustic resonators in EXSCALABAR (see section 2.4.2), the radial and azimuthal modes of propagation would occur at significantly higher frequencies than the longitudinal modes of propagation, of the order ~10000 Hz as opposed to ~1000 Hz, respectively, calculated using equation 2.13. Therefore, if the length of a resonator is much larger than its radius, the acoustic field generated can be assumed to be composed of longitudinal modes only (Miklós *et al.*, 2001). Hence these radial and azimuthal resonances will not interfere with the longitudinal resonances and can be ignored. It follows that the resonant frequencies corresponding to the longitudinal standing pressure waves within a cylindrical cavity can be approximated as

$$F_q = \frac{qc}{2(l + \Delta l)}, \qquad q = 1,2,3, \ldots \qquad (2.14)$$

where $\Delta l = 0.6R$ is the end correction due a mismatch between the 1D field inside the resonator and 3D field outside (in the buffer volume in the EXSCALABAR PAS design; see section 2.4.2), where R is the radius of the resonator (Miklós *et al.*, 2001). Excitation of a PAS cell eigenmode over repeated heating cycles amplifies the photoacoustic pressure signal for detection by a microphone located within the PAS cell (Arnott *et al.*, 1999; Miklós *et al.*, 2001; Moosmüller *et al.*, 2009).

When the light source is operated at a resonant frequency of the acoustic resonator, the pressure at the microphone can be expressed as

$$p = C_n(F_n) b_{abs} P_L, \qquad (2.15)$$

where b_{abs} is the absorption coefficient of the gaseous or aerosol species within the resonator, P_L is the laser power and $C_n(F_n)$ is the cell constant, which describes the sensitivity of the photoacoustic resonator at a given cell resonance frequency, F_n, where $n = jmq$ (Miklós *et al.*, 2001). In theory, for a cylindrical cavity with a resonance quality factor, Q > 50, the cell constant is equal to

$$C_n(F_n) = \frac{(\gamma - 1)Q}{A\pi^2 F_n}, \tag{2.16}$$

where γ is the ratio of isobaric to isochoric specific heats of air, Q is the cell quality factor and A is the cross-sectional area of the resonator (Arnott *et al.*, 1999; Miklós *et al.*, 2001). Equation 2.16 leads to the widely applied formula for photoacoustic spectroscopy within a cylindrical resonator (Arnott *et al.*, 1999),

$$b_{abs} = \frac{P_m}{P_L}\frac{A}{\gamma - 1}\frac{\pi^2 F_n}{Q}, \tag{2.17}$$

where P_m is the microphone signal. The amplitude of the microphone signal at the modulation frequency is linearly related to the sample absorption coefficient. Therefore the microphone signal can be readily calibrated to yield sample absorption directly (e.g. Arnott *et al.*, 2000; Lack *et al.*, 2006, 2012; Schmid *et al.*, 2006). In Chapter 3, I provide details regarding PAS calibrations.

Multi-pass optics are used to increase the circulating light intensity within the PAS cells, which provides increased sensitivity through increased sample heating (e.g. McManus *et al.*, 1995; Nägele and Sigrist, 2000; Lack *et al.*, 2006, 2012). This approach is advantageous for aerosol studies compared to single pass methods employing higher laser powers, as it increases sampling heating without exposing individual particles to large temperature changes which could lead to loss of semi-volatile species through evaporation (McManus *et al.*, 1995; Lack *et al.*, 2006).

2.4.2 PAS design in EXSCALABAR

2.4.2.1 Mechanical layout

The PAS cells, including the resonators, lasers, optical detectors and mirrors, are mounted in parallel to a carbon fibre cage that is formed of a single layer, as shown in Figures 2.2 and 2.15. Each PAS cell is pumped using individual

Toptica iBeam Smart lasers (Toptica Photonics), which have wavelengths of 405, 514 and 658 nm and generate light with powers 300, 100 and 130 mW respectively. Laser wavelengths and line widths were measured using an Avantes spectrometer (CompactLine) for the blue and green wavelengths and a Hamamatsu spectrometer (C11697MB) for red wavelengths. Mirrors are mounted directly to the PAS cells, as shown in Figure 2.16, and can rotate to allow alignment.

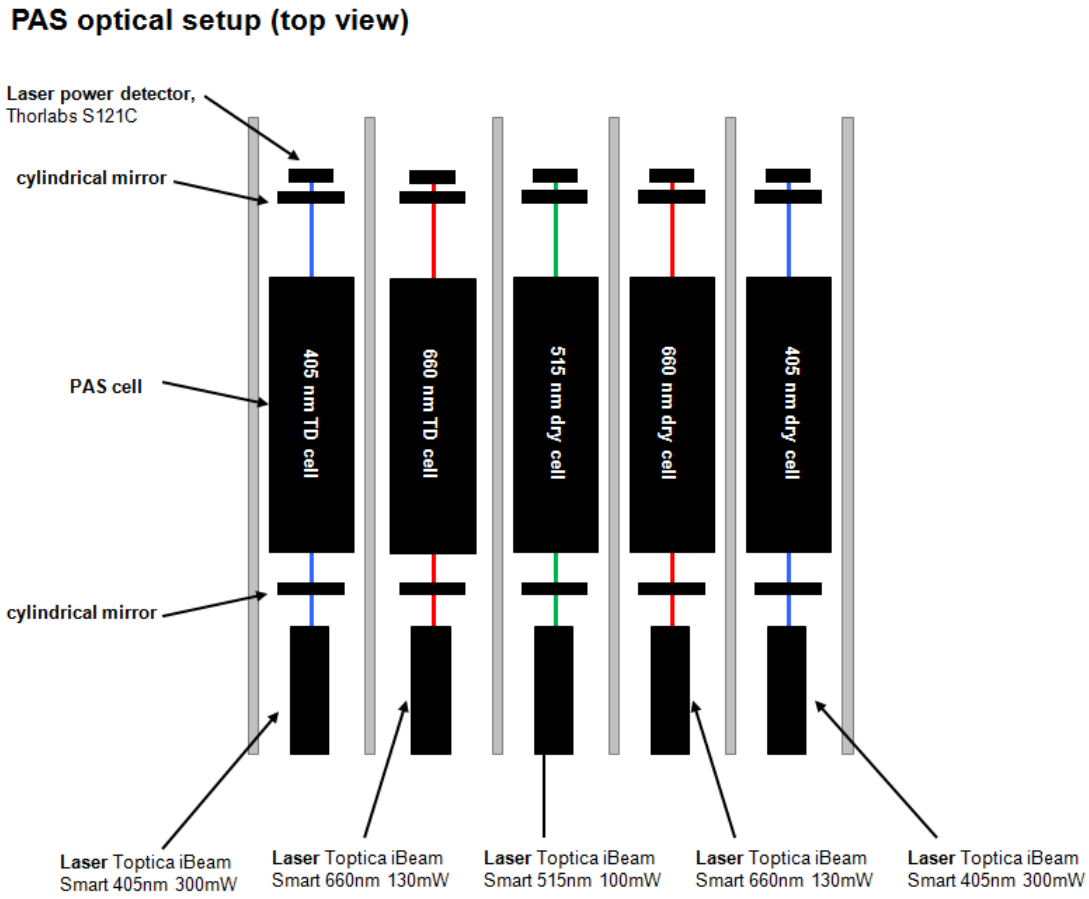

Figure 2.15: *Layout of PAS components and their positions within the carbon fibre cage.*

Photoacoustic detection cells are based on the dual-resonator design of Lack *et al.* (2012a) except that the planar windows were replaced with Brewster angle windows (Thorlabs, BW2502), which minimise reflection losses within the multi-pass optical system. See Figure 2.16 for a computer-aided design drawing of the PAS cell design. Each PAS cell consists of two cylindrical resonator cavities (a lower *signal* and upper *reference* resonator) coupled through buffer volumes on either side for noise suppression (Lack *et al*., 2006).

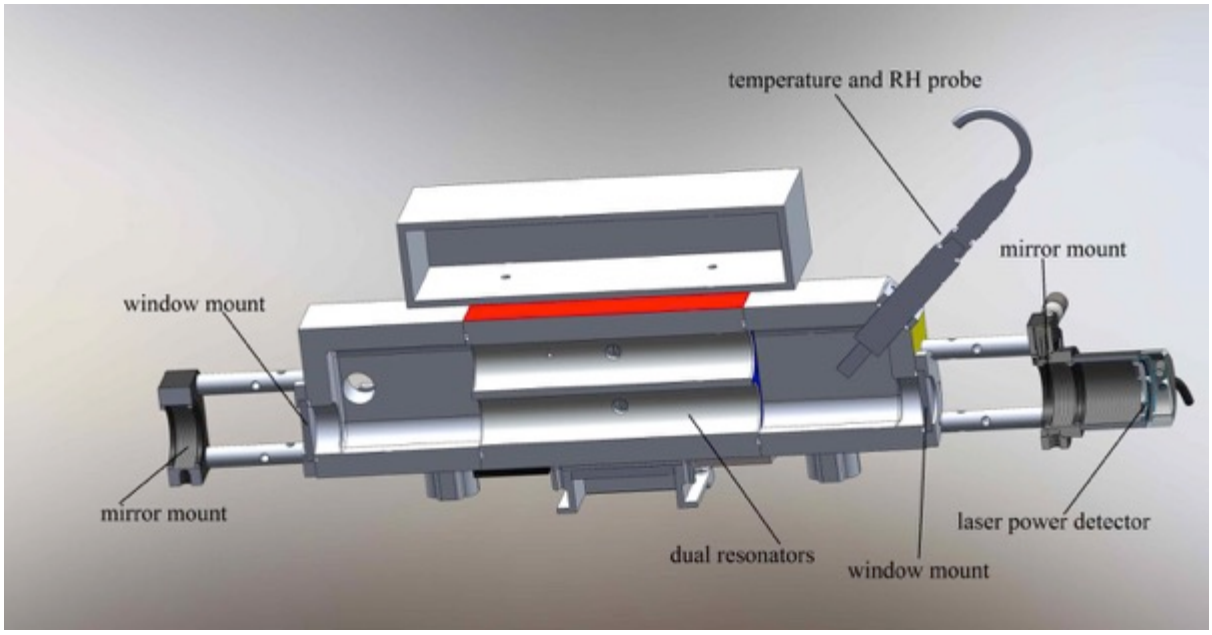

Figure 2.16: *PAS cell design used in the EXSCALABAR instrument.*

The cells are manufactured from aluminium and have a total volume of 200 cm^3. Individual resonant cavities have dimensions of 110 mm length and 9.5 mm radius. The cell is positioned within a multi-pass optical system formed by two cylindrical mirrors located outside of the PAS cell with mirror radii of curvature of 430 mm (front mirror, closest to laser) and 470 mm (back mirror). The concavities of the two mirrors are rotated 90° to each other. Each mirror is coated with a wavelength-specific dielectric coating to yield reflectivities exceeding 99.9 %. Laser light is injected into each multi-pass system through a 2 mm hole in the centre of the first mirror. Light exiting the multi-pass system is measured using a photodiode (Thorlabs, S121C) positioned behind the second mirror. In an optimally aligned system, the laser would pass through the acoustic resonator 182 times (Silver, 2005; Lack *et al.*, 2012a). However, no effort is made to achieve this limit in the current system. Alignment is conducted by visual inspection of the spot pattern only, which almost certainly results in a lower number of passes. Quantifying the number of passes through the resonator is however not critical. Light exiting the resonator is measured using a photodiode, which allows the PAS signal to be corrected for any laser power or alignment instability (Lack *et al.*, 2012a). The acoustic signal is detected using microphones (Knowles Acoustics, EK-23132) positioned half way along the lengths of each resonator to coincide with the pressure antinode corresponding to the lowest-order (n = 1) acoustic eigenmode of the photoacoustic cell.

The sample passes through both resonators but laser light passes only through the lower, *signal* resonator. The photoacoustic response is defined as the magnitude of the frequency domain response at the n = 1 eigenfrequency and is referred to hereafter as the *integrated area* (IA). A speaker (Knowles Acoustics, ES-23127-000) is located in the reference resonator to enable periodic measurement of the cell resonant frequency and quality factor, which change with temperature and pressure (Lack *et al.*, 2012a). Following each speaker measurement, the laser modulation frequency is automatically adjusted to match the derived cell resonance frequency. The responses from the two microphones are passed through a differential amplifier and Fourier-transformed to the frequency domain. Differential amplification removes acoustic and electronic noise common to both resonators at the cell resonance frequency. To account for noise that is not common to both resonators, i.e. background acoustic noise generated due to laser heating of optical windows, the PAS IA for aerosol-filtered air is measured periodically to characterise a background for subsequent subtraction. The uncertainty introduced by this background noise subtraction is assessed in section 2.6.

The PAS theory presented in section 2.4.1 only strictly applies to a single cylindrical resonator. For the dual-resonator PAS design used in EXSCALABAR, the resonant frequencies will be different to those predicted using equation 2.13 due to (i) the resonant cavities not opening to an infinite volume but rather to the finite buffer volumes, which leads to coupling between the two cells and (ii) openings for the microphone, speaker and sample flows, which will distort the acoustic field (Miklós *et al.*, 2001). These differences are another reason to calibrate the PAS cells empirically, as opposed to applying equation 2.17 directly. Calibration of the PAS cells is covered in Chapter 3.

2.5 Sensitivity analysis

Sensitivity is a key assessment criterion for determining instrument performance due to the weak extinction and absorption signals we are trying to measure with the CRDS and PAS instruments. In this section I will introduce the principles used to assess instrument sensitivity followed by an evaluation of the EXSCALABAR minimum sensitivity.

2.5.1 Cavity ring-down spectrometers

Factors that affect the sensitivity of CRDS retrievals of the extinction coefficient include uncertainties in the fitted ring-down times (τ) and baseline drift in the empty cavity ring-down times (τ_0) (Brown, 2003; Mazurenka *et al.*, 2005). Uncertainties in the fitted ring-down times arise due to noise on the PMT signal and due to multi-exponential decays. Hence the minimum sensitivity of a single ring-down event can be determined using

$$b_{ext}^{min} = \frac{R_L}{c} \frac{\Delta\tau_{min}}{\tau_0^2} \; as \; \tau \to \tau_0 \tag{2.18}$$

where $\Delta\tau_{min}$ is the uncertainty in the ringdown time, taken as an integral number of standard deviations in τ_0 (Brown, 2003). Calculated using equation 2.18, Figure 2.17 describes the minimum detectable extinction coefficient that would be observed for a perturbation to the cavity ring-down time, τ_0, such that $\Delta\tau_{min} = \tau_0 - \tau$, which may be due to an aerosol particle, absorbing gaseous species or a noise term.

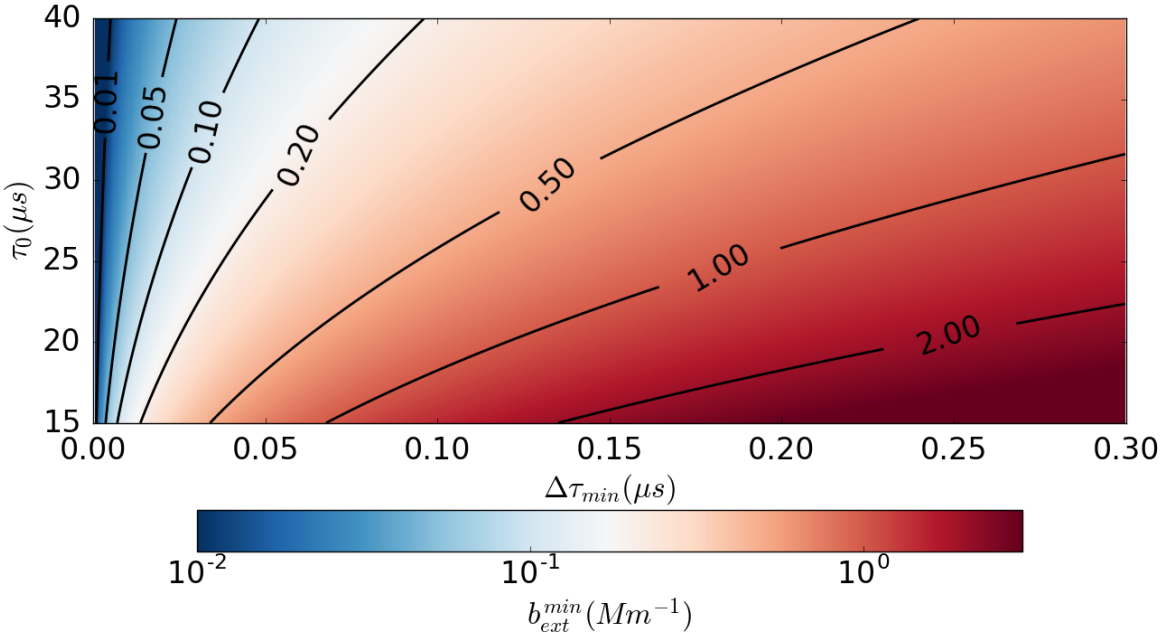

Figure 2.17: *The extinction coefficient corresponding to a perturbation in the ring-down time, $\Delta\tau_{min}$, for a range of empty-cavity ringdown times, τ_0. Shown in black are lines of constant extinction coefficient.*

In order to evaluate b_{ext}^{min}, an exponential function (see equation 2.2) must be fitted to a ring-down event. To illustrate this, Figure 2.18 shows an example ring-down decay for the 405 nm EXSCALABAR CRDS cell. A single

exponential function is fit to the data and the residuals between the PMT signal and fitted data are determined.

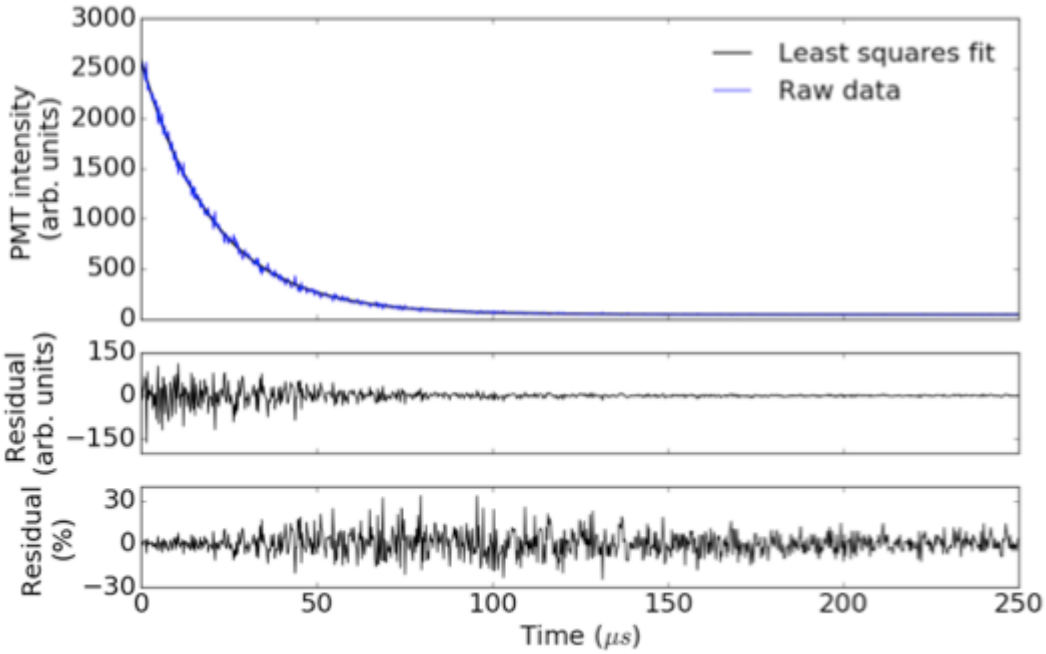

Figure 2.18: *A ring-down event for the 405 nm dry EXSCALABAR CRDS cell.*

The b_{ext}^{min} was calculated by fitting 20000 ring-down events as described above for the 405 nm CRDS cell, which yielded a mean minimum detectable extinction coefficient for single-exponential ring-down events as 0.49 ± 0.03 Mm^{-1}.

The measurement sensitivity is improved by averaging of many ring-down events. The Allan deviation can be used to evaluate the measurement stability and therefore identify the time-scale over which instrumental drifts start to occur due to, for example, drifts in detector sensitivity (Allan, 1966; Werle *et al.*, 1993). It is favourable to use the Allan deviation instead of, for example, the standard deviation due to convergence with increasing averaging time (Allan, 1966). Instrument minimum sensitivity and optimum averaging time can therefore be evaluated using the Allan deviation.

The sensitivity of the EXSCALABAR CRDS system was evaluated by examining measured ring-down times over the course of several hours while the instrument was sampling particle-free air. Particles were filtered out of the air stream, which was dried to a relative humidity below 3 %. Using Figure 2.19, the 1 Hz CRDS extinction coefficient minimum sensitivity is between 0.01–0.04 Mm^{-1}. The optimal sensitivity corresponds to averaging times between 1 and 20

seconds dependent on the CRDS cell, above which measurement drift limits the minimum sensitivity.

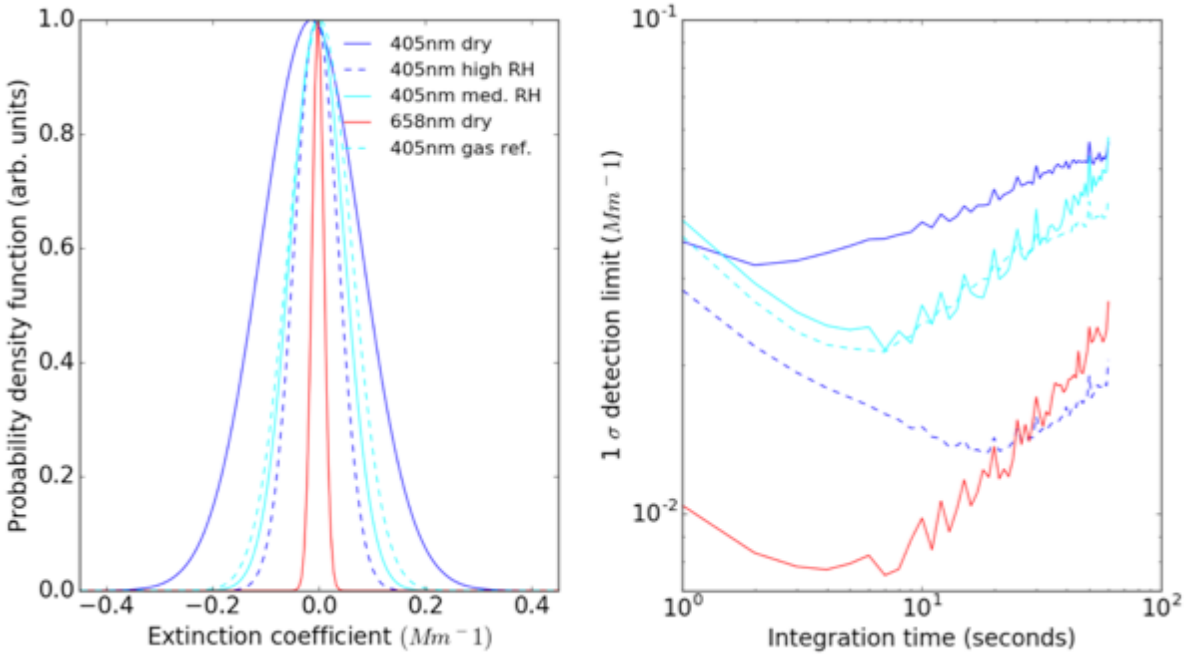

Figure 2.19: *Probability density functions of the extinction coefficients and the corresponding Allan deviations for a range of integration times.*

2.5.2 Photoacoustic spectrometers

The sensitivity of the EXSCALABAR PAS system was evaluated in a similar way to the CRDS system by examining the baseline drift and Allan deviations of absorption coefficients over the course of several hours. Particles were filtered out of the air stream, which was dried to a relative humidity below 3 %. Figure 2.20 (left) shows the range of background absorption coefficients using probability density functions. Figure 2.20 (right) shows the corresponding Allan deviations, which have 1 Hz minimum sensitivities in the range 0.05–0.33 Mm^{-1}. The minimum sensitivity improves as the averaging time is varied between 1–60 seconds.

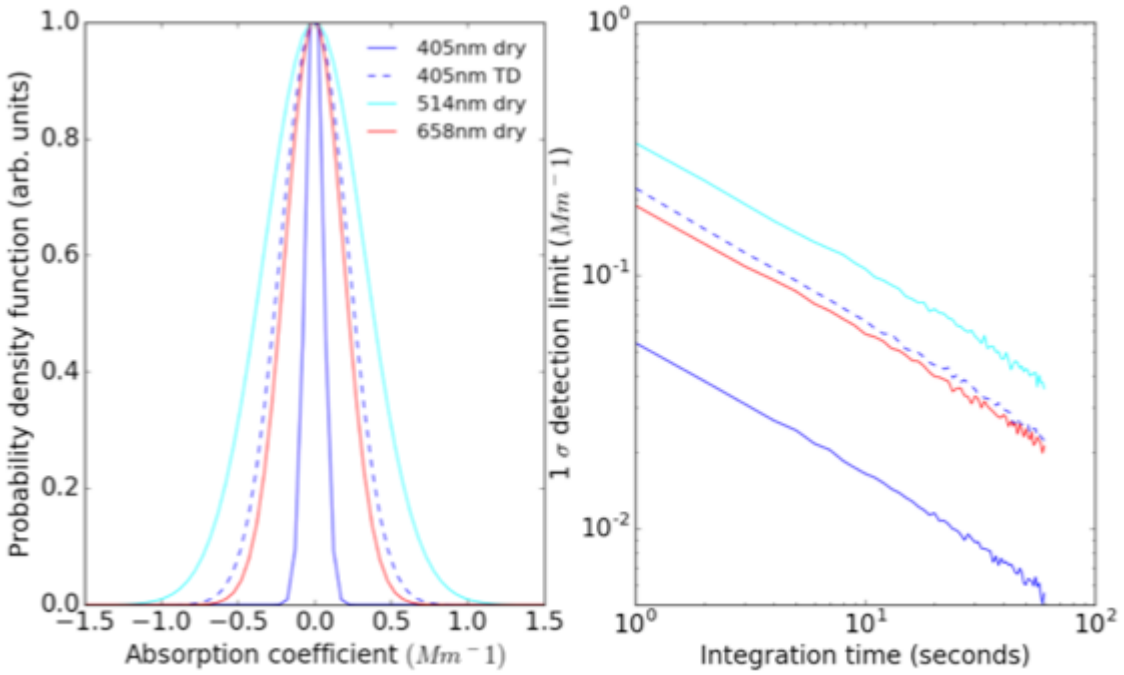

Figure 2.20: *Probability density functions of the absorption coefficients and the corresponding Allan deviations for a range of integration times.*

2.6 Assessing the accuracy of in-flight PAS measurements

The accuracy of PAS absorption measurements is controlled by three factors: (i) the uncertainty in the ozone calibration, (ii) the uncertainty introduced by correcting the ozone calibration for pressure due to any PAS microphone sensitivity pressure dependence and (iii) the in-flight background noise correction used primarily to remove background acoustic noise due to laser heating of optical windows. The accuracy of the CRDS instruments used in this study is assessed in Chapter 3, which is the same for ground-based and in-flight operation and thus will not be discussed further.

In Chapter 3, I validate the accuracy of the PAS calibration in laboratory experiments to be better than 8 %. Calibration accuracies were evaluated by comparing the measured and modelled absorption cross sections of strongly-absorbing nigrosin aerosol. I will use the calibration uncertainties derived in Chapter 3 to calculate the uncertainty that is propagated to in-flight PAS absorption coefficient measurements. Full details of the ozone calibration are provided in Chapter 3, and only minimal detail is provided here to allow assessment of the total PAS in-flight measurement uncertainty.

The second source of PAS measurement uncertainty is due to the PAS cell sensitivity to pressure (Lack *et al.*, 2012a) and therefore PAS microphone calibrations are performed at three pressures in the range ~ 600–1000 mb to reflect the range of pressures encountered during airborne operation. The PAS cells are calibrated by comparing simultaneously the uncalibrated PAS microphone responses and the CRDS-measured absorption coefficients of gaseous ozone. The gradient of the regression between the PAS microphone responses and CRDS absorption measurements to ozone at pressure P is represented by m_P. See for example Figure 3.6. The ratios of PAS calibration factors at two pressures are assessed by evaluating $ratio_P = {m_P}/{m_{P=1000\,mb}}$. Figure 2.21 shows how $ratio_P$ changed with pressure for a series of 51 calibrations performed during the CLoud-Aerosol-Radiation Interactions and Forcing: Year 2017 (CLARIFY) field experiment. The PAS microphone sensitivities varied linearly across this pressure range (600–1000 mb), which allowed for derivation of a linear regression between $ratio_P$ and pressure. Corrections for the pressure dependent microphone sensitivity reached a maximum of 17 % at a minimum pressure of 600 mb. The reason underpinning the change in the 658 nm PAS microphone sensitivity to pressure during the ozone calibrations is unclear, shown in Figure 2.21.

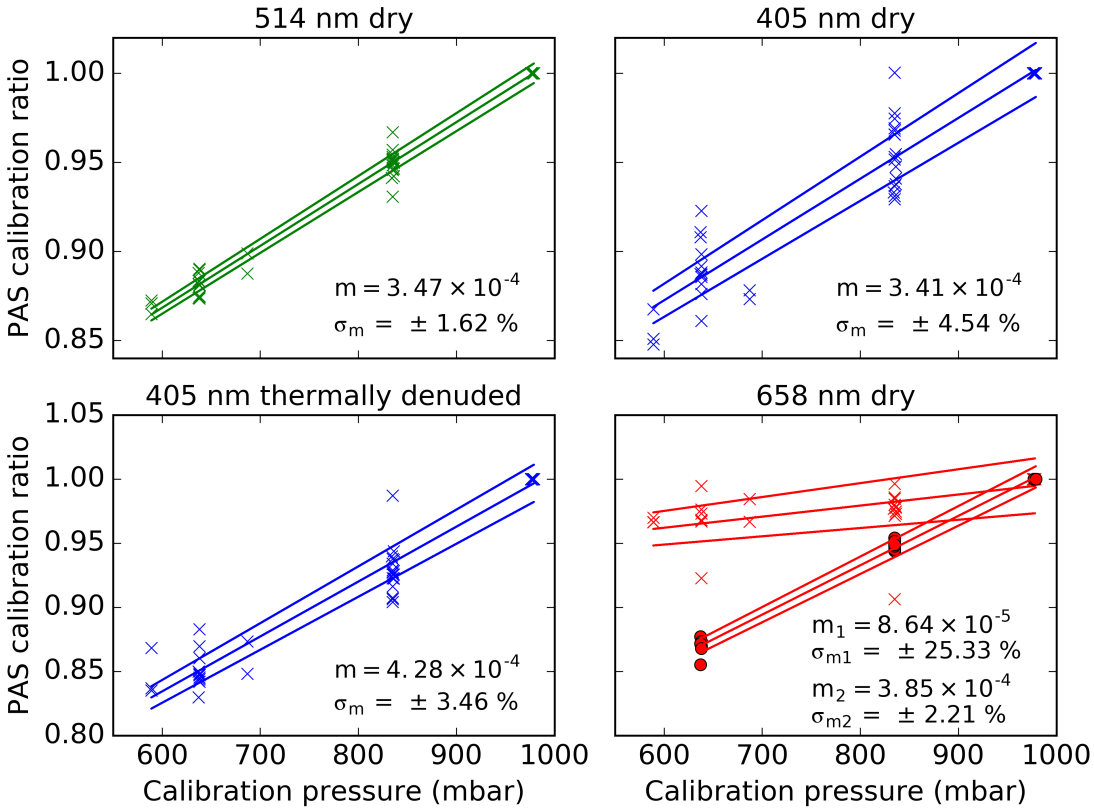

Figure 2.21: *PAS calibration ratios ($ratio_P$) as a function of pressure for all calibrations performed during the CLARIFY campaign. The gradients of the linear regressions (m) and the 1σ fittings uncertainties (σ_m) are shown for each PAS cell. For the 658 nm dry cell, realignment took place during the measurement campaign leading to two linear regressions.*

The uncertainty introduced by applying this pressure-dependent correction to PAS calibrations was estimated by propagating the 1σ fitting uncertainties in the linear regressions between $ratio_P$ and pressure to in-flight PAS measurements. This correction leads to uncertainties in PAS absorption coefficient measurements of 0.0–1.2 % dependent on pressure. The smallest uncertainties were associated with measurements around 1000 mb where there was no correction applied and largest for relatively low pressures where the largest correction was applied.

The third source of PAS measurement uncertainty was due to subtraction of window-generated background noise, which was less stable for airborne operation due to its dependence on pressure. In-flight background noise was characterised periodically by measuring a filtered-air stream, typically for 30 s every 300 s. All data from a flight were then used to derive a background correction as a function of pressure (see Figure 2.22). To evaluate the

uncertainty introduced by this background noise correction, continuous PAS measurements of filtered-air were recorded in the laboratory and the pressure within the PAS cells was varied over the range encountered during airborne operation. This laboratory PAS dataset was then processed using a 30 s averaging time every 300 s to mimic in-flight conditions from which a background noise correction was derived as a function of pressure; see Figure 2.22.

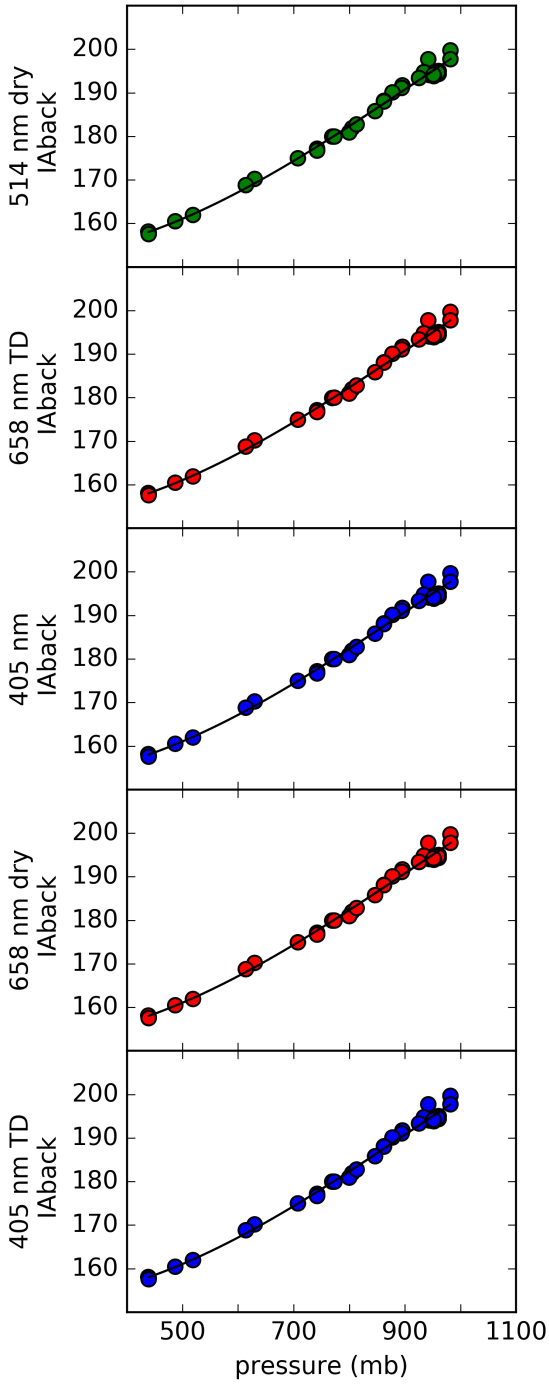

Figure 2.22: *PAS background microphone integrated area (IA) response to filtered-air as a function of pressure for data collected in the laboratory for variable pressure conditions. TD: thermally denuded.*

A background data series was then generated using the background noise correction derived using the data in Figure 2.22. Examining the difference between the continuous filtered-air measurements and the synthetically generated background data series provided the uncertainty in the background noise correction under variable pressure conditions. A time series of the continuous measurements and generated background data series is shown in Figure 2.23.

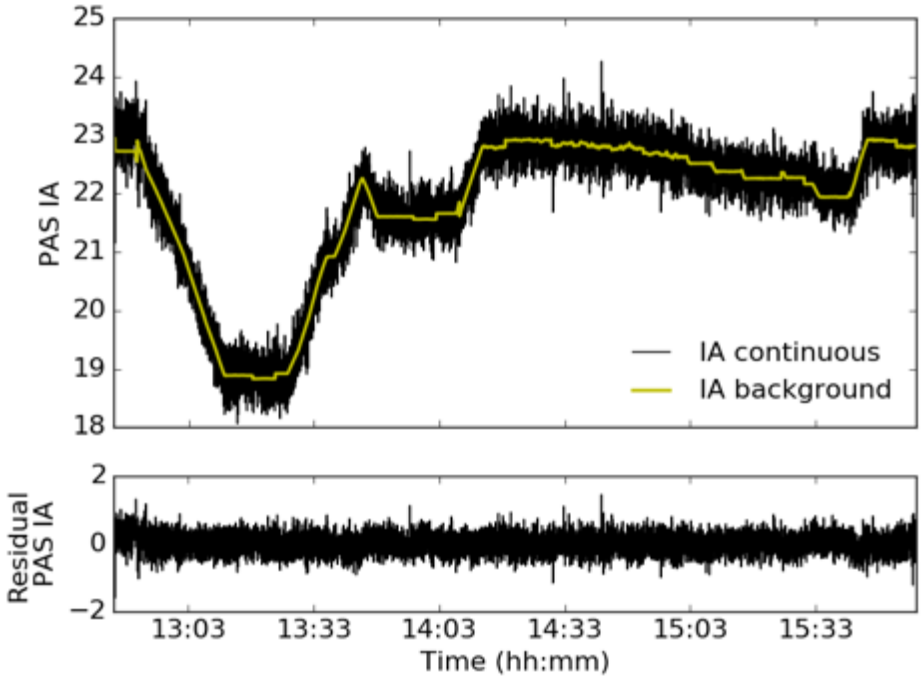

Figure 2.23: *Time series of the continuous PAS microphone integrated area (IA) response to filtered-air (black) and the synthetically generated background data series generated using the correction derived using Figure 2.22. This data corresponds to the 514 nm PAS cell.*

The uncertainty in the background noise correction was found to be normally distributed, which allowed evaluation of the 1σ uncertainty, estimated as 1.27 %. See Figure 2.24.

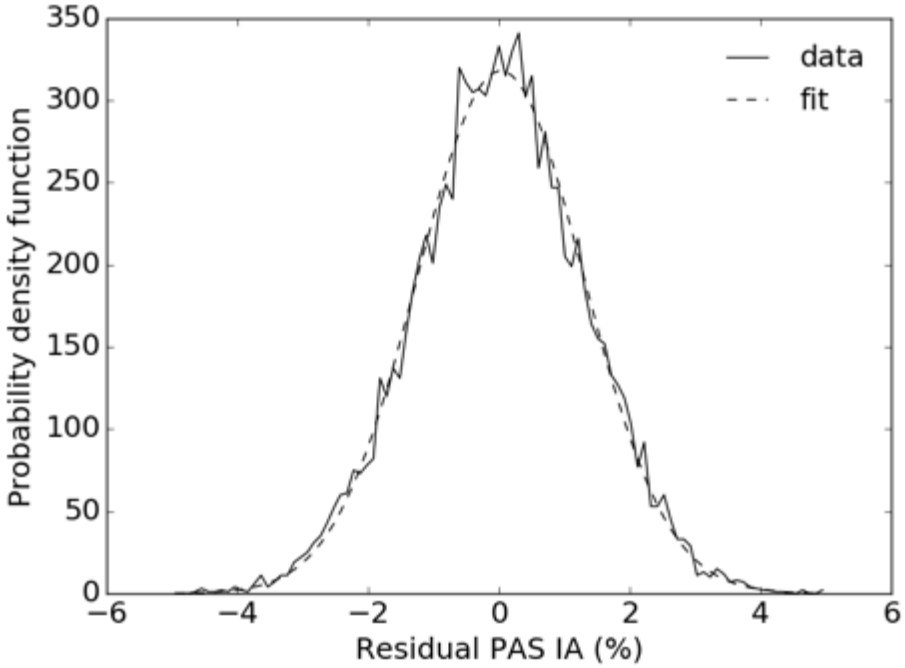

Figure 2.24: *Probability density function of the residual PAS integrated area (IA) between the continuous PAS measurement of filtered-air and the synthetically generated background data series, expressed as a percentage of the continuous PAS measurements. This data corresponds to the 514 nm PAS cell.*

This uncertainty was propagated through in-flight PAS measurements to derive the uncertainties introduced to airborne PAS absorption coefficient measurements by the background noise subtraction. This uncertainty depended on the strength of aerosol absorption and was found to be 0.2, 2.0 and 20.5 % at 100, 10 and 1 Mm^{-1}, respectively, which is shown in Figure 2.25.

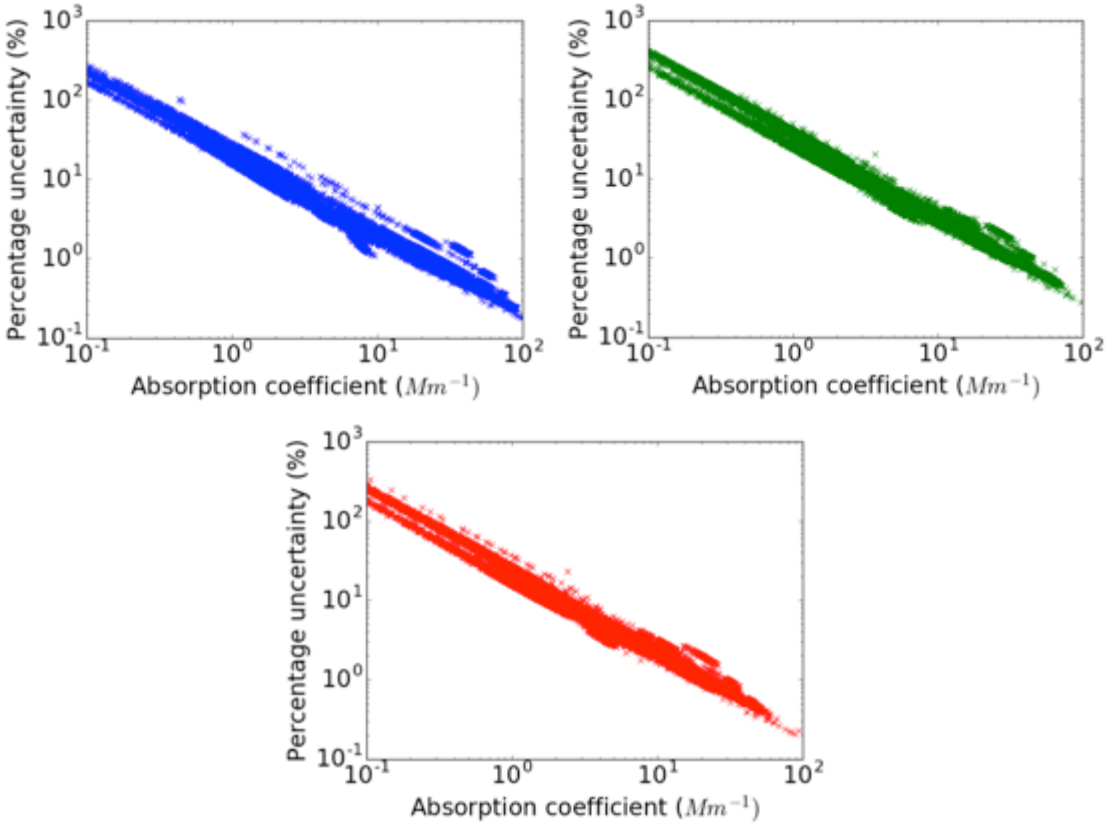

Figure 2.25: *Percentage uncertainty in PAS absorption coefficient measurements for airborne operation due to the pressure-dependent background correction accounting for window-generated acoustic noise.*

The total uncertainty in PAS measurements is therefore the combination of the measurement precision and accuracy, including the PAS calibration accuracy, the pressure-dependent calibration correction uncertainty and the background noise correction uncertainty. These factors were combined in quadrature, leading to total PAS measurement uncertainties of 23.1 % for 1 Mm^{-1} absorption coefficient measurements (independent of pressure) and 8.0–8.1 % for 100 Mm^{-1}, dependent on pressure (600–1000 mb). These uncertainties are in-line with previous estimates for airborne PAS measurements, which were found to be ± 5 % for ground-based measurements with an additional ± 0.5 Mm^{-1} for airborne measurements (Lack *et al.*, 2012a). Figure 2.26 shows the total PAS measurement uncertainty during airborne operation. For absorption coefficient measurements greater than ~5 Mm^{-1}, the total PAS measurement uncertainty is dominated by the uncertainty in the calibration. For absorption coefficients less then ~5 Mm^{-1}, the total PAS measurement uncertainty is dominated by the background noise correction.

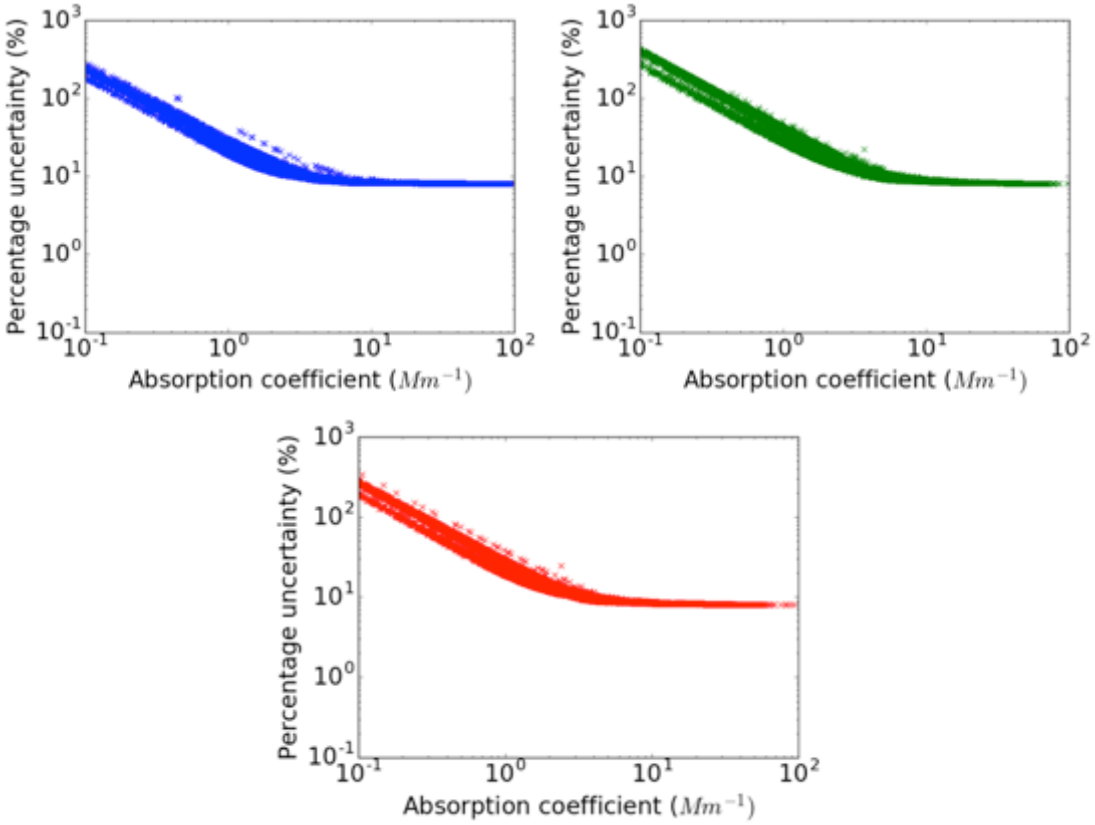

Figure 2.26: *Total percentage uncertainty in PAS absorption coefficient measurements for airborne operation.*

2.7 Conclusions

In this chapter I have introduced a new instrument for the measurement of aerosol absorption and extinction coefficients. The minimum sensitivities of the CRDS and PAS cells when recording data at 1 Hz are in the range 0.01–0.04 Mm^{-1} and 0.05–0.33 Mm^{-1}, respectively. I then assessed the total PAS measurement uncertainty for airborne operation, which was 23.1 % for 1 Mm^{-1} absorption coefficient measurements (independent of pressure) and 8.0–8.1 % for 100 Mm^{-1} measurements. The measurement uncertainty of the CRDS instruments is the same for ground-based and airborne operation, and is assessed in laboratory experiments in Chapter 3.

3 On the accuracy of aerosol photoacoustic spectrometer calibrations using absorption by ozone

Components of this chapter are based on the following publication, a copy of which is provided in Appendix 1: Davies, N. W. *et al.* (2018) 'On the accuracy of aerosol photoacoustic spectrometer calibrations using absorption by ozone', *Atmospheric Measurement Techniques*, 11(4), pp. 2313–2324. doi: 10.5194/amt-11-2313-2018.

Table of contents

3.1 Chapter overview

In this chapter, I describe how the EXSCALABAR PAS calibrations are performed, verify the accuracy of the PAS calibrations, and assess the accuracy with which the PAS and CRDS can retrieve the absorption and extinction coefficients, respectively, under laboratory conditions.

3.2 Introduction

Photoacoustic spectroscopy (PAS) has emerged as the technique of choice for the fast, sensitive and accurate measurement of light-absorption by atmospheric aerosol (Lack *et al.*, 2012a). As highlighted in Chapter 2.4, the EXSCALABAR PAS cell microphones require calibration in order to determine absorption coefficients. There exist a number of approaches described in the literature for calibrating photoacoustic spectrometers including use of known concentrations of nitrogen dioxide (Arnott *et al.*, 2000; Nakayama *et al.*, 2015), polydisperse kerosene soot (Nakayama *et al.*, 2015), oxygen (Tian *et al.*, 2009;

Gillis *et al.*, 2010) and ozone (Lack *et al.*, 2006, 2012a; Bluvshtein *et al.*, 2017). Nitrogen dioxide has been shown to introduce uncertainty into 405 nm PAS cell calibrations due to photolysis (Lack *et al.*, 2012a) and generation of aerosol particles is challenging in the field. Hence, ozone was chosen as the calibrant for our PAS cells.

Gaseous ozone has been used successfully to calibrate photoacoustic spectrometers operating at laser wavelengths of 532 nm, with reported absorption accuracies of 1–5 % (Lack *et al.*, 2006, 2012a). Demonstration of the validity of the ozone calibration approach involved the comparison of PAS measurements to model absorption calculations for laboratory-generated absorbing particles, such as nigrosin dye. Recently, Bluvshtein *et al*. (2017) performed similar experiments to probe the validity of the ozone calibration approach at 404 nm. They found a factor ~2 discrepancy between the PAS response to ozone and nigrosin, which was attributed to an unspecified issue with ozone measurements at these wavelengths. This result has significant implications for photoacoustic spectrometer ozone calibrations at short-visible wavelengths, suggesting that they would lead to overestimation of aerosol absorption by a factor ~2. The focus of this study is to re-evaluate this result.

Given the importance of the Bluvshtein *et al.* (2017) work in motivating this study, a brief overview of the experiments is provided here. Ozone was generated from high purity (99.999 %) oxygen using either a corona discharge ozone generator or, for lower concentrations, a UV lamp. Ozone concentrations in the range 250–1900 ppm were generated and diluted with dry nitrogen in the ratio 1:10 O_2-O_3:N_2. Ozone absorption coefficients were measured using a cavity ring-down spectrometer (CRDS). CRDS measurements made in series versus parallel to the PAS detection cell indicated little difference in ozone concentration and thus minimal loss through the PAS system. Nigrosin was atomised from solution, dried to < 10 % relative humidity, size-selected using a differential mobility analyser (DMA) to yield mobility diameters in the range 250–325 nm and passed through an impactor to remove multiply charged particles. The aerosol stream flowed through a PAS cell at 0.6 L min^{-1}, which was then split evenly between the CRDS cell and a condensation particle counter (CPC). Particle concentrations in the range 200–1500 cm^{-3} were used. PAS-measured

ensemble aerosol absorption coefficients were compared to modelled values computed using Mie theory in combination with the size-selected particle diameters passed by the DMA and complex refractive indices determined via spectroscopic ellipsometry. Experiments were repeated for Pahokee peat fulvic acid and Suwannee river fulvic acid aerosol. The discrepancy between the PAS-measured ensemble absorption coefficients and absorption coefficients calculated using Mie theory differed by a factor of two for all three test aerosols, as shown in Figure 3.1.

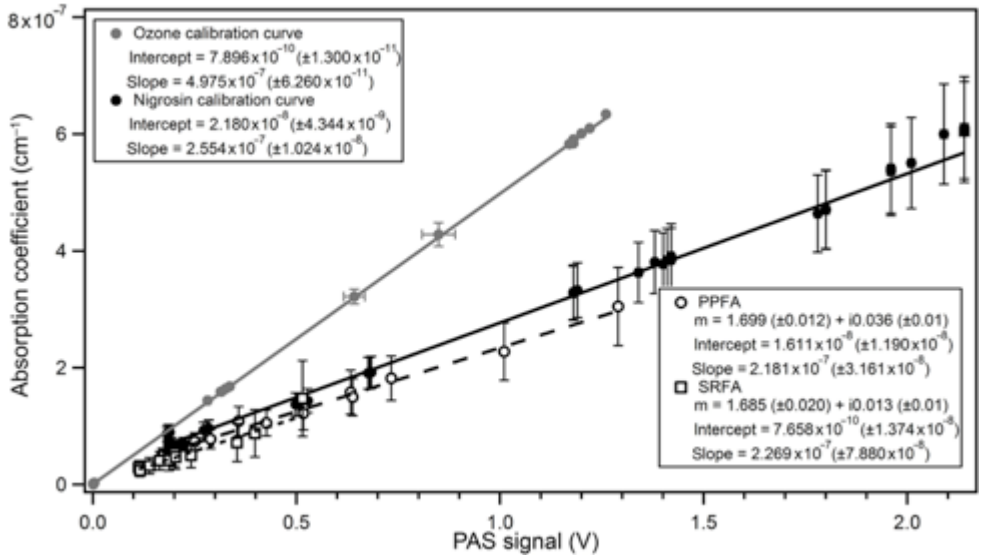

Figure 3.1: *PAS ozone calibration (grey), nigrosin calibration (black filled circles), Pahokee peat fulvic acid calibration (black empty circles) and Suwannee river fulvic acid calibration (black squares). Figure from Bluvshtein et al. (2017).*

Bluvshtein et al. (2017) suggested several reasons for the discrepancy, including contamination by NO_2 and generation of light-scattering particles due to reaction of O_3 with the walls of the instrument. However, no evidence supporting these theories was provided. PAS measurements at wavelengths other than 404 nm were also not available, which prevented an independent check of the PAS responses to ozone and nigrosin at wavelengths that have been reported previously to be well-calibrated using the ozone approach (e.g. Lack *et al.*, 2006).

In this study, a similar set of experiments was performed using EXSCALABAR following the method described above, whereby PAS-measured ensemble absorption cross sections for aerosolised nigrosin are compared to model calculations. Importantly, this comparison is evaluated for three visible wavelengths including the 405 nm wavelength pertinent to the work of

Bluvshtein *et al*. (2017). In the following sections, I provide a description of the experimental setup, ozone calibration apparatus, aerosol generation system and the method by which modelled ensemble aerosol absorption cross sections were calculated. Experimental results and discussion are presented in section 3.8.

3.3 Ensemble absorption cross section

Section 3.5 provides details regarding PAS corrections for cell resonance properties and laser power. Aerosol absorption coefficients (units Mm^{-1}) measured by the photoacoustic spectrometers were converted to ensemble absorption cross sections (units m^2) for comparison to theoretical calculations by dividing by the aerosol number concentrations reported by a CPC (see section 3.6). The ensemble absorption cross section represents the mean of the absorption cross sections corresponding to a range of particles sizes, for example from multiply charged particles (see section 3.7). The ensemble absorption cross section is hereafter referred to as the *absorption cross section*.

3.4 Cavity ring-down spectrometer

Extinction coefficients (units Mm^{-1}) were converted to ensemble extinction cross sections (units m^2), hereafter referred to as extinction cross sections, by dividing by the aerosol number concentrations measured using a CPC. The τ_0 times for both the 405 and 658 nm CRDS channels used in this study were measured before and after experiments where aerosol was passed through the optical cavities. Typical representative ring-down times were 23.1 µs (405 nm) and 34.2 µs (658 nm). A detailed overview of the CRDS cells used in this study is provided in Chapter 2.3.

3.5 Ozone calibration

3.5.1 Determining ozone absorption cross sections

The ozone absorption cross sections were evaluated at all EXSCALABAR CRDS and PAS wavelengths in order to enable accurate calibration. Evaluation of ozone absorption cross sections was achieved by calculating the mean absorption cross section over the spectral width of the laser emission via the equation

$$\frac{1}{\sum I^i}\sum_i \sigma_{o3}^i I^i, \qquad (3.1)$$

where σ_{o3}^i is the ozone absorption cross section at wavelength i and I^i is the intensity of the laser spectra at wavelength i.

Figures 3.2 and 3.3 show the ozone absorption cross sections around the 405 nm and 658 nm wavelengths used in the CRDS and PAS lasers (Gorshelev *et al.*, 2014; Serdyuchenko *et al.*, 2014), overlaid with laser emission spectra measured using an Avantis spectrometer (CompactLine) and Hamamatsu spectrometer (C11697MB), respectively. A cubic spline interpolation was used to calculate the weighted absorption cross section according to equation 3.1. Accurate determination of the ozone absorption cross section in this way is important due to significant wavelength-dependence of the ozone absorption cross section at the wavelengths used.

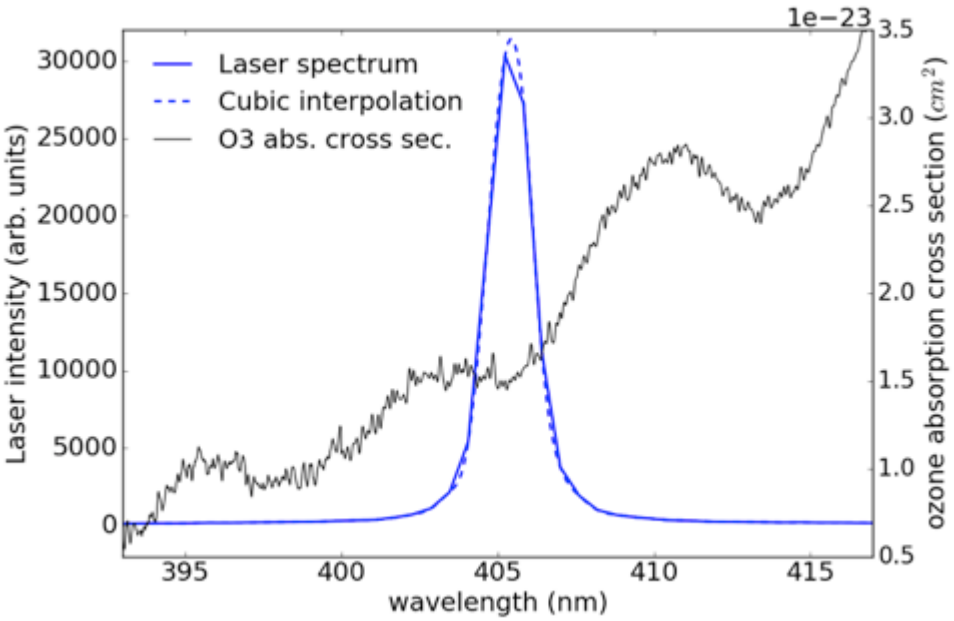

Figure 3.2: *Measured laser spectrum for a 405 nm CRDS laser and a cubic interpolation. Also shown are the ozone absorption cross sections.*

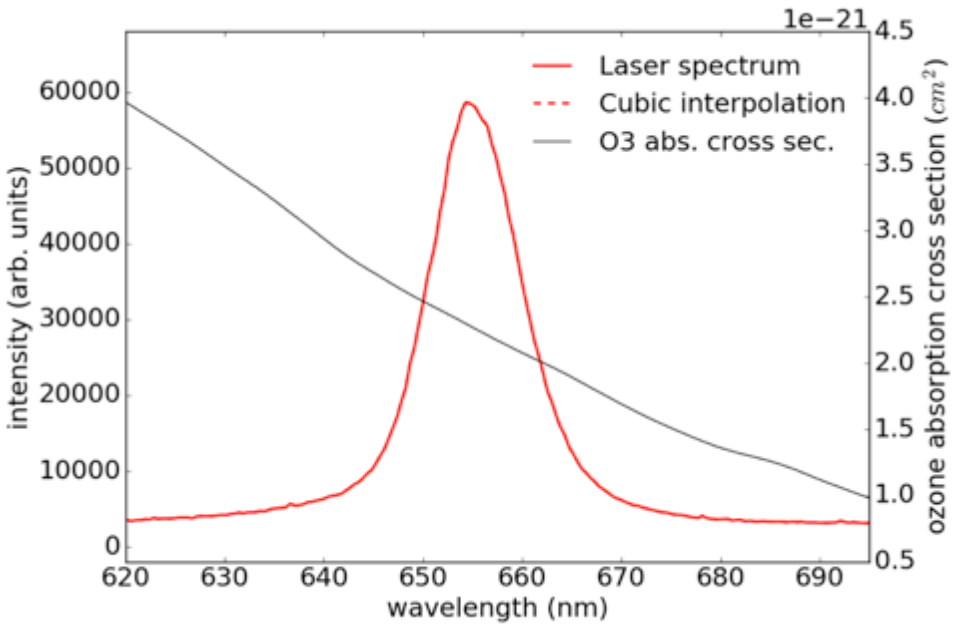

Figure 3.3: *Measured laser spectrum for a 658 nm CRDS laser and a cubic interpolation. Also shown are the ozone absorption cross sections.*

Table 3.1 summarises the ozone absorption cross sections.

Cell	**Peak wavelength (nm)**	**Weighted ozone absorption cross section ($x10^{-23}$ cm^2)**
CRDS cell 1	658.51	218.878
CRDS cells 2, 3 and 4	405.03	1.61662
CRDS cell 5	405.41	1.65327
PAS cell 1	404.92	1.61686
PAS cell 2	658.96	218.734
PAS cell 3	514.38	161.774
PAS cell 4	404.87	1.62803
PAS cell 5	655.22	228.255

Table 3.1: *Mean weighted absorption cross sections of ozone over the PAS and CRDS laser wavelength spectra.*

3.5.2 Experimental details

Gaseous ozone was generated using a coronal discharge ozone generator (Longevity Resources, EXT120-T) from high purity oxygen (99.999 %, BOC, grade N5.0). The ozone-laden stream was split approximately evenly between the PAS and CRDS cells using a manifold equipped with 300 µm diameter

orifices, as shown in Figure 3.4. Teflon tubing was used throughout the flow system to minimise contamination and to reduce ozone losses.

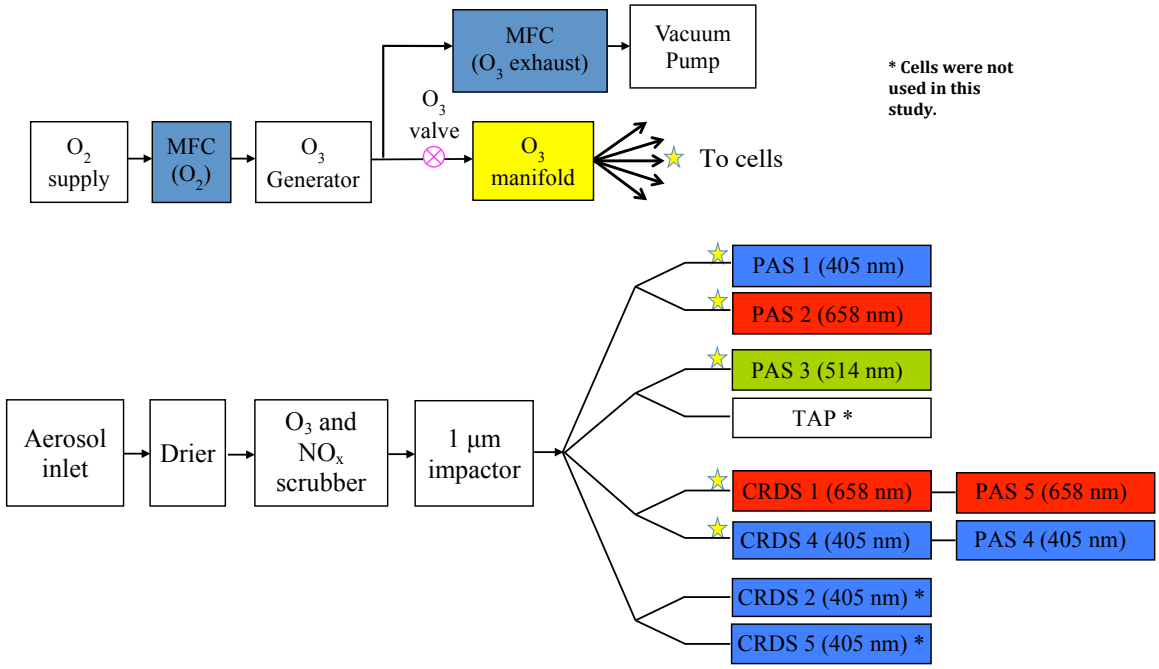

Figure 3.4: *Schematic diagram of the PAS/CRDS experimental setup including the ozone generation system and the relative positions of the PAS and CRDS cells. The stars indicate the ozone flow path, which entered the cells through different ports to the main aerosol flow. The PAS/CRDS wavelengths are centred at 405, 514 and 658 nm respectively. Abbreviations: 'MFC': mass flow controller.*

The 405 nm and 658 nm CRDS cells quantified ozone concentrations for calibration of all five PAS cells. For PAS cells in series with the CRDS channels, *PAS-series*, (PAS 4 and PAS 5 in Figure 3.4), the CRDS-measured extinction coefficients were used directly to calibrate the corresponding in-line PAS channel measurements of IA. This calibration relation between sample extinction and IA was quantified at multiple values of ozone concentration, controlled by varying the discharge frequency on the coronal ozone generator. For PAS cells operated in parallel, *PAS-parallel*, it was necessary to measure accurately the relative ozone splitting ratio with respect to the CRDS flow paths. The following section details the method for characterising this ratio, which was based on monitoring the resonant frequency shift induced by changing the gas composition, and hence speed of sound within the photoacoustic cells (Miklós *et al.*, 2001).

At the start of each calibration cycle, pure oxygen was introduced into the PAS cells through the ozone manifold at a flow rate of 0.02 L min^{-1} per cell, in addition to the 0.98 L min^{-1} filtered-air flow. The oxygen displaced a fraction of the filtered-air flow through each cell, changing the gas composition, speed of sound and thus cell resonant frequency, as shown in Figure 3.5. The ozone flow splitting, $\Delta\nu$, between two PAS cells was calculated using

$$\Delta\nu = \frac{\left(F_r^{air} - F_r^{air+o2}\right)_{PAS-series}}{\left(F_r^{air} - F_r^{air+o2}\right)_{PAS-parallel}} \qquad (3.2)$$

where F_r^{air} and F_r^{air+o2} are the PAS cell resonant frequencies of filtered ambient air and filtered ambient air plus oxygen, respectively, during the two highlighted periods in Figure 3.5. Ozone flow splitting was evaluated between PAS pairs (2,5), (1,4) and (3,5) in Figure 3.4. The ozone splitting ratio represents the fractional difference in the ozone concentrations within two PAS cells due to unequal flow splitting within the ozone manifold. The ozone splitting ratios between cells located in parallel were found to be in the range 2–28 %. Measuring the ozone splitting between PAS cells using the resonant shift method compared extremely well to in-line mass flow measurements, to within 2 %. The 1σ variability between ozone splitting corrections for eight repeat ozone calibrations was ± 1.3 %.

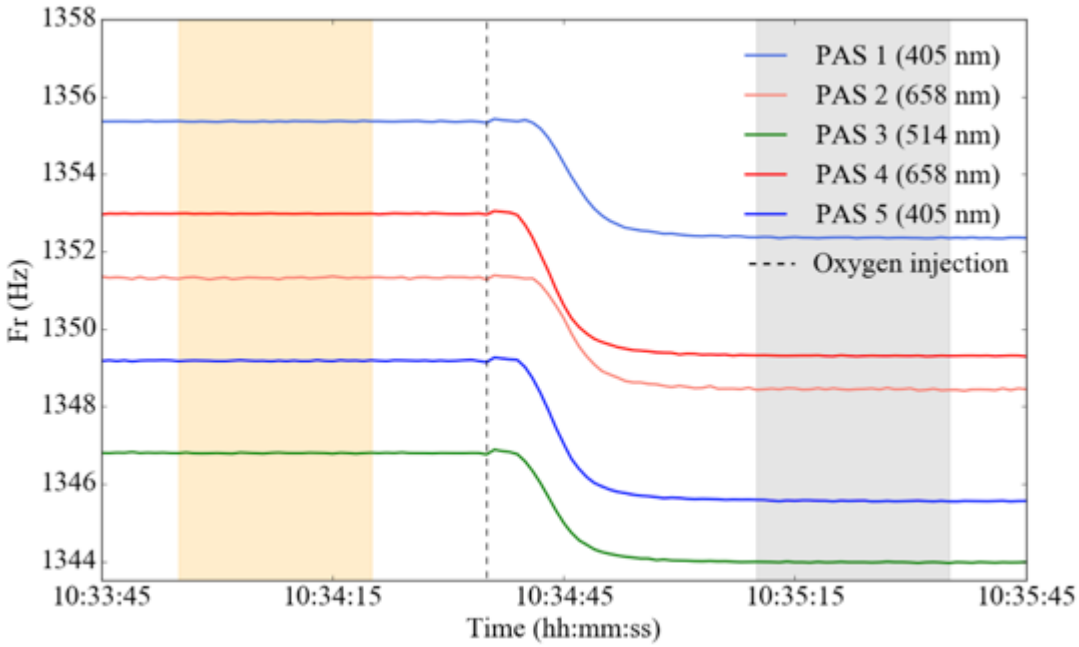

Figure 3.5: *PAS cell resonant frequency as a function of time. Oxygen was introduced into the filtered ambient-air flow at 10:34:35 (dotted line). Mean cell*

resonant frequencies before (orange highlighted region) and after (grey highlighted region) introducing oxygen were computed during the highlighted times.

Following measurement of ozone splitting ratios, the ozone generator was powered and the main calibration started. Calibrations involved the stepwise measurement of nine ozone concentration levels by the CRDS and PAS, as shown in Figure 3.6. At each ozone level, cell resonant frequencies and quality factors were quantified using the cell speakers. Subsequently, 90 seconds of data were collected from which the mean and standard deviation of PAS IA and CRDS extinction were calculated. The minimum and maximum extinction coefficients for ozone shown in Figure 3.6 (1.3 and 27.1 Mm^{-1}, respectively), correspond to ozone mixing ratios of approximately 33–680 ppmv (Serdyuchenko *et al.*, 2014).

The ratios of ozone extinction coefficients measured in the 405 and 658 nm CRDS cells were compared to the ratio of the literature ozone absorption cross sections to test for contamination by absorbing gaseous or aerosol species during ozone calibrations. After accounting for uneven ozone flow splitting between the cells, the ratio of the measured extinction coefficients at 658 and 405 nm agreed with the literature cross section ratio to within 2.0 %. This excellent agreement provides strong evidence that there were no issues with contamination during ozone calibrations.

3.5.3 Analysis of calibration data

Analysis of calibration data involved the following steps. Firstly, corrections were applied to normalise the raw microphone IA, IA_{raw}, by the laser power and cell resonance properties so that the calibration could later be applied to measured data with different laser powers and resonance properties. The corrected photoacoustic response, IA_{norm}, was calculated by multiplying IA_{raw} by the correction factor shown in equation 3.3 (Arnott *et al.*, 1999):

$$C = \frac{F_R}{QP_L} \tag{3.3}$$

where F_R is the cell resonance frequency, Q the cell quality factor and P_L the circulating laser power, as measured by the photodiode. PAS cell quality factors were in the range 87–93.

Secondly, the background signal measured in the absence of ozone or particles, $\mathrm{IA}_{\mathrm{norm}}^{\mathrm{bkg}}$, was characterised. This signal was subsequently subtracted from $\mathrm{IA}_{\mathrm{norm}}$ to yield the background corrected microphone signal, $\mathrm{IA}_{\mathrm{corr}}^{\mathrm{O3}}$. A least-squares linear fit of $\mathrm{IA}_{\mathrm{corr}}^{\mathrm{O3}}$ against CRDS-derived extinction was then performed to determine the PAS calibration coefficient. Figure 3.6 shows an example fit for a 405 nm PAS channel. Across all PAS cells, straight line gradients were typically in the range 0.02–0.32 and R^2 values were consistently >0.999. The mean 1σ fitting uncertainty in the gradient of the linear ozone calibration gradients covering all cells was 0.15 %.

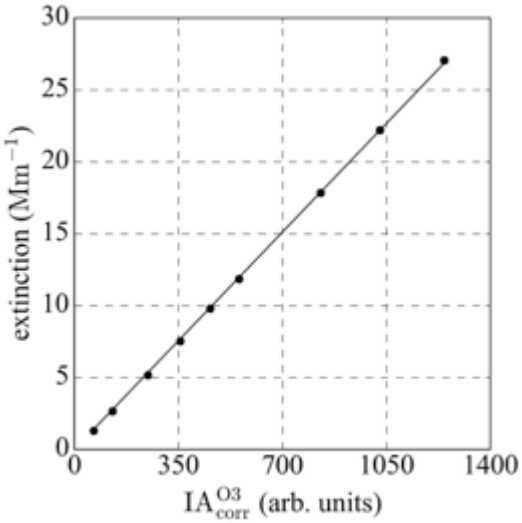

Figure 3.6: *Photoacoustic spectrometer response (microphone integrated area (IA)) and concurrent cavity ring-down spectrometer extinction coefficient for nine ozone concentrations at wavelength 405 nm. Each point is the mean of 90 seconds of 1 Hz data and error bars represent the 2σ precision of each measurement; these are not discernible by eye due to the excellent precision.*

Since there was no green-wavelength CRDS cell available, the 514 nm PAS cell was calibrated by evaluating the 514 nm absorption coefficient using measurements from the 658 nm CRDS cell and equation 3.4:

$$b_{abs\_514} = \frac{b_{ext\_658}}{\sigma_{abs\_658}} \sigma_{abs\_514} \qquad (3.4)$$

where $\sigma_{abs\_658} = 2.19\times10^{-21}$ cm^2 and $\sigma_{abs\_514} = 1.62\times10^{-21}$ cm^2 are the ozone absorption cross sections at the wavelengths of interest (Gorshelev *et al.*, 2014), b_{ext_658} is the extinction coefficient measured using the 658 nm CRDS channel and b_{abs_514} is the absorption measured by the 514 nm PAS channel.

The 658 nm CRDS channel was used to calibrate the 514 nm PAS channel because it extended over a greater range of extinction coefficients (167–1506 Mm^{-1}) than the 405 nm CRDS (1–27 Mm^{-1}). Calibrating the 514 nm channel using the 405 nm CRDS channel, as opposed to the 658 nm channel, lead to comparable absorption coefficients that differed by order 3.2 %.

3.6 Aerosol generation and conditioning

Figure 3.7 shows a schematic diagram of the particle generation setup. Water-soluble nigrosin, a strong light-absorbing dye at visible wavelengths, (Sigma Aldrich, CAS Number 8005-03-6, lot number MKBR1705V, product number 198285-100G) was dissolved into high purity deionised water (VWR Chemicals) with a range of concentrations between 3.2–7.1 grams per litre (g L^{-1}). The solution was drawn into a TSI constant output atomizer (TSI, 3076), which used high purity synthetic air (BOC, 270028-L) at a flow rate of approximately 2.5 L min^{-1}. The generated aerosol was dried to < 10 % relative humidity using a silica gel diffusion drier (Topas, DDU-570) and passed through an electrical ionizer (MSP, 1090). After exiting the ionizer, the aerosol stream was split between a differential mobility analyser (DMA) column (TSI, 3081) and mass flow controller. Flow rates through the mass flow controller were set to regulate the flow through the DMA such that the sample-to-sheath flow ratio was at least 1:10 with a sample flow rate in the range 0.3–0.4 L min^{-1} and sheath flow rate in the range 3.5–4.0 L min^{-1}. This approach ensured that sufficient flow through the ionizer was maintained to ensure a Fuchs' charge distribution was applied to the particles. The flow rate through the DMA decreased with time due to impactor dirtying, which impeded the flow and thus altered the flow splitting between the mass flow controller (MFC) and DMA column. This variation was < 5 % over the course of a test. Section 3.7 provides details of the sensitivity of modelled optical properties of nigrosin to DMA flow rates. The DMA was coupled to a CPC (TSI, 3776) to operate as a scanning mobility particle sizer (SMPS, path A in Figure 3.7), which was used to characterise the atomizer output for periods at the start and end of each experiment. To obtain a quasi-monodisperse aerosol size distribution for optical measurements, the DMA was operated at fixed voltages (path B in Figure 3.7).

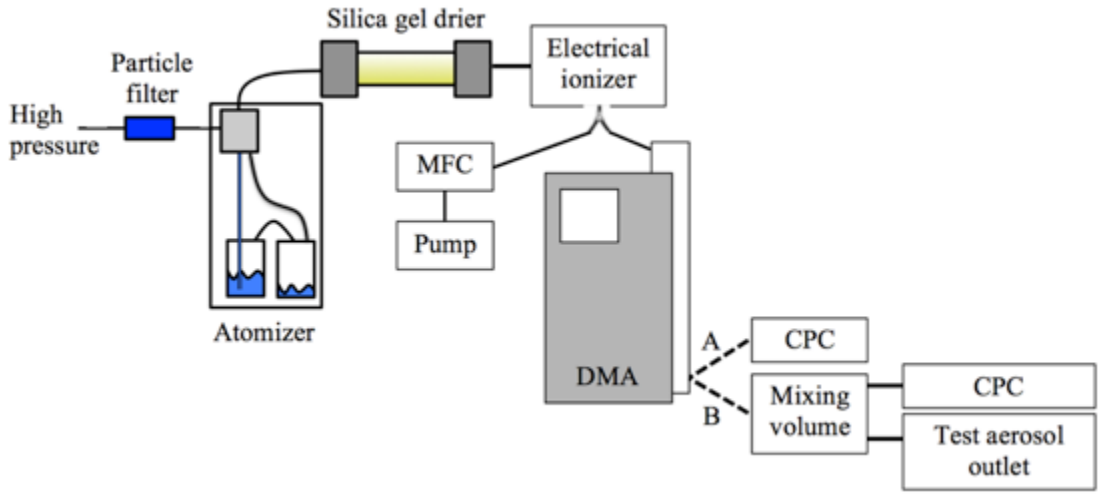

Figure 3.7: *Experimental setup for generating nigrosin aerosol. The dashed lines labelled 'A' and 'B' represent two independent flow lines (changed manually) used for scanning mode (line A) or fixed voltage size-selection mode (line B). Abbreviations: 'MFC': mass flow controllers, 'DMA': differential mobility analyser and 'CPC': condensation particle counter.*

For optical measurements, aerosolised nigrosin was mobility-selected with central diameters in the range 250–425 nm in 25 nm steps. The aerosol flow was split between optical cells as shown in Figure 2.3. All PAS cells were operated in parallel, with two of these cells also having CRDS channels in series as shown previously in Figure 3.4. The flow rate through each cell was 1 L min^{-1} and was controlled using mass flow controllers (Alicat, MC Series), which resulted in a plug-flow residence time within each PAS cell of approximately 12 seconds. To measure the particle number concentration, the mass flow controller on the output of the 514 nm PAS cell was replaced with a second CPC (TSI, 3010), which used a critical orifice to control the flow rate to 1 L min^{-1}. Aerosol number concentrations during experiments ranged from 40–575 cm^{-3}.

The aerosol flow splitting between cells was evaluated to test whether the CPC-measured number count in the 514 nm PAS cell was representative of the other PAS cells. The aerosol number concentration within the mixing volume and at the outlet of each PAS cell was measured in turn using the two CPCs simultaneously. These measurements allowed the particle transmission efficiency through each PAS cell to be determined independently of variations in particle generation stability. Differences between particle transmission through

the 514 nm PAS cell and other PAS cells ranged from 1.1–4.5 %. Particle concentrations were adjusted to account for these variations.

3.7 Modelling ensemble absorption cross sections

It is well established that the use of differential mobility analysis for aerosol size selection leads to the generation of a polydisperse size distribution due in part to multiple charging of particles (e.g. Wiedensohler *et al*., 2012). To correctly model the optical properties of the size-selected sample, the multiplet contributions must be taken into account. Transfer function theory can be used to predict the aerosol size distribution exiting the DMA (Knutson and Whitby, 1975). Mie theory (Bohren and Huffman, 1998) can then be applied to calculate single particle optical cross sections at each diameter in the ensemble. By combining the two theories, the ensemble optical cross sections (hereafter referred to as the *cross section*) for quasi-monodisperse mobility-size-selected aerosol can be calculated. The following section describes how this calculation was implemented.

Firstly, the polydisperse input aerosol size distribution to the DMA was measured (Figure 3.8(a)) using the SMPS. The accuracy of SMPS sizing was confirmed using monodisperse polystyrene latex spheres (ThermoFisher Scientific, 3000 Series Nanosphere Size Standard). Bimodal lognormal distributions were fitted to the SMPS-measured particle size distributions over the diameter range 71–532 nm. Size distributions were measured before and after running mobility-selected nigrosin through the PAS and CRDS cells to characterise the variability in the particle size distribution over time. The impact of observed variability on the size distribution exiting the DMA and, consequently, on the modelled optical cross sections was evaluated by propagating each measured size distribution through the Mie closure routine (described below). Variability in the aerosol generation stability led to a mean standard deviation in the modelled absorption cross sections of 4.3 % for all wavelengths and size-selected diameters.

The DMA transfer function describes the probability of a particle of given diameter exiting the DMA. It is used to derive the quasi-monodisperse size distribution at the DMA outlet when operated at fixed voltage (Knutson and

Whitby, 1975). Figure 3.8(b) describes the diffusional transfer function for a particle with 250 nm mobility diameter calculated using the equations presented by Stolzenburg (1988). The transfer function was evaluated for the DMA geometry and aerosol/sheath flow rates used in this study. I verified my calculations of the transfer function in several ways. The width of the transfer function in the absence of diffusional broadening was verified using the expression presented by Stolzenburg and McMurry (2008). The diffusional broadening parameters used in the transfer function model were also evaluated against the values presented in Stolzenburg (1988), namely the G_{DMA} and $\widetilde{D}$ factors, which agreed to better than 1 %. Finally, the diffusional transfer function was verified quantitatively against the Hagwood *et al*. (1999) simulations, which also used the same Stolzenburg (1988) formulation as used in this work.

To model the quasi-monodisperse aerosol size distribution at the DMA outlet when operated at a fixed voltage, the particle charging efficiencies for the range of particle diameters in the polydisperse input size distribution were calculated using Fuchs' charging theory (Wiedensohler, 1988). Aerosol charging efficiencies were calculated for positive ions with up to six elementary charges (Figure 3.8(c)). Fuchs' charging theory was found to be a good approximation of particle charging efficiencies for the experimental setup described in Figure 3.7. I verified that the modelled ratios of singly to doubly charged particles exiting the DMA agreed with experimentally measured ratios by comparing to measurements made using a Passive Cavity Aerosol Spectrometer Probe (DMT, PCASP-100X). Modelled and measured charge fractions agreed to within 6 % for particles with diameter ≥ 250 nm, with this uncertainty due in part to the limited sizing resolution of the PCASP. Propagating this uncertainty through the Mie closure routine (described below) led to a mean uncertainty of ± 0.93 % in the modelled absorption cross sections for all wavelengths and mobility-selected diameters.

The aerosol size distribution exiting the DMA was calculated by multiplying the polydisperse aerosol size distribution at the DMA input by the DMA diffusional transfer function and the aerosol charging efficiencies for corresponding particle diameters (Figure 3.8(d)).

From the calculated size distribution exiting the DMA, the absorption and extinction cross sections were calculated using Mie theory (Bohren and Huffman, 1998) for each particle diameter in the size distribution, the PAS wavelengths and nigrosin refractive indices from Bluvshtein *et al*. (2017) (Figure 3.8(e)). Mie theory assumes that a particle interacting with radiation is spherical, which is a reasonable assumption for nigrosin particles based on previous studies (e.g. Lack *et al*., 2006). The refractive index values reported by Bluvshtein *et al*. (2017) were chosen to facilitate direct comparison between the two sets of results. The refractive indices used in this analysis were 1.624 ± 0.0063 + (0.1541 ± 0.0081)*i* for 405 nm, 1.622 ± 0.0085 + (0.2594 ± 0.011)*i* for 514 nm and 1.811 ± 0.007 + (0.2476 ± 0.0031)*i* for 658 nm. Sensitivity of the modelled absorption cross section to the imaginary part of the refractive index was quantified using the values and uncertainties presented in Bluvshtein *et al*. (2017), resulting in a mean uncertainty for all wavelengths and mobility-selected diameters of 1.15 %. Similarly, uncertainty in the modelled absorption cross sections due to a ± 5 % change in the DMA aerosol flow rate was 0.21 %.

Finally, the ensemble absorption and extinction cross sections were calculated by weighting the Mie cross sections by the relative number of each size particle exiting the DMA, calculated using

$$\overline{\sigma_{abs}} = \sum_i \sigma_i^{abs} N_i \qquad (3.5)$$

where σ_i^{abs} is the Mie absorption cross section at diameter D_i and N_i is the component of the normalised size distribution at diameter D_i, i.e. the distribution that was assumed to enter the PAS and CRDS cells, such that $\sum N_i = 1$. A similar expression was used to calculate $\overline{\sigma_{ext}}$ where σ_{abs} was replaced by σ_{ext}. The cumulative absorption cross section for 250 nm mobility-selected nigrosin is plotted in Figure 3.8(f). This result highlights the relative importance of the absorption contribution from multiply charged particles. Although this contribution was lower for larger mobility-selected diameter particles, it can still significantly contribute to absorption as shown by the dashed green line in Figure 3.8(f) for 400 nm diameter particles.

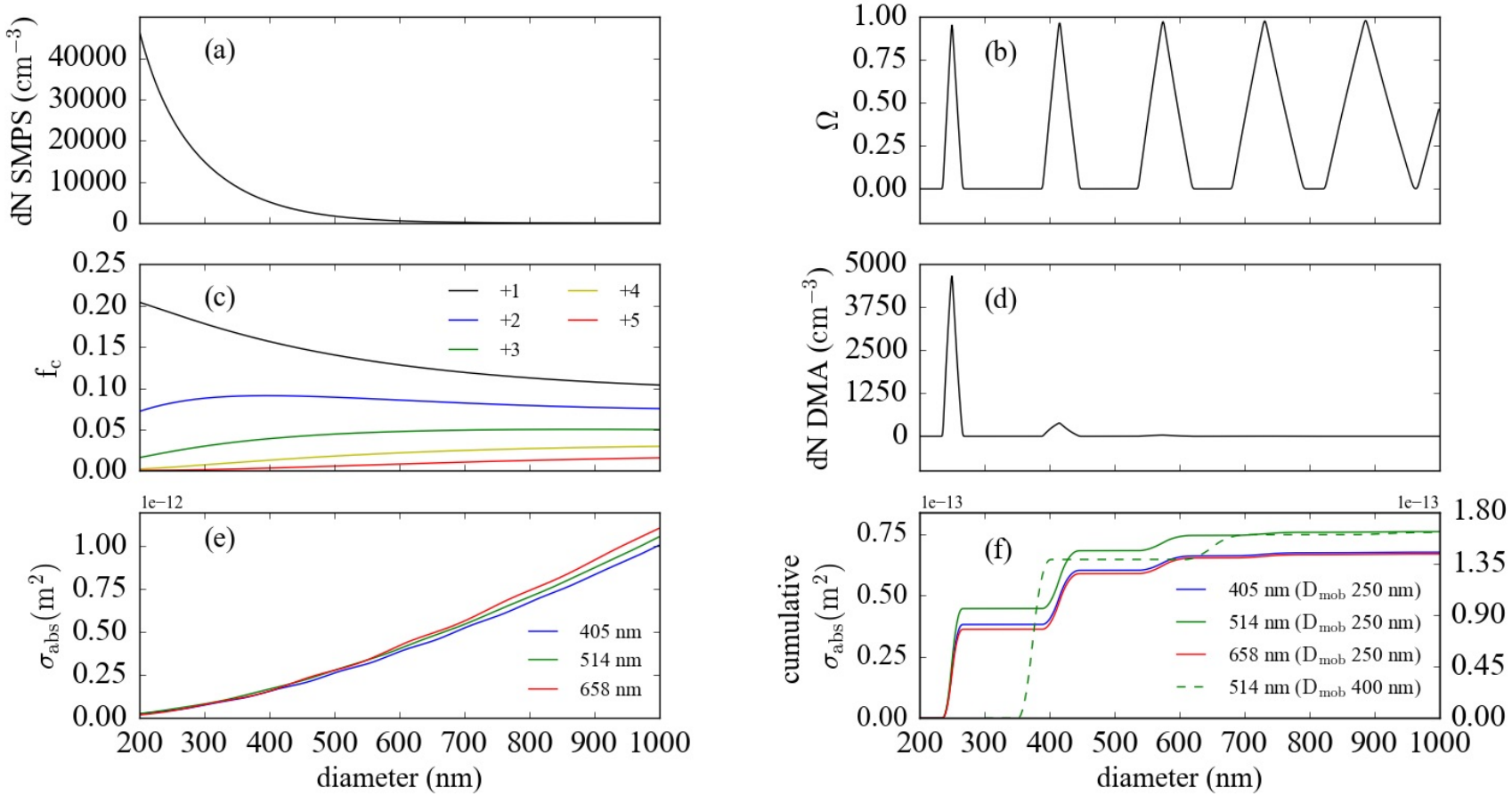

Figure 3.8: *An overview of steps involved in modelling the absorption cross section. (a) SMPS-measured particle size distribution. (b) DMA diffusional transfer function for a fixed DMA voltage corresponding to a mobility-selected diameter of 250 nm. (c) Fuchs' charging probabilities for positively charged particles. The figure legend indicates the magnitude of the positive charge. (d) Modelled size distribution exiting the DMA column when operated at fixed voltage for a mobility diameter of 250 nm. (e) Absorption cross sections calculated using Mie theory for three visible wavelengths of light, as indicated in the figure legend. (f) Cumulative absorption cross sections for nigrosin with a mobility-selected diameter of 250 nm. The dashed green line represents the absorption cross section at wavelength 514 nm corresponding to a 400 nm mobility-selected diameter nigrosin particle using the scale on the right.*

3.8 Results and discussion

Initially, the accuracies of the cavity ring-down spectrometers were verified, as they form an integral part of the photoacoustic spectrometer calibrations. The extinction cross sections for nigrosin with mobility-selected diameters in the range 250–425 nm were measured using CRDS and modelled using Mie theory, as outlined in section 3.7. The mean gradient between the modelled and CRDS-measured extinction cross sections was 0.98 ± 0.01 (2σ fitting uncertainty) as shown in Figure 3.9. Gradients for the 658 nm and 405 nm wavelengths were 0.96 and 1.00, respectively.

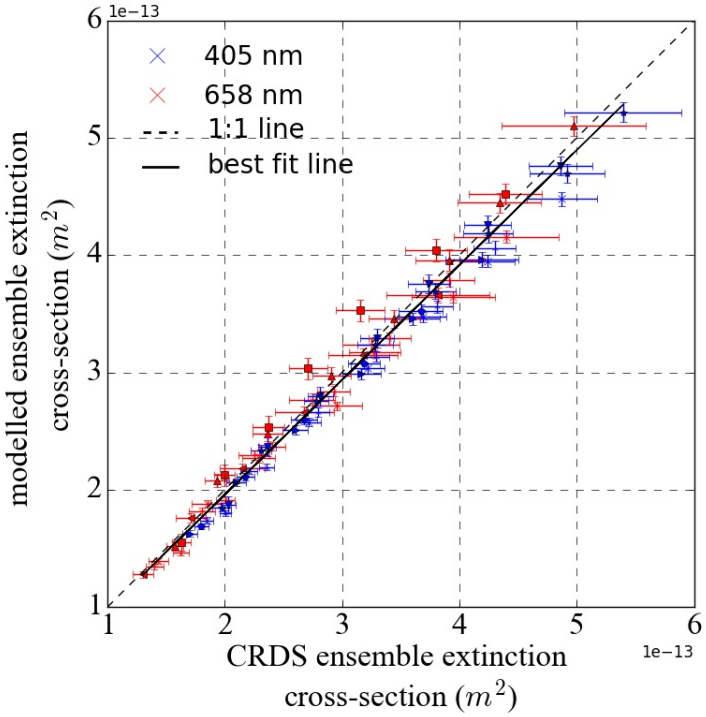

Figure 3.9: *Modelled versus CRDS-measured extinction cross sections for nigrosin aerosol at 405 nm and 658 nm wavelengths.*

The mean gradient between the modelled and PAS-measured absorption cross sections for nigrosin for all five ozone-calibrated PAS cells was 1.08 ± 0.01 (2σ fitting uncertainty) as shown in Figure 3.10. Gradients for the 405, 514 and 658 nm wavelengths were 1.08, 1.07 and 1.09 respectively. These data encompass multiple experimental runs using three independent ozone calibrations.

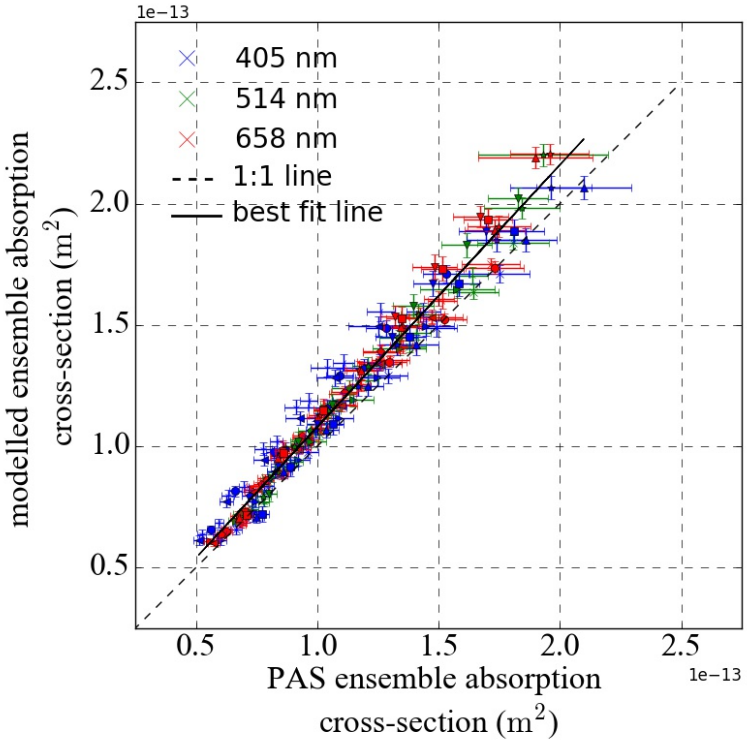

Figure 3.10: *Modelled versus PAS-measured absorption cross sections for nigrosin aerosol at 405, 514 and 658 nm wavelengths.*

The uncertainties in the measured optical cross sections for nigrosin shown by the error bars in Figure 3.9 and Figure 3.10 represent the standard deviations for each 90-second cross section measurement, encompassing the precision in both the associated PAS absorption coefficient and CPC measurements. Modelled optical cross sections may be subject to an additional 5 % bias due to uncertainty in the CPC accuracy (Fletcher *et al.*, 2009). Uncertainties in the modelled cross sections were calculated by combining the uncertainties due to variability in the size distribution, charging distribution and imaginary part of the refractive index in quadrature.

The key result of this work is the demonstration that photoacoustic spectrometers can be calibrated accurately using ozone at short wavelengths (405 nm), which contrasts with the recent results of Bluvshtein *et al.* (2017). A thorough evaluation of model uncertainties has shown that this result is robust, despite uncertainties in the imaginary part of the nigrosin refractive index and variability in the measured polydisperse aerosol size distribution used to calculate model absorption properties. The importance of accurately modelling the contribution of multiply charged particles to capture the optical behaviour of

the quasi-monodisperse distributions used in these experiments was also demonstrated.

Since this study, a separate study by Fischer and Smith (2018) has performed experiments in an attempt to reconcile the differences between the results presented in this chapter and the results of Bluvshtein *et al.* (2017). Fischer and Smith (2018) postulated that this discrepancy might be due to non-thermal relaxation pathways such as photodissociation, which do not transfer thermal energy into the surrounding gas and thus into PAS signal, or due to inefficient energy transfer to the surrounding gas at a rate slower than the laser modulation frequency. To investigate this discrepancy, they examined PAS microphone responses to ozone when the PAS cells were filled with pure N_2 compared to pure O_2, as well as to NO_2 and nigrosin aerosols. A key finding of their study was that the PAS responses to ozone were over 50 % weaker when the cells were filled with N_2 compared to O_2 and when compared to the PAS responses to NO_2 and nigrosin. This difference was attributed to ozone loss via photodissociation within N_2, which was not observed in O_2 due to rapid ozone reformation.

Fischer and Smith (2018) also investigated how the PAS microphone responses varied as the concentration of oxygen was increased within their PAS cells between 0–100 % for a given concentration of ozone. They observed a sharp rise in the PAS sensitivity as 0–20 % of oxygen was added to N_2. For higher fractional oxygen content, the PAS response asymptotically approached an upper limit that was in line with the other calibrants, to within 3 % of the PAS response to NO_2. The explanation for this change in PAS sensitivity as a function of ozone is due to the rate of thermal energy transfer between ozone and the surrounding gas.

The Fischer and Smith (2018) results have implications for the EXSCALABAR PAS ozone calibrations, which suggest that PAS microphone responses may be too low by ~ 10 % for a fractional oxygen content of 20 %. This result is in line with the work presented in this chapter, which found that PAS responses to nigrosin when calibrated using ozone were underestimated by up to 9 % compared to model calculations.

To quantify the impact of this result on our PAS cells, the Fischer and Smith (2018) experiments were repeated by performing ozone calibrations under variable O_2-N_2 PAS cell gas composition. These experiments revealed no systematic calibration bias, in contrast to the Fischer and Smith (2018) study, and is the subject of on-going research.

3.9 Conclusions

This study has shown that the ozone calibration method can be used to calibrate accurately photoacoustic instruments operating at short-visible wavelengths. This result alleviates concerns based on previously published results, which have shown large discrepancy at 404 nm. Using nigrosin aerosol with mobility-selected diameters in the range 250–425 nm, I verified that the measured absorption cross sections using photoacoustic spectroscopy agreed with modelled values to within 8 %. This agreement may be improved even further by application of a small correction for bath gas composition based on the recent work of Fischer and Smith (2018). These results thus provide robust evidence for high accuracy PAS calibration using ozone for optical wavelengths 405, 514 and 658 nm.

4 Examining biases in filter-based aerosol absorption measurements using photoacoustic spectroscopy

4.1 Chapter overview

In this chapter, I evaluate biases in filter-based absorption measurements by direct comparison to photoacoustic measurements for a range of aerosol sources. I will then assess the impact that biases in filter-based absorption measurements have on the single scattering albedo, absorption Ångström exponent and the attribution of absorption to black and brown carbon.

4.2 Introduction

Filter-based absorption photometry is used widely to determine aerosol absorption coefficients and has considerable benefits including that it is relatively inexpensive, portable and capable of unattended measurements for

long periods of time (Baumgardner *et al.*, 2012). Filter-based instruments measure the light transmittance across a filter continuously, which changes as particles are deposited onto the filter, providing a measure of aerosol absorption (see section 4.3) (Lin *et al.*, 1973). Figure 4.1 shows the key elements of a filter-based absorption photometer.

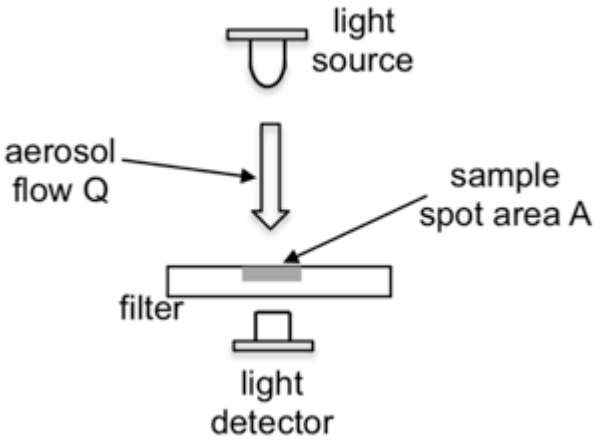

Figure 4.1: *Key components of a filter-based absorption photometer. Figure from Müller et al. (2014).*

Absorption coefficients determined using filter-based absorption photometry can be subject to measurement artefacts due to (i) scattering of light away from the light-detector leading to erroneous apparent absorption (Bond *et al.*, 1999) and (ii) enhanced absorption as particles are deposited onto the filter. The latter leads to multiple scattering between the particles and filter medium, providing multiple opportunities for absorption, which depends on the filter loading such that an increase in the number of deposited absorbing particles reduces the multiple scattering between the filter and particle layers (Liousse *et al.*, 1993; Bond *et al.*, 1999; Weingartner *et al.*, 2003). This artefact leads to lower absorption coefficients for highly loaded filters relative to lightly loaded filters, known as the particle shadowing effect (Weingartner *et al.*, 2003). These artefacts depend on the number of particles deposited onto the filter and their optical properties (Bond *et al.*, 1999; Weingartner *et al.*, 2003). A number of empirical and semi-empirical correction schemes have been derived to correct for artefacts in filter-based absorption photometers. This study will focus on correction schemes derived for use with glass-fibre Pallflex E70-2075W filters; these filters have been used widely with the Particle Soot Absorption Photometer (PSAP, Radiance Research) (Bond *et al.*, 1999; Virkkula *et al.*, 2005; Virkkula, 2010; Müller *et al.*, 2014). These correction schemes are also

valid for any similar instruments using this filter substrate, for example the Tricolor Absorption Photometer (TAP, Brechtel Manufacturing) used in this study, described in section 4.4.2 (Ogren *et al.*, 2017).

Another potentially significant measurement artefact in filter-based absorption photometry is due to liquid-like organic aerosols spreading across the filter fibres (Lack *et al.*, 2008). The mechanisms proposed for this artefact include a change in the physical shape and therefore optical properties of deposited particles, or coating effects whereby deposited particle absorption is enhanced via a lensing effect (Subramanian *et al.*, 2007; Cappa *et al.*, 2008; Lack *et al.*, 2008).

Lack *et al*. (2008) found PSAP absorption coefficients were biased high in the range 12 % to > 200 % at 532 nm compared to photoacoustic measurements of aerosol absorption for aerosols over the Gulf of Mexico, which included BC, nitrate, sulphate and organic aerosols from shipping emissions. These PSAP biases were found to be positively correlated to the organic aerosol mass concentration. Lack *et al*. (2008) further concluded that the biases were correlated more strongly to the ratio of the organic aerosol to light-absorbing carbon mass rather than to organic mass alone. To verify these measurements, Cappa *et al*. (2008) performed laboratory experiments using secondary organic aerosol (SOA) derived from the ozonolysis of α-pinene, which had a single scattering albedo (SSA) > 0.998 at 532 nm. A key finding of this study was that for external mixtures of SOA and soot, the PSAP absorption could be biased high by a factor 2.6 compared to photoacoustic spectroscopy, consistent with the findings of Lack *et al*. (2008). Cappa *et al*. (2008) also found that the magnitude of the absorption bias was strongly dependent upon the filter transmittance and that the bias was both immediate (clean filter) and cumulative (filter previously exposed to absorbing material). The results from both of these studies (Cappa *et al.*, 2008; Lack *et al.*, 2008) were independent of the correction scheme applied (Bond *et al.*, 1999; Virkkula *et al.*, 2005).

More recently, Subramanian *et al*. (2010) derived the BC mass absorption coefficient (MAC) at 660 nm for fresh and 1–2 day-old aerosol emissions in and around Mexico City by dividing the absorption coefficients measured using a

PSAP by the BC mass concentrations measured using a single particle soot photometer (SP2, Droplet Measurement Technologies). For the fresh emissions, they found a ~50 % enhancement in their measured BC MAC relative to the value reported by Bond and Bergstrom (2006), whose review was based on an extensive range of measurements including PAS and extinction minus scattering measurements. The BC MAC bias was attributed in part to an over-estimation of the absorption coefficients measured by the PSAP due to externally mixed liquid-like organic matter. However, the BC MAC values for the relatively thickly coated, aged BC further from the city were in line with those estimated by Bond and Bergstrom (2006), suggesting that biases in filter-based absorption measurements relating to high organic aerosol loading may only be present when organic aerosol is externally mixed with BC (Subramanian *et al.*, 2010). Indeed, another explanation for this finding could be that absorption enhancements were observed for fresh emissions but not for aged emissions due to loss of semi-volatile species. Subramanian *et al.* (2010) provided evidence for this argument, noting that although aged air masses were generally associated with more thickly coated BC, some aged air masses were associated with thinly coated BC, which could be due to increased likelihood for wet scavenging of the relatively hydrophilic, thickly coated BC aerosols.

Using a similar methodology, McMeeking *et al*. (2011) derived the BC MAC at 550 nm using PSAP and SP2 measurements for urban pollution aerosols around the UK, reporting organic aerosol mass concentrations in the range 1–7 μg m^{-3}. The work by Lack *et al*. (2008) indicates that a positive absorption bias of up to 50 % would be expected, however, no bias in the BC MAC was observed. McMeeking *et al*. (2011) postulated that this result could be due to limitations in the PSAP and SP2 measurements or a physical effect whereby absorption enhancement due to coatings was offset by the collapse of fractal BC aggregates (McMeeking *et al.*, 2011). Indeed, another explanation for this discrepancy could have been that the organic aerosol sampled here was not quasi-liquid like.

Biases in filter-based absorption photometry measurements can limit the accurate determination of key climate-relevant parameters including, for example, the aerosol SSA and absorption Ångström exponent (AAE) (e.g.

Sherman and McComiskey, 2018). Biases can also impact the accuracy with which the aerosol composition can be attributed when using the AAE to differentiate between BC, BrC and dust (e.g. Bergstrom *et al.*, 2007). Using the AAE to attribute aerosol composition utilises the varying spectral signatures of aerosols by evaluating the inherent power law wavelength dependence of their optical properties (Bergstrom *et al.*, 2007). The absorption contribution of BrC is commonly assessed by (i) attributing all absorption at long visible wavelengths (i.e. in the range 660–1000 nm depending on the available wavelengths of the instrument) to BC, assuming negligible absorption by BrC, (ii) evaluating the theoretical black carbon absorption contribution by extrapolating to shorter wavelengths using an assumed AAE of 1 and (iii) attributing the difference between measured absorption and theoretical BC absorption to BrC (e.g. Kirchstetter *et al.*, 2004; Clarke *et al.*, 2007; Yang *et al.*, 2009; Kirchstetter and Thatcher, 2012; Zhu *et al.*, 2017). Using a BC AAE of 1 may introduce additional uncertainty to aerosol source apportionment studies, which has been found to be in the range 0.8–1.7 (Gyawali *et al.*, 2009; Lack and Cappa, 2010; Lack and Langridge, 2013). Backman *et al*. (2014) assessed the sensitivity of the PSAP-derived AAE to the Bond *et al*. (1999) and Virkkula (2010) correction schemes for measurements recorded on the central Highveld in South Africa, which was dominated by fossil-fuel burning activities including coal-fired power plants. They found that the AAE varied between 1.34 to 1.96 dependent upon the PSAP correction scheme applied, which led to different conclusions regarding the aerosol composition and source (Backman *et al.*, 2014).

The aim of this study is primarily to evaluate biases in filter-based absorption photometry across a range of visible wavelengths and for a range of aerosol sources. I assess biases by comparing absorption coefficients determined using a TAP at wavelengths of 467, 528 and 652 nm to photoacoustic measurements made during a series of research flights aboard the UK Facility for Airborne Atmospheric Measurements (FAAM) BAe-146-301 aircraft. Aerosol sources sampled include urban aerosol emissions over London, fresh biomass burning aerosol (BBA) over West Africa and aged BBA over the Southeast Atlantic Ocean. I follow the methodology of Lack *et al*. (2008) by looking at the absorption biases as a function of organic aerosol concentration, extending their study by looking at a greater range of wavelengths and aerosol sources as

well as evaluating additional correction schemes, namely those developed by Virkkula (2010) and Müller *et al*. (2014). I then assess the impact that biases in filter-based absorption photometry have on the aerosol SSA and AAE and the impact that biases can have on the source apportionment of BrC.

4.3 Methodology and measurements

4.3.1 Principles of filter-based absorption photometry

Filter-based absorption photometers measure the light transmitted through a filter as particles are deposited onto the filter such that the attenuation can be defined as

$$I = -ln\left(\frac{I_s}{I_r}\right), \tag{4.1}$$

where I_s and I_r are the intensities of light transmitted through a filter corresponding to a sample spot (i.e. an area of the filter with deposited aerosols) and reference spot (i.e. an area of the filter without deposited aerosols), respectively (Ogren *et al.*, 2017). The absorption coefficient can thus be determined using

$$b_{ap}^{raw} = \frac{A}{Q\Delta t}(I(t+\Delta t) - I(t)), \tag{4.2}$$

where A is the area of the aerosol deposited onto a filter, Q is the flow rate of the aerosol-laden stream pulled through a filter, Δt is the time between successive measurements of light attenuation and $I(t)$ and $I(t+\Delta t)$ are the light attenuations at times t and $t+\Delta t$ (Ogren *et al.*, 2017). To correct b_{ap}^{raw} for apparent and enhanced absorption, I applied the correction schemes developed by Bond *et al*. (1999), Virkkula, (2010) and Müller *et al*. (2014), which will be referred to as b_{ap}^{B1999}, b_{ap}^{V2010} and b_{ap}^{M2014} respectively; see section 4.3.2–4.3.4.

4.3.2 The Bond et al. (1999) correction scheme (B1999)

The Bond *et al*. (1999) correction scheme was developed empirically by comparing PSAP absorption coefficients to reference absorption coefficients determined using the difference between extinction as measured by an optical extinction cell and scattering coefficients measured using a nephelometer. This correction scheme was clarified by Ogren (2010). Test aerosols included

polydisperse nigrosin aerosol and ammonium sulphate. Bond *et al*. (1999) found that

$$b_{ap}^{B1999} = f(Tr)b_{ap}^{raw} - sb_{sp}, \quad (4.3)$$

with

$$f(Tr) = \frac{0.85}{K_2(1.0796Tr + 0.71)}, \quad (4.4)$$

$$s = \frac{K_1}{K_2}, \quad (4.5)$$

and where b_{sp} is the scattering coefficient, K_1=0.02, K_2=1.22 and Tr is the normalised filter transmittance, defined as (Ogren *et al.*, 2017)

$$Tr = \frac{I_s(t)/I_r(t)}{I_s(0)/I_r(0)}. \quad (4.6)$$

This correction scheme was derived at the wavelength 550 nm and is generally assumed to apply over the entire range of visible wavelengths, though there is no empirical basis for this assumption (Bond *et al.*, 1999; Ogren, 2010).

4.3.3 The Virkkula (2010) correction scheme (V2010)

The Virkkula *et al.* (2005) correction scheme and the subsequent Virkkula (2010) erratum were derived for the PSAP wavelengths 467, 530 and 660 nm, which is reflected by the $f(Tr, \lambda)$ term described below. The scheme was derived by comparing absorption coefficients determined using a multi-wavelength PSAP to those measured using either photoacoustic spectroscopy or to absorption derived by subtracting scattering from extinction measurements, using measurements from a nephelometer and an optical extinction cell, respectively (Virkkula *et al.*, 2005). Calibration aerosols included kerosene soot, graphite, diesel soot, ammonium sulphate and polystyrene latex spheres. Virkkula (2010) proposed that

$$b_{ap}^{V2010} = f(Tr, \lambda)b_{ap}^{raw} - sb_{sp}, \quad (4.7)$$

where

$$f(Tr, \lambda) = k_0 + k_1(h_0 + h_1\omega_0)ln(Tr), \quad (4.8)$$

and where k_0, k_1, h_0, h_1 and s are wavelength dependent constants and ω_0 is the wavelength dependent SSA. The values of the constants used in this study were taken directly from Table 1 in Virkkula (2010): $k_0^{467\,nm} = 0.377$, $k_0^{530\,nm} = 0.358$, $k_0^{660\,nm} = 0.352$, $k_1^{467\,nm} = -0.640$, $k_1^{530\,nm} = -0.640$, $k_1^{660\,nm} = -0.674$, $h_0^{467\,nm} = 1.16$, $h_0^{530\,nm} = 1.17$, $h_0^{660\,nm} = 1.14$, $h_1^{467\,nm} = -0.63$, $h_1^{530\,nm} = -0.71$, $h_1^{660\,nm} = -0.72$, $s^{467\,nm} = 0.015$, $s^{530\,nm} = 0.017$ and $s^{660\,nm} = 0.022$ (Virkkula, 2010). The wavelengths at which these constants were derived differ to those used in the TAP by 2 nm and 8 nm at the green and red wavelengths, respectively. It is unclear how these constants depend on wavelength. Hence to assess the impact that this wavelength mismatch might have on the absorption coefficients derived using the V2010 correction scheme, the single-wavelength V2010 constants, i.e. those derived using reference measurements at all three wavelengths, were also applied to TAP measurements. These were taken from Table 1 in Virkkula (2010): $k_0^{ave} = 0.362$, $k_1^{ave} = -0.651$, $h_0^{ave} = 1.159$, $h_1^{ave} = -0.687$ and $s^{ave} = 0.018$. Using the single-wavelength V2010 constants was found to have a minor impact on the results of this study and is discussed in section 4.6. The Virkkula (2010) correction is an iterative correction scheme due to its dependence on the SSA. Hence the algorithm was run 10 times for each time-step, which was sufficient for the absorption coefficient to converge to a single value with a precision better than 0.001 Mm^{-1}. An initial value for the SSA of 0 was assumed.

4.3.4 The Müller et al. (2014) correction scheme (M2014)

The constrained two-stream (CTS) algorithm developed by Müller *et al*. (2014) includes a two-stream radiative transfer model that explicitly accounts for the optical properties of the filter substrate and deposited particles and is constrained by either the Bond *et al.* (1999), Virkkula *et al.* (2005) or Virkkula (2010) parameterisations. This section covers the key equations from Müller *et al*. (2014) to show how they have been implemented in this study and the reader is referred to Müller *et al*. (2014) for a full derivation. The M2014 correction scheme makes use of the relationship between the absorption coefficient and the change in particle absorption optical depth, δ_{ap}, on the filter medium between two measurements separated by a time-step Δt, as represented by:

$$b_{ap}^{M2014} = \frac{A}{Q\Delta t}\big(\delta_{ap}(t+\Delta t) - \delta_{ap}(t)\big), \tag{4.9}$$

For each time-step, δ_{ap} was calculated iteratively by minimising the difference between the measured total optical depth, δ_{tot} (filter + particles) and the relative optical depth, δ_{CTS}, which is the change in total optical depth of the filter system after collecting a particle relative to the unloaded filter. A Newton-type solver was applied, as suggested by Müller *et al*. (2014), and required ten iterations to converge to a precision better than 0.001 Mm^{-1}. δ_{tot} was calculated from measurements of the filter, with and without aerosol, using equation 4.1. The equations outlined in Müller *et al*. (2014) were used to calculate δ_{CTS} and are included here for clarity.

$$\delta_{CTS} = \frac{F_s^{exp}\delta_{sp} + F_a^{exp}\delta_{ap}}{F_f^{mod}}, \tag{4.10}$$

where δ_{sp} is the particle scattering optical depth, calculated using

$$\delta_{sp} = \frac{Q\Delta t}{A}\sum_{t=0}^{t} b_{sp}(t), \tag{4.11}$$

$$F_s^{exp} = \delta_{sp}\left(a_5 + \big(a_0 + a_1 g_p\big)e^{-\left(\frac{ln(\delta_{sp})+a_4^2}{a_3+a_4 g_p}\right)^4}\right), \tag{4.12}$$

where $a_0 = 0.1509$, $a_1 = -0.1611$, $a_2 = 4.5414$, $a_3 = -5.7062$, $a_4 = -1.9031$, $a_5 = 0.01$ and g_p is the average weighted particle asymmetry parameter (see equation 4.23). Using the V2010 empirical correction,

$$F_{a,V2010}^{exp} = \sqrt{\left(\frac{c_1}{c_2 h_0}\right)^2 - \frac{2\delta_{ap}}{c_2 h_0}} + \frac{c_1}{c_2 h_0}, \tag{4.13}$$

where c_1, c_2, h_0, h_1 and s correspond to the wavelength dependent constants k_0, k_1, h_0, h_1 and s as defined in section 4.3.3, corresponding to the Virkkula (2010) parameterisation. Finally,

$$F_f^{mod}\big(\delta_{ap}, \delta_{sp}, g_p\big) = \frac{\delta\big(\delta_{ap}=0, \delta_{sp}, g_p\big) + \delta\big(\delta_{ap}, \delta_{sp}=0, g_p\big)}{\delta\big(\delta_{ap}, \delta_{sp}, g_p\big)}, \tag{4.14}$$

where

$$\delta(\delta_{ap}, \delta_{sp}, g_p) = -ln\left(T_{2L}(\delta_{ap}, \delta_{sp}, g_p)\right) + ln\left(T_{2L}(\delta_{ap} = 0, \delta_{sp} = 0, g_p = 0)\right), \quad (4.15)$$

$$T_{2L} = \frac{T_1 T_2}{1 - R_1(1 - T_2)}, \quad (4.16)$$

and T_1 and T_2 represent the filter transmittances of the particle-loaded and particle-free layers, respectively. These are represented by layers 1a and 1b in Müller *et al*. (2014), respectively. The filter transmittance and reflectance are given by

$$T = \frac{2}{[2 - \omega_0(1 + g)]sinh(K\delta_e/\mu_1)/K + 2cosh(K\delta_e/\mu_1)} \quad (4.17)$$

and

$$R = \frac{\omega_0(1 - g)sinh\left(K\delta_e/\mu_1\right)/K}{[2 - \omega_0(1 + g)]sinh\left(K\delta_e/\mu_1\right)/K + 2cosh\left(K\delta_e/\mu_1\right)}, \quad (4.18)$$

where

$$\delta_e = \chi\delta_{sf} + \delta_{sp} + \chi\delta_{af} + \delta_{ap}, \quad (4.19)$$

$$K = \sqrt{(1 - \omega_0)(1 - \omega_0 g)}, \quad (4.20)$$

$$\omega_0 = \frac{\chi\delta_{sf} + \delta_{sp}}{\chi\delta_{sf} + \delta_{sp} + \chi\delta_{af} + \delta_{ap}}, \quad (4.21)$$

and

$$g = \frac{\chi g_f \delta_{sf} + g_p \delta_{sp}}{\chi\delta_{sf} + \delta_{sp}}. \quad (4.22)$$

The filter scattering optical depths used in this study were $\delta_{sf}^{467} = 7.76$, $\delta_{sf}^{530} = 7.69$ and $\delta_{sf}^{660} = 7.34$ and the filter absorption optical depths used were $\delta_{af}^{467} = 0.033$, $\delta_{af}^{530} = 0.038$ and $\delta_{af}^{660} = 0.019$, as measured by Müller *et al*. (2014) for the same type of filters. Small differences between wavelengths that the filter optical properties were measured at by Müller *et al*. (2014) (467, 530, 660 nm) compared to those at which the TAP measures (467, 528, 652 nm) were assumed to be negligible. Following the nomenclature of M2014, for filter layer 1 (the particle-loaded filter layer) $\chi = 0.2$ and for layer 2 (the unloaded

filter layer) $\chi = 0.8$. This choice of χ values assumes that the particle penetration depth into the filter was 20 % and accounts for the fractional filter optical depths corresponding to each layer. The value used for μ_1 was $1/\sqrt{3}$. The value g_p is the average weighted asymmetry parameter of all particles deposited onto the filter, given by

$$g_p = \frac{\sum_i b_{sp}^i g_p^i}{\sum_i b_{sp}^i}, \tag{4.23}$$

where i represents the i th ensemble of particles with scattering coefficient b_{sp}^i. This equation is different to the equation presented by Müller *et al*. (2014) who recommended using individual particle scattering cross sections (as opposed to ensemble scattering coefficients). I used equation 4.23 as opposed to the recommended formulation because nephelometer measurements represent an ensemble. In this study, bulk asymmetry parameters (i.e. corresponding to an ensemble of particles) were calculated for each time-step using the parameterisation

$$g_p = -7.143889 b_{sp}^3 + 7.464439 b_{sp}^2 - 3.96356 b_{sp} + 0.9893, \tag{4.24}$$

where b_{sp} is the backscattering ratio measured using a nephelometer (Andrews *et al.*, 2006; Müller *et al.*, 2014).

To confirm the accuracy of the implementation of the M2014 algorithm used during this analysis, equations 4.15–4.22 were used to reproduce the results in Figure 6 of the Müller *et al*. (2014) study, which were verified against intermediate results (T. Müller, personal communication, 2016).

4.3.5 Determining the absorption Ångström exponent

The spectral dependence of aerosol absorption can be approximated by a power law relationship with a wavelength-dependent constant referred to as the AAE (Moosmüller *et al.*, 2011). It follows that the AAE is the negative slope of the logarithm of the absorption coefficient as a function of the logarithm of wavelength, defined as

$$AAE(\lambda_1, \lambda_2) = -\frac{ln\left(b_{ap}(\lambda)\right)}{ln(\lambda)}. \tag{4.25}$$

The value of BC's AAE is commonly assumed to be 1 for wavelengths in the visible and near-infrared (Moosmüller *et al.*, 2009, 2011; Lack and Langridge, 2013).

4.4 Measurements and instrumentation

All measurements presented in this study were made aboard the UK's BAe-146-301 large Atmospheric Research Aircraft (ARA) operated by the Facility for Airborne Atmospheric Measurements (FAAM; www.faam.ac.uk).

This section provides information on the filter-based, photoacoustic, nephelometry and aerosol composition instrumentation used aboard the aircraft and introduces the environments in which measurements were made.

4.4.1 Aerosol sampling and conditioning

An important strength of this dataset is that the TAP, PAS and cavity ring-down spectrometer (CRDS) instruments used to sample aerosol optical properties all shared a common sample inlet and were subject to the same flow conditioning, as described in Chapter 2.2.2. Aerosols were drawn into the aircraft through a modified Rosemount inlet (Trembath *et al.*, 2012) and distributed to the instruments as shown in Figure 2.3.

4.4.2 Tricolor Absorption Photometer (TAP)

The TAP is a commercially available (Brechtel) version of the Continuous Light Absorption Photometer (CLAP), described by Ogren *et al*. (2017). The TAP comprises of eight sample filter spots and two reference filter spots. The aerosol-laden air passes through one sample spot at a time, which allows for eight times the filter lifetime compared to single-spot photometers. The filtered air is re-circulated through one of the reference spots to enable the attenuation calculation (see equation 4.1) (Ogren *et al.*, 2017). Upon reaching a pre-defined filter transmittance set point, the TAP automatically changes to the next available sample filter spot. Pallflex (E70-2075W) glass-fibre filters with 47 mm diameter were used, which were nominally identical to the filters used to derive the correction schemes applied in this study (see sections 4.3.2–4.3.4). The TAP provides measurements at three wavelengths with peaks centred at 467, 528 and 652 nm. The LEDs are cycled through each wavelength once per second, providing absorption measurements at 1 Hz at all wavelengths. The

inlet of the TAP is heated to 35.2 ± 0.2 °C to minimise the effects of changing temperature and to prevent water condensing onto the filter. The built-in digital low-pass filter was disabled in all measurements to enable calculation of the absorption coefficients from the raw photodiode measurements. To understand the impact of disabling the low-pass filtering on instrument sensitivity, the TAP was run for ~3 h while it sampled filtered room air to characterise the noise in the system. Uncorrected absorption coefficients, b_{ap}^{raw}, were calculated at 1 Hz, and the average and standard deviation for each time interval Δt ($1 < \Delta t < 1000$ s) were calculated. The 1-sigma detection limits at 30 s averaging time were 0.71, 1.37 and 0.89 Mm^{-1} at wavelengths 652, 528 and 467 nm, respectively. Ogren *et al*. (2017) calculated the mean 1-sigma detection limit in their 28 instruments over all three wavelengths to be 0.33 Mm^{-1}. The difference between the detection limit measured in this study and that presented in Ogren *et al*. (2017) is likely due to running without low-pass digital filtering in the current study. TAP internal particle losses were estimated to be < 1 % for particles with diameters in the range 0.03–2.5 μm (Ogren *et al.*, 2017).

To determine the areas of the spots resulting from particle deposition onto the filter, nigrosin (product number 198285-100G) was atomised from solution, dried to < 10 % relative humidity using a silica gel diffusion drier (Topas, DDU-570) and sampled by the TAP. The areas of the eight sample spots were determined by measuring the number of pixels corresponding to the diameter of each spot in a magnified digital photograph leading to areas in the range 32.4–36.8 mm^2, which depended on the spot number. Filter spot sizes were determined using nigrosin rather than from the samples themselves as the spot edges were clearly defined. The spot edges of the deposited ambient aerosol were difficult to detect as the filter spot was changed at the start of each day when measurements were taken. It was possible to detect the aerosol spot for measurements that corresponded to high loadings of absorbing aerosol. In these cases there was evidence of aerosols spreading across the filter and the area of the spots was larger by 5–20 %. However, this observation is based on a limited sample of three aerosol spots and the time scale for spread across the filter is unclear. Therefore this analysis used the areas determined using the clearly defined nigrosin spots, and therefore provides a lower limit of area and thus absorption coefficient (see equation 4.2).

4.4.3 Photoacoustic and cavity ring-down spectrometers

The photoacoustic and cavity ring-down spectrometers used in this study are described in Chapter 2. Much of this analysis relies on accurate PAS absorption measurements. The total PAS measurement uncertainty is comprised of the measurement precision and accuracy, which was assessed in Chapter 2.6.

The PAS operated at wavelengths 405, 514 and 658 nm and the CRDS operated at wavelengths 405 and 658 nm. Absorption and extinction coefficients determined using PAS and CRDS were interpolated to the TAP wavelengths using AAE values derived from PAS measurements using equation 4.25. Scattering coefficients used in the TAP correction schemes (see section 4.3.2–4.3.4) were derived by subtracting PAS absorption coefficients from CRDS extinction coefficients.

4.4.4 Additional measurements

Nephelometer measurements (TSI 3563) were used to derive the aerosol asymmetry parameter needed to apply the Müller *et al*. (2014) TAP correction scheme (see section 4.3.4) and were corrected according to Müller *et al*. (2011). A Time-Of-Flight Aerosol Mass Spectrometer (TOF-AMS) (e.g. Drewnick *et al*., 2005) measured the aerosol composition. The TOF-AMS and TAP data were aligned by matching the rising and falling edges of the peaks in organic aerosol (OA) mass concentrations and absorption coefficients.

4.4.5 Residence times

All absorption, scattering and extinction coefficient data measured using the PAS, TAP, CRDS and nephelometer were recorded at 1 Hz. Data was subsequently averaged to 30 seconds during post-flight analysis to reduce the noise in these measurements and to aid temporal alignment of the PAS and TAP for direct comparisons. To account for time lags between the PAS and TAP, an optimisation routine was run that maximised the correlation coefficient (R^2) between the absorption coefficients determined using the PAS and TAP by delaying one instrument relative to the other. The delay time between the TAP relative to the PAS was 20 s, which was determined in laboratory conditions. There was no time lag between the PAS and CRDS when using an averaging time of 30 seconds. Time alignment was verified by visually confirming that the rising and falling edges of the peaks in the absorption coefficients were aligned.

4.5 Flights and meteorology

This study uses data collected aboard the FAAM aircraft during 30 research flights (each 3-4 hours duration) in three distinct regions: London (three flights, 17 to 20 July 2017, from 1.7° W to 2.0° E and from 50.6° to 52.9° N), West Africa (three flights, 28 February to 1 March 2017, from 14.2° to 17.6 °W and from 9.6° to 14.8° N) and the Southeast Atlantic Ocean (24 flights, 16 August to 7 September 2017, from 8.0° to 18.6° W and from 4.6° N to 10.9° S). Figure 4.2 shows a map with the flight tracks indicated. All flights involved straight and level runs as well as deep profiles. Figure 4.2 shows the mean aerosol optical depths (AODs) measured using the Moderate Resolution Imaging Spectroradiometer (MODIS) instruments aboard the Terra and Aqua satellite platforms (Remer *et al.*, 2013) for each measurement period. The mean AOD for each region is shown corresponding to all satellite overpasses during the flight periods for both MODIS instruments. Figure 4.2 also shows time series of the columnar AOD values measured using the AErosol RObotic NETwork (AERONET) for the Chilbolton and Oxford (~ 95 km southwest and northwest of London respectively), Dakar (West Africa) and Ascension Island (Southeast Atlantic Ocean) sites.

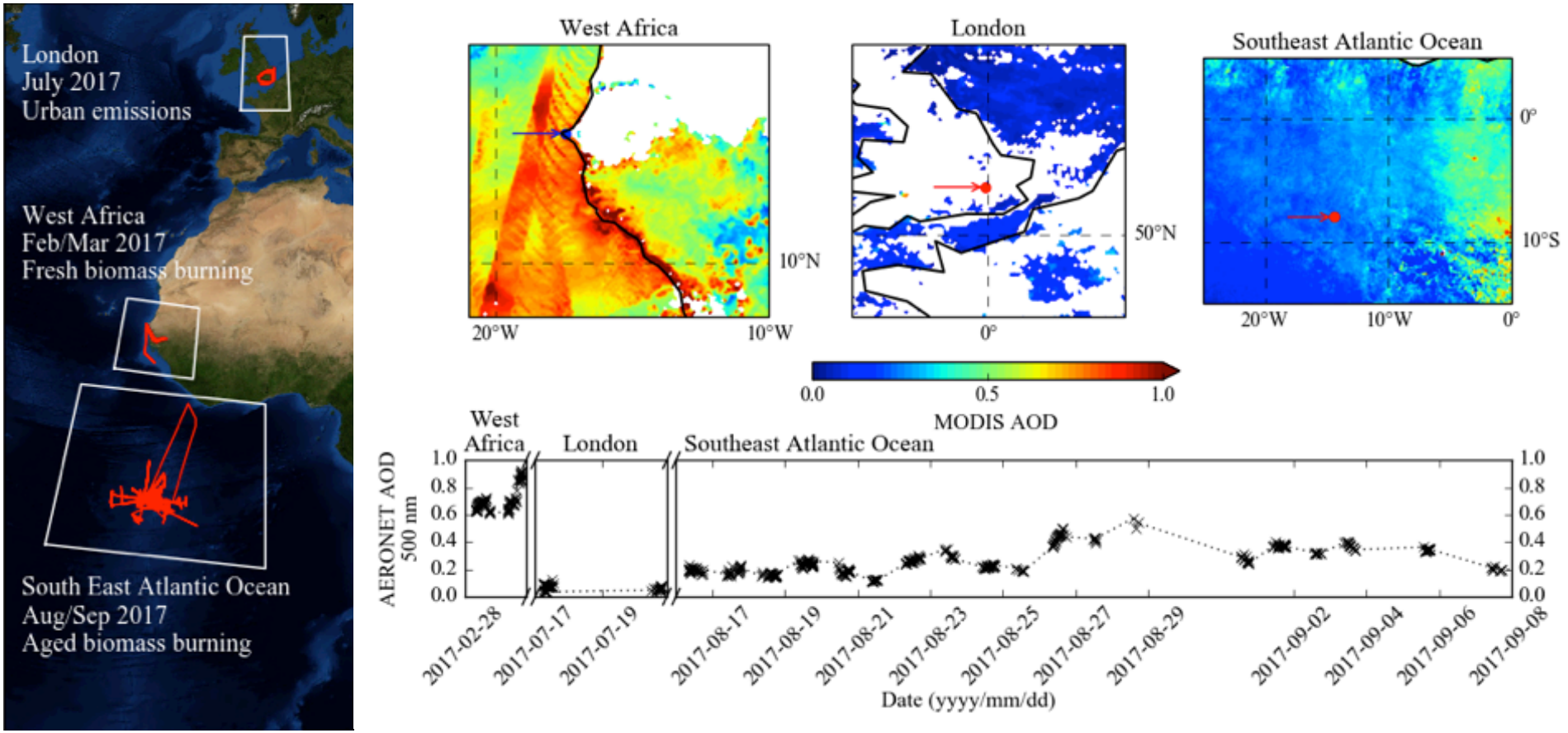

Figure 4.2: *FAAM research aircraft flight tracks (red) over London in the United Kingdom (July 2017), West Africa (February and March 2017) and the Southeast Atlantic (August and September 2017). For each of the geographical areas highlighted in the white boxes, the mean aerosol optical depths (AODs) measured using the Moderate Resolution Imaging Spectroradiometer (MODIS) satellite instruments are displayed. A time series of AErosol RObotic NETwork (AERONET) data shows AOD values at 500 nm corresponding to each measurement period. Note the discontinuous AERONET AOD time axis. AERONET sites are shown on the MODIS AOD plots by arrows.*

Urban emissions: during 17-20th July 2017, back trajectory analysis shows north-westerly flow brought air masses from over the Irish Sea to London (Rolph *et al.*, 2017; Stein *et al.*, 2015; available at http://ready.arl.noaa.gov/HYSPLIT_traj.php); see Figure 4.3. Similar back trajectories were observed for flights on the 20th July. Flights provided measurements of regional background aerosol (Northwest London) as well as the London pollution plume (Southeast London). AOD values of ~0.0–0.13 were measured using the AERONET sites at Chilbolton and Oxford during the measurement period, as shown in Figure 4.2. Mean in-flight carbon monoxide (CO) concentrations were 98 ppbv indicating the presence of fossil fuel burning, for example from transport emissions and industrial processes (e.g. Dentener *et al.*, 2001). These flights predominantly sampled the boundary layer with a maximum aircraft altitude of 2.2 km.

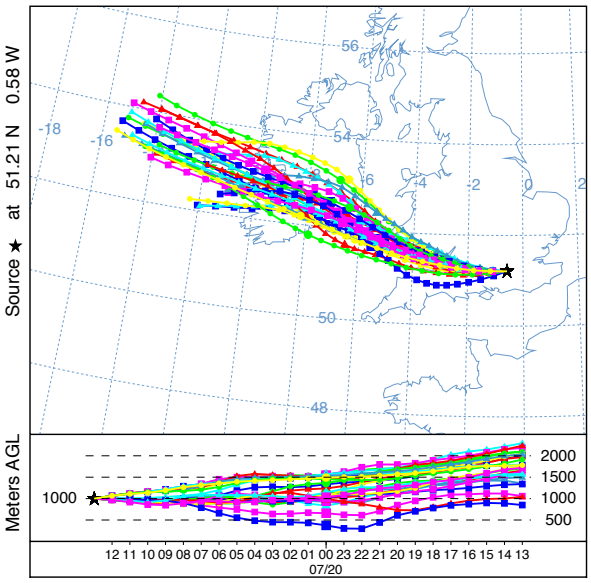

Figure 4.3: *HYSPLIT ensemble back-trajectory models at 1000 m above ground level (AGL) ending at 13:00 pm on 17th July 2017 at 51.21° N and 0.58° E.*

Fresh biomass burning emissions: flights over West Africa were dominated by freshly emitted BBA, encountering similar conditions to those sampled during previous FAAM flight campaigns at the same time of year (e.g. AMMA-SOP-0; DABEX; Haywood *et al.*, 2008). Low-level flying through visible smoke plumes enabled measurements of fresh BBA within a few minutes of emission. During the measurement period, MODIS measured mean AOD values ~ 0.5–0.7 over large swaths of West Africa, > 1.0 near to the coast and ~ 0.5–1.0 over the Atlantic Ocean offshore of West Africa and AERONET reported AOD values in the range ~ 0.5–0.9 over Dakar, as shown in Figure 4.2. Many flights targeted

measurements close to the source and so were dominated by BBA emissions. There was little influence of dust on the PAS, TAP and CRDS measurements because of the 1.3 μm impactor used, with the particle number size distribution of dust dominated by coarse mode (> 1 μm) particles. Mean in-flight CO concentrations were 175 ppb although concentrations greater than 14000 ppbv were measured when flying through plumes close to the aerosol source, indicative of fresh biomass burning emissions (Dentener *et al.*, 2001).

Aged biomass burning emissions: flights around Ascension Island sampled aged biomass burning aerosols transported from mainland Southern Africa in a general anticyclonic circulation (e.g. Garstang *et al.*, 1996; Zuidema *et al.*, 2016). East of ~ 8° W, MODIS reported mean AOD values generally between 0.1–0.5 and up to ~ 0.8 in the east of the area in which flights occurred. AERONET consistently measured AOD values between 0.1–0.5 over Ascension Island (the campaign base) during the entire four week measurement period. Mean CO concentrations were 126 ppbv, confirming that emission likely originated from a combustion source. Flights were performed in both the boundary layer and free troposphere. Based on HYSPLIT back trajectories, aerosols had generally undergone ~ 1 week of atmospheric transport since emission (Haywood *et al.*, in preparation).

4.6 Results and discussion

4.6.1 TAP-PAS comparisons

The primary result of this study is that the absorption coefficients determined using a TAP and PAS are linearly correlated and that the slope (R_{abs}) is dependent upon the aerosol source, measurement wavelength and the correction scheme applied to the TAP measurements. Scatter plots showing the relationship between absorption coefficients measured simultaneously by the TAP and PAS for urban, fresh and aged BBA are shown in Figures 4.4–4.6 respectively. A summary of R_{abs} can be found in Table 4.1. Tight correlations between TAP and PAS measurements were observed across all aerosol sources and for all correction schemes. The largest TAP biases were observed for measurements associated with urban aerosol emissions and the lowest biases were observed for aged BBA.

Aerosol source	Wavelength	B1999				V2010				M2014 V2010 parameterisation			
		Slope	R^2	P_{10}	P_{90}	Slope	R^2	P_{10}	P_{90}	Slope	R^2	P_{10}	P_{90}
Urban	467	1.36	0.88	0.99	1.71	1.38	0.87	0.99	1.76	1.16	0.89	0.92	1.41
	528	1.45	0.89	1.11	1.79	1.37	0.88	1.03	1.70	1.17	0.88	0.94	1.40
	652	1.40	0.68	1.14	1.76	1.27	0.69	1.01	1.58	1.00	0.62	0.81	1.27
Fresh BBA	467	1.25	0.97	1.11	1.46	1.30	0.97	1.13	1.54	1.09	0.95	0.84	1.24
	528	1.30	0.97	1.17	1.53	1.23	0.97	1.08	1.44	1.08	0.96	0.84	1.22
	652	1.24	0.96	1.19	1.70	1.09	0.97	0.92	1.32	0.99	0.95	0.76	1.17
Aged BBA	467	1.18	0.99	1.10	1.39	1.21	0.99	1.11	1.42	1.11	0.98	0.99	1.30
	528	1.21	0.99	1.12	1.42	1.16	0.99	1.05	1.35	1.07	0.98	0.95	1.26
	652	1.18	0.99	1.11	1.42	1.08	0.99	1.00	1.29	1.01	0.99	0.89	1.18

Table 4.1: *A summary of the slopes (R_{abs}) between PAS and TAP absorption coefficients. Correlation coefficients (R^2) are also provided. P_{10} and P_{90} are the 10^{th} and 90^{th} percentiles of each dataset. All absorption coefficients correspond to > 1 Mm^{-1}. All linear regressions were forced through the origin.*

For the B1999 correction scheme, the range of TAP biases across all aerosol sources was 1.18–1.45. The smallest biases were consistently associated with 467 nm or 652 nm wavelength measurements and largest for 528 nm wavelength measurements. An interesting feature of this result is that the B1999 scheme led to the largest biases at 528 nm, which is the wavelength closest to the wavelength at which the scheme was derived.

For the V2010 correction scheme, the range of TAP biases across all aerosol sources was 1.08–1.38. The largest biases were consistently at 405 nm and smallest at 652 nm. Relative to the B1999 correction scheme, the V2010 scheme reduced the biases at 528 and 652 nm by 5–15 % while it increased the bias at 467 nm by 2–5 %, dependent on the aerosol source. The sensitivity of TAP biases to the wavelength dependent constants used in the V2010 scheme was investigated due to the mismatch in the TAP wavelengths and those for which the V2010 correction scheme was derived. Applying the single-wavelength V2010 correction scheme (i.e. applicable at all wavelengths) decreased TAP biases by 7–9 % at 467 nm, increased biases by 1 % at 528 nm and increased biases by 6–8 % at 652 nm.

For the M2014 correction scheme, the range of TAP biases across all aerosol sources was 0.99–1.17. The M2014 scheme reduced TAP biases relative to the B1999 and V2010 schemes by 7–40 % and 7–27 %, respectively, dependent on the aerosol source and wavelength. The most significant reductions in TAP biases were for urban aerosol emissions and had the most impact on measurements at wavelength 652 nm. As discussed in section 4.3.4, the M2014 correction scheme applied here used the wavelength-dependent Virkkula (2010) parameterisation, in contrast to Müller *et al*. (2014), who applied the Virkkula *et al*. (2005) parameterisation. Although not shown, applying the Virkkula *et al*. (2005) parameterisation to TAP data in this study would act to decrease TAP biases by 3–4 % at 467 nm, increase biases by 1–2 % at 528 nm and by 3 % at 652 nm.

The R_{abs} from Figures 4.4–4.6 provide the mean TAP absorption coefficient biases for all measurements corresponding to each measurement wavelength and aerosol source, but it is also pertinent to examine the range of biases

corresponding to individual 30-s average measurements. Examining the 10th and 90th percentiles of each dataset (see Table 4.1) revealed that 10 % of TAP measurements were biased by greater than 1.71–1.79, 1.46–1.70 and 1.39–1.42 for urban, fresh BBA and aged BBA when corrected using the B1999 scheme, respectively, dependent on wavelength. The M2014 scheme reduced the biases, with 10 % of measurements biased greater than 1.27–1.41, 1.17–1.24 and 1.18–1.30 for urban, fresh BBA and aged BBA, respectively, dependent on wavelength.

The TAP biases exhibited a strong wavelength dependence. The lowest biases were associated with the 652 nm wavelength measurements and the largest biases with the 467 nm wavelength measurements when the V2010 and M2014 schemes were applied to TAP measurements for all aerosol sources. The one exception was when the M2014 scheme was applied to urban aerosol measurements, which led to the largest biases at wavelength 528 nm. TAP biases were also largest at wavelength 528 nm when corrected using the B1999 scheme for all aerosol sources.

To summarise, the M2014 scheme consistently led to the lowest biases across all measurement wavelengths and aerosol sources investigated. The largest biases were associated with TAP measurements corrected using the B1999 scheme at wavelengths 528 and 652 nm and when using the V2010 scheme at wavelength 467 nm for all aerosol sources.

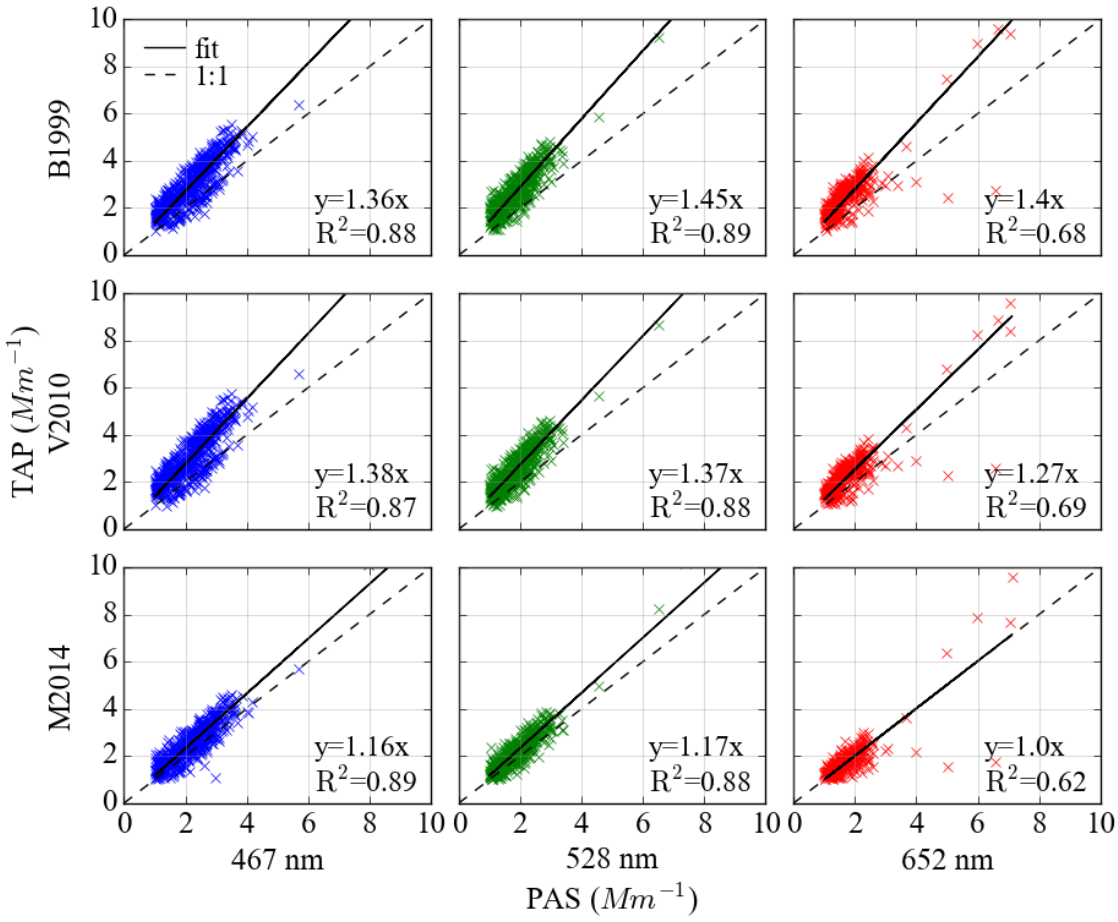

Figure 4.4: *Absorption coefficients measured by PAS versus TAP for urban emissions around London in July 2017. The columns correspond to: column 1: 467 nm, column 2: 528 nm, and column 3: 652 nm wavelengths and the rows correspond to the B1999, V2010 and M2014 corrections. All absorption coefficients correspond to > 1 Mm^{-1}. All linear regressions were forced through the origin.*

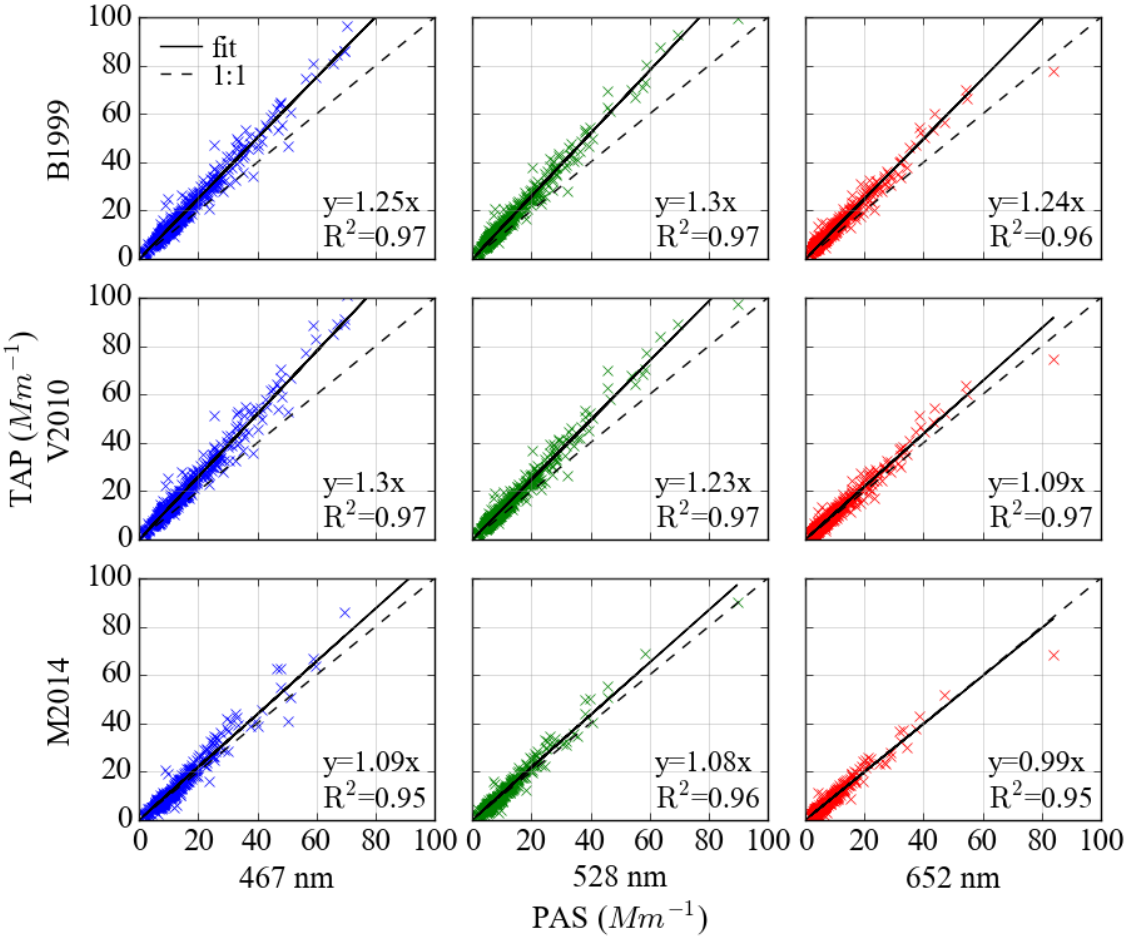

Figure 4.5: *As Figure 4.4 but for fresh biomass burning aerosols over Senegal in February and March 2017.*

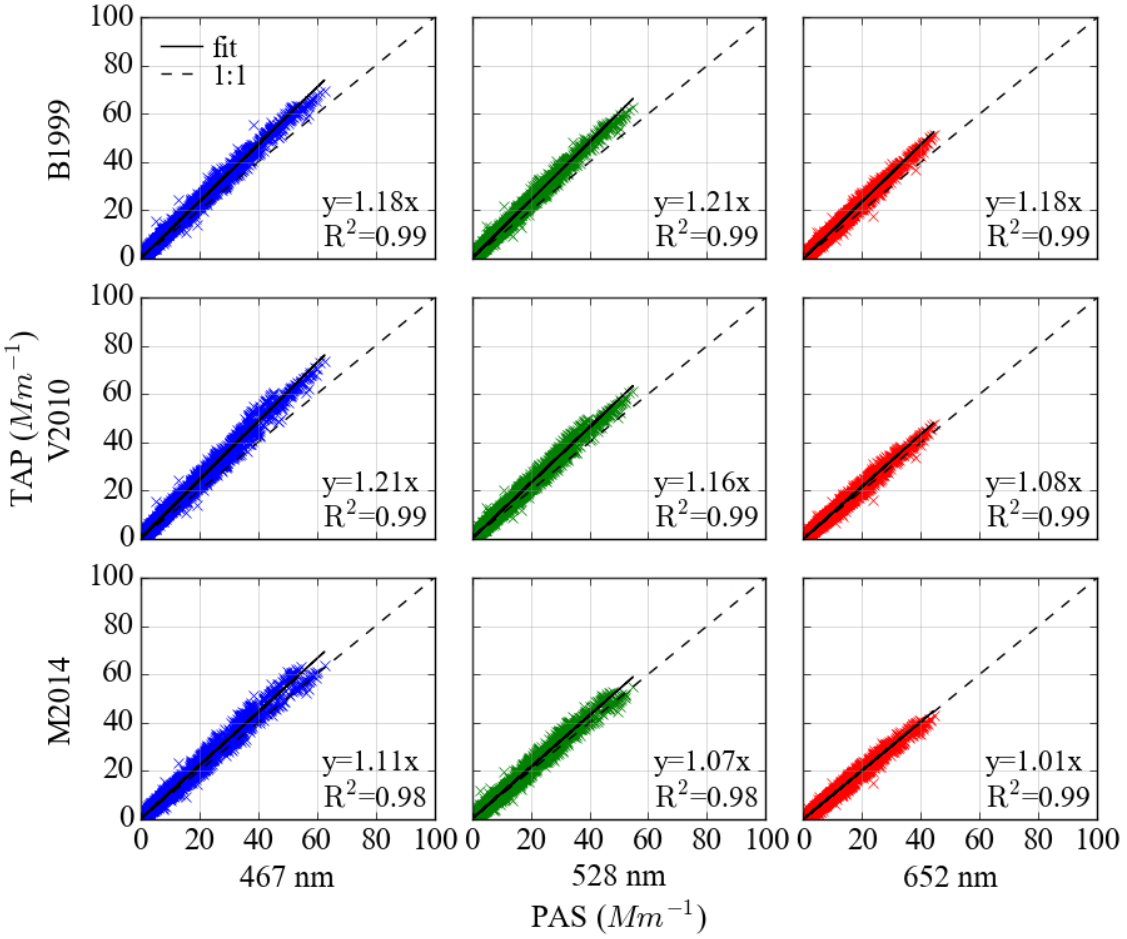

Figure 4.6: *As Figure 4.4 but for aged biomass burning aerosols over the Southeast Atlantic Ocean in August and September 2017.*

4.6.2 Evaluating TAP biases as a function of the organic aerosol mass concentration

The biases of −1 to 45 % observed in this study are at the lower end of those measured by Lack *et al*. (2008) and Cappa *et al*. (2008), who reported biases of 12 % to ~200 %, dependent upon the OA concentration. To investigate this apparent discrepancy, I evaluated the TAP biases as a function of the OA mass concentration measured using an Aerodyne Aerosol Time of Flight Mass Spectrometer (TOF-AMS, Aerodyne Research Inc.) (e.g. Drewnick *et al*., 2005).

Figure 4.7 (a–c) shows how TAP biases vary with OA mass concentration for TAP measurements corrected using the B1999 correction scheme, for direct comparison with the Lack *et al*. (2008) study. The linear relationship between the PSAP biases and OA observed by Lack *et al*. (2008) is superimposed for reference. For urban emissions (Figure 4.7a), TAP biases and OA mass are positively correlated and the trend is broadly consistent with that observed by

Lack *et al*. (2008). There is however no correlation for fresh (Figure 4.7b) or aged BBA (Figure 4.7c).

TAP biases were also plotted as a function of the ratio of the mass concentrations of OA to light-absorbing carbon (LAC), denoted by $R_{OA/LAC}$. This variable was calculated using the method outlined by Lack *et al*. (2008) by (i) assuming that all absorbing mass is black carbon, (ii) converting the mass absorption coefficient (MAC) of black carbon (BC) at 532 nm (7.75 $m^2\,g^{-1}$) to the PAS measurement wavelength 528 nm by using equation 4.25 and a BC AAE of 1 and (iii) dividing the PAS-measured absorption coefficient at wavelength 528 nm by the BC MAC at 528 nm. Hence the mass concentration of LAC was calculated as $LAC = {b_{ap,528\,nm}^{PAS}}/{MAC_{528\,nm}^{BC}}$ such that $R_{OA/LAC} = {OA}/{LAC}$ (Bond and Bergstrom, 2006; Lack *et al.*, 2008). Figure 4.7 (d) shows that the TAP bias is positively correlated with $R_{OA/LAC}$ for urban aerosol emissions when TAP measurements were corrected using the B1999 correction. This result is consistent with the Lack *et al*. (2008) observation although the current study shows lower biases. A likely contributor to this discrepancy is that all absorption was assumed to be due to BC to provide consistency with the Lack *et al*. (2008) study, but this assumption is poor for BBA emissions (e.g. Andreae and Gelencsér, 2006) as it provides a maximum bound on the MAC value, a minimum bound on absorption attributed to LAC and therefore a maximum bound on $R_{OA/LAC}$. A more realistic approach would be to use the MAC value corresponding to BC plus BrC. Using a lower MAC to account for absorption contributions from both BC and BrC would lead to lower $R_{OA/LAC}$ values than those shown in Figure 4.7 (d–f) and better agreement with the Lack *et al*. (2008) study. Correcting the TAP data using the M2014 correction scheme reduces the positive correlation between TAP biases and both R_{OA} and $R_{OA/LAC}$ as shown in Figure 4.7 (g–i). This result further demonstrates the improvement provided by using the M2014 scheme.

This analysis was repeated at wavelengths 467 nm and 652 nm (see Appendix B). Measurements at 652 nm, where BrC absorbs relatively weakly (e.g. Andreae and Gelencsér, 2006), revealed relatively stronger correlations between TAP biases and R_{OA} and $R_{OA/LAC}$ compared to 528 nm measurements

for TAP measurements corrected using the B1999 scheme, improving the agreement with Lack *et al.* (2008). Measurements at 467 nm, where BrC absorbs relatively strongly, revealed relatively weaker correlations between TAP biases and $R_{OA/LAC}$ compared to 528 nm measurements, reducing the agreement with Lack *et al.* (2008), due in part to attributing all absorption to BC. However, TAP biases showed no dependence on R_{OA} and $R_{OA/LAC}$ when TAP measurements were corrected using the M2014 scheme at 652 nm and a tenuous dependence at 467 nm. This finding is an interesting result that opposes the above argument. The reasons underpinning this result are unclear.

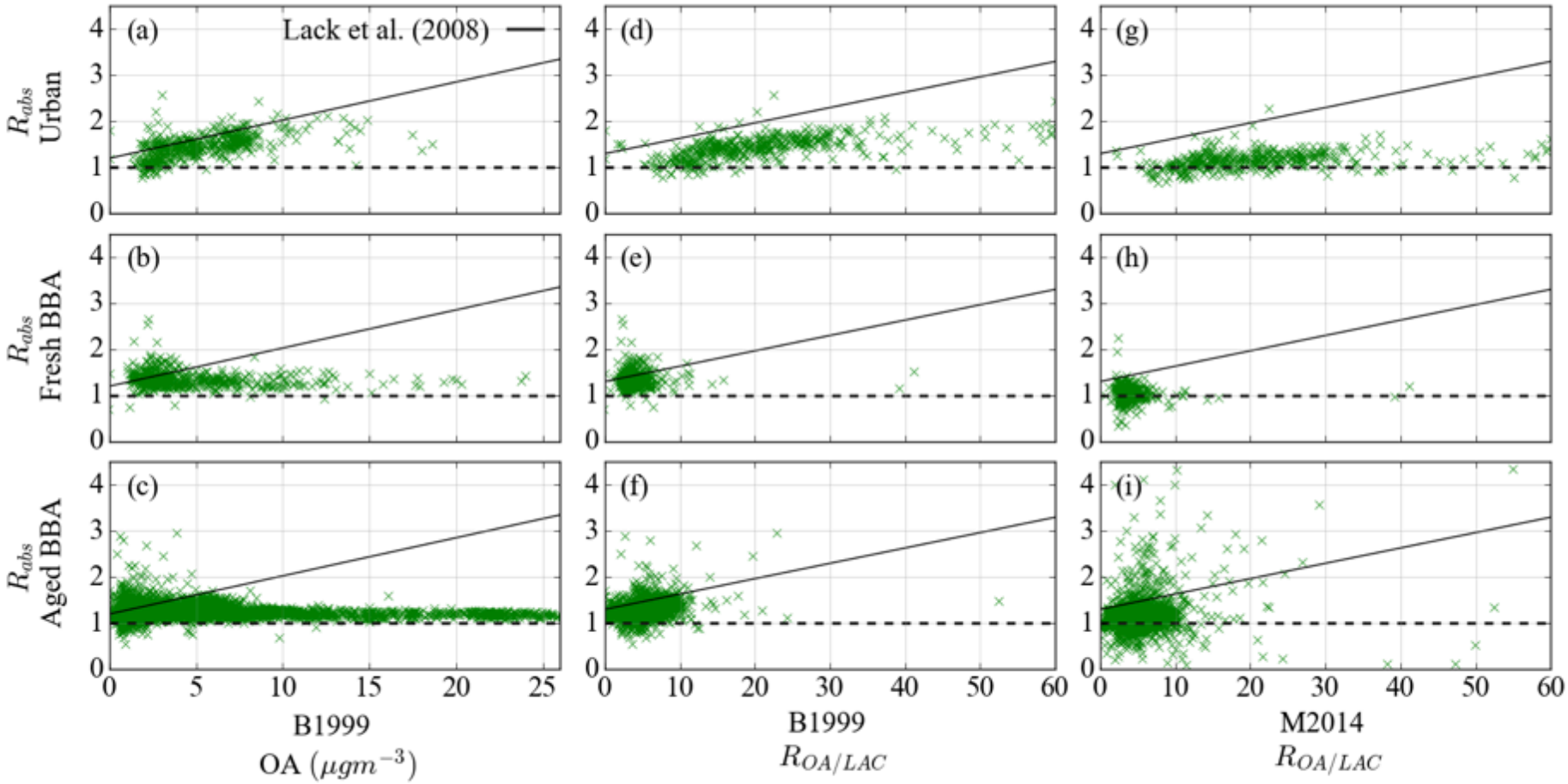

Figure 4.7: *The ratio of TAP to PAS absorption coefficients at 528 nm as a function of the organic aerosol (OA) mass concentration using the B1999 correction scheme (a-c) and as a function of the ratio of the organic aerosol to light-absorbing carbon (LAC) mass concentrations when using the B1999 correction scheme (d-f) and using the M2014 correction scheme (g-i). All absorption coefficients correspond to > 1 Mm^{-1}.*

A key result of this analysis is to show that biases observed in filter-based aerosol absorption measurements are strongly dependent on the type of aerosol being sampled. Correlating biases to aerosol composition information may provide tight constraint for a single source study such as the work by Lack *et al.* (2008) for aerosol emissions over the Gulf of Mexico, but care must be taken when generalising results to other aerosol types.

4.6.3 An assessment of the impact of TAP biases on climate relevant parameters

I now assess the impact that TAP biases may have on climate relevant parameters including the (i) aerosol single scattering albedo, (ii) absorption Ångström exponent and (iii) a simplified method for absorption attribution.

4.6.3.1 Single scattering albedo

Figure 4.8 shows histograms of the SSA derived using PAS or TAP together with CRDS for the aerosol sources described in section 4.5 and for the TAP corrections described in section 4.3.2–4.3.4.

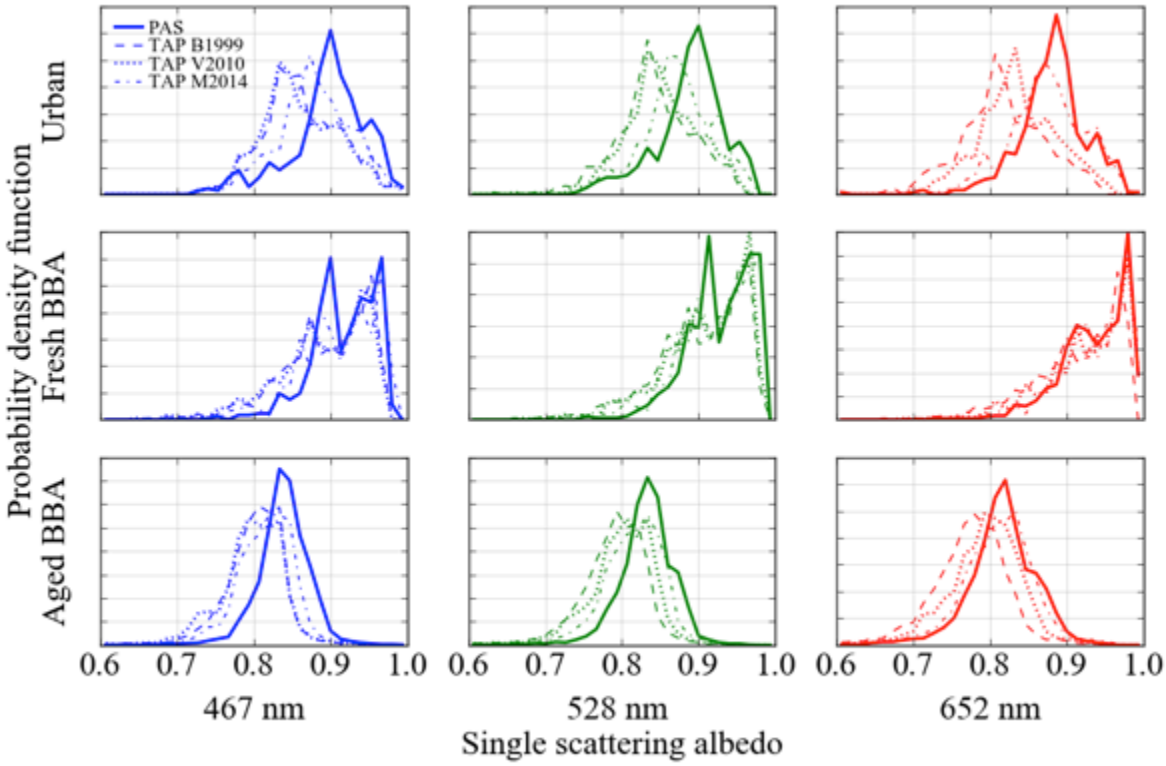

Figure 4.8: *Probability density functions of the single scattering albedo derived using (i) PAS and CRDS and (ii) TAP and CRDS for the range of TAP correction schemes outlined in section 4.3.2–4.3.4 at wavelengths 467, 528 and 652 nm. All absorption coefficients correspond to > 1 Mm^{-1}.*

The SSA is biased towards lower values when derived using TAP measurements, consistent with the results in Figures 4.4–4.6 which typically show a ~0–45 % high bias in TAP-derived absorption. Campaign-mean SSA values derived using PAS and CRDS measurements for each measurement campaign are summarised in Table 4.2.

Aerosol source	Wavelength	Mean SSA			
		PAS	B1999	V2010	M2014
Urban	467	0.89	0.86	0.86	0.88
	528	0.88	0.84	0.85	0.87
	652	0.88	0.81	0.83	0.87
Fresh BBA	467	0.92	0.89	0.89	0.91
	528	0.93	0.90	0.91	0.92
	652	0.93	0.91	0.93	0.93
Aged BBA	467	0.84	0.80	0.79	0.81
	528	0.83	0.79	0.80	0.81
	652	0.81	0.77	0.79	0.81

Table 4.2: *Campaign-mean single scattering albedo (SSA) derived using PAS and CRDS measurements and TAP and CRDS measurements.*

The mean SSA values derived using TAP and CRDS measurements matched those derived using PAS measurements most closely for fresh BBA aerosols, which were biased low by 0.00–0.03, dependent on measurement wavelength and the TAP correction scheme applied. The SSA values were most different for urban aerosols, which were biased low by 0.01–0.07, dependent on wavelength and the TAP correction scheme applied. This result is consistent with the results in Table 4.1, which highlights that TAP biases were largest for urban aerosol measurements. The wavelength dependence of the TAP-derived SSA values depended on the correction scheme applied. SSA values derived using the M2014 correction scheme agreed most closely with those derived using PAS measurements for all measurement wavelengths and correction schemes.

4.6.3.2 Absorption Ångström exponent

Figure 4.9 shows histograms of the AAE values derived by performing linear regressions between the logarithms of the PAS-measured absorption

coefficients and the PAS measurement wavelengths (405–658 nm) using equation 4.25. It also shows the same information for the TAP-derived AAE values. The AAE values were calculated for the aerosol sources outlined in section 4.5 and TAP correction schemes outlined in section 4.3.2–4.3.4. The B1999 scheme was not able to reproduce the range of AAE values determined using PAS measurements, which is likely related to its derivation at a single wavelength.

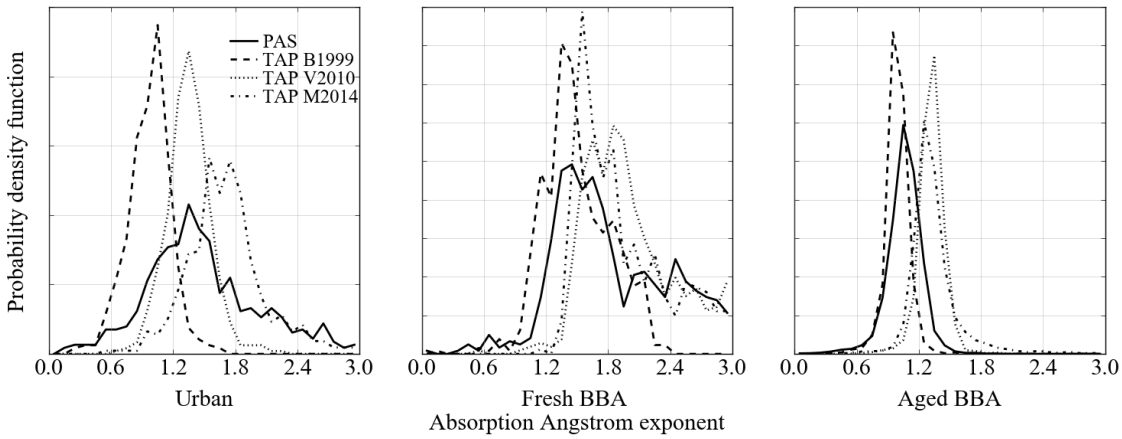

Figure 4.9: *Probability density functions of the absorption Ångström exponents derived for PAS and TAP measurements using the range of TAP correction schemes as outlined in section 4.3.2–4.3.4. All absorption coefficients correspond to > 1 Mm^{-1}.*

The AAE values were strongly dependent on the TAP correction scheme applied. Campaign-mean AAE values are summarised in Table 4.3, which highlights that the highest mean AAE values were associated with fresh BBA emissions and the lowest for aged BBA emissions.

Aerosol source	**Mean AAE**			
	PAS	**B1999**	**V2010**	**M2014**
Urban	1.51	0.97	1.35	1.75
Fresh BBA	1.91	1.50	2.27	2.05
Aged BBA	1.06	0.99	1.32	1.36

Table 4.3: *Campaign-mean absorption Ångström exponent (AAE) derived using PAS and CRDS measurements and TAP and CRDS measurements.*

The V2010 scheme led to mean AAE values that were in closest agreement with the AAE values derived using PAS measurements for urban aerosols, whereas the M2014 scheme provided the closest match for fresh BBA and the B1999 scheme for aged BBA. It is unclear why the different TAP correction

schemes perform so differently for the different aerosol sources sampled. However, what is clear from this analysis is that there are large uncertainties in this important climate parameter when calculated from filter-based absorption measurements, and that these uncertainties are strongly source and correction scheme dependent.

4.6.3.3 Absorption attribution

The accuracy of the simplified method for BrC absorption attribution outlined in section 4.2 will now be examined in light of the uncertainties in TAP-derived AAE values described in section 4.6.3.2. In this method, I will perform idealised calculations to (i) evaluate how the absorption of BC $\left(b_{ap,BC}\right)$ varies with wavelength, (ii) evaluate how the absorptions of the source aerosol species in question $\left(b_{ap,tot}^{urban}, b_{ap,tot}^{fresh\ BBA}, b_{ap,tot}^{aged\ BBA}\right)$ vary with wavelength and (iii) attribute the difference in absorption to absorption by BrC such that $b_{ap,BrC}^{urban} = b_{ap,tot}^{urban} - b_{ap,BC}$, $b_{ap,BrC}^{fresh\ BBA} = b_{ap,tot}^{fresh\ BBA} - b_{ap,BC}$ and $b_{ap,BrC}^{aged\ BBA} = b_{ap,tot}^{aged\ BBA} - b_{ap,BC}$. The dependence of $b_{ap,tot}^{urban}$, $b_{ap,tot}^{fresh\ BBA}$ and $b_{ap,tot}^{aged\ BBA}$ to wavelength will be evaluated using the mean PAS-derived and TAP-derived AAE values from Figure 4.9 (Table 4.3). The fraction of light-absorption due to BrC can thus be calculated as (Kirchstetter and Thatcher, 2012; Backman *et al.*, 2014)

$$f_{BrC}(\lambda) = \frac{b_{ap,BrC}(\lambda)}{b_{ap,tot}(\lambda)}. \qquad (4.26)$$

Assuming that the PAS-derived BrC absorption contribution is accurate will allow evaluation of the uncertainty in the TAP-derived BrC absorption contribution.

The dependence of $b_{ap,BC}$ to wavelength was simulated by using equation 4.25 to extrapolate an arbitrary absorption of 1 at wavelength 660 nm to shorter wavelengths. This simulation assumed that all absorption at long visible wavelengths was due to BC and that BC has an AAE of 1 (e.g. Bergstrom *et al.*, 2002). The black lines in Figure 4.10 (a–c) show the modelled BC absorption. The dependences of $b_{ap,tot}^{urban}$, $b_{ap,tot}^{fresh\ BBA}$ and $b_{ap,tot}^{aged\ BBA}$ to wavelength were evaluated in a similar way, achieved by extrapolating an arbitrary absorption of 1 at wavelength 660 nm to shorter wavelengths using the mean PAS-derived AAE values for each aerosol type based on the data presented in Figure 4.9.

These extrapolations are shown by the blue lines in Figure 4.10 (a–c). Extrapolations were repeated for the TAP-derived AAE values for each TAP correction scheme, shown by the green, red and purple lines in Figure 4.10 (a–c). The fraction of light-absorption attributed to BrC is represented by f_{BrC}, which was determined using equation 4.26 by taking the ratio of $b_{ap,BrC}^{urban}$ to $b_{ap,tot}^{urban}$, with similar relations for fresh and aged BBA. f_{BrC} is a wavelength dependent variable, which reflects the wavelength dependence of BrC absorption (e.g. Kirchstetter *et al.*, 2004). f_{BrC} is shown in Figure 4.10 (d–f).

These calculations show that the fraction of absorption attributed to BrC derived using PAS measurements at 405 nm is 16 %, 26 % and 2 % for urban, fresh BBA and aged BBA emissions, respectively. f_{BrC} is underestimated when derived using TAP measurements corrected using the B1999 scheme and in the cases of urban aerosol and aged BBA emissions, f_{BrC} is unphysical (negative). f_{BrC} is consistently overestimated when derived using TAP measurements corrected using the M2014, irrespective of aerosol type. To summarise, f_{BrC} can be in error by as much as 17 % depending on the aerosol type and correction scheme applied to the TAP. This error is relatively small compared to the uncertainties that are inherent with this method of absorption attribution (Lack and Langridge, 2013).

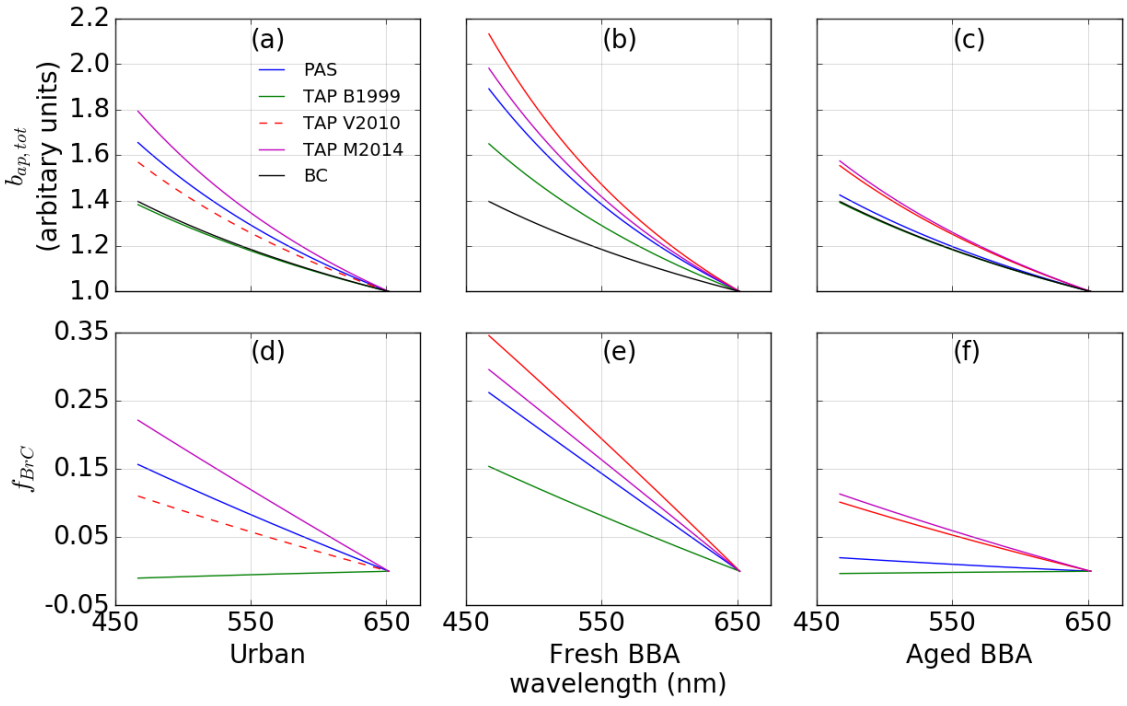

Figure 4.10: *(a–c) Extrapolated absorption assuming a BC AAE of 1 and PAS and TAP AAE values taken as the mean values in Figure 4.9 for urban, fresh*

BBA and aged BBA. (d–f) The fraction of absorption by BrC was computed as the difference between the BC and PAS absorption and the BC and TAP absorption. The TAP B1999 and BC have similar values in (a).

4.7 Conclusions

Measurement artefacts in a commercially available filter-based absorption photometer (TAP) were evaluated as a function of wavelength and aerosol source. A range of correction schemes have been proposed in the literature to account for these artefacts and thus to maximise the accuracy of aerosol absorption coefficients determined using this technique, although biases can remain. Three correction schemes were applied, which all reduced the TAP mean bias to within −1 to +45 % of the PAS absorption, dependent upon aerosol source and wavelength. The largest biases were associated with urban aerosols and the lowest for aged BBA. The M2014 correction scheme consistently led to the lowest biases across all wavelengths and aerosol sources. To my knowledge, this study is the first to demonstrate the improved performance of the M2014 correction scheme as a function of wavelength and across multiple aerosol sources for ambient aerosol sampling.

Biases in filter-based absorption measurements were strongly source dependent. On no occasion were the very large biases of > 200 % noted in the Lack *et al*. (2008) study observed. However, it should be noted that the Lack *et al*. (2008) results are consistent with the source dependence observed in the current study.

The high bias in absorption determined using a filter-based measurement system resulted in a low bias in the single scattering albedo of up to 0.07. The largest biases in SSA were for urban aerosols at wavelength 652 nm. The M2014 scheme consistently led to SSA values that were most closely matched to those derived using PAS measurements across all wavelengths and aerosol sources.

A broader range of AAE values were derived using PAS compared to TAP, which depended strongly on the correction scheme applied to the TAP measurements. The largest discrepancies in the AAE values were for TAP measurements of urban aerosols corrected using the B1999 scheme, which

were biased low by a mean of 0.54. Best agreement with AAE values derived using PAS measurements was obtained when TAP measurements of (i) urban aerosols were corrected using the V2010 scheme, (ii) fresh BBA were corrected using the M2014 scheme and (iii) aged BBA were corrected using the B1999 scheme. This result highlights that the AAE is strongly source and correction scheme dependent.

The strong aerosol source dependence of biases observed in this study cautions against extrapolating results more widely to other aerosol types. Further analyses exploring biases in filter-based absorption coefficient measurements may help to address this issue. However, given the empirical nature of the correction schemes and strong source and wavelength dependencies, even this is unlikely to fully bound uncertainties associated with filter-based absorption measurements to the high level of confidence that can be achieved using alternative methods.

Throughout this analysis, no correction was applied to PAS measurements accounting for potential biases in ozone calibrations, as discussed in section 3.8. Based on the Fischer and Smith (2018) study, EXSCALABAR PAS ozone calibrations may have led to an underestimation of the absorption coefficients by up to 10 %, which would broadly act to increase the agreement between PAS and TAP measurements.

5 Investigating the sensitivity of the direct radiative effect to aerosol and cloud optical properties using offline radiative transfer, satellite observations and a global climate model

Table of contents

5.1 Rationale, aims and objectives

Biomass burning aerosol (BBA) plumes are advected over the Southeast Atlantic Ocean during the African dry season (July–September), and typically overlie semi-permanent marine stratiform clouds that are ubiquitous in the region (e.g. de Graaf *et al.*, 2012, 2014). This environment provides a unique opportunity to study the aerosol direct radiative effect (DRE), which is poorly understood and is not represented well in global aerosol models in this region (Myhre *et al.*, 2013b; de Graaf *et al.*, 2014; Zuidema *et al.*, 2016).

Zuidema *et al.* (2016) highlighted the poor representation of BBA in global aerosol models over the Southeast Atlantic Ocean by examining the direct radiative forcing (DRF) using the AeroCom suite of global aerosol models, shown in Figure 5.1. The models in Figure 5.1 consist of both chemistry-transport models (GMI MERRA, GOCART, TM5, GEOS CHEM, OsloCTM2, IMPACT) and chemistry-climate models (GISS modelE, GISS MATRIX, HadGEM2-ES, BCC AGCM, INCA, SPRINTARS, NCAR CAM3, CAM4-Oslo, MPIHAM, CAM5.1 MAM3) (Schulz *et al.*, 2006; Myhre *et al.*, 2013b). Chemistry-transport models use prescribed reanalysis meteorological data whereas chemistry-climate models simulate their own internal meteorology, which may lead to different simulated cloud fields (e.g. Textor *et al.*, 2006). Differences in the AeroCom models' cloud fields due to meteorology was minimised by nudging the meteorology to reanalysis data; see Myhre *et al.* (2013b) for more details. This ensemble of global aerosol model simulations showed that even the sign of the DRF was uncertain. This result can be understood using Figure 1.8, which shows that the DRF changes sign at the critical single scattering albedo, dependent on the aerosol single scatteing albedo (SSA) and the underlying surface reflectance. A positive DRF (warming) would result if the BBA resided above highly reflective cloud whereas a negative DRF (cooling) would result in the absence of cloud; see Figures 1.8 and 1.9 (e.g. Keil and Haywood, 2003). Key factors driving the model diversity shown in Figure 5.1 included uncertainties in the vertical distribution of aerosol (e.g. Zarzycki and Bond, 2010; Samset *et al.*, 2013; Peers *et al.*, 2015), the aerosol single scattering albedo (e.g. Myhre *et al.*, 2008, 2013b) and how this evolved during the biomass burning season due to changing aerosol composition (Eck *et al.*, 2013), aerosol spatial distribution and an inaccurate representation of the

underlying cloud deck (Zuidema *et al.*, 2016). Another explanation for the diversity in modelled DRF shown in Figure 5.1 could be related to the inability of global aerosol models to resolve variability on spatial scales that are smaller than their grid cell size (Qian *et al.*, 2010). Model resolution can impact the DRF, or equivalently DRE, significantly due to sub-grid processes that vary with resolution in a non-linear way, for example chemical reactions that depend on aerosol concentration, aerosol hygroscopic growth and spatial variability of aerosol emissions (e.g. Haywood *et al.*, 1997; Bian *et al.*, 2009; Gustafson Jr. *et al.*, 2011).

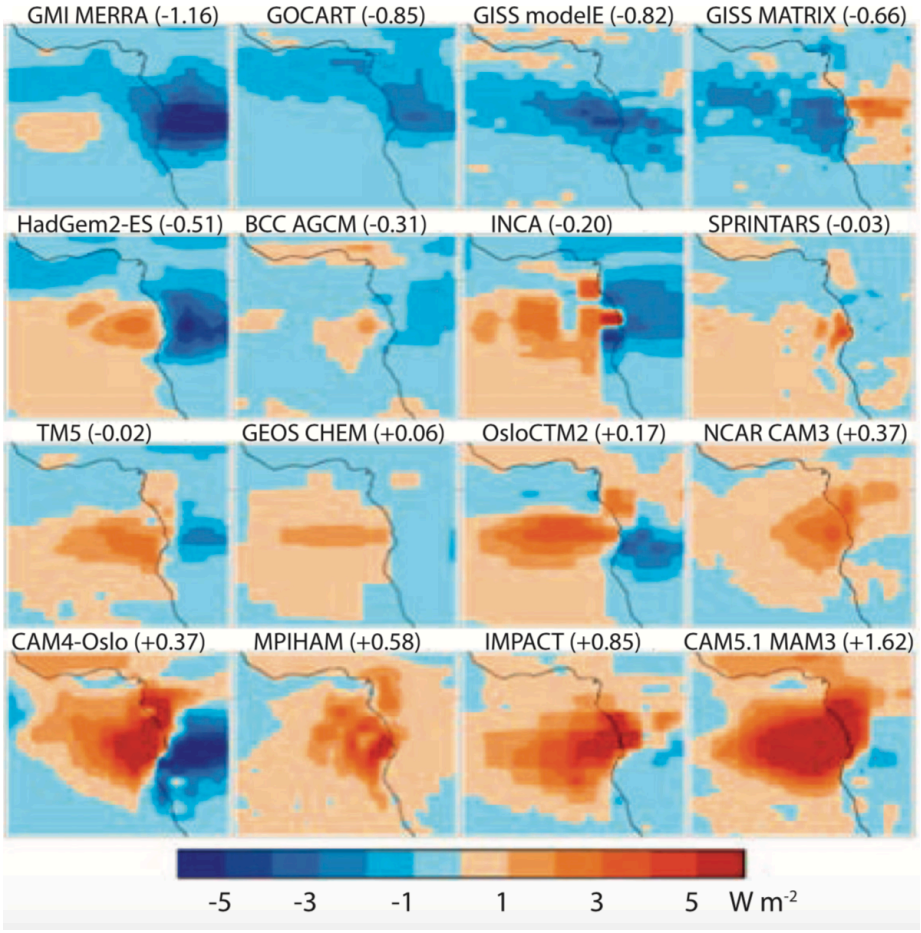

Figure 5.1: *Mean direct radiative forcing over the Southeast Atlantic Ocean during August–September using the AeroCom global aerosol models. Figure from Zuidema et al. (2016).*

Global aerosol model uncertainty in predicting the DRE over the Southeast Atlantic Ocean was further demonstrated by comparing HadGEM2 climate model simulations to SCHIAMACHY satellite observations of the aerosol DRE over clouds, hereafter called the above cloud direct radiative effect (ACDRE), corresponding to BBA in August and September 2006–2009 (de Graaf *et al.*, 2014). The mean ACDRE was a factor of five lower in climate model

simulations (6 W m^{-2}) than satellite observations (30 to 35 W m^{-2}). The instantaneous ACDRE satellite observations (up to ~150 W m^{-2}) were not reproduced in the climate model simulations (up to ~42 W m^{-2}). Peers *et al.* (2015) independently examined the range of ACDRE values for BBA overlying cloud across the Southeast Atlantic Ocean during August 2006 using the Polarization and Directionality of Earth Reflectances (POLDER) satellite instrument, shown in Figure 5.2. ACDRE values were in line with SCIAMACHY observations, with 0.2 % of retrievals greater than 220 W m^{-2}.

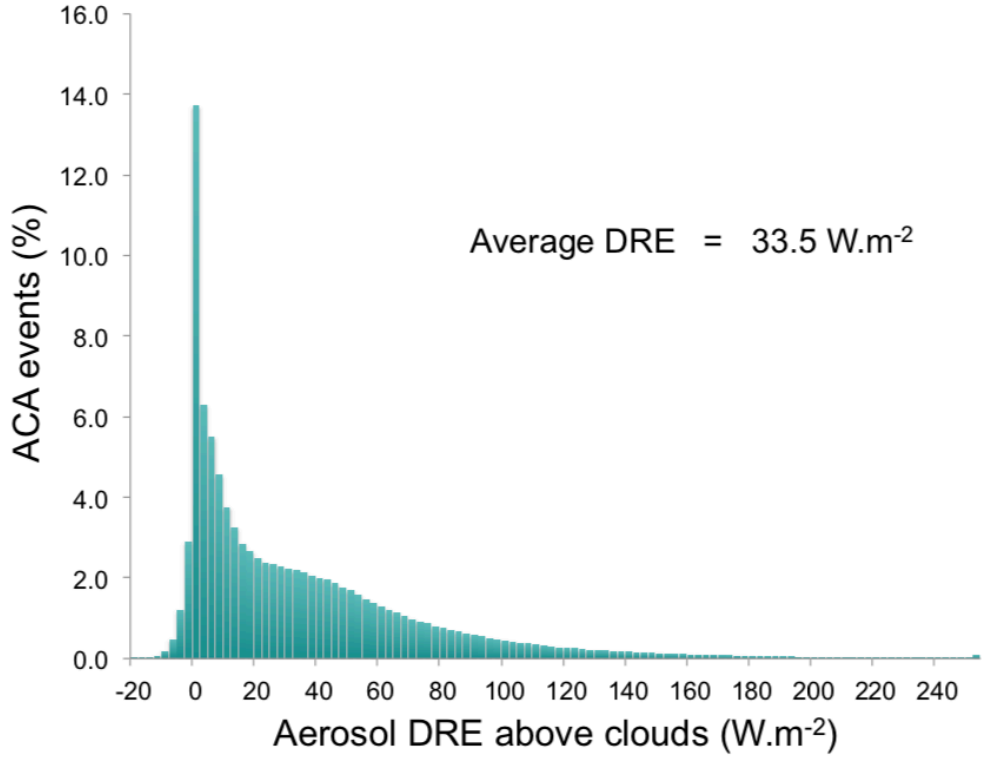

Figure 5.2: *Frequency distribution of the above cloud aerosol direct radiative effect (DRE) over the Southeast Atlantic Ocean during August 2006 for cloud optical depth ≥ 3 and cloud fractions of 1. Figure from* Peers *et al.* (2015).

The poor agreement between the HadGEM2 simulations and satellite observations was attributed in part to a lack of representation of the episodic nature of aerosol emissions and lack of absorption by brown carbon in the HadGEM2 simulations (de Graaf *et al.*, 2014). However, these factors did not fully resolve the large discrepancy in ACDRE, which was attributed to an inaccurate representation of cloud brightness. Another explanation for this finding could have been related to sub-grid scale variability within the climate model grid boxes. If the AOD and COD were independent, there could have been areas of high AOD overlying areas of high COD, which would have led to

large positive ACDRE values. However, if the AOD and COD fields were heavily spatially averaged, many of these high ACDRE values would have been lost.

In this chapter, I will investigate the sensitivity of the aerosol DRE to aerosol and cloud optical properties, as outlined in the objectives below. To achieve this aim, I will implement an offline atmospheric radiative transfer model, 'Suite Of Community RAdiative Transfer codes based on Edwards and Slingo' (SOCRATES), used within the Met Office's Hadley Centre Global Environment Model version 3 (HadGEM3), using aerosol and cloud properties measured over the Southeast Atlantic Ocean during the Southern African Fire-Atmosphere Research Initiative (SAFARI) 2000 measurement campaign. The HadGEM3 climate model simulations in this chapter use the Global Model of Aerosol Processes (GLOMAP) aerosol scheme whereas the HadGEM2 climate model simulations in the studies highlighted previously used the Coupled Large-scale Aerosol Simulator for Studies In Climate (CLASSIC) bulk aerosol scheme. The GLOMAP aerosol scheme allows both the aerosol mass and number concentration to vary as well as allowing the physical and chemical properties of aerosols to evolve interactively including accounting for internal mixing of aerosol species. In contrast, the CLASSIC aerosol scheme represents each aerosol species as externally mixed with specified physical and optical properties (Mann *et al.*, 2010; Johnson *et al.*, 2016).

Next, I examine the sensitivity of the ACDRE to the spatial variability of aerosol and cloud optical depths. I initially perform SOCRATES simulations to determine the mean and range of ACDRE values corresponding to the aerosol and cloud optical depths observed by the POLDER satellite instrument over the Southeast Atlantic Ocean during August and September 2006. The impact on modelled ACDRE values due to averaging AOD and COD values over a range of spatial scales is evaluated. I then assess how the ACDRE depends on the degree of spatial averaging of the aerosol and cloud optical properties by comparing the POLDER observations to HadGEM3 climate model simulations at three spatial resolutions.

The objectives of this chapter are to:

1) Describe the SOCRATES radiative transfer model used to determine radiative fluxes throughout the atmosphere.
2) Use the SOCRATES radiative transfer model to investigate the sensitivity of the direct radiative effect to aerosol and cloud properties as a function of the solar zenith angle.
3) Investigate the sensitivity of the direct radiative effect to the aerosol single scattering albedo and assess the uncertainty introduced to the direct radiative effect due to biases in single scattering albedo determined using filter-based absorption measurements of aged biomass burning aerosols.
4) Investigate the sensitivity of the direct radiative effect to the absorption Ångström exponent and assess the uncertainty introduced to the direct radiative effect due to biases in the absorption Ångström exponent determined using filter-based absorption measurements of aged biomass burning aerosols.
5) Investigate the sensitivity of the above cloud direct radiative effect to variability in aerosol and cloud optical depths using SOCRATES simulations, constrained using POLDER satellite observations of biomass burning aerosols over the Southeast Atlantic Ocean.
6) Compare the above cloud direct radiative effect determined using POLDER satellite observations to a global climate model (HadGEM3) over the Southeast Atlantic Ocean.
7) Investigate the sensitivity of the above cloud direct radiative effect to sub-grid variability by evaluating HadGEM3 at three spatial resolutions over the Southeast Atlantic Ocean.

5.2 Assessing the sensitivity of the direct radiative effect to aerosol and cloud properties using SOCRATES

5.2.1 An introduction to SOCRATES

5.2.1.1 Overview

To investigate the impact that aerosols have on the Earth's energy budget, one can evaluate the radiative transfer equation, which describes how electromagnetic radiation propagates through the atmosphere and depends on absorption and scattering processes (Zdunkowski *et al.*, 2007). More specifically, the radiative transfer equation describes how radiances (units *W*

$m^{-2}\,sr^{-1}$) change throughout the atmosphere, defined as the energy transferred by electromagnetic radiation in a specific direction through a unit area perpendicular to the direction of travel (Wallace and Hobbs, 2006). All SOCRATES simulations in this chapter used a simplified version of the radiative transfer equation such that radiative fluxes, otherwise known as irradiances (units $W\ m^{-2}$), as opposed to radiances could be evaluated (Seinfeld and Pandis, 2006). Fluxes were determined by utilising the two-stream approximation whereby radiances were integrated over the upward-facing and downward-facing hemispheres (Zdunkowski *et al.*, 2007). The radiative transfer equation was simplified further by utilising the plane-parallel atmosphere approximation whereby atmospheric optical properties are assumed to be independent of the horizontal position, i.e. that radiation is only allowed to enter or leave at the model level base or top and that there is no horizontal 'leakage' of radiation out of the atmospheric column (Manners *et al.*, 2015). This simplification has been found to be a good approximation of a real atmosphere when vertical variations in radiation dominate over horizontal variations (Zdunkowski *et al.*, 2007). Fluxes were evaluated at the top of the Earth's atmosphere to enable quantification of the net change in energy balance due to an external perturbation in aerosol (Stocker *et al.*, 2013).

5.2.1.2 The calculation of fluxes throughout the atmosphere

The atmosphere is divided into N homogeneous layers as shown in Figure 5.3 (Manners *et al.*, 2015). The boundaries of these layers, known as levels, are labelled from 0 to N. Optical properties of atmospheric constituents are prescribed in each atmospheric layer whilst monochromatic fluxes are calculated at each level.

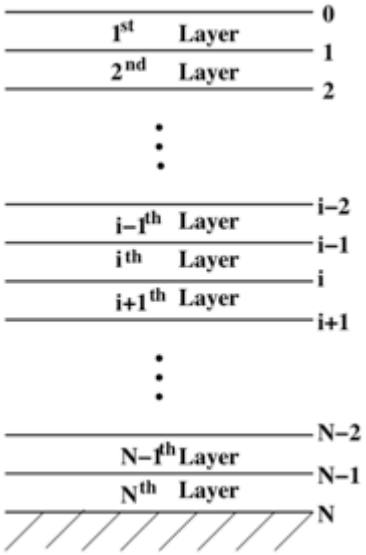

Figure 5.3: *Vertical atmospheric layers in SOCRATES. Figure from Manners et al. (2015).*

Solar radiation is comprised of direct and diffuse components where the former refers to unscattered direct solar radiation and the latter refers to direct radiation that has been scattered (Zdunkowski *et al.*, 2007). SOCRATES calculates fluxes in discrete spectral bands within which all quantities are treated as independent of frequency such that the total flux in an atmospheric layer is given by

$$F = \sum_j F_j^{(b)}, \tag{5.1}$$

where $F_j^{(b)}$ is the partial flux corresponding to flux in wavelength band j (Manners *et al.*, 2015). Fluxes corresponding to absorbing gaseous species are calculated within subdivided wavelength bands to account for relatively high resolution absorption features compared to, for example, aerosol absorption spectra. The atmospheric fluxes at layer i are denoted as: U_i is the upward flux, V_i is the total downward flux (direct plus diffuse) and Z_i is the direct solar flux. The upwelling and downwelling direct and diffuse fluxes are thus calculated using

$$U_{i-1} = T_i U_i + R_i V_{i-1} + S_i^+ \tag{5.2}$$

$$V_i = T_i V_{i-1} + R_i U_i + S_i^- \tag{5.3}$$

$$Z_i = T_0 Z_{i-1} \tag{5.4}$$

where R and T are the diffuse transmission and reflection coefficients, T_0 is the direct transmission coefficient and $S^{\pm}$ are the terms representing the direct solar flux at a layer i such that

$$S_i^+ = c_{1i} Z_{i-1}, \tag{5.5}$$

$$S_i^- = c_{2i} Z_{i-1}, \tag{5.6}$$

where c_{1i} and c_{2i} are functions of the optical properties of the atmospheric layer. There is no downwelling diffuse radiation at the top of the atmosphere, hence the following boundary condition can be imposed

$$V_0 = Z_0 = \frac{S_0}{cos(\theta)}, \tag{5.7}$$

where θ is the solar zenith angle. At the surface level (N), the boundary condition is

$$U_N = \left(\mathcal{R}_p^s - \mathcal{R}_p^d\right) Z_N + \mathcal{R}_p^d V_N, \tag{5.8}$$

where $\mathcal{R}_p^s$ and $\mathcal{R}_p^d$ are the direct and diffuse planetary surface albedos, respectively (Manners *et al.*, 2015).

5.2.1.3 δ-rescaling of aerosol and cloud optical properties

Although the two-stream approximation significantly reduces model complexity and computational expense, it introduces uncertainties into upwelling and downwelling fluxes when the optical properties of particulate constituents are input into an atmospheric model (Joseph *et al.*, 1976). These particulates can have highly asymmetric phase functions that typically have strong forward scattering components, which are poorly captured by the two-stream radiative transfer equation. Using the δ-rescaling transformation accounts for this strong forward scattering, which has been found to reproduce fluxes to within 0.5 % of those modelled by integrating over the scattering phase function (Joseph *et al.*, 1976). The δ-rescaling parameters are

$$\tau \rightarrow \tau(1 - \omega f) \tag{5.9}$$

$$\omega \rightarrow \frac{\omega(1-f)}{(1-\omega f)} \tag{5.10}$$

$$g \rightarrow \frac{(g-f)}{(1-f)}, \tag{5.11}$$

where $f = g^2$ and g is the asymmetry parameter (Manners *et al.*, 2015).

5.2.1.4 Atmospheric optical properties

The optical properties in each atmospheric layer must be defined so that fluxes at each atmospheric level can be calculated (see Figure 5.3). Optical properties are set by attributing a specific extinction coefficient, specific scattering coefficient, asymmetry parameter and f parameter to each layer such that

$$k_e = \sum_j k_e^j q_j \tag{5.12}$$

$$k_s = \sum_j k_s^j \, q_j \tag{5.13}$$

$$g = \frac{\sum_j k_s^j g_j}{\sum_j k_s^j} \tag{5.14}$$

$$f = \frac{\sum_j k_s^j f_j}{\sum_j k_s^j}, \tag{5.15}$$

where j represents each optically active atmospheric constituent and q_j represents the mass mixing ratios, i.e. the mass of molecules or particles per cubic metre of air divided by the mass of one cubic metre of air (Seinfeld and Pandis, 2006; Manners *et al.*, 2015).

5.2.2 Aerosol, cloud, atmospheric and other setup parameters

To run SOCRATES simulations, one has to specify which atmospheric constituents to include in the radiative transfer model, including aerosols, clouds and gases along with their mass mixing ratios as a function of altitude. The aerosol optical properties are generated prior to running SOCRATES. I used the size distribution and refractive indices determined during the Southern African Fire-Atmosphere Research Initiative (SAFARI) measurement campaign from the year 2000 (Haywood *et al.*, 2003b; Keil and Haywood, 2003). The primary aim of the SAFARI campaign was to determine the optical and physical

properties of BBA over Namibia and the Southeast Atlantic Ocean in September 2000. These properties were evaluated by processing over 80 hours of flight data from a range of instrumentation including size distribution measurements, organic and elemental carbon mass concentration measurements, and optical absorption and scattering coefficient measurements. While Haywood *et al.* (2003) fitted the aerosol size distribution with three log-normal modes to account for the presence of mineral dust close to the biomass burning sources, I use a single log-normal biomass burning aerosol mode as this introduces errors of typically less than 5 % in optical parameters at 0.55 μm. See Table 5.1 for details of the aerosol and cloud properties determined using SAFARI measurements, which are used throughout the rest of this chapter. The density of biomass burning aerosols used to determine the specific extinction, absorption and scattering coefficients was taken from Reid and Hobbs (1998).

Biomass burning aerosol		**Stratiform cloud**	
Height	1.8 – 3.7 km 1.77 – 3.66 km*	Height	0.40 – 0.68 km 0.42 – 0.74 km*
Mode radius	0.12 μm	Cloud droplet effective radius	8.5 μm
Particle lognormal distribution standard deviation	1.3	Liquid water content	Variable
Refractive index (550 nm)	1.541 + 0.018i	Liquid water path	Variable
Single scattering albedo (550 nm)	0.89	Cloud fraction	1
Mass mixing ratio	Variable	--	--
Density**	1350 kg m^{-3}	--	--

Table 5.1: *Aerosol and cloud properties based on measurements during the Southern African Fire-Atmosphere Research Initiative (SAFARI) measurement campaign* (Haywood *et al.*, 2003b; Keil and Haywood, 2003). **Due to the finite resolution of the vertical levels in SOCRATES, these are the closest available heights of the aerosol and cloud layers. **The biomass burning aerosol density was taken from Reid and Hobbs (1998).*

Biomass burning aerosol optical properties were generated using Mie theory based on Bohren and Huffman (1998) for dry, spherical particles using the size

distribution and refractive indices in Table 5.1. BBA optical properties change as a function of relative humidity due to aerosol hygroscopic growth, which changes both the particle size and the effective refractive index. In this case, volume weighted averages of the refractive indices of BBA (Table 5.1) and water (1.333 + 1.960×10^{-9}i at 550 nm) were calculated as a function of wavelength, which were used in Mie calculations to determine the optical properties of BBA as a function of relative humidity. The optical properties of BBA are shown in Figure 5.4.

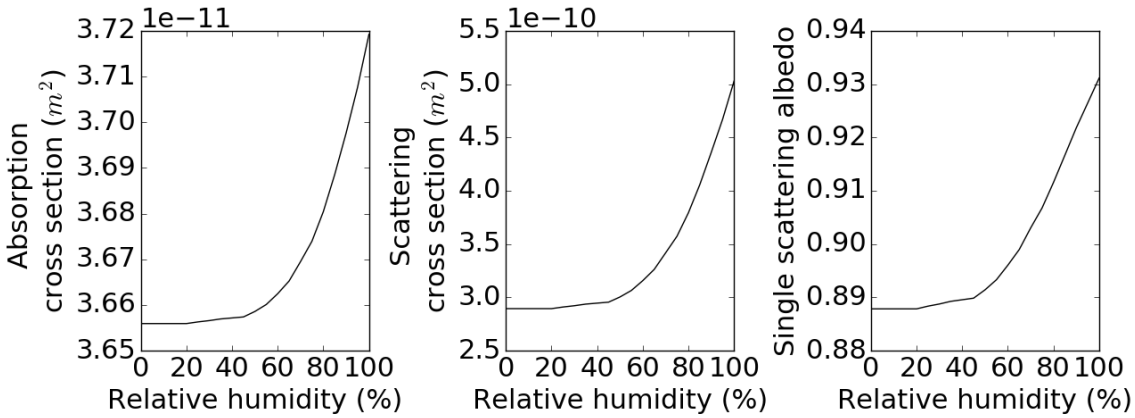

Figure 5.4: *The dependence of the absorption cross section, scattering cross section and the single scattering albedo of biomass burning aerosol to relative humidity at wavelength 550 nm.*

The ocean surface reflectance uses a modified version of the Barker surface reflectance (Barker and Li, 1995; Walters *et al.*, 2017). The standard McClatchey *et al.* (1972) profiles of atmospheric temperature, pressure, water vapour mass mixing ratio and ozone mass mixing ratio are used corresponding to the tropics, which are specified on 133 levels between 0–108 km above the ocean surface where the lowest levels are separated by 0.1 km and the upper levels by 1.1 km. Values are linearly interpolated between the levels. Atmospheric gases contributing to Rayleigh scattering and light-absorption are O_2, O_3, N_2O, CO_2, CH_4 and water vapour. O_2, N_2O and CO_2 are assumed to be well mixed throughout the atmosphere. The atmospheric profiles of O_3, water vapour and atmospheric temperature are shown in Figure 5.5.

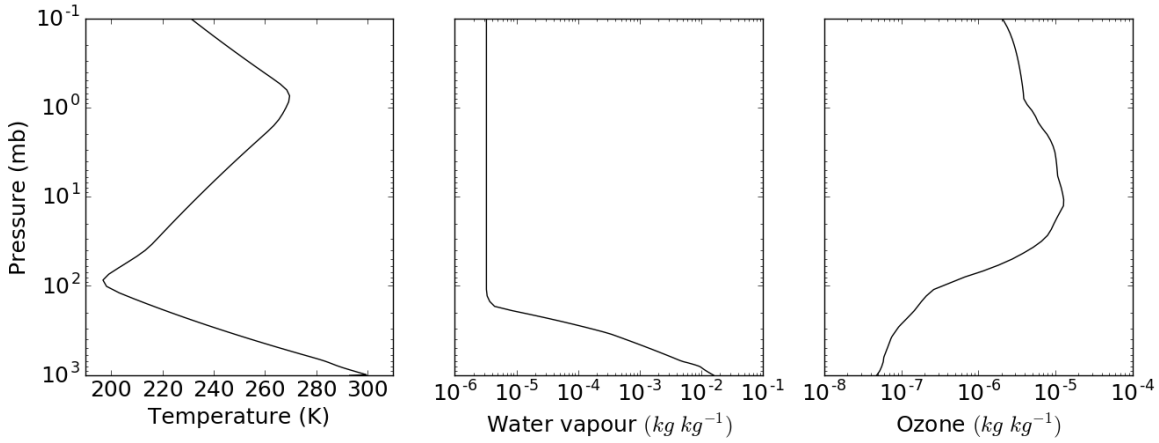

Figure 5.5: *Tropical atmospheric profiles of temperature, water vapour mass mixing ratio and ozone mass mixing ratio as a function of pressure based on McClatchey et al. (1972).*

The radiative transfer equations are solved for 260 wavelengths in the shortwave region of the electromagnetic spectrum in the range 0.175–10.000 μm. A maximum random overlap cloud scheme is used (e.g. Tian and Curry, 1989). In all simulations, Rayleigh scattering is enabled. A two-stream Eddington approximation (e.g. Unno and Spiegel, 1966) with δ-rescaling is used for all calculations of the aerosol radiative forcing. δ-rescaling is turned off for calculations of the aerosol and cloud optical depths.

5.2.3 DRE sensitivities

In this section, I will evaluate how the DRE depends on the (i) solar zenith angle, (ii) aerosol optical depth (AOD) and (iii) cloud optical depth (COD), which will be used to inform the choice of the range and resolution of these parameters when generating look-up tables later.

5.2.3.1 Solar zenith angle

I initially investigated how the DRE depends on the solar zenith angle using the aerosol and cloud properties in Table 5.1 for dry aerosol, as well as an AOD of 0.5 to approximate the mean AOD determined by the MODIS sensor at the height of the biomass burning season (Zuidema *et al.*, 2016) and a COD of 9.0 based on the mean value determined using the MODIS sensor during August and September 2006–2011 (Meyer *et al.*, 2013). Figure 5.6 shows that the DRE in cloudy skies (i.e. ACDRE) reaches a maximum when the sun is directly overhead, i.e. for a solar zenith angle of 0°, and decreases as the sun moves towards the horizon, i.e. for increasing solar zenith angle. However, the DRE shows different behaviour for an aerosol layer in clear sky (i.e. free from cloud)

overlying ocean, which reaches a maximum value at a solar zenith angle of ~60°. This result is qualitatively similar to the dependence of the direct radiative forcing on solar zenith angle in the study of Keil and Haywood (2003). The result shown in Figure 5.6 is also consistent with the results of Haywood and Shine (1997) and Boucher *et al.* (1998), although these studies modelled purely scattering sulphate aerosol in cloud-free conditions, which showed a more pronounced peak at ~60° because in those cases the aerosol was entirely scattering rather than partially absorbing. The dependence of the DRE to solar zenith angle in cloud-free skies is due in part to a higher proportion of the forward scattered irradiance becoming upward-scattered as the solar zenith angle increases (Haywood and Shine, 1997). For the cloudy skies case, the dependence of DRE to solar zenith angle is due to a reduction of the irradiance available for multiple scattering, and therefore a reduction in the aerosol light-absorption, between the aerosol and cloud layers as the solar zenith angle increases.

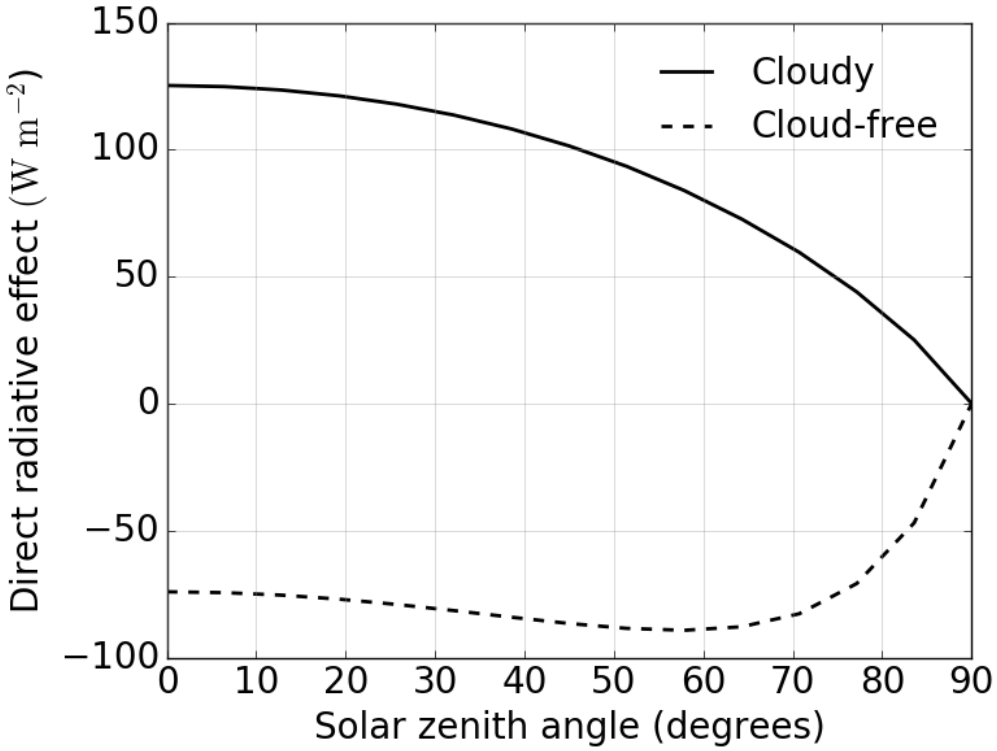

Figure 5.6: *The dependence of the direct radiative effect on the solar zenith angle for an aerosol optical depth of 0.5 and cloud optical depth of 9.0. The remaining SOCRATES setup parameters are detailed in Table 5.1.*

5.2.3.2 Aerosol and cloud optical and microphysical properties

Here I investigate the dependence of the DRE on the aerosol and cloud optical depths using the aerosol and cloud properties outlined in Table 5.1.

SOCRATES simulations were initially run that varied the cloud effective radius, r_{eff}, between 4–20 μm while keeping the COD constant by changing the cloud liquid water content, which verified that the aerosol DRE above cloud is not sensitive to r_{eff} for a fixed COD. This finding justified using a cloud r_{eff} equal to 8.5 μm in the modelling studies that follow.

Figure 5.7 shows that the aerosol DRE varies in a non-linear way as a function of AOD and COD using the properties in Table 5.1 for dry aerosol and for a solar zenith angle of 0°. The DRE is most sensitive to changes in AOD when aerosol is above thick cloud (high COD) and most sensitive to COD when an optically thick aerosol layer overlies thin cloud (low COD). This result is qualitatively similar to previous studies (e.g. Meyer *et al.*, 2013). Figure 5.7 also shows that the high radiative forcings observed in de Graaf *et al.* (2012, 2014) and Peers *et al.* (2015) are easily achievable with a COD ~20 and AOD ~1.2. This result highlights the potential impact that sub-grid variability of aerosol and cloud properties might have on the direct radiative effect within a global climate model and may explain the discrepancy between the satellite and model DRE values in de Graaf *et al.* (2014).

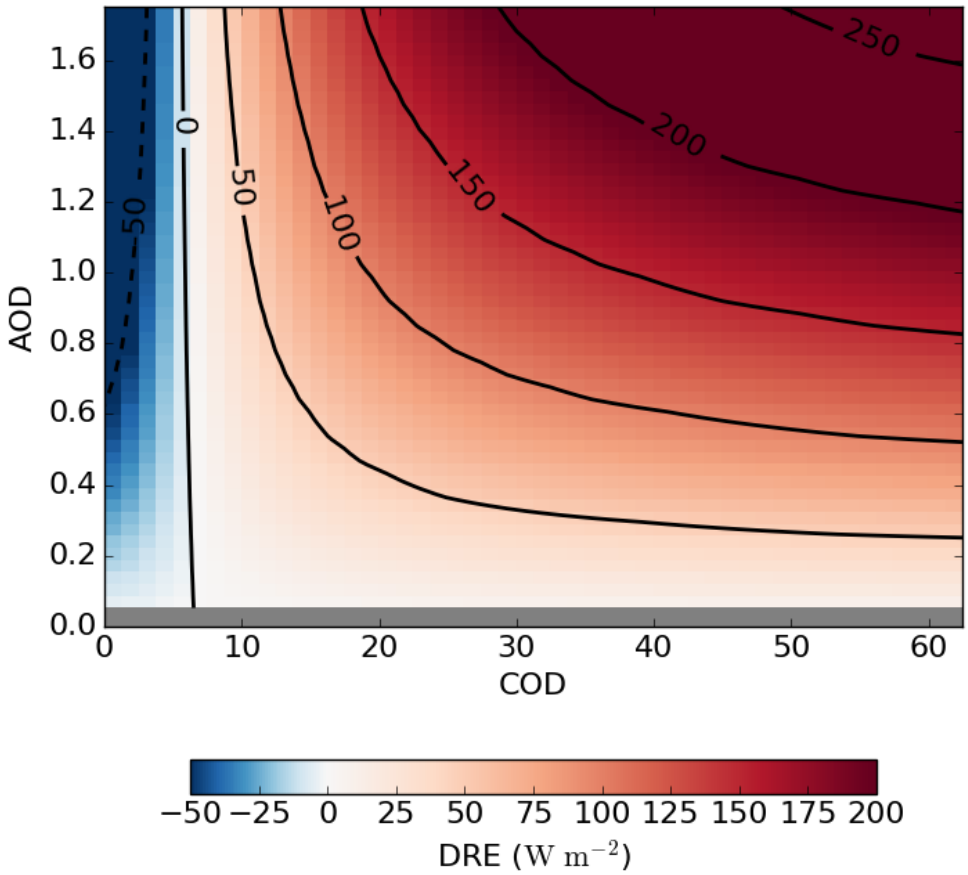

Figure 5.7: *The dependence of the direct radiative effect (DRE) to aerosol optical depth (AOD) and cloud optical depth (COD) for a solar zenith angle of 0° and for dry aerosol. Aerosol and cloud properties were as per Table 5.1. Lines of constant DRE are represented by the black lines (solid lines are positive and dashed lines negative).*

The data presented in Figure 5.7 scales with the solar zenith angle according to Figure 5.6. The range of latitudes used in later studies in this chapter (see section 5.4) is 20.0°S to 0.0°, which have corresponding solar zenith angles in the range 0° to 90° during the months August and September, dependent on latitude.

5.2.4 Summary of DRE sensitivities

In this section I have shown that the cloud optical depth, as opposed to the aerosol optical depth, governs the sign of the DRE for the BBA investigated. Aerosols and clouds are equally important for governing the magnitude of the positive DRE associated with BBA above clouds. These results are consistent with, and highlight the utility of, the simple aerosol radiative model presented in Chapter 1, which showed that the aerosol radiative forcing changes sign depending on the aerosol SSA and surface albedo (Figure 1.8). The DRE is relatively insensitive to AOD and most sensitive to the underlying surface

albedo for thin clouds. The DRE is most sensitive to changes in AOD over thick clouds. In the next section, I will evaluate how uncertain aerosol optical properties impact the DRE in greater detail.

5.3 Investigating the impact of uncertain aerosol absorption measurements on the direct radiative effect

In this section, I will use SOCRATES to investigate the sensitivity of the DRE to the SSA and AAE of BBA. I will then assess the uncertainty introduced to the DRE due to uncertainties in SSA and AAE measurements determined using TAP compared to PAS measurements presented in Chapter 4.

5.3.1 Single scattering albedo

To evaluate the sensitivity of the DRE to aerosol SSA, an aerosol model was used corresponding to aged BBA based on the SAFARI measurement campaign, as detailed in Table 5.1 (Haywood *et al.*, 2003b; Keil and Haywood, 2003). This aerosol model was based on refractive indices that varied between 1.53 to 1.58 (real part) and 0.018 to 0.026 (imaginary part) between wavelengths 0.2 to 40.0 μm. The AOD was set to 0.5 to approximate the mean AOD determined by the MODIS sensor at the height of the biomass burning season (Zuidema *et al.*, 2016). To adjust the SSA, a wavelength-independent scaling factor between 2.0 and 3.0 was applied to the imaginary part of the refractive index and the BBA optical properties regenerated using Mie theory, which were input into the atmospheric model. The cloud properties used during this analysis are provided in Table 5.1.

Figure 5.8 shows how the DRE changes as a function of SSA for a range of COD values between 0–10, which includes a cloud-free case, at solar zenith angle 0°. The expected behaviour is observed implied by the simple model of Chapter 1 (section 1.3), i.e. that the DRE is always negative for the cloud-free case and the DRE is always positive for thick cloud (COD=10), independent of the aerosol SSA. For the intermediate cases where the COD is in the range 1–5, the DRE is sometimes positive and sometimes negative, dependent on the SSA. The critical SSA (see equation 1.13) is defined as the SSA where the DRE swaps sign. The critical SSA for the case study shown in Figure 5.8 for COD = 1 is ~0.83–0.84, for COD = 3 is ~ 0.95–0.96 and for COD = 5 is ~0.98. This result differs to Figure 5.7, which shows no positive DRE values for

COD=1, due to the lower single scattering albedos used within SOCRATES simulations to generate Figure 5.8 (0.77 to 0.83) compared to those used to generate Figure 5.7 (0.89). This result is qualitatively similar to the Keil and Haywood (2003) study, who observed critical single scattering albedos for BBA based on SAFARI measurements in the range 0.86–0.93 dependent upon on cloud optical depth. The mean SSA at 528 nm for aged BBA aerosol measurements determined using PAS and CRDS measurements from Chapter 4 is shown by the thin coloured vertical line. The mean SSA at 528 nm determined using TAP and CRDS measurements is shown by the thick coloured vertical line, where the range is due to the TAP correction scheme applied.

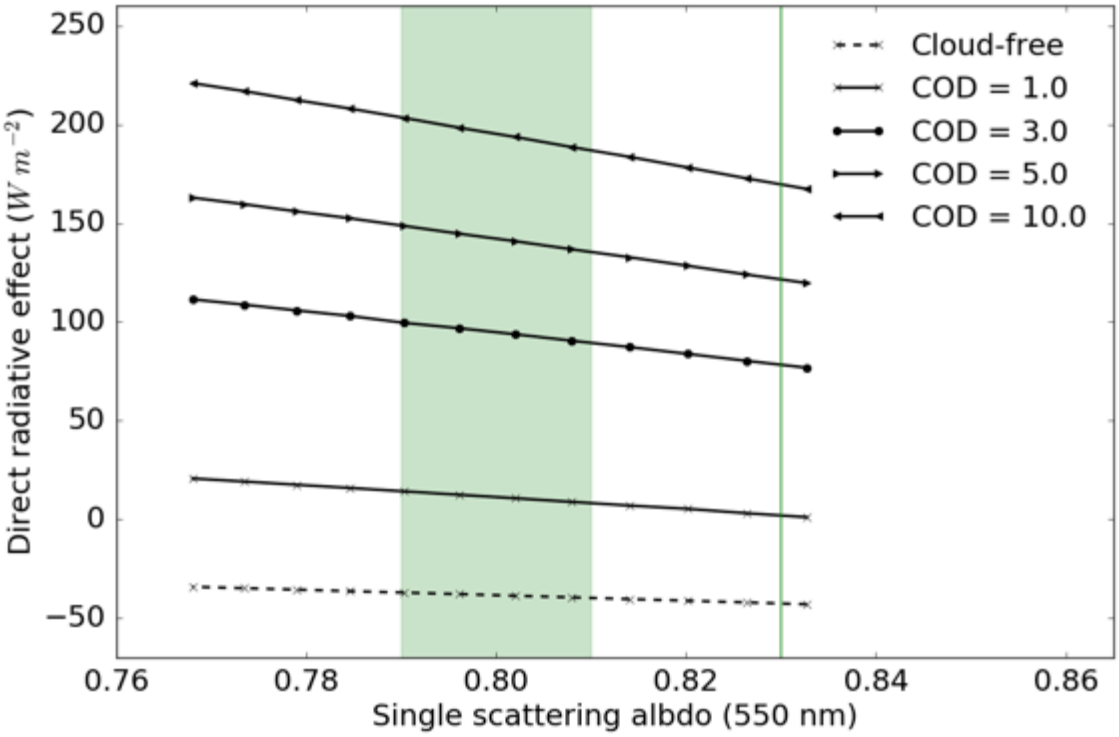

Figure 5.8: *The total direct radiative effect over the solar spectrum (0.175–10 μm) for variable single scattering albedo and cloud optical depth (COD) for solar zenith angle 0°. Also shown is the DRE for the no cloud case (dashed black line). Highlighted by the thin vertical green line is the mean single scattering albedo determined using PAS measurements corresponding to aged BBA. The green area represents the range of mean SSA values determined using TAP measurements; the range of values comes from SSA values derived using the range of TAP correction schemes. The aerosol optical depth was set to 0.5. The remaining aerosol and cloud properties can be found in Table 5.1.*

It is clear from Figure 5.8 that if aged BBA optical properties were based on TAP measurements compared to PAS measurements, the associated DRE

would be consistently overestimated when aerosols reside above thick cloud and underestimated when aerosols reside above ocean. TAP biases led to lowest absolute biases in the DRE for the cloud-free case, which overestimated the DRE by 2.8 to 5.5 W m^{-2} (7 to 13 %), dependent on the TAP correction scheme applied. TAP biases led to largest absolute biases in the DRE for high COD, which underestimated the DRE by 17.5 to 33.9 W m^{-2} (10 to 20 %) for COD = 10, dependent on the TAP correction scheme applied. The largest percentage biases in DRE were associated with thin cloud (COD = 1), which overestimated the DRE by 6.5 to 12.4 W m^{-2} (361 to 689 %); these large percentage errors are due to DRE values that are close to zero. This data is summarised in Table 5.2. This analysis was repeated for a lower AOD of 0.1, which led to similar DRE percentage biases (not shown).

Cloud	DRE PAS (W m^{-2})	DRE TAP (W m^{-2})	TAP bias (%)
Cloud-free	−42.6	−39.8 to −37.1	7 to 13
COD=1	1.8	8.3 to 14.2	361 to 689
COD=3	78.2	89.5 to 99.6	14 to 27
COD=5	121.5	135.5 to 148.7	12 to 22
COD=10	169.5	187.0 to 203.4	10 to 20

Table 5.2: *The direct radiative effect (DRE) corresponding to mean aerosol single scattering albedos derived using PAS and TAP absorption measurements corresponding to the data in Figure 5.8.*

5.3.2 The wavelength dependence of absorption (absorption Ångström exponent)

Here I assess the impact that uncertainty in the AAE has on the aerosol DRE. As in the previous subsection, aerosol optical properties are based on SAFARI rather than CLARIFY measurements of aged BBA over the Southeast Atlantic Ocean. I initially generated absorption cross sections as a function of wavelength using Mie theory based on the aerosol size distribution and refractive indices detailed in Table 5.1, shown by the black line in Figure 5.9. The AAE was determined by applying a least-squares regression analysis to the absorption cross section as a function of wavelength using equation 4.25. This analysis yielded an AAE of 1.55, which will be referred to as AAE_{SAFARI}. I then varied AAE_{SAFARI} by ± 0.3, which is the maximum difference between the mean AAE values derived using PAS compared to TAP measurements of aged BBA measured during the CLARIFY measurement campaign, corresponding to

data presented in Figure 4.9. Starting at wavelength 400 nm, absorption cross sections were extrapolated to longer wavelengths using AAE_{SAFARI} by ± 0.3, shown by the dashed lines in Figure 5.9.

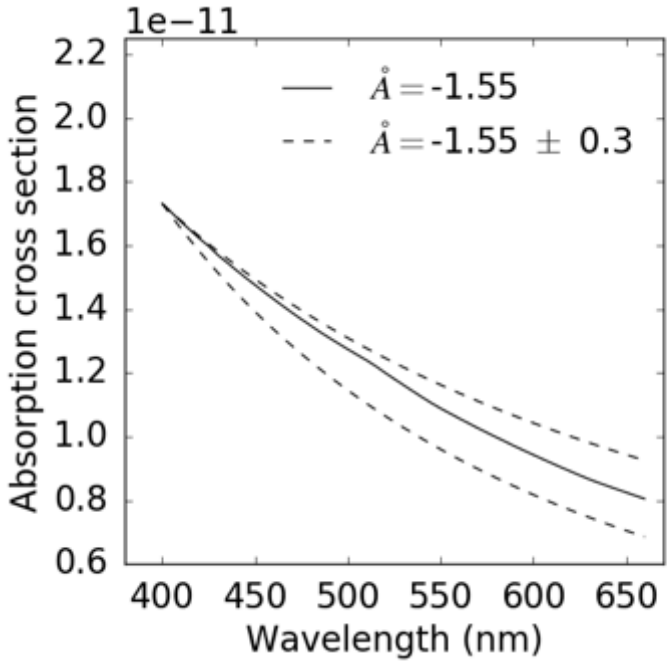

Figure 5.9: *Absorption cross sections as a function of wavelength generated using the aerosol size distribution and refractive indices corresponding to SAFARI measurements of aged biomass burning aerosols (solid line). The dashed lines show how the absorption cross sections vary when the absorption Ångström exponent is varied by ± 0.3. The extrapolation starts from wavelength 400 nm.*

A scaling factor was applied to the imaginary refractive indices corresponding to aged BBA (Table 5.1), which adjusted the wavelength dependence of the absorption cross sections generated using Mie theory. The scaling factor was varied to minimise the difference between the modified absorption cross sections generated using Mie theory and the absorption cross sections corresponding to AAE_{SAFARI} ± 0.3 (dashed lines in Figure 5.9). These modified aerosol optical properties were input into the SOCRATES radiation code according to the parameters in Table 5.1 and the impact on the DRE evaluated. The spectrally dependent DRE was evaluated in the range 400 to 660 nm as opposed to the DRE corresponding to the full solar spectrum, which is shown in Table 5.3. The largest uncertainty introduced to the DRE if aerosol optical properties were based on the AAE determined using TAP rather than PAS measurements was for thick cloud (COD=10). The DRE could be biased high by up to 9.2 W m^{-2} or biased low by up to 34.6 W m^{-2}.

Cloud	DRE (W m^{-2}) AAE_{SAFARI}	DRE (W m^{-2}) AAE_{SAFARI} ± 0.3
Cloud-free	−29.7	−35.9 to −28.1
COD=1	−14.8	−27.4 to −11.5
COD=3	14.4	−7.4 to 20.1
COD=5	31.1	3.7 to 38.1
COD=10	49.2	14.6 to 58.4

Table 5.3: *The direct radiative effect (DRE) over the wavelength range 400–660 nm based on the SAFARI aerosol optical properties and based on modified SAFARI aerosol optical properties.*

The DRE was only evaluated in the range 400 to 660 nm for two reasons. The uncertainty in the aged BBA AAE in Chapter 4 was determined as the mean difference between TAP and PAS measurements, which was based on the wavelength range 405 to 658 nm. It is unclear how the AAE determined using TAP or PAS would change over a wider wavelength range. The second reason for only evaluating the DRE over the wavelength range 400 to 660 nm was due to the scaling factor applied to the imaginary refractive indices. This scaling factor was wavelength-dependent and was optimised to minimise the absorption cross sections generated using Mie theory corresponding to SAFARI-measured aged BBA so that they overlay the absorption efficiencies corresponding to AAE_{SAFARI} ± 0.3. It is unclear how these scaling factors would be extrapolated outside of this wavelength range.

5.3.3 Summary of the sensitivity of the direct radiative effect to aerosol absorption measurements

To summarise, this analysis examined the sensitivity of the DRE to aerosol SSA (Figure 5.8 and Table 5.2) and to aerosol AAE (Figure 5.9 and Table 5.3) using aerosol optical properties based on refractive indices corresponding to SAFARI measurements of aged BBA. If aerosol optical properties were based on TAP rather than PAS measurements of single scattering albedo, uncertainties introduced to the DRE may be as large as 33.9 W m^{-2}. Likewise, if aerosol properties were based on measurements of the absorption Ångström exponent based on TAP rather than PAS measurements, uncertainties in the DRE may be as large as 34.6 W m^{-2}. Both of these DRE uncertainties correspond to COD of 10 and could be larger under certain conditions such as for higher aerosol and/or cloud optical depths. This result highlights the utility of state-of-the-art

PAS aerosol absorption coefficient measurements compared to traditional filter-based methods.

A limitation of this analysis is that the wavelength dependence of the imaginary part of the refractive index based on SAFARI measurements was assumed to be the same as CLARIFY measurements of aged BBA. Ideally, refractive indices based on CLARIFY measurements would have been used. However, the CLARIFY dataset consisting of optical and physical properties of aged BBA has not yet been fully developed enough to infer the refractive indices.

5.4 Evaluating the dependence of the above cloud direct radiative effect to sub-grid variability

5.4.1 Introduction

The aim of this section is to evaluate the sensitivity of the ACDRE to the spatial variability of the underlying aerosol and cloud optical properties for biomass burning aerosols over the Southeast Atlantic Ocean. I initially perform offline radiative transfer simulations to determine ACDRE values corresponding to each AOD-COD pair observed using the POLDER satellite instrument. I then average the POLDER AOD and COD observations over increasingly larger geographical areas and perform offline radiative transfer simulations to determine new sets of ACDRE values for each spatial resolution. Subsequently, I examine how the mean and range of the ACDRE values vary as a function of spatial variability of aerosol and cloud optical depths using probability density fucntions.

The second way that I evaluate the sensitivity of the ACDRE to spatial variability is by evaluating how well a global climate model (HadGEM3) is able to reproduce the ACDRE using POLDER satellite observations as a reference. I then assess whether increasing the climate model resolution alters the agreement to these satellite observations.

5.4.2 POLDER

The POLDER instrument was aboard the PARASOL satellite between March 2006 and December 2009, in the A-train series of satellites (Waquet *et al.*, 2013). POLDER was able to simultaneously determine the COD, the above cloud AOD (ACAOD), above cloud SSA (ACSSA) and ACDRE. To determine

these, the POLDER algorithm minimised the difference between measured and modelled total and polarised radiances at multiple scattering angles and wavelengths by varying the aerosol size distribution, aerosol refractive indices and cloud droplet effective radii for each 5.3 × 6.2 km pixel (Peers *et al.*, 2015). POLDER used a combination of up to seven aerosol lognormal modes with modal radii varying between 0.06 to 0.16 μm and geometric standard deviation 0.4, a variable imaginary refractive index between 0.00 to 0.05, as well as varying the cloud effective radius between 5 to 26 μm (Peers *et al.*, 2015). Under certain conditions, POLDER was unable to retrieve aerosol and cloud properties, in which case filters were applied to remove these data. These included pixels with COD < 3, AOD < 0.05 as well as filters accounting for high cloud and/or aerosol inhomogeneity, where the algorithm does not retrieve the aerosol and cloud properties accurately (Waquet *et al.*, 2013; Peers *et al.*, 2015). The ACDRE values determined using POLDER during August 2006 are shown in Figure 5.2.

5.4.3 Assessing the sensitivity of the aerosol ACDRE to sub-grid variability using SOCRATES and POLDER

5.4.3.1 Method

POLDER determined the AOD and COD for each pixel at a spatial resolution ~5 km, subsequently performing radiative transfer calculations to determine the ACDRE. To investigate the impact that sub-grid variability might have on the ACDRE, which is controlled by the underlying aerosol and cloud properties, the POLDER measurements of AOD and COD would need to be transformed to a coarser resolution (e.g. averaged over larger geographical areas) and the radiative transfer calculations re-run. As this transformation would require direct access to the POLDER algorithm and processing, instead I performed separate radiative transfer calculations with SOCRATES using the aerosol size distribution, refractive indices and cloud microphysical properties measured over the Southeast Atlantic Ocean during the SAFARI measurement campaign (Haywood *et al.*, 2003b; Keil and Haywood, 2003); see Table 5.1. Using these different aerosol and cloud properties combined with differences in the radiation schemes led to different ACDRE values compared to those determined by the POLDER retrieval algorithm. However, the difference in the absolute magnitude of ACDRE values is rather less important than the relative impact of spatial

variability of the aerosol and cloud properties on the mean and distribution of the ACDRE in this study.

To investigate the impact that sub-grid variability has on the ACDRE, I investigated how the mean and range ACDRE changed as a function of the spatial resolution of the AOD and COD in a domain with latitude 20.0°S to 0.0° and longitude 10.0W° to 13.5E°. To implement this analysis, I generated a lookup table of ACDRE values for AOD values in the range 0.05 to 1.75 in 50 intervals, COD values in the range 0.0 to 52.9 in 50 intervals and for solar zenith angles in the range 19° to 47° in 29 intervals. These ranges covered values observed by POLDER during August and September 2006. The lookup table was generated by running SOCRATES simulations for the aerosol and cloud properties in Table 5.1 using mass mixing ratios of biomass burning aerosol and cloud liquid water content that matched the AOD and COD values. A cloud fraction of 1 was assumed for all cloudy-sky simulations. When searching lookup tables in the analyses that follow, a nearest neighbour approach was used to locate DRE values corresponding to each AOD-COD-SZA triplet.

5.4.3.2 Extreme spatial averaging

Holding both the AOD and COD fixed over the entire domain represents the extreme in spatial averaging. In this case, the domain-mean AOD and COD retrieved using POLDER during August and September 2006 were 0.41 and 11.1, respectively. The mean solar zenith angle (SZA) for all POLDER observations over the same period was 31.7°. The corresponding ACDRE for the mean AOD-COD-SZA triplet was located within the predetermined lookup table, which was +21.5 W m^{-2}. Three additional scenarios were investigated using the AOD and COD values retrieved using POLDER, which represented relatively relaxed spatial averaging: (i) domain-mean AOD and variable COD, (ii) variable AOD and domain-mean COD and (iii) variable AOD and variable COD. These cases were examined for both variable and mean SZA. For the variable cases, AOD, COD and SZA varied on a pixel-by-pixel basis. The corresponding ACDRE for each AOD-COD-SZA triplet was located within the predetermined lookup table. The mean and range of ACDRE values for these cases is shown in Figure 5.10 and summarised in Table 5.4.

A key feature of Figure 5.10 is that the large ACDRE values are removed and the range of values narrowed when the variability in the COD and/or AOD is suppressed. The ACDRE is almost always positive when the COD is held constant due to having reflective cloud everywhere. This result suggests that the ACDRE is relatively strongly dependent on the COD compared to the AOD for typical conditions over the Southeast Atlantic Ocean. The loss of large positive ACDRE values when suppressing variability in the AOD and COD fields is due to the non-linear dependence of the DRE on AOD and COD, shown in Figure 5.7.

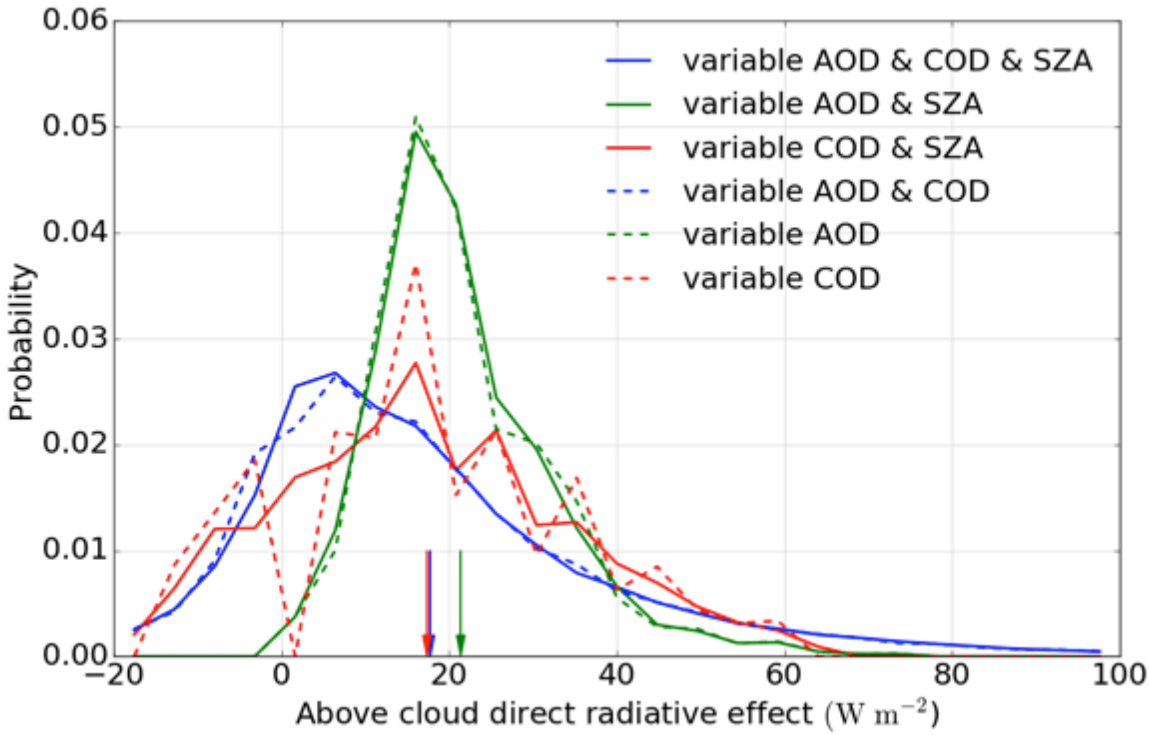

Figure 5.10: *Probability density functions of the above cloud direct radiative effect determined using SOCRATES for the aerosol and cloud properties in Table 5.1 and for AOD and COD values retrieved using POLDER. The arrows highlight the mean values. AOD: aerosol optical depth. COD: cloud optical depth. SZA: solar zenith angle.*

Averaging conditions			**ACDRE (W m^{-2})**
AOD	**COD**	**SZA**	
Fixed	Fixed	Fixed	21.5
Variable	Fixed	Fixed	21.4
Fixed	Variable	Fixed	17.4
Variable	Variable	Fixed	17.9

Variable	Fixed	Variable	21.4
Fixed	Variable	Variable	17.3
Variable	Variable	Variable	17.7

Table 5.4: *Above cloud direct radiative effect (ACDRE) associated with a range of spatial averaging conditions corresponding to data in Figure 5.10.*

Figure 5.10 also shows that the ranges of ACDRE values were similar regardless of whether the SZA was held fixed at the mean value or allowed to vary. Figure 5.6 shows that the dependence of ACDRE varies approximately linearly within the range of SZA values 20 to 47°, which suggests that ACDRE values associated with SZA values higher and lower than the mean SZA may cancel out.

Thus far I have investigated the two extremes in spatial averaging by (i) using a domain mean AOD and COD (i.e. maximal spatial averaging) and (ii) by using AOD and COD values that vary on a pixel-by-pixel basis (i.e. minimal spatial averaging), as well as intermediate cases by holding either the AOD or COD fixed. This result verified that the mean ACDRE is relatively insensitive to variability in the AOD and COD, which was in the range 17.7 to 21.5 W m^{-2} for the two extreme cases.

5.4.3.3 Variable spatial averaging

To investigate the relationship between the ACDRE and the degree of spatial averaging, I averaged the AOD and COD values observed using POLDER over a range of spatial scales between 0.05° to 3.0°, subsequently locating each AOD-COD pair within the lookup table generated using SOCRATES for aerosol and cloud properties described in Section 5.2.2.

The method of averaging involved the following steps: (i) setting up a mesh of latitude and longitude grid boxes with resolution between 0.05° to 3.0°, (ii) populating the grid boxes for a given variable (e.g. AOD) for all POLDER overpasses during August and September 2006 and (iii) computing the average value within each grid box. Upon closer inspection, it should be noted that this method might have biased the variable that was being averaged. Another way of performing this averaging method (not done in this thesis) would be to compute the average value within each grid box for each POLDER overpass,

subsequently computing the average within each grid box corresponding to all overpasses.

Figure 5.11 shows the spatial distribution of AOD observed by POLDER and how the large AOD values are lost under heavy averaging. Figure 5.12 shows how the range of AOD values observed on a pixel-by-pixel basis compares to spatially averaged AOD values over the range of scales 0.05° to 3.0° latitude/longitude. Surprisingly, the AOD appears to be only weakly dependent on the degree of spatial averaging. Figure 5.12 shows the expected behaviour, where the largest spatial averaging (red) is characterised by a relatively narrower distribution and the lowest spatial averaging (blue) by a broader distribution.

Figure 5.13 shows how the COD varies as a function of spatial averaging. The COD shows a relatively stronger sensitivity to the degree of spatial averaging compared to the AOD. Again, the narrowest COD distributions are associated with the largest spatial averaging, shown in Figure 5.14. An explanation for the stronger dependence of COD to spatial averaging is likely related to the higher spatial variability of clouds compared to aerosols. Figures 5.12 and 5.14 both highlight that even a small degree of spatial averaging (0.05°) detracts significantly from the pixel-by-pixel POLDER observations.

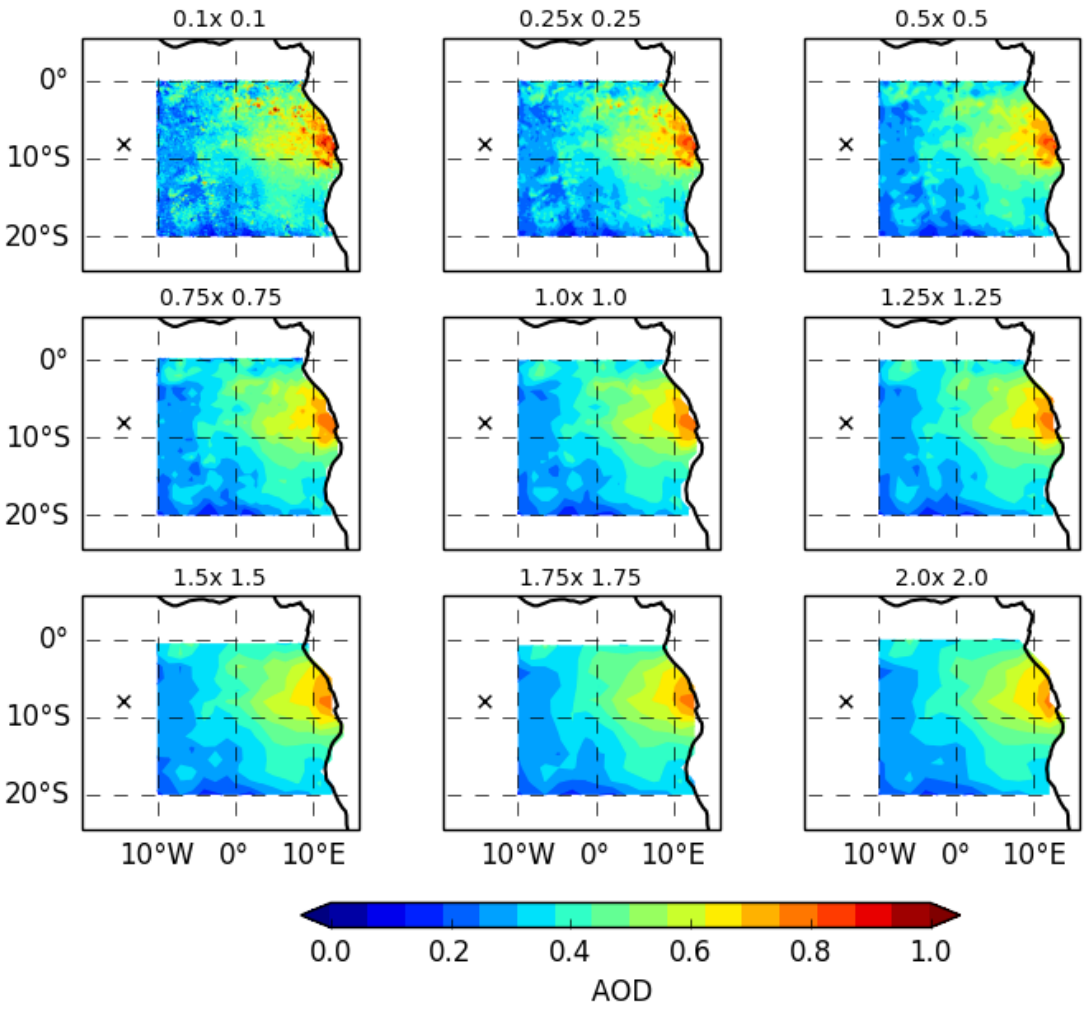

Figure 5.11: *The mean aerosol optical depth (AOD) observed by POLDER over the Southeast Atlantic Ocean during August and September 2006. The AOD is averaged over resolutions 0.1° to 2.0° latitude/longitude. The mean AOD was 0.41. The black crosses represent Ascension Island.*

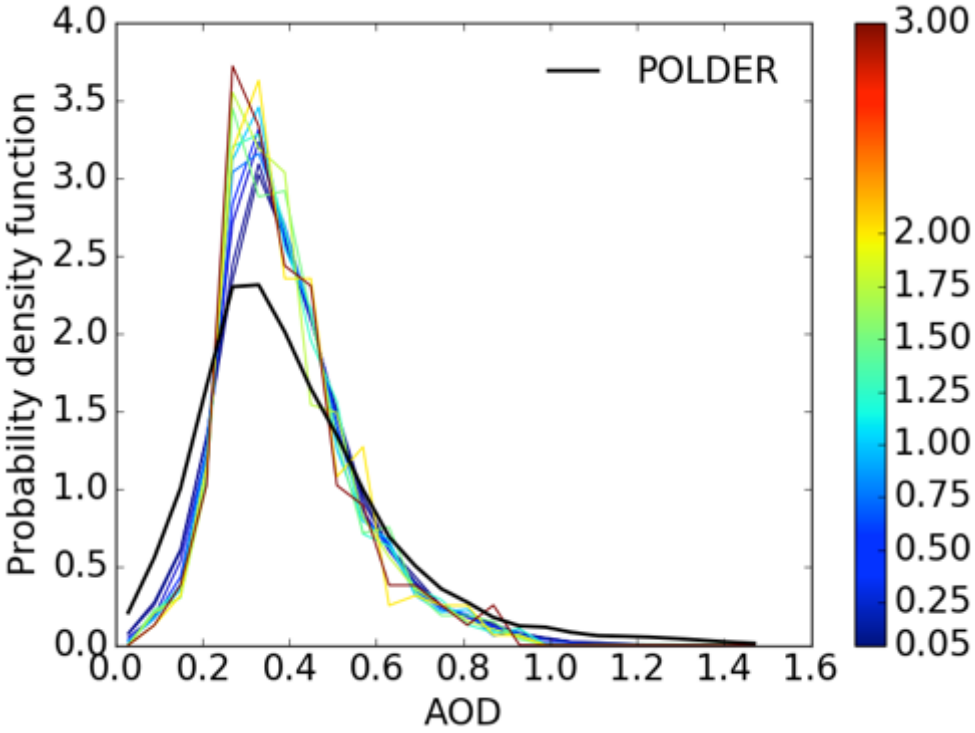

Figure 5.12: *Probability density functions of the aerosol optical depth (AOD) observed by POLDER over the Southeast Atlantic Ocean during August and September 2006 (black line). In the coloured lines are averaged POLDER AOD values over the resolution range 0.05° to 3.0° latitude/longitude.*

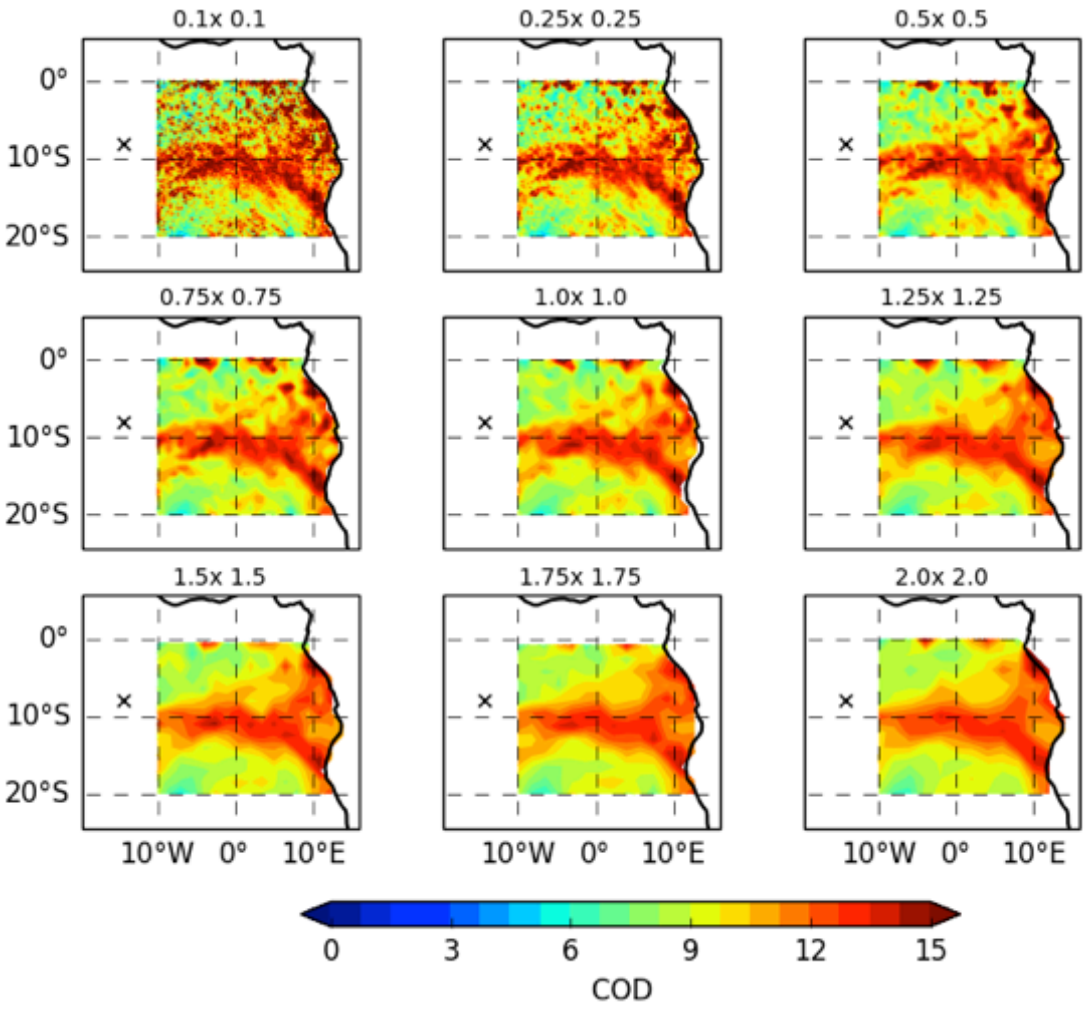

Figure 5.13: *The mean cloud optical depth (COD) observed by POLDER over the Southeast Atlantic Ocean during August and September 2006. The COD is averaged over resolutions 0.1° to 2.0° latitude/longitude. The mean COD was 11.11 (for COD > 3). The black crosses represent Ascension Island.*

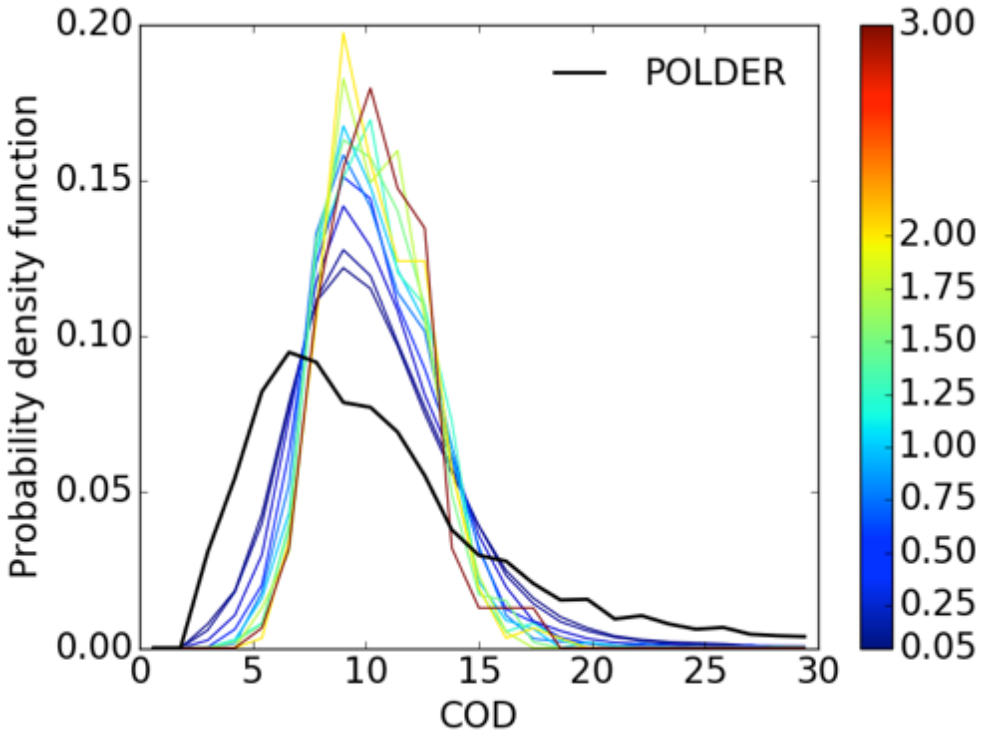

Figure 5.14: *Probability density functions of the cloud optical depth (COD) observed by POLDER over the Southeast Atlantic Ocean during August and September 2006 (black line). In the coloured lines are averaged POLDER COD values over the resolution range 0.05° to 3.0° latitude/longitude.*

For each AOD-COD pair corresponding to those values shown in Figures 5.11 and 5.13, the associated ACDRE values were located within the predetermined lookup table (see section 5.4.3.1). Figure 5.15 shows how the ACDRE varies as a function of the degree of spatial averaging of the underlying AOD and COD fields. The high AOD and COD values observed by POLDER (Figures 5.11 and 5.13) are lost during spatial averaging. The removal of these two features appears to remove the high ACDRE values and to narrow the distribution of ACDRE, as shown in Figure 5.16. This result could explain the relatively narrow range of ACDRE values in global climate models relative to satellite observations observed in de Graaf *et al.* (2014) and Peers *et al.* (2016).

The ACDRE appears to depend weakly on the degree of spatial averaging. As expected, the high resolution (blue) leads to the widest distribution of ACDRE compared to the coarsest resolution (red). An explanation for the insensitivity of ACDRE to spatial averaging could be that the impact that the spatially averaged AOD and COD fields have on the DRE cancel out, leaving the DRE unchanged. These results were insensitive to aerosol hygroscopic growth for the atmospheric setup used.

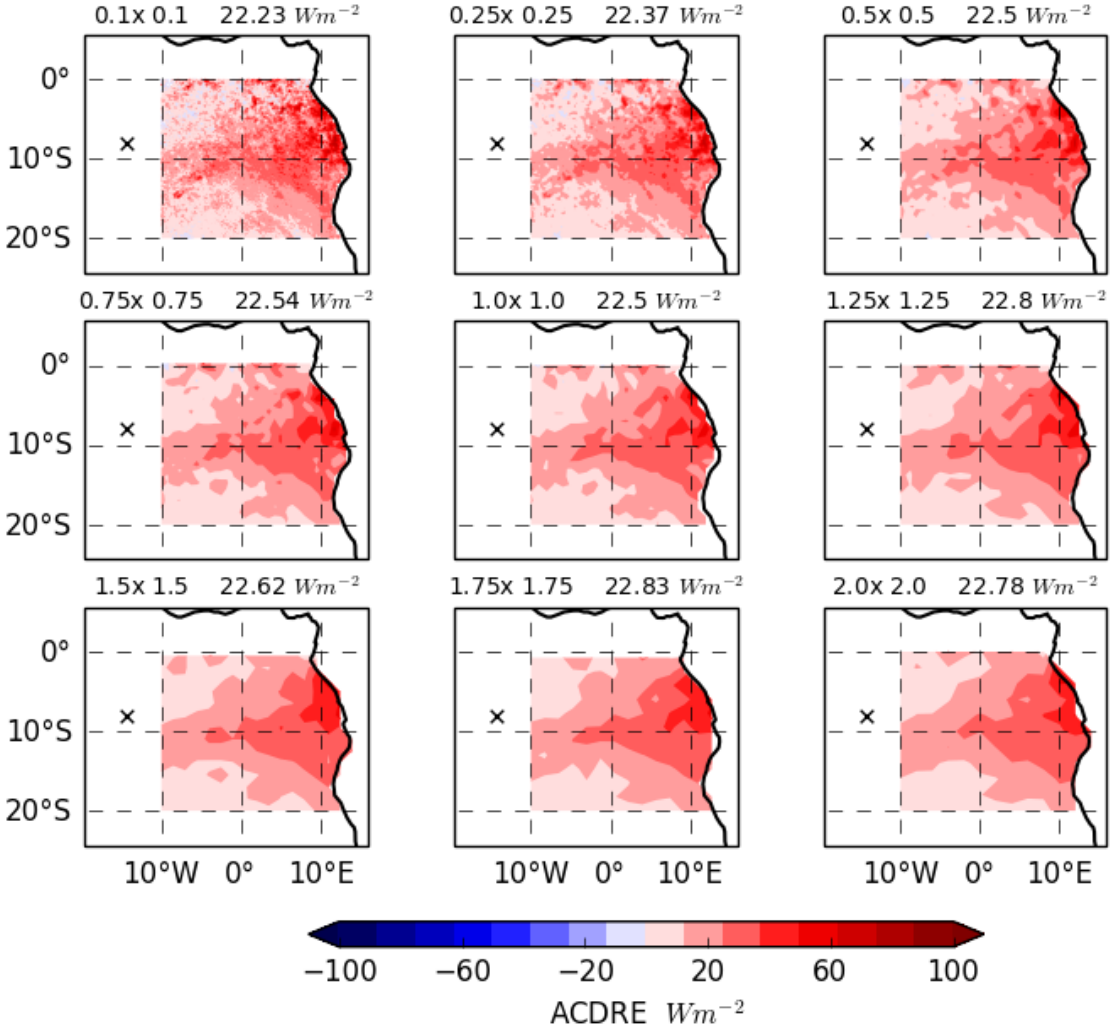

Figure 5.15: *The mean above cloud direct radiative effect (ACDRE) during August and September 2006 determined with SOCRATES using the aerosol and cloud properties in Table 5.1 for AOD and COD values corresponding to those observed using POLDER (Figures 5.11 and 5.13). The mean ACDRE is shown at the top of each subplot corresponding to each resolution between 0.1° to 2.0° latitude/longitude. The black crosses represent Ascension Island.*

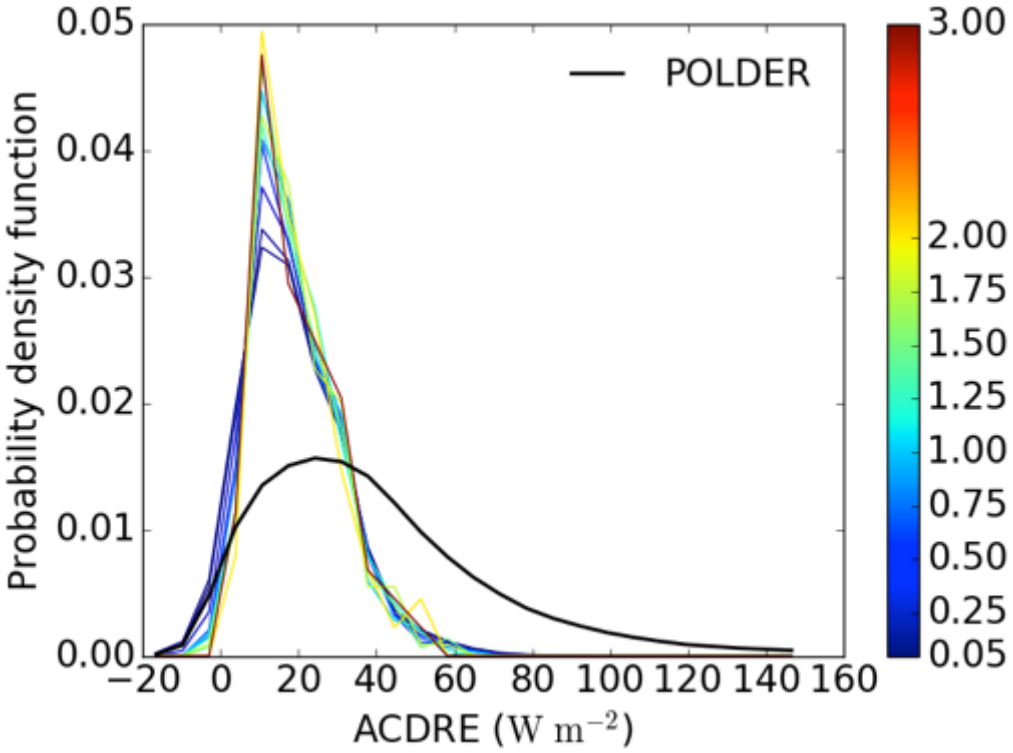

Figure 5.16: *Probability density functions of the aerosol above cloud direct radiative effect (ACDRE) determined using SOCRATES for the AOD and COD observed by POLDER over the Southeast Atlantic Ocean during August and September 2006 (black line). In the coloured lines are averaged ACDRE over the resolution range 0.05° to 3.0° latitude/longitude.*

This analysis assumed a cloud fraction of 1 throughout the cloudy-sky simulations. This assumption was made to match the POLDER observations, which filtered data for areas of high cloud heterogeneity and only processed areas with a cloud fraction equal to 1 (Peers *et al.*, 2015). This assumption will skew the ACDRE to high values. It is not obvious how the clear-sky or all-sky (clear-sky plus cloudy-sky) DRE would depend on variability of AOD and COD. For the clear-sky case, the dependence of the clear-sky DRE on spatial resolution could mirror the results shown in Figure 5.16 due to the large-scale aerosol haze, which is only weakly sensitive to spatial averaging, as shown in Figure 5.11. On the other hand, the clear-sky DRE could show a stronger dependence on spatial averaging if the insensitivity to spatial averaging of the cloudy-sky DRE (Figure 5.15) is due to the net effect of applying spatial averaging to the AOD and COD fields.

This analysis is limited in that it was only able to assess the sensitivity of aerosol ACDRE to changes in AOD relative to COD. Studies suggest that AOD

and COD may correlate in this region due to a semi-indirect effect whereby absorbing aerosols overlying clouds warm and stabilise the lower troposphere (e.g. Adebiyi *et al.*, 2015). However, no evidence for this observation was apparent.

The next step is to run a global climate model at variable spatial resolution to assess whether sub-grid variability affects the ACDRE and if so, what the underlying controlling factors are.

5.4.4 Assessing the sensitivity of the aerosol ACDRE to sub-grid variability using a global climate model

5.4.4.1 Method

The Hadley Centre Global Environment Model version 3 (HadGEM3) was run for July, August and September 2006 using hourly time steps. The horizontal winds in HadGEM3 model simulations, hereafter referred to as the *model*, were nudged to meteorological reanalysis data, and the sea surface temperatures prescribed, during 2006. HadGEM3 simulations were atmosphere-only runs. The first month (July) was used to allow the model to equilibrate, hence only the months August and September were evaluated scientifically. The model was run at three spatial resolutions, N96 (1.875° × 1.25° or ~135 km), N216 (0.83° × 0.56° or ~60 km) and N512 (0.35° × 0.234° or ~25 km). The biomass burning aerosol emissions inventory was based on the Global Fire Emissions Database 4 with small fires (GFED4s) (van der Werf *et al.*, 2017), used in the Coupled Model Intercomparison Project Phase 6 (Eyring *et al.*, 2016). The GFED4s dataset was specified at 0.25° latitude/longitude resolution, which was re-gridded to coarser resolution in all cases.

To enable comparison to POLDER satellite observations, several filters were applied to the model data based on those applied to POLDER observations (see section 5.4.2). Model data was discarded for grid cells with total column COD < 3. Model data contaminated by mid and high level altitude clouds was discarded by filtering out grid cells with mid-level or high-level cloud fractions > 0.0. The model data was collocated in time and space with the POLDER observations. To collocate the model data and satellite observations in time, a

weighted mean of the hourly model data closest to the satellite overpass was performed such that the weighted mean DRE was calculated as

$$DRE^{mean} = x \cdot DRE^{t1} + (x - 1) \cdot DRE^{t2} \qquad (5.16)$$

where $DRE^{t1,t2}$ are the instantaneous model DRE values at times $t1$ and $t2$, which are the model times either side of the POLDER overpass time over the Southeast Atlantic Ocean region, and x is the fraction of each instantaneous model DRE. For example, if the POLDER overpass time was 13:20, the two model times $t1$ and $t2$ would equal 13:00 and 14:00, respectively and x would equal 0.33. Spatial collocation was performed by searching for satellite observations within ± 0.625° latitude and ± 0.9375° longitude of the model latitude and longitude grid cell midpoints, respectively. The collocation boundaries were chosen as they represent the midpoint between adjacent model coordinates for the standard N96 model resolution. Table 5.5 provides details of the total number of available model data after applying the various filters.

Constraint	**Number of model points (N96)**	**Number of model points (N216)**	**Number of model points (N512)**
Total points	29 500	141 900	735 280
COD > 3	19 509	97 565	492 228
Collocation with POLDER	3925	21555	114 377
Mid-level and high-level cloud fraction > 0	3539	19436	104 383

Table 5.5: *Details of the filters applied to the HadGEM3 model data and the remaining number of model points after applying each filter (cumulative).*

The modelled ACDRE was evaluated to allow comparison to the POLDER satellite retrievals and was calculated using the total and clear-sky radiative forcings, such that

$$DRE_{cloudy} = \frac{DRE_{all} - \left((1 - clfr)DRE_{clear}\right)}{clfr}, \qquad (5.17)$$

where DRE_{all} is the all-sky direct radiative effect, DRE_{clear} is the clear-sky (i.e. cloud-free) direct radiative effect and $clfr$ is the grid cell cloud fraction.

Equation 5.17 effectively isolated the cloudy portion of the model grid box such that the DRE became ACDRE and cloud fraction became 1.

5.4.4.2 Aerosol ACDRE

The ACDRE values are shown for HadGEM3 model simulations and POLDER observations in Figure 5.17 (spatially) and in Figure 5.18 (probability density functions) for the N96, N216 and N512 model resolutions.

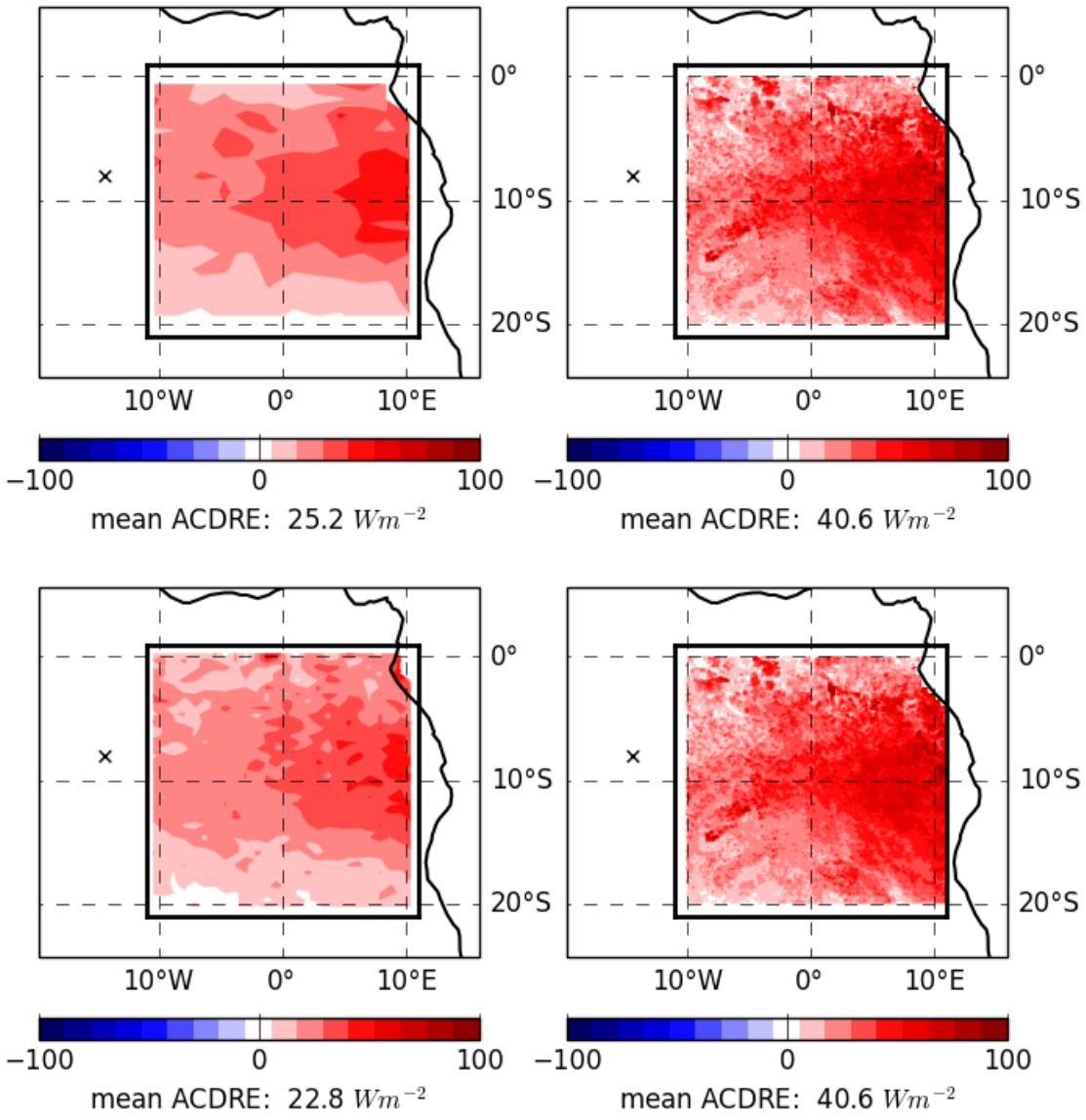

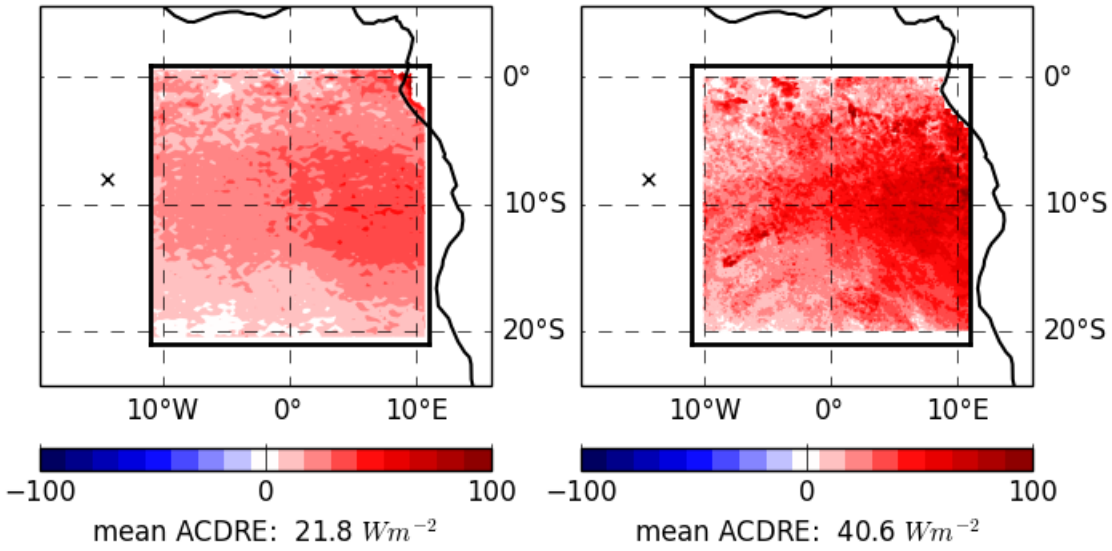

Figure 5.17: *The above cloud direct radiative effect (ACDRE) over the Southeast Atlantic Ocean. HadGEM3 model simulations are on the left and POLDER satellite observations on the right. These represent the two-month means (August and September) in 2006. The HadGEM3 model data were filtered according to Table 5.5 and the POLDER data were filtered according to section 5.4.2. The top, middle and bottom HadGEM3 plots correspond to the N96, N216 and N512 resolution simulations, respectively. GFED4s monthly emissions files were used. The black crosses represent Ascension Island.*

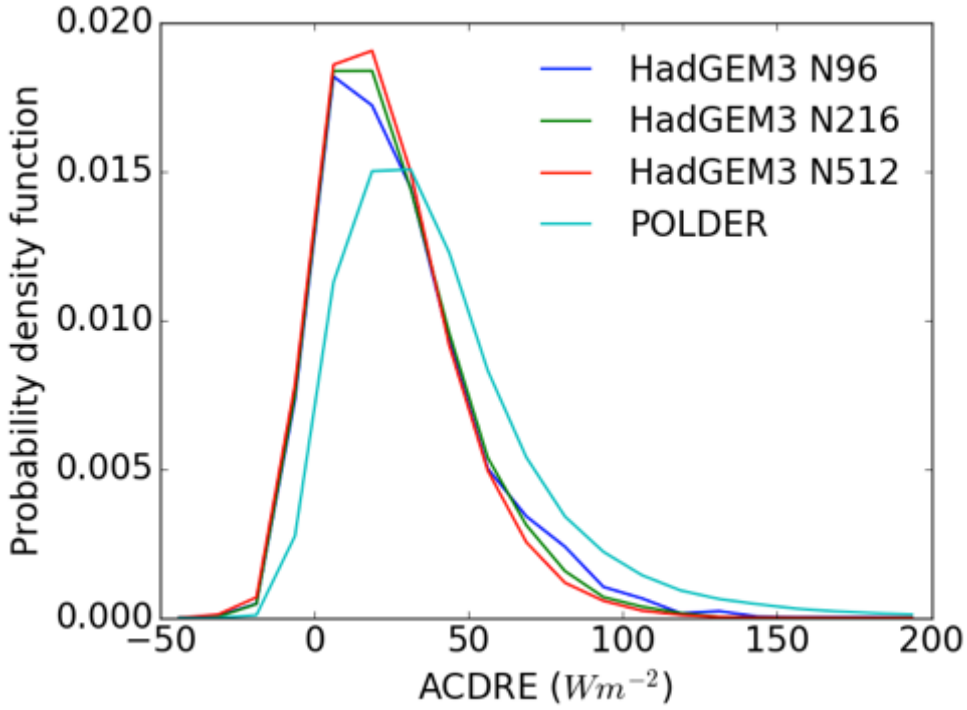

Figure 5.18: *Probability density functions of the above cloud direct radiative effect (ACDRE) for HadGEM3 model simulations and POLDER observations using the same data as Figure 5.17.*

In terms of spatial correlation, the model simulations appear to represent the key features of the POLDER observations, with a zonal band of high ACDRE along ~10°S reaching a maximum near to the coast and decreasing to the north and south. The model significantly underestimates the mean ACDRE compared to POLDER observations, by 38 to 46 %, dependent on model spatial resolution. The range of model ACDRE values is narrower and systematically lower than the POLDER observations. The mean modelled ACDRE is lower for higher model spatial resolution, which decreases from 25.2 to 21.8 W m^{-2} for the N96 compared to N512 simulation, respectively. This result is consistent with the findings in section 5.4.3 using SOCRATES and POLDER. The range of ACDRE values is almost identical for all model resolutions, as shown in Figure 5.18, although one could tenuously conclude that the higher resolution model simulations are associated with a narrower range of ACDRE values.

This result provides evidence against the argument presented in section 5.1, which reasoned that the low bias in modelled ACDRE in de Graaf *et al.* (2014) could be caused by overlooking sub-grid variability of the aerosol and cloud properties. Effectively, the AOD and COD values in climate models are heavily spatially averaged, which may lead to a loss of extreme DRE values due to the non-linear dependence of the DRE on AOD and COD, as shown in Figure 5.7. Hence one would expect a higher resolution climate model to lead to a larger mean and range of DRE values, when in fact only a tenuous dependence is observed (Figure 5.18). To investigate the cause of this apparent discrepancy, I will examine how the simulated cloud and aerosol optical properties vary with model resolution.

5.4.4.3 COD, ACAOD and aerosol ACSSA

The COD, ACAOD and ACSSA are the variables controlling the magnitude and sign of the ACDRE (see Chapter 1.3). Hence I now examine how each of these variables differs between the three HadGEM3 model simulations to understand which is the dominant driver of the ACDRE dependence on model resolution shown in Figures 5.17 and 5.18.

Figure 5.19 shows how the modelled COD varies with model resolution. The COD spatial distribution is more homogeneous and is characterised by lower

values in the model simulations than POLDER observations. The model simulations miss the zonal band of cloud at latitude ~10°S and the characteristic semi-permanent stratocumulus cloud deck often observed during August and September in this domain (e.g. Adebiyi *et al.*, 2015). The mean COD is lower, and the range of COD values significantly narrower, in the model compared to POLDER observations, irrespective of model resolution; see Figures 5.19 and 5.20, respectively. There appears to be no trend between COD and model resolution, as the mean COD is highest for model resolution N216 and lowest for N512. Figure 5.20 confirms this hypothesis, showing that the range of COD values is almost identical for all model resolutions. This result is surprising as one might expect a relatively inhomogeneous COD distribution in the higher model resolution simulation compared to the lower resolution, as evidenced over a small area in the northwest corners of the model domains in Figure 5.19. As the model COD values depend weakly and approximately invariantly on model resolution, COD likely does not govern the dependence of ACDRE to resolution highlighted in Figure 5.17.

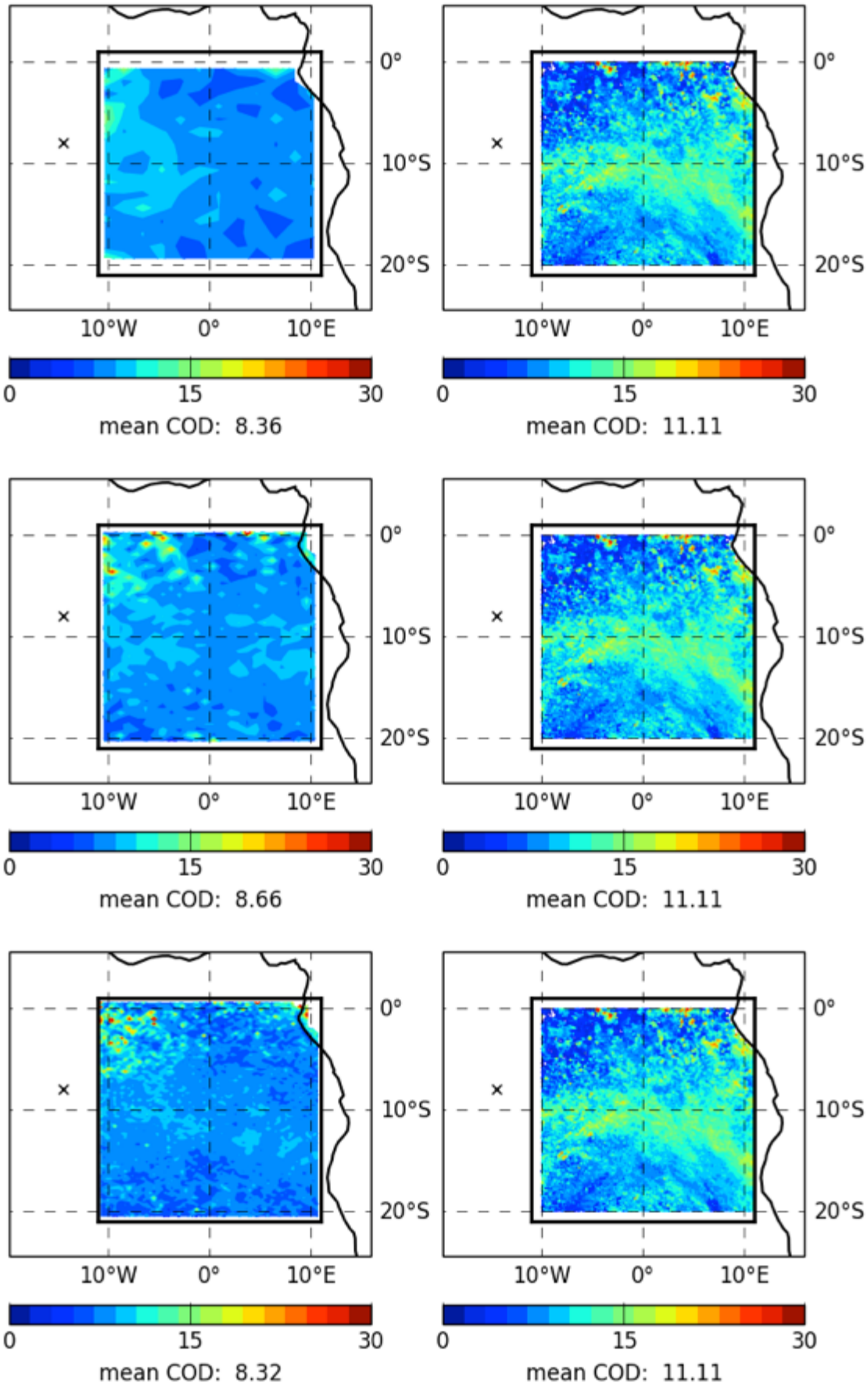

Figure 5.19: *The total cloud optical depth (COD) over the Southeast Atlantic Ocean. HadGEM3 model simulations are on the left and POLDER satellite observations on the right. These represent the two-month means (August and*

September) in 2006. The HadGEM3 model data were filtered according to Table 5.5 and the POLDER data were filtered according to section 5.4.2. The top, middle and bottom HadGEM3 plots correspond to the N96, N216 and N512 resolution simulations, respectively. The black crosses represent Ascension Island.

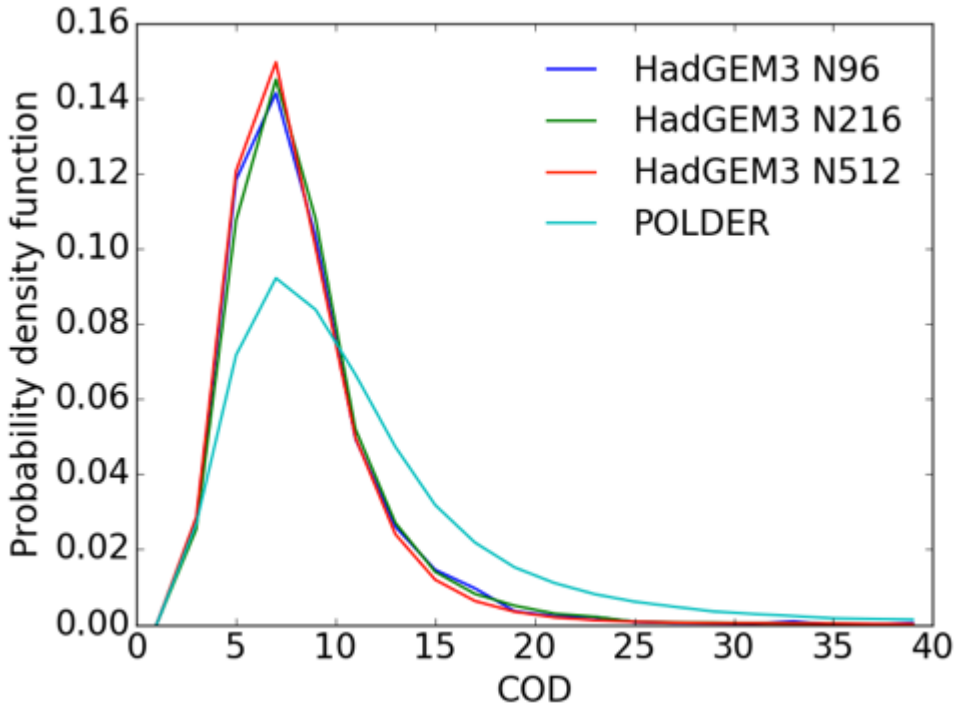

Figure 5.20: *Probability density functions of the total cloud optical depth (COD) for HadGEM3 model simulations and POLDER observations using the same data as Figure 5.19.*

To evaluate the above cloud aerosol optical depth (ACAOD) and the above cloud single scattering albedo (ACSSA), the cloud top heights needed to be determined. The ACAOD and ACSSA were determined by implementing an algorithm that searched for cloud liquid water content (LWC) above a pre-set threshold, starting at a predetermined altitude and moving towards the ocean surface. To inform the choice of the threshold cloud LWC at which a cloud top height was defined as well as the height at which to start the algorithm, the cloud LWCs were evaluated for all model points, shown in Figure 5.21.

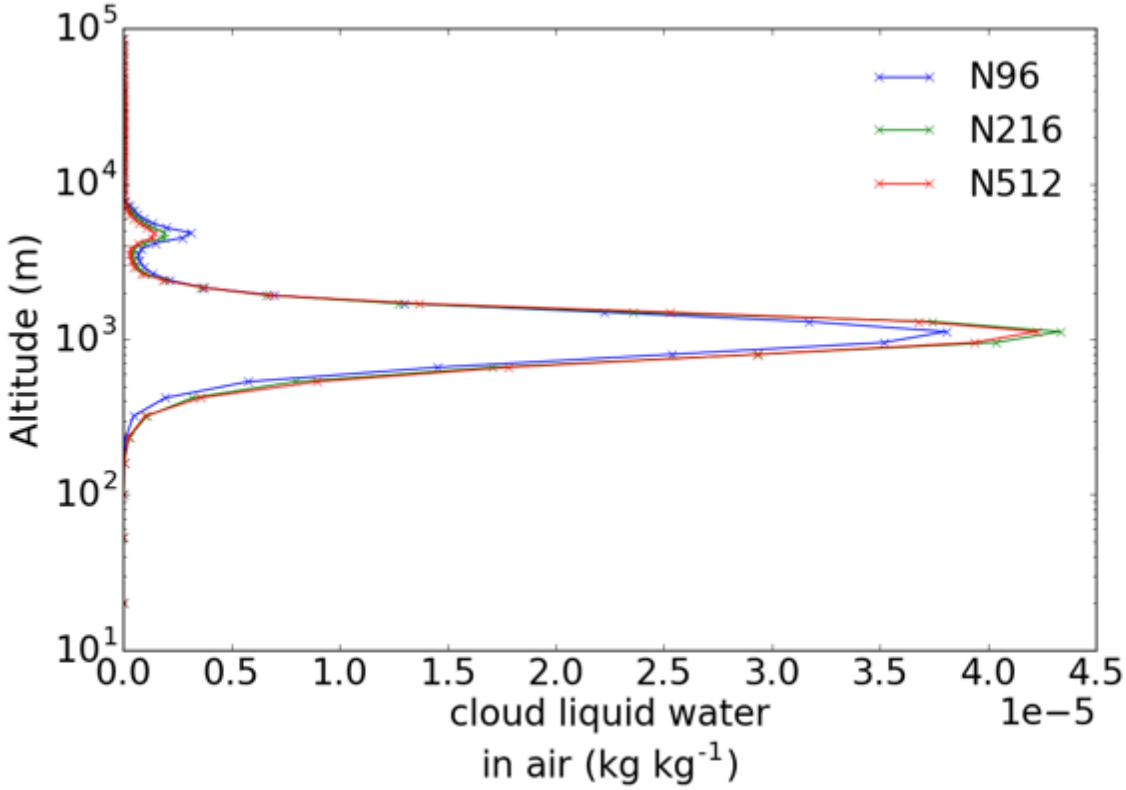

Figure 5.21: *Mean cloud liquid water content as a function of altitude. Each point represents the average over all model latitudes and longitudes and for all model times in August and September 2006.*

The cloud top height search algorithm started at an altitude of 3500 m to avoid contamination by mid level cloud at ~5 km, as shown in Figure 5.21. Cloud top heights were defined for each model grid point upon reaching a cloud LWC greater than a pre-set threshold. Initially, a cloud LWC threshold of 5×10^{-5} kg kg^{-1} was chosen. The ACAOD values were then determined by integrating the extinction coefficients as a function of altitude above the cloud tops. The ACSSA values were determined using a similar method, by dividing the integrated scattering coefficients by the integrated extinction coefficients above the cloud tops. This process was repeated for cloud LWC thresholds between 5×10^{-5} kg kg^{-1} and 1×10^{-6} kg kg^{-1} to investigate the sensitivity of the ACAOD and ACSSA to cloud top height values derived using the previously described algorithm. The ACAOD and ACSSA converge as the cloud top height LWC threshold decreases (see appendix C) and are almost identical for cloud top heights derived using cloud liquid water contents 1×10^{-5} to 1×10^{-6} kg kg^{-1}. If a too-high cloud LWC threshold was chosen, the algorithm would penetrate more deeply into the cloud, effectively lowering the cloud top height and include hydrated aerosol, which would lead to higher ACAOD and ACSSA values. On

the other hand, if the cloud LWC threshold is too low, one risks falsely identifying cloud tops, leadings to ACAOD values that are too low. A cloud LWC threshold value of 1×10^{-5} kg kg^{-1} was chosen, which avoids the inclusion of hydrated aerosol and avoids the risk of false cloud top identifications; this is because it is the largest cloud LWC threshold that leads to convergence in aerosol optical properties (see appendix C). For the remainder of this analysis, the ACAOD and ACSSA values corresponding to the cloud top heights defined using a cloud LWC 1×10^{-5} kg kg^{-1} will be used.

The model ACAOD at 550 nm partially captures the spatial distribution of ACAOD observed using POLDER, which is characterised by higher ACAOD near to the coast, as shown in Figure 5.22. The mean model ACAOD is underestimated significantly compared to POLDER observations, by 39 %, and the range of model ACAOD values systematically lower than the POLDER observations, as shown in Figure 5.23. The modelled mean and range of ACAOD values is invariant to model resolution, although one could argue that the range of ACAOD values is greater in the N96 simulation than in the N512 simulation, but this is tenuous. A reason underpinning the insensitivity of the modelled mean ACAOD to resolution may be related to the emissions inventory, which emitted the same mass of BBA to the atmosphere, irrespective of the model or emissions inventory resolution. A reason for the apparent insensitivity of the ACAOD spatial distribution to model resolution, as shown in Figure 5.22, could be related to the location of BBA emissions. BBA was emitted to the atmosphere predominantly over the African continent, which was subsequently lofted and advected over the Southeast Atlantic Ocean. During this time, the aerosols diffused and may have been better characterised as a homogeneous background haze that vary over spatial scales larger than the N96 grid cell box, rather than well defined plumes with areas of high and low AOD as might be expected close to emission.

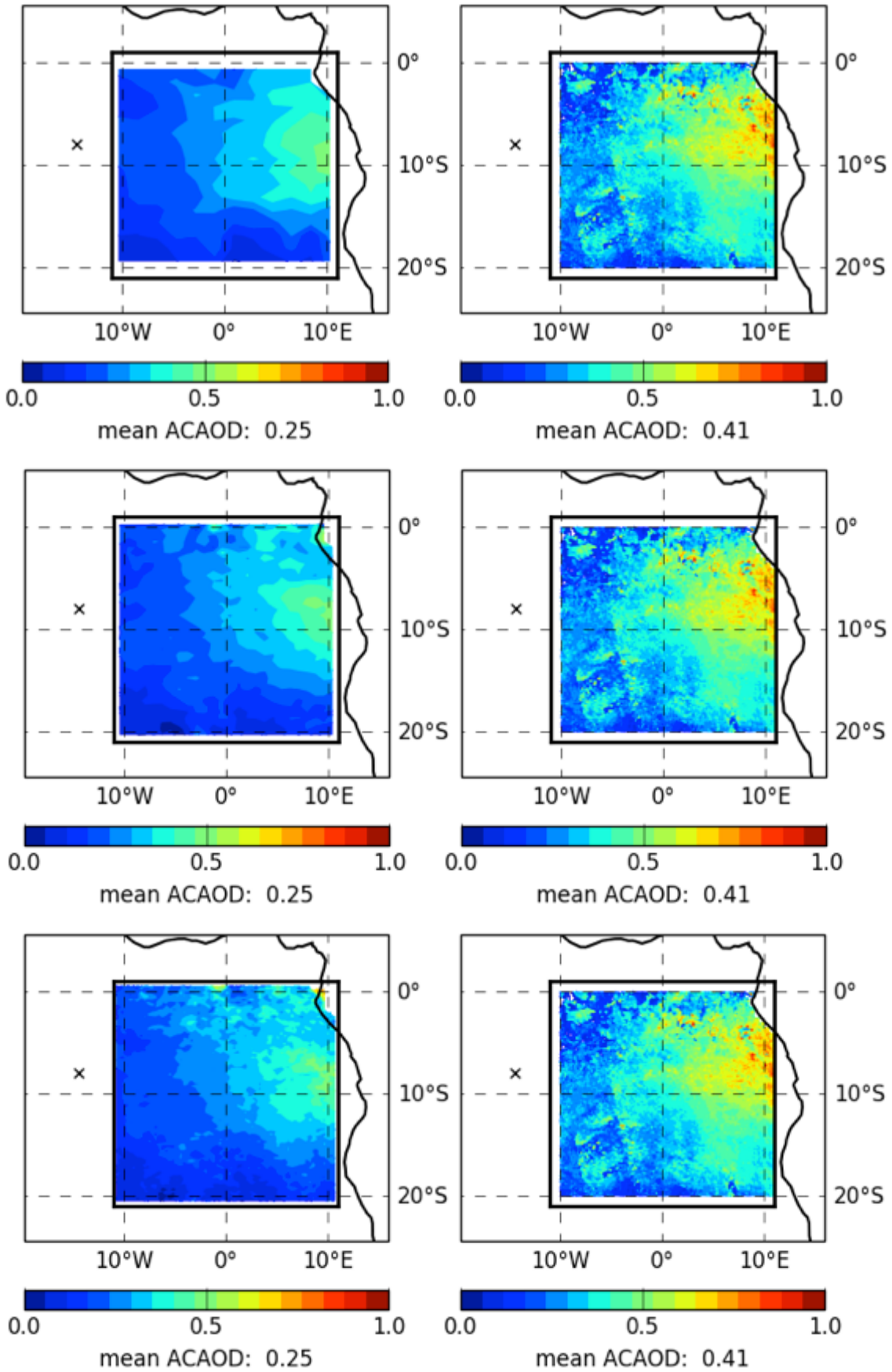

Figure 5.22: *Mean above cloud aerosol optical depth (ACAOD) at 550 nm for August and September 2006. HadGEM3 model simulations are on the left, which were filtered according to Table 5.5. POLDER retrievals are on the right.*

The cloud top height diagnostic started at an altitude of 3500 m above ground level with a cloud liquid water content threshold of 1×10^{-5} kg kg^{-1}. The top, middle and bottom HadGEM3 plots correspond to the N96, N216 and N512 resolution simulations, respectively. The black crosses represent Ascension Island.

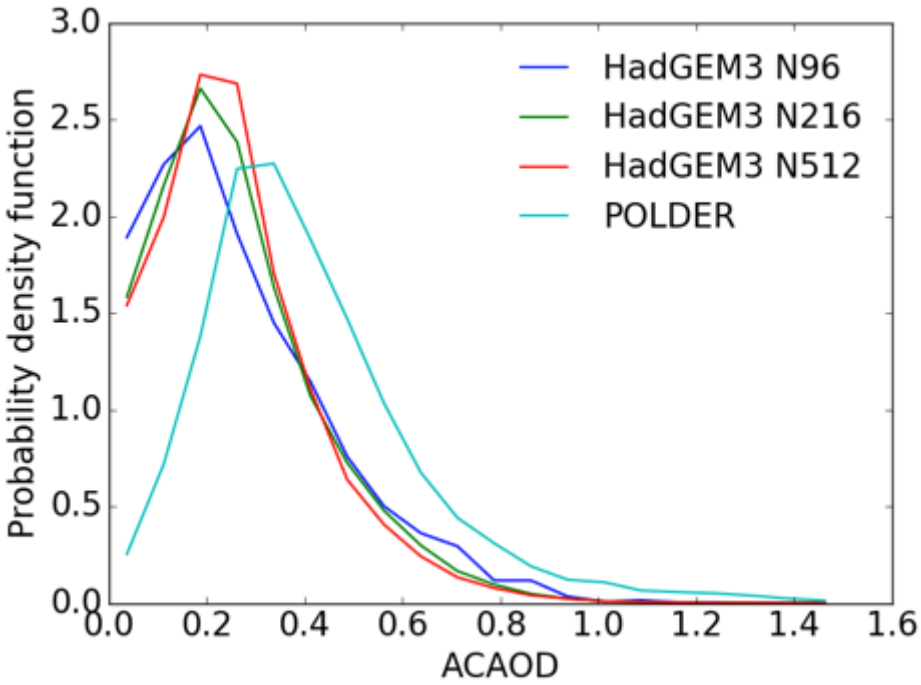

Figure 5.23: *Probability density functions of the above cloud aerosol optical depth (ACAOD) at 550 nm for HadGEM3 model simulations and POLDER observations using the same data as Figure 5.22.*

Similarly, the model ACSSA at 550 nm partially captures the POLDER observations such that the most absorbing aerosols are located near to the coast, between ~10°S to 20°S, there is a band of constant ACSSA along latitude band 10°S, and there are less absorbing aerosols to the north and south; see Figure 5.24. The modelled ACSSA is significantly lower (~6 %) in the model simulations compared to POLDER observations, which is shown clearly by the range of ACSSA values in Figure 5.25. The mean ACSSA is only weakly dependent on model resolution, which increases from 0.80 to 0.81 between the N96 and N216 simulations. The range of ACSSA values is smaller in the N96 compared to the N216 and N512 simulations, shown in Figure 5.25, although this is tenuous. A lower ACSSA should lead to a higher ACDRE in the model simulations compared to the satellite observations, which suggests that other factors counteract this effect and control the dependence in modelled ACDRE with model resolution.

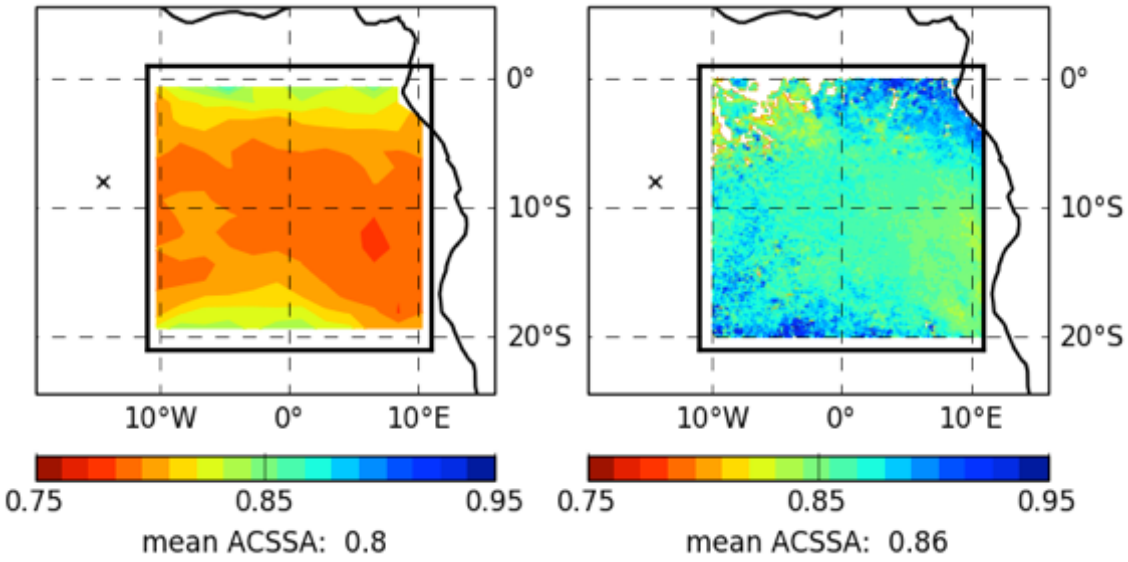
0°
10°S
20°S
10°W
0°
10°E
0.75
0.85
0.95
mean ACSSA: 0.8
0°
10°S
20°S
10°W
0°
10°E
0.75
0.85
0.95
mean ACSSA: 0.86

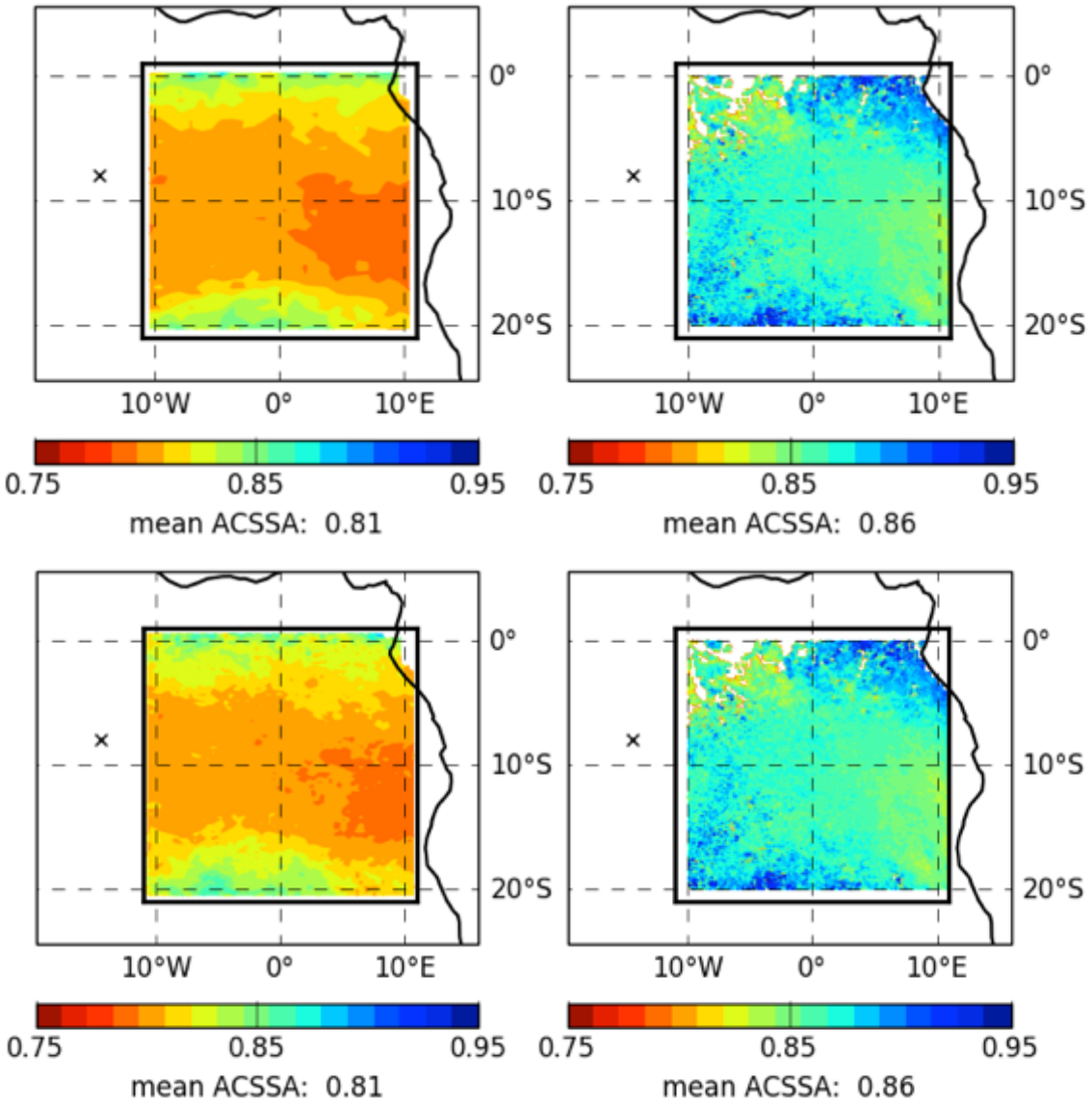

Figure 5.24: *Mean above cloud aerosol single scattering albedo (ACSSA) at 550 nm for August and September 2006. HadGEM3 model simulations are on the left, which were filtered according to Table 5.5. POLDER retrievals are on the right. The cloud top height diagnostic started at an altitude of 3500 m above ground level with a cloud liquid water content threshold of 1×10^{-5} kg kg^{-1}. The top, middle and bottom HadGEM3 plots correspond to the N96, N216 and N512 resolution simulations, respectively. The black crosses represent Ascension Island.*

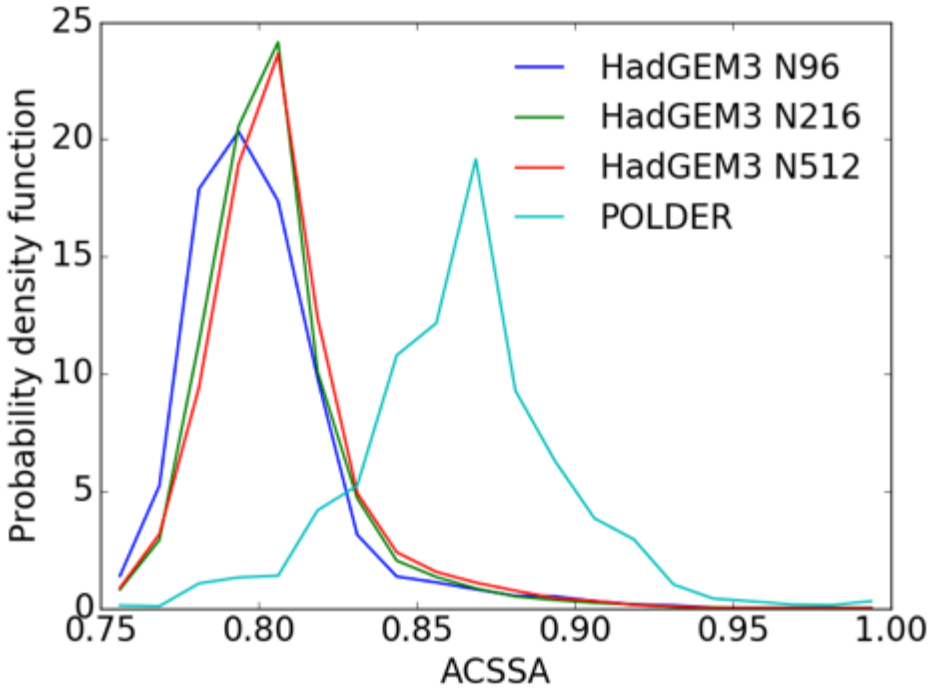

Figure 5.25: *Probability density functions of the aerosol above cloud single scattering albedo (ACSSA) at 550 nm for HadGEM3 model simulations and POLDER observations using the same data as Figure 5.24.*

It follows that the significant underestimation of large ACDRE values seen in HadGEM3 compared to POLDER observations is caused by too low ACAOD and COD values. However, as the COD does not change systematically with model resolution, the decrease in the mean HadGEM3 ACDRE as model resolution increases is likely related to a combination of the small changes in the ranges of ACAOD and ACSSA values, as shown in Figures 5.23 and 5.25. I confirmed that the COD and ACAOD are independent, which may impact the AOD due to aerosol entrainment into clouds or impact the COD via the semi-indirect effect (e.g. Ten Hoeve *et al.*, 2012), although it in unclear how these effects would vary with model resolution.

5.5 Conclusions

In this chapter, I described briefly the equations used within an offline radiative transfer code (SOCRATES), which was used to evaluate the sensitivity of the DRE to aerosol and cloud optical properties and subsequently how the ACDRE depends on the spatial variability of AOD and COD.

The first key result of this chapter was the impact that biases in traditional filter-based absorption measurements can have on the DRE due to uncertainties in aerosol SSA and AAE based on TAP measurements compared to PAS

measurements. If the aerosol optical properties were tuned to match the SSA derived using TAP rather than PAS measurements, the DRE could be overestimated by 17.5 to 33.9 W m^{-2}, dependent on the TAP correction scheme applied. The largest absolute biases in the DRE were associated with aerosols overlying thick clouds (COD=10). Similarly, tuning aerosol optical properties to match the AAE determined using TAP rather than PAS measurements led to DRE values that were biased high by up to 9.2 W m^{-2} and biased low by up to 34.6 W m^{-2} when overlying thick clouds (COD=10). This asymmetric uncertainty range was caused by modification to the wavelength dependence of the aerosol absorption (see Figure 5.9). This result highlights the large uncertainties that may be introduced into climate models if aerosol properties are derived from traditional filter-based absorption measurements compared to accurate PAS measurements. However, it should be highlighted that representative sampling capturing the variability of aerosol properties is equally important as the accuracy of the aerosol properties.

Secondly, I aimed to assess the dependence of the ACDRE on the spatial variability of aerosol and cloud optical properties, which was not obvious due to the non-linear dependence of the DRE on AOD and COD. To assess this dependence, offline radiative transfer simulations were run using an aerosol model based on SAFARI-2000 biomass burning aerosol measurements over the Southeast Atlantic Ocean. Model AOD and COD values were constrained using the POLDER satellite instrument, which retrieved the AOD and COD over a similar domain during August and September 2006. The impact on the ACDRE to spatial variability of the AOD and COD was evaluated over a range of scales. The extreme in spatial averaging used a single value for AOD and COD over the Southeast Atlantic Ocean domain, which led to an ACDRE of 21.5 W m^{-2}. At the other extreme, ACDRE was determined on a pixel-by-pixel basis, which led to a mean ACDRE of 17.7 W m^{-2}. A range of intermediate cases were evaluated that varied the degree of spatial averaging between 0.05° to 3.0° latitude/longitude. This result confirmed that the mean ACDRE was only weakly dependent on the spatial variability of the AOD and COD fields. However, the very strong radiative forcings that were observed in POLDER were simply not present when spatial averaging was applied with resolutions typical of a climate model. Hence comparisons of extreme values in

observations against climate model results were somewhat irrelevant. This analysis was limited by the resolution of the lookup table used to determine the DRE for each AOD-COD pair.

Lastly, a global climate model (HadGEM3) was run at three spatial resolutions to investigate how the ACDRE depends on model resolution. The key finding was that the ACDRE becomes smaller as the model resolution increases, in line with the previous result using SOCRATES and POLDER. To understand this result, the COD, ACAOD and ACSSA were examined. COD was invariant to model spatial resolution, which is surprising as one might expect a relatively inhomogeneous COD distribution in the higher compared to lower model resolution. The characteristic stratocumulus cloud deck associated with this region was also missing. ACAOD and ACSSA were derived by integrating aerosol optical properties above the cloud tops, which were defined using a cloud top height search algorithm that searched for cloud liquid water content above a pre-determined threshold. The mean ACAOD was invariant to model resolution, which can be explained due to the constant BBA mass emitted to the atmosphere. The insensitivity of the ACAOD spatial distribution to model resolution can be explained as BBA is predominantly emitted over the African continent, which has time to diffuse as it is advected over the Southeast Atlantic Ocean, leading to a homogeneous aerosol haze as opposed to well defined plumes. The ACSSA was also only weakly dependent on model resolution. The ACAOD and ACSSA were likely responsible for the ACDRE dependence to model resolution. The HadGEM3 models significantly underestimated both the ACAOD and COD, which resulted in a systematic discrepancy with the satellite observations. Two key areas for future research are (i) to investigate why the modelled spatial cloud fields differ significantly compared to the satellite observations and (ii) to investigate why the modelled atmospheric aerosol loadings are significantly lower compared to the POLDER satellite observations. To address the latter, the impact on the modelled ACDRE due to using daily rather than monthly emissions inventories should be examined.

Throughout this chapter, I would have ideally used the optical and physical properties of aged BBA based on the CLARIFY-2017 measurement campaign over the Southeast Atlantic Ocean in my SOCRATES simulations. Using

CLARIFY-2017 data would have made use of the accurate and up-to-date EXSCALABAR optical coefficient measurements. However, using this data would have required a radiative closure study to be performed, using aerosol size distribution measurements, optical coefficient measurements and radiation measurements to iteratively vary the real and imaginary parts of the BBA refractive index until all measurements agree most closely, which is the subject of on-going research.

6 Summary and future work

Table of contents

6.1 Overview

In this Chapter, I reiterate the importance of and provide a brief justification for the study of aerosol optical properties within Earth's atmosphere. The aims of this thesis are restated and a summary of the main results presented. This chapter concludes with a discussion of the limitations of the various analyses and suggestions for routes for extension.

6.2 Motivation and aims

Aerosol-radiation interactions are estimated to contribute a global mean effective radiative forcing of −0.45 (−0.95 to +0.05) W m^{-2}, offsetting a potentially significant but poorly constrained fraction of the positive effective radiative forcing associated with greenhouse gases (2.26 to 3.40) W m^{-2} (Myhre *et al.*, 2013a). One of the major factors governing the uncertainty in estimates of aerosol direct radiative forcing is the poorly constrained aerosol single scattering albedo (SSA). Accurate determination of aerosol SSA is limited by uncertainties in aerosol absorption estimates, which could potentially be underestimated by up to a factor of two in global climate models (Stier *et al.*, 2007; Shindell *et al.*, 2013).

The three main types of absorbing aerosols are black carbon, brown carbon, and mineral dust (Myhre *et al.*, 2013a). Aerosol absorption is dominated by black carbon, which may exert the next largest positive radiative forcing after carbon dioxide (Stocker *et al.*, 2013). Climate models generally only crudely represent the optical properties of black and brown carbon and how these evolve with time. Stronger observational constraints are required to assess the

attribution of absorption and reduce uncertainty in estimates of direct radiative forcing (e.g. Alexander *et al*., 2008; Bond *et al*., 2013; Liu *et al*., 2014; Myhre *et al*., 2013b; Saleh *et al*., 2014; Wang *et al*., 2018).

The aims of my PhD were therefore to:

1. Develop a state-of-the-art instrument for the measurement of aerosol optical properties.
2. To evaluate biases in traditional filter-based absorption measurements for a range of aerosol sources.
3. Evaluate the sensitivity of the direct radiative effect to aerosol and cloud optical properties and their spatial variability.

6.3 Thesis summary, limitations and directions for future research

In this section, I will provide an overview and highlight the key results of each chapter from this thesis, including key limitations and uncertainties corresponding to each analysis. I will then suggest potential directions for future research including areas of on-going research.

6.3.1 EXtinction, SCattering and Absorption of Light for AirBorne Aerosol Research (EXSCALABAR)

In Chapter 2, I described a new instrument used for the measurement of aerosol optical and physical properties including absorption determined using photoacoustic spectroscopy (PAS) and filter-based absorption photometry using a Tricolor Absorption Photometer (TAP), extinction coefficients determined using cavity ring-down spectroscopy (CRDS) and size distributions using a Passive Cavity Aerosol Spectrometer Probe (PCASP). Optical properties were determined at three fixed wavelengths in the range 405 to 658 nm. Using thermally denuded PAS channels enabled evaluation of the enhanced absorption due to the lensing effect. CRDS measurements at elevated relative humidity 70 % and 90 % enabled evaluation of the dependence of aerosol extinction coefficients on hygroscopic growth.

An initial instrument characterisation was performed assessing the minimum sensitivities of the suite of instruments. The minimum sensitivities of the PAS, CRDS and TAP when recording data at 1 Hz were in the range 0.05–0.33 Mm^{-1}, 0.01–0.04 Mm^{-1} and 18.54–34.78 Mm^{-1}, respectively. These changed to

0.01–0.06 Mm^{-1}, 0.02–0.05 Mm^{-1} and 0.71–1.37 Mm^{-1} for the PAS, CRDS and TAP for a 30 second averaging time.

Airborne PAS measurements were subject to uncertainty due to the need to subtract background noise measurements from the aerosol measurements, which varied as a function of pressure. The uncertainty associated with this background noise correction was estimated as 0.2, 2.0 and 20.5 % at absorption coefficients 100, 10 and 1 Mm^{-1}, respectively. PAS measurements were subject to additional uncertainty due to the calibration accuracy, which is discussed in the next subsection.

An area of on-going research is related to improving the PAS cell design to minimise the measurement sensitivity to background window-generated acoustic noise caused by laser heating of the optical windows. The benefits of this design would be twofold: the background noise correction and its associated uncertainty would be eliminated and the minimum sensitivity of PAS absorption measurements could be improved by an order of magnitude.

6.3.2 Photoacoustic spectrometer ozone calibration accuracy

In Chapter 3, I assessed the accuracy of the PAS ozone calibration procedure by comparing the PAS-measured absorption cross sections to model calculations using laboratory-generated aerosol. This work was motivated in part as Bluvshtein *et al.* (2017) suggested that calibrating PAS cells using ozone may lead to biases in absorption measurements of up to 100 %. The second motivation for this study was to validate the accuracy of the PAS and CRDS absorption and extinction measurements under laboratory conditions.

To achieve these aims, nigrosin aerosol was generated from solution, mobility-size selected using a differential mobility analyser and passed to the PAS and CRDS cells for sampling, which allowed the PAS- and CRDS-measured absorption and extinction cross sections to be compared to model calculations.

The key result of this experiment was the verification that ozone calibrations can be used to calibrate photoacoustic spectrometers accurately. It was found that the PAS-measured ensemble absorption cross sections compared to model calculations to within 7 to 9 %, dependent on the measurement

wavelength. The CRDS-measured extinction cross sections were found to agree with model calculations to within 0 to 4 %, dependent on the measurement wavelength. This result clearly demonstrates that ozone calibrations are suitable for PAS and that EXSCALABAR PAS and CRDS measurements are accurate to better than 9 % for ground-based measurements.

Since this study, Fischer and Smith (2018) performed additional experiments examining the differences between the findings presented in Chapter 3 and those in Bluvshtein *et al.* (2017). Their results suggest that a small correction (~ 10 %) needs to be applied to EXSCALABAR PAS measurements to account for non-thermal relaxation pathways due to the EXSCALABAR PAS calibration procedure using air rather than pure oxygen. Research is on-going examining how the PAS cell gas composition affects the sensitivity of ozone calibrations. Although a 10 % correction for calibration bias would improve the agreement to modelled calculations, to within 1–3 %, initial results suggest that there is no systematic calibration bias, in contrast to the Fischer and Smith (2018) study.

6.3.3 Biases in filter-based absorption measurements

In Chapter 4, I examined biases in filter-based absorption measurements using a commercially available Tricolor Absorption Photometer (TAP, Brechtel) by comparison to PAS absorption measurements. A key strength of this study was that the aerosol-laden stream sampled by the TAP, PAS and CRDS instruments shared a common inlet and was subject to the same flow conditioning. Biases in TAP absorption measurements were investigated at the wavelengths 467, 528 and 652 nm for urban, fresh biomass burning aerosol (BBA) and aged BBA emissions. The Bond *et al.* (1999), Virkkula (2010) and Müller *et al.* (2014) correction schemes were applied to TAP measurements, which aimed to minimise measurement biases.

The largest biases were associated with urban aerosol emissions, which had mean biases of up to 45 %. The Müller *et al.* (2014) correction scheme consistently reduced biases most significantly across all aerosol sources and measurement wavelengths, to within −1 to 17 % of PAS absorption measurements. The impact of TAP measurement biases on the single scattering albedo (SSA) and absorption Ångström exponent (AAE) was also

evaluated. The SSA was found to be biased low by up to 0.07 and the AAE in error by ± 0.54. The AAE varied strongly with aerosol source type and with the correction scheme applied to TAP measurements; this is a key climate-relevant parameter and the reasons driving its diversity should be the subject of future research. A simple method for the attribution of absorption to black and brown carbon found that the fraction of light attributed to brown carbon could be in error by up to 17 % due to uncertainties in the TAP-derived aerosol AAE.

The key conclusion from this analysis is that biases are strongly source dependent and caution should be exercised when extrapolating results more widely to other aerosol types.

6.3.4 Investigating the sensitivity of the direct radiative effect

In Chapter 5, I initially assessed the sensitivity of the direct radiative effect (DRE) to the aerosol SSA and AAE and subsequently the impact on the DRE that could arise from developing an aerosol model based on TAP absorption measurements compared to PAS measurements. The DRE may be uncertain by up to 33.9 W m^{-2} if aerosol optical properties were based on TAP compared to PAS measurements of aerosol SSA. Similarly, the DRE may be uncertain by up to 34.6 W m^{-2} if aerosol optical properties were based on TAP compared to PAS measurements of the aerosol AAE. These uncertainties correspond to an aerosol layer (AOD=0.5) overlying thick cloud (COD=10). This result highlights the value of PAS compared to traditional filter-based absorption measurements. However, it should be noted that representative sampling of aerosol is equally important as the measurement accuracy for constraining aerosol optical properties within global climate models. This analysis was limited in that the aerosol optical and microphysical properties were based on SAFARI-2000 rather than CLARIFY-2017 measurements; the latter includes state-of-the-art EXSCALABAR measurements. This limitation was due to time constraints preventing the processing of the CLARIFY-2017 dataset to obtain self-consistent aerosol refractive indices using in-situ optical coefficient measurements, size distribution measurements and radiation measurements within a radiative closure experiment framework.

In Chapter 5, I then assessed the sensitivity of the DRE to aerosol and cloud optical properties and their spatial variability. Offline radiative transfer

simulations were performed using SOCRATES assessing how the DRE changes with both aerosol optical depth (AOD) and cloud optical depth (COD) for BBA. A significant finding was that the DRE depends on the AOD and COD in a non-linear way and is most sensitive to AOD when BBA overlies thick cloud and most sensitive to COD when an optically thick aerosol layer overlies thin cloud. It should be noted that the former is associated with positive DRE and large absolute changes in DRE whilst the latter changes from negative to positive DRE and has large percentage changes in DRE.

Due to this non-linear dependence, it was unclear how the spatial variability of the AOD and COD fields would affect the DRE. To examine this sensitivity, two extreme cases were assessed: (i) the DRE was evaluated corresponding to a single AOD and single COD, taken as the mean of the POLDER observations during August and September 2006 over a domain within the Southeast Atlantic Ocean and (ii) the DRE was evaluated corresponding to each POLDER-observed AOD-COD pair on a pixel-by-pixel basis and the mean DRE value calculated. All AOD-COD pairs were located within a predetermined lookup table of DRE values generated using SOCRATES. The former resulted in a DRE of 21.5 W m^{-2} and the latter 17.7 W m^{-2}. To see whether there was a trend in the DRE as a function of the degree of spatial averaging, POLDER observations of AOD and COD measured over the Southeast Atlantic Ocean during August and September 2006 were averaged over a range spatial scales between 0.05° to 3.0° latitude/longitude. The mean DRE was insensitive to the spatial variability of the AOD and COD over the spatial of scales investigated, limited by the resolution of the predetermined DRE lookup tables. Even upon a small degree of spatial averaging, the range of DRE values was significantly reduced compared to satellite observations (de Graaf *et al.*, 2014; Peers *et al.*, 2015).

Next, a global climate model (HadGEM3) was run at three spatial resolutions, N96 (1.875° × 1.25° or ~135 km), N216 (0.83° × 0.56° or ~60 km) and N512 (0.35° × 0.234° or ~25 km). The key finding from this analysis was that the above cloud direct radiative effect (ACDRE) was only weakly dependent on model spatial resolution, which decreased with increasing model resolution, consistent with the previous result using SOCRATES and POLDER. The mean

ACDRE values for the N96, N216 and N512 simulations were 25.2, 22.8 and 21.8 W m^{-2}, respectively. The above cloud aerosol optical depth (ACAOD) and above cloud single scattering albedo (ACSSA) were found to be the factors controlling the dependence of ACDRE to model resolution. This result is surprising, as one would expect a larger mean and range of ACDRE values for a more highly resolved model due to higher inhomogeneity in AOD and COD values, i.e. before significant spatial averaging. The insensitivity of ACAOD was postulated to be related to the long-range transport from aerosol emission from the African continent to subsequent detection over the Southeast Atlantic Ocean. Due to the large distances between aerosol emission and detection, spatial variability in ACAOD may have been over distances typically greater than ~100 km (i.e. the coarsest model resolution grid box). It is unclear why the modelled spatial COD differed significantly compared to the satellite observations and why higher HadGEM3 model resolution led to similar ranges of COD values, which should be the subject of future research. Another key future research area should be an investigation into why the modelled atmospheric aerosol loadings are significantly lower compared to the POLDER satellite observations and whether using daily rather than monthly aerosol emissions inventories improves this discrepancy.

6.4 The future of aerosol research

Relevant to the absorbing aerosol focus in this thesis, Samset *et al.* (2018) reiterated that there is significant uncertainty and much research required to characterise the impact of absorbing aerosol on radiative forcing and on the climate system. Key areas that Samset *et al.* (2018) recommended to improve constraints on aerosol absorption in the short-term included (i) greater dialogue between observational and modelling communities, (ii) consistent use of black carbon terminology to differentiate between fresh/collapsed and young/old aerosols and (iii) rigorous account of brown carbon within observations and climate models. In the longer-term, recommendations included (i) an improvement of aerosol microphysical properties within climate models, (ii) improve satellite remote sensing of absorbing aerosols including retrievals above cloud and (iii) constraining black carbon emissions, transport, aging and geographical and vertical distributions.

More generally and as alluded to previously, the accuracy of aerosol measurements compared to the spatial and temporal representativeness of those measurements is of key importance if we are to reduce the uncertainty associated with aerosol radiative forcing. Whilst in-situ measurements are essential for constraining satellite observations, and potentially climate model simulations, they can only ever represent a snapshot in time and space. Global climate models typically have grid spacing in the range ~100 to 500 km (Myhre *et al.*, 2013b), satellite retrievals typically have pixel widths in the range 3 to 10 km (e.g. Remer *et al.*, 2013; Peers *et al.*, 2015), and in-situ measurements can be highly variable over distances of metres, with each air mass sampled containing an ensemble of aerosol types, sizes, mixing states and shapes. Although the climate model grid cell average aerosol properties do not represent the range of aerosol properties observed using satellite or in-situ observations, it raises the question: do the grid cell average aerosol properties lead to the same radiative forcing compared to the mean effect due to the more variable sub-grid scale properties?

Schutgens *et al.* (2016) went some way to answering this question, who investigated the strength of sampling errors, which result if high resolution observations are used to constrain relatively coarse global climate model simulations. A key finding of this study was that discrepancies in aerosol properties such as AOD or aerosol number concentrations could be up to 160 %, if observations with resolution 10 km are used to constrain global climate models with resolution 200 km. One obvious way to reduce this discrepancy is to increase climate model resolution, although Schutgens *et al.* (2016) suggested that this would need to be of the order ~50 km before there is any significant reduction in sampling errors, and ultimately would need to be at a higher resolution than the observations to eliminate sampling errors completely.

The future of aerosol research may ultimately depend on the climate change trajectory that we end up following. Under RCP8.5, the relatively small impact that aerosols would have on climate forcing would be dwarfed by the impact of greenhouse gas warming. In this case, aerosol research may focus on evaluating geo-engineering scenarios such as solar radiation management, including, for example, stratospheric aerosol injection (Stocker *et al.*, 2013).

Stratospheric aerosol injection would be an extreme response to counteract global warming induced by greenhouse gases, which has numerous potential shortcomings and harmful side effects.

Aerosols also degrade air quality and are a major factor in human health, which damage the respiratory and cardiovascular systems and are responsible for an estimated 4.2 million deaths per year globally, the fifth highest morbidity factor is 2015 (Cohen *et al.*, 2017). Although mortality due to long-term exposure to aerosols fell during 1990 to 2015 in high-income countries, the total deaths increased globally, highlighting the substantial public health challenge. Although the current safe annual mean level of particulate matter exposure with aerodynamic diameter < 2.5 μm is 10 μg m^{-3} (World Health Organization, 2006), this is often significantly higher, particularly for those living in developing countries or large cities (e.g. van Donkelaar *et al.*, 2015). Continual measurement of atmospheric aerosol concentrations, composition and size are essential in aiding epidemiological studies for assessing the impact of aerosol pollution, which ultimately guide policies to reduce these harmful pollutants (Kim *et al.*, 2015).

References

Abel, S. J. *et al.* (2003) 'Evolution of biomass burning aerosol properties from an agricultural fire in southern Africa', *Geophysical Research Letters*, 30(15), p. 1783. doi: 10.1029/2003GL017342.

Adachi, K., Chung, S. H. and Buseck, P. R. (2010) 'Shapes of soot aerosol particles and implications for their effects on climate', *Journal of Geophysical Research*, 115(D15), pp. 1–9. doi: 10.1029/2009JD012868.

Adebiyi, A. A., Zuidema, P. and Abel, S. J. (2015) 'The convolution of dynamics and moisture with the presence of shortwave absorbing aerosols over the southeast Atlantic', *Journal of Climate*, 28(5), pp. 1997–2024. doi: 10.1175/JCLI-D-14-00352.1.

Akagi, S. K. *et al.* (2011) 'Emission factors for open and domestic biomass burning for use in atmospheric models', *Atmospheric Chemistry and Physics*, 11(9), pp. 4039–4072. doi: 10.5194/acp-11-4039-2011.

Albrecht, B. A. (1989) 'Aerosols, Cloud Microphysics, and Fractional Cloudiness', *Science*, 245(4923), pp. 1227–1230. doi: 10.1126/science.245.4923.1227.

Alexander, D. T. L., Crozier, P. A. and Anderson, J. R. (2008) 'Brown Carbon Spheres in East Asian Outflow and Their Optical Properties', *Science*, 321(5890), pp. 833–836. doi: 10.1126/science.1155296.

Alfaro, S. C. *et al.* (1997) 'Modeling the size distribution of a soil aerosol produced by sandblasting', *Journal of Geophysical Research*, 102(D10), pp. 11239–11249. doi: 10.1029/97JD00403.

Allan, D. W. (1966) 'Statistics of Atomic Frequency Standards', *Proceedings of the IEEE*, 54(2), pp. 221–230. doi: 10.1109/PROC.1966.4634.

Amann, M., Klimont, Z. and Wagner, F. (2013) 'Regional and Global Emissions of Air Pollutants: Recent Trends and Future Scenarios', *Annual Review of Environment and Resources*, 38(1), pp. 31–55. doi: 10.1146/annurev-environ-052912-173303.

Anderson, T. L. *et al.* (1996) 'Performance characteristics of a high-sensitivity, three-wavelength, total scatter/backscatter nephelometer', *Journal of Atmospheric and Oceanic Technology*, 13(5), pp. 967–986. doi: 10.1175/1520-0426(1996)013<0967:PCOAHS>2.0.CO;2.

Anderson, T. L. *et al.* (2003) 'Mesoscale Variations of Tropospheric Aerosols', *Journal of the Atmospheric Sciences*, 60(1), pp. 119–136. doi: 10.1175/1520-0469(2003)060<0119:MVOTA>2.0.CO;2.

Andreae, M. O. and Gelencsér, A. (2006) 'Black carbon or brown carbon? The nature of light-absorbing carbonaceous aerosols', *Atmospheric Chemistry and Physics*, 6(10), pp. 3131–3148. doi: 10.5194/acp-6-3131-2006.

Andreae, M. O. and Merlet, P. (2001) 'Emission of trace gases and aerosols from biomass burning', *Global Biogeochemical Cycles*, 15(4), pp. 955–966. doi: 10.1029/2000GB001382.

Andreae, M. O. and Rosenfeld, D. (2008) 'Aerosol-cloud-precipitation interactions. Part 1. The nature and sources of cloud-active aerosols', *Earth-Science Reviews*, 89(1–2), pp. 13–41. doi: 10.1016/j.earscirev.2008.03.001.

Andrews, E. *et al.* (2006) 'Comparison of methods for deriving aerosol asymmetry parameter', *Journal of Geophysical Research Atmospheres*, 111(D5), pp. 1–16. doi: 10.1029/2004JD005734.

Andrews, E. and Larson, S. M. (1993) 'Effect of Surfactant Layers on the Size Changes of Aerosol Particles as a Function of Relative Humidity',

Environmental Science and Technology, 27(5), pp. 857–865. doi: 10.1021/es00042a007.
Ångström, A. (1929) 'On the Atmospheric Transmission of Sun Radiation and on Dust in the Air', *Geografiska Annaler*, 11(2), pp. 156–166. doi: 10.1080/20014422.1929.11880498.
Arnott, W. P. *et al.* (1999) 'Photoacoustic spectrometer for measuring light absorption by aerosol: Instrument description', *Atmospheric Environment*, 33(17), pp. 2845–2852. doi: 10.1016/S1352-2310(98)00361-6.
Arnott, W. P. *et al.* (2005) 'Towards aerosol light-absorption measurements with a 7-wavelength aethalometer: Evaluation with a photoacoustic instrument and 3-wavelength nephelometer', *Aerosol Science and Technology*, 39(1), pp. 17–29. doi: 10.1080/027868290901972.
Arnott, W. P., Moosmüller, H. and Walker, J. W. (2000) 'Nitrogen dioxide and kerosene-flame soot calibration of photoacoustic instruments for measurement of light absorption by aerosols', *Review of Scientific Instruments*, 71(12), pp. 4545–4552. doi: 10.1063/1.1322585.
Asmi, A. *et al.* (2013) *Aerosol decadal trends-Part 2: In-situ aerosol particle number concentrations at GAW and ACTRIS stations*, *Atmospheric Chemistry and Physics*. doi: 10.5194/acp-13-895-2013.
Atkinson, R. and Arey, J. (2003) 'Atmospheric degradation of volatile organic compounds', *Chemical Reviews*, 103(12), pp. 4605–4638. doi: 10.1021/cr0206420.
Backman, J. *et al.* (2014) 'Differences in aerosol absorption Ångström exponents between correction algorithms for a particle soot absorption photometer measured on the South African Highveld', *Atmospheric Measurement Techniques*, 7(12), pp. 4285–4298. doi: 10.5194/amt-7-4285-2014.
Bahadur, R. *et al.* (2012) 'Solar absorption by elemental and brown carbon determined from spectral observations', *Proceedings of the National Academy of Sciences*, 109(43), pp. 17366–17371. doi: 10.1073/pnas.1205910109.
Barker, H. W. and Li, Z. (1995) 'Improved Simulation of Clear-Sky Shortwave Radiative Transfer in the CCC-GCM', *Journal of Climate*, 8, pp. 2213–2223. doi: 10.1175/1520-0442(1995)008<2213:ISOCSS>2.0.CO;2.
Baumgardner, D. *et al.* (2012) 'Soot reference materials for instrument calibration and intercomparisons: A workshop summary with recommendations', *Atmospheric Measurement Techniques*, 5(8), pp. 1869–1887. doi: 10.5194/amt-5-1869-2012.
Behera, S. N. *et al.* (2013) 'Ammonia in the atmosphere: A review on emission sources, atmospheric chemistry and deposition on terrestrial bodies', *Environmental Science and Pollution Research*, 20(11), pp. 8092–8131. doi: 10.1007/s11356-013-2051-9.
Bellouin, N. *et al.* (2011) 'Aerosol forcing in the Climate Model Intercomparison Project (CMIP5) simulations by HadGEM2-ES and the role of ammonium nitrate', *Journal of Geophysical Research Atmospheres*, 116(D20), pp. 1–25. doi: 10.1029/2011JD016074.
Bellouin, N. *et al.* (2013) 'Estimates of aerosol radiative forcing from the MACC re-analysis', *Atmospheric Chemistry and Physics*, 13(4), pp. 2045–2062. doi: 10.5194/acp-13-2045-2013.
Berden, G., Peeters, R. and Meijer, G. (2000) 'International Reviews in Physical Chemistry Cavity ring-down spectroscopy : Experimental schemes and applications', *International Reviews in Physical Chemistry*, 19(4), pp. 565–

607. doi: 10.1080/014423500750040627.
Bergstrom, R. W. *et al.* (2007) 'Spectral absorption properties of atmospheric aerosols', *Atmospheric Chemistry and Physics*, 7(23), pp. 5937–5943. doi: 10.5194/acp-7-5937-2007.
Bergstrom, R. W., Russell, P. B. and Hignett, P. (2002) 'Wavelength Dependence of the Absorption of Black Carbon Particles: Predictions and Results from the TARFOX Experiment and Implications for the Aerosol Single Scattering Albedo', *Journal of atmospheric Sciences*, 59, pp. 567–577. doi: 10.1175/1520-0469(2002)059<0567:WDOTAO>2.0.CO;2.
Bian, H. *et al.* (2009) 'Sensitivity of aerosol optical thickness and aerosol direct radiative effect to relative humidity', *Atmospheric Chemistry and Physics*, 9(7), pp. 2375–2386. doi: 10.5194/acp-9-2375-2009.
Bindoff, N. L. *et al.* (2013) 'Detection and Attribution of Climate Change: from Global to Regional', in Stocker, T. F. et al. (eds) *Climate Change 2013: The Physical Science Basis. Contribution of Working Group I to the Fifth Assessment Report of the Intergovernmental Panel on Climate Change*. Cambridge, United Kingdom and New York, NY, USA: Cambridge University Press, pp. 867–952. doi: 10.1017/CBO9781107415324.028.
Bluvshtein, N. *et al.* (2017) 'Calibration of a multi-pass photoacoustic spectrometer cell using light-absorbing aerosols', *Atmospheric Measurement Techniques*, 10(3), pp. 1203–1213. doi: 10.5194/amt-10-1203-2017.
Bohren, C. F. and Huffman, D. R. (1998) *Absorption and Scattering of Light by Small Particles*. New York: Wiley. doi: 10.1002/9783527618156.
Bond, T. C. *et al.* (2004) 'A technology-based global inventory of black and organic carbon emissions from combustion', *Journal of Geophysical Research: Atmospheres*, 109(D14), pp. 1–43. doi: 10.1029/2003JD003697.
Bond, T. C. *et al.* (2007) 'Historical emissions of black and organic carbon aerosol from energy-related combustion, 1850-2000', *Global Biogeochemical Cycles*, 21(2), pp. 1–16. doi: 10.1029/2006GB002840.
Bond, T. C. *et al.* (2013) 'Bounding the role of black carbon in the climate system: A scientific assessment', *Journal of Geophysical Research Atmospheres*, 118(11), pp. 5380–5552. doi: 10.1002/jgrd.50171.
Bond, T. C., Anderson, T. L. and Campbell, D. (1999) 'Calibration and Intercomparison of Filter-Based Measurements of Visible Light Absorption by Aerosols', *Aerosol Science and Technology*, 30(6), pp. 582–600. doi: 10.1080/027868299304435.
Bond, T. C. and Bergstrom, R. W. (2006) 'Light Absorption by Carbonaceous Particles: An Investigative Review', *Aerosol Science and Technology*, 40(1), pp. 27–67. doi: 10.1080/02786820500421521.
Bond, T. C., Habib, G. and Bergstrom, R. W. (2006) 'Limitations in the enhancement of visible light absorption due to mixing state', *Journal of Geophysical Research Atmospheres*, 111(20), pp. 1–13. doi: 10.1029/2006JD007315.
Boucher, O. *et al.* (1998) 'Intercomparison of models representing direct shortwave radiative forcing by sulphate aerosols', *Journal of Geophysical Research*, 103(D14), pp. 16979–16998. doi: 10.1029/98JD00997.
Boucher, O. *et al.* (2013) 'Clouds and Aerosols', in *Climate Change 2013 - The Physical Science Basis. Contribution of Working Group I to the Fifth Assessment Report of the Intergovernmental Panel on Climate Change [Stocker, T.F., D. Qin, G.-K. Plattner, M. Tignor, S.K. Allen, J. Boschung, A. Nauels, Y. Xia*. Cambridge, United Kingdom and New York, NY, USA:

Cambridge University Press, pp. 571–658. doi: 10.1017/CBO9781107415324.016.
Boucher, O. and Anderson, T. L. (1995) 'General circulation model assessment of the sensitivity of direct climate forcing by anthropogenic sulfate aerosols to aerosol size and chemistry', *Journal of Geophysical Research*, 100(D12), pp. 26117–26134. doi: 10.1029/95JD02531.
Brown, S. S. (2003) 'Absorption Spectroscopy in High-Finesse Cavities for Atmospheric Studies', *Chemical Reviews*, 103(12), pp. 5219–5238. doi: 10.1021/cr020645c.
Burrows, S. M. *et al.* (2009) 'Bacteria in the global atmosphere – Part 2: Modeling of emissions and transport between different ecosystems', *Atmospheric Chemistry and Physics*, 9(23), pp. 9281–9297. doi: 10.5194/acp-9-9281-2009.
Cappa, C. D. *et al.* (2008) 'Bias in filter-based aerosol light absorption measurements due to organic aerosol loading: Evidence from laboratory measurements', *Aerosol Science and Technology*, 42(12), pp. 1022–1032. doi: 10.1080/02786820802389285.
Cappa, C. D. *et al.* (2012) 'Radiative Absorption Enhancements Due to the Mixing State of Atmospheric Black Carbon', *Science*, 337(6098), pp. 1078–1081. doi: 10.1126/science.1223447.
Carslaw, K. S. *et al.* (2010) 'A review of natural aerosol interactions and feedbacks within the Earth system', *Atmospheric Chemistry and Physics*, 10(4), pp. 1701–1737. doi: 10.5194/acp-10-1701-2010.
Chakrabarty, R. K. *et al.* (2010) 'Brown carbon in tar balls from smoldering biomass combustion', *Atmospheric Chemistry and Physics*, 10(13), pp. 6363–6370. doi: 10.5194/acp-10-6363-2010.
Charlson, R. J. *et al.* (1991) 'Perturbation of the northern hemisphere radiative balance by backscattering from anthropogenic sulfate aerosols', *Tellus B*, pp. 152–163. doi: 10.3402/tellusa.v43i4.11944.
Chen, Y. and Bond, T. C. (2010) 'Light absorption by organic carbon from wood combustion', *Atmospheric Chemistry and Physics*, 10(4), pp. 1773–1787. doi: 10.5194/acp-10-1773-2010.
Chung, C. E. *et al.* (2012a) 'Carbonaceous aerosol AAE inferred from in-situ aerosol measurements at the Gosan ABC super site, and the implications for brown carbon aerosol', *Atmospheric Chemistry and Physics*, 12(14), pp. 6173–6184. doi: 10.5194/acp-12-6173-2012.
Chung, C. E., Ramanathan, V. and Decremer, D. (2012b) 'Observationally constrained estimates of carbonaceous aerosol radiative forcing', *Proceedings of the National Academy of Sciences*, 109(29), pp. 11624–11629. doi: 10.1073/pnas.1203707109.
Clarke, A. *et al.* (2007) 'Biomass burning and pollution aerosol over North America: Organic components and their influence on spectral optical properties and humidification response', *Journal of Geophysical Research Atmospheres*, 112(D12), pp. 1–13. doi: 10.1029/2006JD007777.
Cohen, A. J. *et al.* (2017) 'Estimates and 25-year trends of the global burden of disease attributable to ambient air pollution: an analysis of data from the Global Burden of Diseases Study 2015', *The Lancet*. The Author(s). Published by Elsevier Ltd. This is an Open Access article under the CC BY 4.0 license, 389(10082), pp. 1907–1918. doi: 10.1016/S0140-6736(17)30505-6.
Collaud Coen, M. *et al.* (2010) 'Minimizing light absorption measurement artifacts of the Aethalometer: Evaluation of five correction algorithms',

Atmospheric Measurement Techniques, 3(2), pp. 457–474. doi: 10.5194/amt-3-457-2010.
Collaud Coen, M. *et al.* (2013) 'Aerosol decadal trends-Part 1: In-situ optical measurements at GAW and IMPROVE stations', *Atmospheric Chemistry and Physics*, 13(2), pp. 869–894. doi: 10.5194/acp-13-869-2013.
Collins, M. *et al.* (2013) 'Long-term Climate Change: Projections, Commitments and Irreversibilty', in Stocker, T. F. et al. (eds) *Climate Change 2013: The Physical Science Basis. Contribution of Working Group I to the Fifth Assessment Report of the Intergovernmental Panel on Climate Change*. Cambridge, United Kingdom and New York, NY, USA: Cambridge University Press, pp. 1029–1136.
Cubasch, U. *et al.* (2013) 'Introduction', in Stocker, T. F. et al. (eds) *Climate Change 2013: The Physical Science Basis. Contribution of Working Group I to the Fifth Assessment Report of the Intergovernmental Panel on Climate Change*. Cambridge, United Kingdom and New York, NY, USA: Cambridge University Press, pp. 119–158. doi: 10.2753/JES1097-203X330403.
Dentener, F. *et al.* (2001) 'Atmospheric Chemistry and Greenhouse Gases', in Houghton, J. T. et al. (eds) *Climate Change 2001: The Scientific Basis. Contribution of Working Group I to the Third Assessment Report of the Intergovernmental Panel on Climate Change*. Cambridge, United Kingdom and New York, NY, USA: Cambridge University Press, p. 881.
van Donkelaar, A. *et al.* (2015) 'Use of Satellite Observations for Long-Term Exposure Assessment of Global Concentrations of Fine Particulate Matter', *Environmental health perspectives*, 123(2), pp. 135–143. doi: 10.1289/ehp.1408646.
Drewnick, F. *et al.* (2005) 'A new time-of-flight aerosol mass spectrometer (TOF-AMS) - Instrument description and first field deployment', *Aerosol Science and Technology*, 39(7), pp. 637–658. doi: 10.1080/02786820500182040.
Eck, T. F. *et al.* (2013) 'A seasonal trend of single scattering albedo in southern African biomass-burning particles: Implications for satellite products and estimates of emissions for the world's largest biomass-burning source', *Journal of Geophysical Research Atmospheres*, 118(12), pp. 6414–6432. doi: 10.1002/jgrd.50500.
Everest, M. A. and Atkinson, D. B. (2008) 'Discrete sums for the rapid determination of exponential decay constants.', *The Review of scientific instruments*, 79(2), p. 23108. doi: 10.1063/1.2839918.
Eyring, V. *et al.* (2016) 'Overview of the Coupled Model Intercomparison Project Phase 6 (CMIP6) experimental design and organization', *Geoscientific Model Development*, 9(5), pp. 1937–1958. doi: 10.5194/gmd-9-1937-2016.
Facchini, M. C. *et al.* (2008) 'Primary submicron marine aerosol dominated by insoluble organic colloids and aggregates', *Geophysical Research Letters*, 35(17), pp. 1–5. doi: 10.1029/2008GL034210.
Feng, Y., Ramanathan, V. and Kotamarthi, V. R. (2013) 'Brown carbon: A significant atmospheric absorber of solar radiation', *Atmospheric Chemistry and Physics*, 13(17), pp. 8607–8621. doi: 10.5194/acp-13-8607-2013.
Fischer, D. A. and Smith, G. D. (2018) 'Technical Note : Can ozone be used to calibrate aerosol photoacoustic spectrometers ?', *Atmospheric Measurement Techniques Discussions*, pp. 1–12.
Fletcher, R. A. *et al.* (2009) 'Calibration of a condensation particle counter using a NIST traceable method', *Aerosol Science and Technology*, 43(5), pp. 425–441. doi: 10.1080/02786820802716735.

Fox, C. *et al.* (2017) *The EXSCALABAR instrument*.
Fuchs, H. *et al.* (2008) 'Determination of Inlet Transmission and Conversion Efficiencies for in Situ Measurements of the Nocturnal Nitrogen Oxides, NO3,N2O5 and NO2, via Pulsed Cavity Ring-Down Spectroscopy', *Analytical Chemistry*, 80(15), pp. 6010–6017. doi: 10.1021/ac8007253.
Fuller, K. A. (1995) 'Scattering and Absorption Cross Sections of Compounded Spheres. II. Calculations for External Aggregation', *Journal of the Optical Society of America A*, 12(5), pp. 881–892. doi: 10.1364/JOSAA.12.000881.
Fuller, K. A., Malm, W. C. and Kreidenweis, S. M. (1999) 'Effects of mixing on extinction by carbonaceous particles', *Journal of Geophysical Research*, 104(D13), pp. 15941–15954. doi: 10.1029/1998JD100069.
Gantt, B. *et al.* (2011) 'Wind speed dependent size-resolved parameterization for the organic mass fraction of sea spray aerosol', *Atmospheric Chemistry and Physics*, 11(16), pp. 8777–8790. doi: 10.5194/acp-11-8777-2011.
Garstang, M. *et al.* (1996) 'Horizontal and vertical transport of air over southern Africa', *Journal of Geophysical Research Atmospheres*, 101(D19), pp. 23721–23736. doi: 10.1029/95JD00844.
Giglio, L. *et al.* (2010) 'Assessing variability and long-term trends in burned area by merging multiple satellite fire products', *Biogeosciences*, 7(3), pp. 1171–1186. doi: 10.5194/bg-7-1171-2010.
Giglio, L., Randerson, J. T. and Van Der Werf, G. R. (2013) 'Analysis of daily, monthly, and annual burned area using the fourth-generation global fire emissions database (GFED4)', *Journal of Geophysical Research: Biogeosciences*, 118(1), pp. 317–328. doi: 10.1002/jgrg.20042.
Gillis, K. A., Havey, D. K. and Hodges, J. T. (2010) 'Standard photoacoustic spectrometer: Model and validation using O2 A-band spectra', *Review of Scientific Instruments*, 81(6), pp. 64902–1–64902–13. doi: 10.1063/1.3436660.
Ginoux, P. *et al.* (2012) 'Global-scale attribution of anthropogenic and natural dust sources and their emission rates based on MODIS Deep Blue aerosol products', *Reviews of Geophysics*, 50(3), pp. 1–36. doi: 10.1029/2012RG000388.
Global Atmospheric Watch (2016) *WMO/GAW Aerosol Measurement procedures guidelines and recommendations*, *World Meteorological Organization*. Geneva.
Gorshelev, V. *et al.* (2014) 'High spectral resolution ozone absorption cross-sections - Part 1: Measurements, data analysis and comparison with previous measurements around 293 K', *Atmospheric Measurement Techniques*, 7(2), pp. 609–624. doi: 10.5194/amt-7-609-2014.
de Graaf, M. *et al.* (2012) 'Retrieval of the aerosol direct radiative effect over clouds from spaceborne spectrometry', *Journal of Geophysical Research Atmospheres*, 117(7), pp. 1–18. doi: 10.1029/2011JD017160.
de Graaf, M. *et al.* (2014) 'Aerosol direct radiative effect of smoke over clouds over the southeast Atlantic Ocean from 2006 to 2009', *Geophysical Research Letters*, 41(21), pp. 7723–7730. doi: 10.1002/2014GL061103.
Gregory, J. M. *et al.* (2004) 'A new method for diagnosing radiative forcing and climate sensitivity', *Geophysical Research Letters*, 31(3), pp. 1–4. doi: 10.1029/2003GL018747.
Guenther, A. *et al.* (1995) 'A global model of natural volatile organic compound emissions', *Journal of Geophysical Research*, 100(D5), pp. 8873–8892. doi: 10.1029/94JD02950.
Gustafson Jr., W. I., Qian, Y. and Fast, J. D. (2011) 'Downscaling aerosols and

the impact of neglected subgrid processes on direct aerosol radiative forcing for a representative global climate model grid spacing', *Journal of Geophysical Research Atmospheres*, 116(D13), pp. 1–28. doi: 10.1029/2010JD015480.

Gyawali, M. *et al.* (2009) 'In situ aerosol optics in Reno, NV, USA during and after the summer 2008 California wildfires and the influence of absorbing and non-absorbing organic coatings on spectral light absorption', *Atmospheric Chemistry and Physics*, 9(20), pp. 8007–8015. doi: 10.5194/acp-9-8007-2009.

Hagwood, C., Sivathanu, Y. and Mulholland, G. (1999) 'The DMA Transfer Function with Brownian Motion a Trajectory/Monte-carlo Approach', *Aerosol Science and Technology*, 30, pp. 40–61.

Hallett, J., Hudson, J. G. and Rogers, C. F. (1989) 'Characterization of combustion aerosols for haze and cloud formation', *Aerosol Science and Technology*, 10(1), pp. 70–83. doi: 10.1080/02786828908959222.

Hallquist, M. *et al.* (2009) 'The formation, properties and impact of secondary organic aerosol: current and emerging issues', *Atmospheric Chemistry and Physics*, 9(14), pp. 5155–5236. doi: 10.5194/acp-9-5155-2009.

Hansen, J., Sato, M. and Ruedy, R. (1997) 'Radiative forcing and climate response', *Journal of Geophysical Research*, 102(D6), pp. 6831–6864. doi: 10.1029/96JD03436.

Haywood, J. *et al.* (2003a) 'Radiative properties and direct radiative effect of Saharan dust measured by the C-130 aircraft during SHADE: 1. Solar spectrum', *Journal of Geophysical Research*, 108(D18), p. 8577. doi: 10.1029/2002JD002687.

Haywood, J. . M., Ramaswamy, V. and Donner, L. J. (1997a) 'A limited-area-model case study of the effects of sub-grid scale variations in relative humidity and cloud upon the direct radiative forcing of sulfate aerosol', *Geophysical Research Letters*, 24(2), pp. 143–146. doi: 10.1029/96GL03812.

Haywood, J. M. *et al.* (1997b) 'General circulation model calculations of the direct radiative forcing by anthropogenic sulfate and fossil-fuel soot aerosol', *Journal of Climate*, 10(7), pp. 1562–1577. doi: 10.1175/1520-0442(1997)010<1562:GCMCOT>2.0.CO;2.

Haywood, J. M. *et al.* (2003b) 'The mean physical and optical properties of regional haze dominated by biomass burning aerosol measured from the C-130 aircraft during SAFARI 2000', *Journal of Geophysical Research: Atmospheres*, 108(D13), pp. 1–14. doi: 10.1029/2002JD002226.

Haywood, J. M. *et al.* (2008) 'Overview of the dust and biomass-burning experiment and African monsoon multidisciplinary analysis special observing period-0', *Journal of Geophysical Research Atmospheres*, 113(23), pp. 1–20. doi: 10.1029/2008JD010077.

Haywood, J. M. (no date) 'Overview of the CLARIFY-2017 campaign; motivation, rationale, deployment and initial results.'

Haywood, J. M. and Boucher, O. (2000) 'Estimates of the Direct and Indirect Radiative Forcing Due to Tropospheric Aerosols: A Review', *Reviews of Geophysics*, 38(4), pp. 513–543. doi: 10.1029/1999RG000078.

Haywood, J. M. and Shine, K. P. (1995) 'The effect of anthropogenic sulfate and soot aerosol on the clear sky planetary radiation budget', *Geophysical Research Letters*, 22(5), pp. 603–606. doi: 10.1029/95GL00075.

Haywood, J. M. and Shine, K. P. (1997) 'Multi-spectral calculations of the direct radiative forcing of tropospheric sulphate and soot aerosols using a column

model', *Quarterly Journal of the Royal Meteorological Society*, 123(543), pp. 1907–1930. doi: 10.1002/qj.49712354307.
Heintzenberg, J. and Charlson, R. J. (1996) 'Design and applications of the integrating nephelometer: A review', *Journal of Atmospheric and Oceanic Technology*, 13(5), pp. 987–1000. doi: 10.1175/1520-0426(1996)013<0987:DAAOTI>2.0.CO;2.
Herich, H. *et al.* (2009) 'Water uptake of clay and desert dust aerosol particles at sub- and supersaturated water vapor conditions', *Physical Chemistry Chemical Physics*, 11(36), pp. 7804–7809. doi: 10.1039/b901585j.
Hodges, J. T., Looney, J. P. and Zee, R. D. Van (1996) 'Response of a ring-down cavity to an arbitrary excitation', *Journal of Chemical Physics*, 105(23), pp. 10278–10288. doi: 10.1063/1.472956.
Hodnebrog, Ø., Myhre, G. and Samset, B. H. (2014) 'How shorter black carbon lifetime alters its climate effect', *Nature Communications*, 5(5065), pp. 1–7. doi: 10.1038/ncomms6065.
Ten Hoeve, J. E., Jacobson, M. Z. and Remer, L. A. (2012) 'Comparing results from a physical model with satellite and in situ observations to determine whether biomass burning aerosols over the Amazon brighten or burn off clouds', *Journal of Geophysical Research Atmospheres*, 117(8), pp. 1–19. doi: 10.1029/2011JD016856.
Holben, B. N. *et al.* (1998) 'AERONET—A Federated Instrument Network and Data Archive for Aerosol Characterization', *Remote Sensing of Environment*, 66(1), pp. 1–16. doi: 10.1016/S0034-4257(98)00031-5.
Huneeus, N., Chevallier, F. and Boucher, O. (2012) 'Estimating aerosol emissions by assimilating observed aerosol optical depth in a global aerosol model', *Atmospheric Chemistry and Physics*, 12(10), pp. 4585–4606. doi: 10.5194/acp-12-4585-2012.
Hungershoefer, K. *et al.* (2008) 'Modelling the optical properties of fresh biomass burning aerosol produced in a smoke chamber: Results from the EFEU campaign', *Atmospheric Chemistry and Physics*, 8(13), pp. 3427–3439. doi: 10.5194/acp-8-3427-2008.
IPCC (2014) 'Summary for Policymakers', in Field, C. B. et al. (eds) *Climate Change 2014: Impacts, Adaptation and Vulnerability. Part A: Global and Sectoral Aspects. Contribution of Working Group II to the Fifth Assessment Report of the Intergovernmental Panel on Climate Change*. Cambridge, United Kingdom and New York, NY, USA: Cambridge University Press, pp. 1–32. doi: 10.1016/j.renene.2009.11.012.
Jacobson, M. Z. (2000) 'A physically-based treatment of elemental carbon optics: Implications for global direct forcing of aerosols', *Geophysical Research Letters*, 27(2), pp. 217–220. doi: 10.1029/1999GL010968.
Jacobson, M. Z. (2002) 'Analysis of aerosol interactions with numerical techniques for solving coagulation, nucleation, condensation, dissolution, and reversible chemistry among multiple size distributions', *Journal of Geophysical Research Atmospheres*, 107(19), pp. 1–23. doi: 10.1029/2001JD002044.
Jennings, S. G. and Pinnick, R. G. (1980) 'Relationships between visible extinction, absorption and mass concentration of carbonaceous smokes', *Atmospheric Environment*, 14(10), pp. 1123–1129. doi: 10.1016/0004-6981(80)90176-6.
Jickells, T. D. *et al.* (2005) 'Global Iron Connections Between Desert Dust, Ocean Biogeochemistry, and Climate', *Science*, 308(5718), pp. 67–71. doi: 10.1126/science.1105959.

Jimenez, J. L. *et al.* (2009) 'Evolution of Organic Aerosols in the Atmosphere', *Science*, 326(5959), pp. 1525–1529. doi: 10.1126/science.1180353.
Jo, D. S. *et al.* (2016) 'A global simulation of brown carbon: Implications for photochemistry and direct radiative effect', *Atmospheric Chemistry and Physics*, 16(5), pp. 3413–3432. doi: 10.5194/acp-16-3413-2016.
Johnson, B. T. *et al.* (2016) 'Evaluation of biomass burning aerosols in the HadGEM3 climate model with observations from the SAMBBA field campaign', *Atmospheric Chemistry and Physics*, 16(22), pp. 14657–14685. doi: 10.5194/acp-16-14657-2016.
Joseph, J. H., Wiscombe, W. J. and Weinman, J. A. (1976) 'The Delta-Eddington Approximation for Radiative Flux Transfer', *Journal of the Atmospheric Sciences*, pp. 2452–2459. doi: 10.1175/1520-0469(1976)033<2452:TDEAFR>2.0.CO;2.
Junker, C. and Liousse, C. (2008) 'A global emission inventory of carbonaceous aerosol from historic records of fossil fuel and biofuel consumption for the period 1860-1997', *Atmospheric Chemistry and Physics*, 8(5), pp. 1195–1207. doi: 10.5194/acp-8-1195-2008.
Kacenelenbogen, M. *et al.* (2011) 'An accuracy assessment of the CALIOP/CALIPSO version 2/version 3 daytime aerosol extinction product based on a detailed multi-sensor, multi-platform case study', *Atmospheric Chemistry and Physics*, 11(8), pp. 3981–4000. doi: 10.5194/acp-11-3981-2011.
Keil, A. and Haywood, J. M. (2003) 'Solar radiative forcing by biomass burning aerosol particles during SAFARI 2000 : A case study based on measured aerosol and cloud properties', *Journal of Geophysical Research*, 108(D13), pp. 1–10. doi: 10.1029/2002JD002315.
Kim, K. H., Kabir, E. and Kabir, S. (2015) 'A review on the human health impact of airborne particulate matter', *Environment International*. Elsevier Ltd, 74, pp. 136–143. doi: 10.1016/j.envint.2014.10.005.
Kirchstetter, T. W., Novakov, T. and Hobbs, P. V. (2004) 'Evidence that the spectral dependence of light absorption by aerosols is affected by organic carbon', *Journal of Geophysical Research: Atmospheres*, 109(D21), pp. 1–12. doi: 10.1029/2004JD004999.
Kirchstetter, T. W. and Thatcher, T. L. (2012) 'Contribution of organic carbon to wood smoke particulate matter absorption of solar radiation', *Atmospheric Chemistry and Physics*, 12(14), pp. 6067–6072. doi: 10.5194/acp-12-6067-2012.
Klimont, Z., Smith, S. J. and Cofala, J. (2013) 'The last decade of global anthropogenic sulfur dioxide: 2000-2011 emissions', *Environmental Research Letters*, 8(1), pp. 1–6. doi: 10.1088/1748-9326/8/1/014003.
Knutson, E. O. and Whitby, K. T. (1975) 'Aerosol classification by electric mobility: apparatus, theory, and applications', *Journal of Aerosol Science*, 6(6), pp. 443–451. doi: 10.1016/0021-8502(75)90060-9.
Koga, S. and Tanaka, H. (1999) 'Modeling the methanesulfonate to non-sea-salt sulfate molar ratio and dimethylsulfide oxidation in the atmosphere', *Journal of Geophysical Research Atmospheres*, 104(D11), pp. 13735–13747. doi: 10.1029/1999JD900069.
Kogelnik, H. and Li, T. (1966) 'Laser Beams and Resonators', *Applied Optics*, 5(10), pp. 1550–1567. doi: 10.1364/AO.5.001550.
Kok, J. F. (2011) 'A scaling theory for the size distribution of emitted dust aerosols suggests climate models underestimate the size of the global dust cycle', *Proceedings of the National Academy of Sciences*, 108(3), pp.

1016–1021. doi: 10.1073/pnas.1014798108.
Lack, D. A. *et al.* (2006) 'Aerosol Absorption Measurement using Photoacoustic Spectroscopy: Sensitivity, Calibration, and Uncertainty Developments', *Aerosol Science and Technology*, 40(9), pp. 697–708. doi: 10.1080/02786820600803917.
Lack, D. A. *et al.* (2008) 'Bias in Filter-Based Aerosol Light Absorption Measurements Due to Organic Aerosol Loading: Evidence from Ambient Measurements', *Aerosol Science and Technology*, 42(12), pp. 1033–1041. doi: 10.1080/02786820802389277.
Lack, D. A. *et al.* (2012a) 'Aircraft Instrument for Comprehensive Characterization of Aerosol Optical Properties, Part 2: Black and Brown Carbon Absorption and Absorption Enhancement Measured with Photo Acoustic Spectroscopy', *Aerosol Science and Technology*, 46(5), pp. 555–568. doi: 10.1080/02786826.2011.645955.
Lack, D. A. *et al.* (2012b) 'Brown carbon and internal mixing in biomass burning particles', *Proceedings of the National Academy of Sciences*, 109(37), pp. 14802–14807. doi: 10.1073/pnas.1206575109.
Lack, D. A. and Cappa, C. D. (2010) 'Impact of brown and clear carbon on light absorption enhancement, single scatter albedo and absorption wavelength dependence of black carbon', *Atmospheric Chemistry and Physics*, 10(9), pp. 4207–4220. doi: 10.5194/acp-10-4207-2010.
Lack, D. A. and Langridge, J. M. (2013) 'On the attribution of black and brown carbon light absorption using the Ångström exponent', *Atmospheric Chemistry and Physics*, 13(20), pp. 10535–10543. doi: 10.5194/acp-13-10535-2013.
Lamarque, J. F. *et al.* (2010) 'Historical (1850-2000) gridded anthropogenic and biomass burning emissions of reactive gases and aerosols: Methodology and application', *Atmospheric Chemistry and Physics*, 10(15), pp. 7017–7039. doi: 10.5194/acp-10-7017-2010.
Langridge, J. M. *et al.* (2011) 'Aircraft Instrument for Comprehensive Characterization of Aerosol Optical Properties , Part I : Wavelength-Dependent Optical Extinction and Its Relative Humidity Dependence Measured Using Cavity Ringdown Spectroscopy', *Aerosol Science and Technology*, 45(11), pp. 1305–1318. doi: 10.1080/02786826.2011.592745.
de Leeuw, G. *et al.* (2011) 'Production Flux of Sea Spray Aerosol', *Reviews of Geophysics*, 49(2), pp. 1–39. doi: 10.1029/2010RG000349.1.INTRODUCTION.
Lehmann, K. K. and Romanini, D. (1996) 'The superposition principle and cavity ring-down spectroscopy', *Journal of Chemical Physics*, 105(23), pp. 10263–10277. doi: 10.1063/1.472955.
Li, Z. *et al.* (2009) 'Uncertainties in satellite remote sensing of aerosols and impact on monitoring its long-term trend: A review and perspective', *Annales Geophysicae*, 27(7), pp. 2755–2770. doi: 10.5194/angeo-27-2755-2009.
Lin, C. I., Baker, M. and Charlson, R. J. (1973) 'Absorption coefficient of atmospheric aerosol: a method for measurement.', *Applied optics*, 12(6), pp. 1356–1363. doi: 10.1364/AO.12.001356.
Lin, G. *et al.* (2014) 'Radiative forcing of organic aerosol in the atmosphere and on snow: Effects of SOA and brown carbon', *Journal of Geophysical Research: Atmospheres*, 119(12), pp. 7453–7476. doi: 10.1002/2013JD021186.
Liousse, C., Cachier, H. and Jennings, S. G. (1993) 'Optical and thermal

measurements of black carbon aerosol content in different environments: Variation of the specific attenuation cross-section, sigma (σ)', *Atmospheric Environment Part A, General Topics*, 27(8), pp. 1203–1211. doi: 10.1016/0960-1686(93)90246-U.
Liu, D. *et al.* (2015a) 'The effect of complex black carbon microphysics on the determination of the optical properties of brown carbon', *Geophysical Research Letters*, 42(2), pp. 613–619. doi: 10.1002/2014GL062443.
Liu, J. *et al.* (2014) 'Brown carbon in the continental troposphere', *Geophysical Research Letters*, 41(6), pp. 2191–2195. doi: 10.1002/2013GL058976.
Liu, S. *et al.* (2015b) 'Enhanced light absorption by mixed source black and brown carbon particles in UK winter', *Nature Communications*, 6(8435), pp. 1–10. doi: 10.1038/ncomms9435.
Loeb, N. G. and Su, W. (2010) 'Direct aerosol radiative forcing uncertainty based on a radiative perturbation analysis', *Journal of Climate*, 23(19), pp. 5288–5293. doi: 10.1175/2010JCLI3543.1.
Lu, Z., Zhang, Q. and Streets, D. G. (2011) 'Sulfur dioxide and primary carbonaceous aerosol emissions in China and India, 1996-2010', *Atmospheric Chemistry and Physics*, 11(18), pp. 9839–9864. doi: 10.5194/acp-11-9839-2011.
Malavelle, F. F. *et al.* (2017) 'Strong constraints on aerosol-cloud interactions from volcanic eruptions', *Nature*. Nature Publishing Group, 546(7659), pp. 485–491. doi: 10.1038/nature22974.
Mann, G. W. *et al.* (2010) 'Description and evaluation of GLOMAP-mode : a modal global aerosol microphysics model for the UKCA composition-climate model', *Geoscientific Model Development*, 3(2), pp. 519–551. doi: 10.5194/gmd-3-519-2010.
Manners, J. *et al.* (2015) *SOCRATES Technical Guide Suite Of Community RAdiative Transfer codes based on Edwards and Slingo*. Exeter.
Martin, J. *et al.* (1996) 'Cavity ring-down spectroscopy with Fourier-transform-limited light pulses', *Chemical Physics Letters*, 258(5–6), pp. 63–70. doi: 10.1016/0009-2614(96)00609-4.
Martins, J. V. *et al.* (1998) 'Effects of black carbon content, particle size, and mixing on light absorption by aerosols from biomass burning in Brazil', *Journal of Geophysical Research*, 103(D24), pp. 32041–32050. doi: 10.1029/98JD02593.
Massoli, P. *et al.* (2009) 'Uncertainty in light scattering measurements by TSI nephelometer: Results from laboratory studies and implications for ambient measurements', *Aerosol Science and Technology*, 43(11), pp. 1064–1074. doi: 10.1080/02786820903156542.
Masson-Delmotte, V. *et al.* (2013) 'Information from Paleoclimate Archives', in Stocker, T. F. et al. (eds) *Climate Change 2013: The Physical Science Basis. Contribution of Working Group I to the Fifth Assessment Report of the Intergovernmental Panel on Climate Change*. Cambridge, United Kingdom and New York, NY, USA.: Cambridge University Press, pp. 383–464. doi: 10.1017/CBO9781107415324.013.
Matsui, H. and Mahowald, N. (2017) 'Development of a global aerosol model using a two-dimensional sectional method: 2. Evaluation and sensitivity simulations', *Journal of Advances in Modeling Earth Systems*, 9(4), pp. 1887–1920. doi: 10.1002/2017MS000937.
Mazurenka, M. *et al.* (2005) '4 Cavity ring-down and cavity enhanced spectroscopy using diode lasers', *Annual Reports Section 'C' (Physical Chemistry)*, 101, pp. 100–142. doi: 10.1039/b408909j.

McClatchey, R. A. *et al.* (1972) *Optical Properties of the Atmosphere*.
McComiskey, A. *et al.* (2008) 'Direct aerosol forcing: Calculation from observables and sensitivities to inputs', *Journal of Geophysical Research Atmospheres*, 113(9), pp. 1–16. doi: 10.1029/2007JD009170.
McManus, J. B., Kebabian, P. L. and Zahniser, M. S. (1995) 'Astigmatic mirror multipass absorption cells for long-path-length spectroscopy', *Applied Optics*, 34(18), pp. 3336–3348.
McMeeking, G. R. *et al.* (2011) 'Black carbon aerosol mixing state, organic aerosols and aerosol optical properties over the United Kingdom', *Atmospheric Chemistry and Physics*, 11(17), pp. 9037–9052. doi: 10.5194/acp-11-9037-2011.
Meijer, G. *et al.* (1994) 'Coherent cavity ring down spectroscopy', *Chemical Physics Letters*, 217(1–2), pp. 112–116. doi: 10.1016/0009-2614(93)E1361-J.
Meyer, K. *et al.* (2013) 'Estimating the direct radiative effect of absorbing aerosols overlying marine boundary layer clouds in the southeast Atlantic using MODIS and CALIOP', *Journal of Geophysical Research Atmospheres*, 118(10), pp. 4801–4815. doi: 10.1002/jgrd.50449.
Meyer, K., Platnick, S. and Zhang, Z. (2015) 'Simultaneously inferring above-cloud absorbing aerosol optical thickness and underlying liquid phase cloud optical and microphysical properties using MODIS', *Journal of Geophysical Research Atmospheres*, 120(11), pp. 5524–5547. doi: 10.1002/2015JD023128.
Mikhailov, E. F. *et al.* (2006) 'Optical properties of soot-water drop agglomerates: An experimental study', *Journal of Geophysical Research*, 111(D7), pp. 1–16. doi: 10.1029/2005JD006389.
Miklós, A., Hess, P. and Bozóki, Z. (2001) 'Application of acoustic resonators in photoacoustic trace gas analysis and metrology', *Review of Scientific Instruments*, 72(4), pp. 1937–1955. doi: 10.1063/1.1353198.
Miles, R. E. H. *et al.* (2011) 'Sources of Error and Uncertainty in the Use of Cavity Ring Down Spectroscopy to Measure Aerosol Optical Properties', *Aerosol Science and Technology*, 45(11), pp. 1360–1375. doi: 10.1080/02786826.2011.596170.
Moffet, R. C. and Prather, K. A. (2009) 'In-situ measurements of the mixing state and optical properties of soot with implications for radiative forcing estimates', *Proceedings of the National Academy of Sciences*, 106(29), pp. 11872–11877. doi: 10.1073/pnas.0900040106.
Moosmüller, H. *et al.* (2011) 'Absorption Ångström coefficient, brown carbon, and aerosols: Basic concepts, bulk matter, and spherical particles', *Atmospheric Chemistry and Physics*, 11(3), pp. 1217–1225. doi: 10.5194/acp-11-1217-2011.
Moosmüller, H., Chakrabarty, R. K. and Arnott, W. P. (2009) 'Aerosol light absorption and its measurement: A review', *Journal of Quantitative Spectroscopy and Radiative Transfer*, 110(11), pp. 844–878. doi: 10.1016/j.jqsrt.2009.02.035.
Moss, R. H. *et al.* (2010) 'The next generation of scenarios for climate change research and assessment', *Nature*. Nature Publishing Group, 463(7282), pp. 747–756. doi: 10.1038/nature08823.
Moteki, N., Kondo, Y. and Nakamura, S. (2010) 'Method to measure refractive indices of small nonspherical particles: Application to black carbon particles', *Journal of Aerosol Science*. Elsevier, 41(5), pp. 513–521. doi: 10.1016/j.jaerosci.2010.02.013.

Müller, T. *et al.* (2011) 'Design and performance of a three-wavelength LED-based total scatter and backscatter integrating nephelometer', *Atmospheric Measurement Techniques*, 4(6), pp. 1291–1303. doi: 10.5194/amt-4-1291-2011.
Müller, T., Virkkula, A. and Ogren, J. A. (2014) 'Constrained two-stream algorithm for calculating aerosol light absorption coefficient from the Particle Soot Absorption Photometer', *Atmospheric Measurement Techniques*, 7(12), pp. 4049–4070. doi: 10.5194/amt-7-4049-2014.
Murphy, D. M. *et al.* (2006) 'Single-peptide mass spectrometry of tropospheric aerosol particles', *Journal of Geophysical Research Atmospheres*, 111(23), pp. 1–15. doi: 10.1029/2006JD007340.
Murphy, D. M. *et al.* (2011) 'Decreases in elemental carbon and fine particle mass in the United States', *Atmospheric Chemistry and Physics*, 11(10), pp. 4679–4686. doi: 10.5194/acp-11-4679-2011.
Myhre, G. *et al.* (2008) 'Modeling of the solar radiative impact of biomass burning aerosols during the Dust and Biomass-burning Experiment (DABEX)', *Journal of Geophysical Research Atmospheres*, 113(23), pp. 1–10. doi: 10.1029/2008JD009857.
Myhre, G. *et al.* (2013a) 'Anthropogenic and Natural Radiative Forcing', in Stocker, T. F. et al. (eds) *Climate Change 2013: The Physical Science Basis. Contribution of Working Group I to the Fifth Assessment Report of the Intergovernmental Panel on Climate Change*. Cambridge, United Kingdom and New York, NY, USA: Cambridge University Press, pp. 659–740. doi: 10.1017/ CBO9781107415324.018.
Myhre, G. *et al.* (2013b) 'Radiative Forcing of the Direct Aerosol Effect from AeroCom Phase II Simulations', *Atmospheric Chemistry and Physics*, 13(4), pp. 1853–1877. doi: 10.5194/acp-13-1853-2013.
Myhre, G. and Samset, B. H. (2015) 'Standard climate models radiation codes underestimate black carbon radiative forcing', *Atmospheric Chemistry and Physics*, 15(5), pp. 2883–2888. doi: 10.5194/acp-15-2883-2015.
Nägele, M. and Sigrist, M. W. (2000) 'Mobile laser spectrometer with novel resonant multipass photoacoustic cell for trace-gas sensing', *Applied Physics B*, 70(6), pp. 895–901. doi: 10.1007/PL00021151.
Nakayama, T. *et al.* (2015) 'Characterization of a Three Wavelength Photoacoustic Soot Spectrometer (PASS-3) and a Photoacoustic Extinctiometer (PAX)', *Journal of the Meteorological Society of Japan. Ser. II*, 93(2), pp. 285–308. doi: 10.2151/jmsj.2015-016.
O'Keefe, A. and Deacon, D. A. G. (1988) 'Cavity ring-down optical spectrometer for absorption measurements using pulsed laser sources', *Review of Scientific Instruments*, 59, pp. 2544–2551. doi: 10.1063/1.1139895.
Ogren, J. a. (2010) 'Comment on "Calibration and Intercomparison of Filter-Based Measurements of Visible Light Absorption by Aerosols"', *Aerosol Science and Technology*, 44(8), pp. 589–591. doi: 10.1080/02786826.2010.482111.
Ogren, J. A. *et al.* (2017) 'Continuous Light Absorption Photometer for Long-Term Studies', *Atmospheric Measurement Techniques*, 10(12), pp. 4805–4818. doi: 10.5194/amt-10-4805-2017.
Osborne, S. R. *et al.* (2008) 'Physical and optical properties of mineral dust aerosol during the Dust and Biomass-burning Experiment', *Journal of Geophysical Research Atmospheres*, 113(D23), pp. 1–14. doi: 10.1029/2007JD009551.
Park, R. J. *et al.* (2010) 'A contribution of brown carbon aerosol to the aerosol

light absorption and its radiative forcing in East Asia', *Atmospheric Environment*. Elsevier Ltd, 44(11), pp. 1414–1421. doi: 10.1016/j.atmosenv.2010.01.042.
Peers, F. *et al.* (2015) 'Absorption of aerosols above clouds from POLDER/PARASOL measurements and estimation of their direct radiative effect', *Atmospheric Chemistry and Physics*, 15(8), pp. 4179–4196. doi: 10.5194/acp-15-4179-2015.
Peers, F. *et al.* (2016) 'Comparison of aerosol optical properties above clouds between POLDER and AeroCom models over the South East Atlantic Ocean during the fire season', *Geophysical Research Letters*, 43(8), pp. 3991–4000. doi: 10.1002/2016GL068222.
van Poppel, L. H. *et al.* (2005) 'Electron tomography of nanoparticle clusters: Implications for atmospheric lifetimes and radiative forcing of soot', *Geophysical Research Letters*, 32(24), pp. 1–4. doi: 10.1029/2005GL024461.
Qian, Y., Gustafson Jr., W. I. and Fast, J. D. (2010) 'An investigation of the sub-grid variability of trace gases and aerosols for global climate modeling', *Atmospheric Chemistry and Physics*, 10(14), pp. 6917–6946. doi: 10.5194/acp-10-6917-2010.
Radney, J. G. *et al.* (2014) 'Dependence of soot optical properties on particle morphology: Measurements and model comparisons', *Environmental Science and Technology*, 48(6), pp. 3169–3176. doi: 10.1021/es4041804.
Raut, J. C. and Chazette, P. (2008) 'Radiative budget in the presence of multi-layered aerosol structures in the framework of AMMA SOP-0', *Atmospheric Chemistry and Physics*, 8(22), pp. 6839–6864. doi: 10.5194/acp-8-6839-2008.
Redemann, J. *et al.* (2005) 'Suborbital Measurements of Spectral Aerosol Optical Depth and Its Variability at Subsatellite Grid Scales in Support of CLAMS 2001', *Journal of the Atmospheric Sciences*, 62(4), pp. 993–1007. doi: 10.1175/JAS3387.1.
Reid, S. and Hobbs, P. V (1998) 'Physical and optical properties of young smoke from individual biomass fires in Brazil', *Journal of Geophysical Research*, 103(D24), pp. 32013–32030. doi: 10.1029/98JD00159.
Remer, L. A. *et al.* (2013) 'MODIS 3 km aerosol product: Algorithm and global perspective', *Atmospheric Measurement Techniques*, 6(7), pp. 1829–1844. doi: 10.5194/amt-6-1829-2013.
Riahi, K. *et al.* (2011) 'RCP 8.5-A scenario of comparatively high greenhouse gas emissions', *Climatic Change*, 109(1), pp. 33–57. doi: 10.1007/s10584-011-0149-y.
Ridley, D. A. *et al.* (2016) 'An observationally constrained estimate of global dust aerosol optical depth', *Atmospheric Chemistry and Physics*, 16(23), pp. 15097–15117. doi: 10.5194/acp-16-15097-2016.
Riziq, A. A. *et al.* (2007) 'Optical properties of absorbing and non-absorbing aerosols retrieved by cavity ring down (CRD) spectroscopy', *Atmospheric Chemistry and Physics*, 7(6), pp. 1523–1536. doi: 10.5194/acp-7-1523-2007.
Rolph, G., Stein, A. and Stunder, B. (2017) 'Real-time Environmental Applications and Display sYstem: READY', *Environmental Modelling and Software*. Elsevier Ltd, 95, pp. 210–228. doi: 10.1016/j.envsoft.2017.06.025.
Romanini, D., Kachanov, A. A. and Stoeckel, E. (1997) 'Cavity ringdown spectroscopy : broad band absolute absorption measurements', *Chemical*

Physics Letters, 270(5–6), pp. 546–550. doi: 10.1016/S0009-2614(97)00407-7.
Romanini, D. and Lehmann, K. K. (1993) 'Ring-down cavity absorption spectroscopy of the very weak HCN overtone bands with six , seven , and eight stretching quanta', *Journal of Chemical Physics*, 99(9), pp. 6287–6301. doi: 10.1063/1.465866.
Russell, L. M. *et al.* (2010) 'Carbohydrate-like composition of submicron atmospheric particles and their production from ocean bubble bursting', *Proceedings of the National Academy of Sciences*, 107(15), pp. 6652–6657. doi: 10.1073/pnas.0908905107.
Ryder, C. L. *et al.* (2013) 'Optical properties of Saharan dust aerosol and contribution from the coarse mode as measured during the Fennec 2011 aircraft campaign', *Atmospheric Chemistry and Physics*, 13(1), pp. 303–325. doi: 10.5194/acp-13-303-2013.
Saleh, R. *et al.* (2014) 'Brownness of organics in aerosols from biomass burning linked to their black carbon content', *Nature Geoscience*, 7(9), pp. 647–650. doi: 10.1038/ngeo2220.
Saleh, R. *et al.* (2015) 'Contribution of brown carbon and lensing to the direct radiative effect of carbonaceous aerosols from biomass and biofuel burning emissions', *Journal of Geophysical Research: Atmospheres*, 120(19), pp. 10285–10296. doi: 10.1002/2015JD023697.
Samset, B. H. *et al.* (2013) 'Black carbon vertical profiles strongly affect its radiative forcing uncertainty', *Atmospheric Chemistry and Physics*, 13(5), pp. 2423–2434. doi: 10.5194/acp-13-2423-2013.
Samset, B. H. *et al.* (2018) 'Aerosol Absorption: Progress Towards Global and Regional Constraints', *Current Climate Change Reports*. Current Climate Change Reports, 4(2), pp. 65–83. doi: 10.1007/s40641-018-0091-4.
Samset, B. H. and Myhre, G. (2011) 'Vertical dependence of black carbon, sulphate and biomass burning aerosol radiative forcing', *Geophysical Research Letters*, 38(24), pp. 1–5. doi: 10.1029/2011GL049697.
Scherer, J. J. *et al.* (1997) 'Cavity Ringdown Laser Absorption Spectroscopy : History , Development , and Application to Pulsed Molecular Beams', *Chemical Reviews*, 97(1), pp. 25–51. doi: 10.1021/cr930048d.
Schmid, O. *et al.* (2006) 'Spectral light absorption by ambient aerosols influenced by biomass burning in the Amazon Basin – I. Comparison and field calibration of absorption measurement techniques', *Atmospheric Chemistry and Physics*, 6(11), pp. 3443–3462. doi: 10.5194/acp-6-3443-2006.
Schnaiter, M. *et al.* (2003) 'UV-VIS-NIR spectral optical properties of soot and soot-containing aerosols', *Journal of Aerosol Science*, 34(10), pp. 1421–1444. doi: 10.1016/S0021-8502(03)00361-6.
Schulz, M. *et al.* (2006) 'Radiative forcing by aerosols as derived from the AeroCom present-day and pre-industrial simulations', *Atmospheric Chemistry and Physics*, 6(12), pp. 5225–5246. doi: 10.5194/acp-6-5225-2006.
Schutgens, N. A. J. *et al.* (2016) 'Will a perfect model agree with perfect observations? The impact of spatial sampling', *Atmospheric Chemistry and Physics*, 16(10), pp. 6335–6353. doi: 10.5194/acp-16-6335-2016.
Schwarz, J. P. *et al.* (2013) 'Global-scale seasonally resolved black carbon vertical profiles over the Pacific', *Geophysical Research Letters*, 40(20), pp. 5542–5547. doi: 10.1002/2013GL057775.
Seinfeld, J. H. and Pandis, S. N. (2006) *ATMOSPHERIC From Air Pollution to*

Climate Change SECOND EDITION.
Serdyuchenko, A. *et al.* (2014) 'High spectral resolution ozone absorption cross-sections - Part 2: Temperature dependence', *Atmospheric Measurement Techniques*, 7(2), pp. 625–636. doi: 10.5194/amt-7-625-2014.
Shao, Y. *et al.* (2011) 'Dust cycle: An emerging core theme in Earth system science', *Aeolian Research*. Elsevier B.V., 2(4), pp. 181–204. doi: 10.1016/j.aeolia.2011.02.001.
Sherman, J. P. and McComiskey, A. (2018) 'Measurement-based climatology of aerosol direct radiative effect, its sensitivities, and uncertainties from a background southeast U.S. site', *Atmospheric Chemistry and Physics*, 18(6), pp. 4131–4152. doi: 10.5194/acp-18-4131-2018.
Shindell, D. T. *et al.* (2013) 'Radiative forcing in the ACCMIP historical and future climate simulations', *Atmospheric Chemistry and Physics*, 13(6), pp. 2939–2974. doi: 10.5194/acp-13-2939-2013.
Shine, K. P. *et al.* (2003) 'A comparison of model-simulated trends in stratospheric temperatures', *Quarterly Journal of the Royal Meteorological Society*, 129(590), pp. 1565–1588. doi: 10.1256/qj.02.186.
Siegman, A. E. (1986) *Anthony E. Siegman*. Palo Alto: Miller/Scheier Associates.
Silver, J. A. (2005) 'Simple dense-pattern optical multipass cells', *Applied optics*, 44(31), pp. 6545–6556. doi: 10.1364/AO.44.006545.
Stein, A. F. *et al.* (2015) 'Noaa's hysplit atmospheric transport and dispersion modeling system', *Bulletin of the American Meteorological Society*, 96, pp. 2059–2077. doi: 10.1175/BAMS-D-14-00110.1.
Stier, P. *et al.* (2007) 'Aerosol absorption and radiative forcing', *Atmospheric Chemistry and Physics*, 7(19), pp. 5237–5261. doi: 10.5194/acp-7-5237-2007.
Stocker, T. F. *et al.* (2013) 'Technical Summary', in Stocker, T. F. et al. (eds) *Climate Change 2013 - The Physical Science Basis. Contribution of Working Group I to the Fifth Assessment Report of the Intergovernmental Panel on Climate Change*. Cambridge, United Kingdom and New York, NY, USA: Cambridge University Press, pp. 33–115. doi: 10.1017/CBO9781107415324.005.
Stolzenburg, M. (1988) 'An ultrafine aerosol size distribution measuring system', (JANUARY 1988). Available at: https://www.researchgate.net/publication/230691922_An_Ultrafine_Aerosol_Size_Distribution_System.
Stolzenburg, M. R. and McMurry, P. H. (2008) 'Equations Governing Single and Tandem DMA Configurations and a New Lognormal Approximation to the Transfer Function', *Aerosol Science and Technology*, 42(6), pp. 421–432. doi: 10.1080/02786820802157823.
Subramanian, R. *et al.* (2007) 'Yellow Beads and Missing Particles: Trouble Ahead for Filter-Based Absorption Measurements', pp. 630–637. doi: 10.1080/02786820701344589.
Subramanian, R. *et al.* (2010) 'Black carbon over Mexico: The effect of atmospheric transport on mixing state, mass absorption cross-section, and BC/CO ratios', *Atmospheric Chemistry and Physics*, 10(1), pp. 219–237. doi: 10.5194/acp-10-219-2010.
Taylor, K. E., Stouffer, R. J. and Meehl, G. A. (2012) 'An overview of CMIP5 and the experiment design', *Bulletin of the American Meteorological Society*, 93(4), pp. 485–498. doi: 10.1175/BAMS-D-11-00094.1.
Textor, C. *et al.* (2006) 'Analysis and quantification of the diversities of aerosol

life cycles within AeroCom', *Atmospheric Chemistry and Physics*, 6(7), pp. 1777–1813. doi: 10.5194/acp-6-1777-2006.
Tian, G., Moosmüller, H. and Arnott, P. W. (2009) 'Simultaneous photoacoustic spectroscopy of aerosol and oxygen A-band absorption for the calibration of aerosol light absorption measurements', *Aerosol Science and Technology*, 43(11), pp. 1084–1090. doi: 10.1080/02786820903170972.
Tian, L. and Curry, J. A. (1989) 'Cloud overlap statistics', *Journal of Geophysical Research*, 94(D7), pp. 9925–9935. doi: 10.1029/JD094iD07p09925.
Toll, V. *et al.* (2017) 'Volcano and Ship Tracks Indicate Excessive Aerosol-Induced Cloud Water Increases in a Climate Model', *Geophysical Research Letters*, 44(24), p. 12,492-12,500. doi: 10.1002/2017GL075280.
Trembath, J., Bart, M. and Brooke, J. (2012) *FAAM Technical Note: Efficiencies of Modified Rosemount Housings for sampling Aerosol on a Fast Atmospheric Research Aircraft*. Cranfield, UK. Available at: https://www.faam.ac.uk/index.php/faam-documents/science-instruments/1673-inlet-efficiency/file.
Twomey, S. (1974) 'Pollution and the Planetary Albedo', *Atmospheric Environment*, 8(12), pp. 1251–1256. doi: 10.1016/0004-6981(74)90004-3.
Unno, W. and Spiegel, E. A. (1966) 'The Eddington Approximation in the Radiative Heat Equation', *Publications of the Astronomical Society of Japan*, 18(2), pp. 85–95.
Vaughan, M. A. *et al.* (2004) 'Fully automated analysis of space-based lidar data: an overview of the CALIPSO retrieval algorithms and data products', *Laser Radar Techniques for Atmospheric Sensing*, 5575, p. 15. doi: 10.1117/12.572024.
Virkkula, A. *et al.* (2005) 'Modification, Calibration and a Field Test of an Instrument for Measuring Light Absorption by Particles', *Aerosol Science and Technology*, 39(1), pp. 68–83. doi: 10.1080/027868290901963.
Virkkula, A. (2010) 'Correction of the Calibration of the 3-wavelength Particle Soot Absorption Photometer (3λ PSAP)', *Aerosol Science and Technology*, 44(8), pp. 706–712. doi: 10.1080/02786826.2010.482110.
van Vuuren, D. P. *et al.* (2011) 'RCP2.6: Exploring the possibility to keep global mean temperature increase below 2°C', *Climatic Change*, 109(1), pp. 95–116. doi: 10.1007/s10584-011-0152-3.
Wallace, J. M. and Hobbs, P. V. (2006) *Atmospheric Science: An Introductory Survey*. Second. Burlington, Massachusetts: Elsevier.
Walters, D. *et al.* (2017) 'The Met Office Unified Model Global Atmosphere 6.0/6.1 and JULES Global Land 6.0/6.1 configurations', *Geoscientific Model Development*, 10(4), pp. 1487–1520. doi: 10.5194/gmd-10-1487-2017.
Wang, X. *et al.* (2014) 'Exploiting simultaneous observational constraints on mass and absorption to estimate the global direct radiative forcing of black carbon and brown carbon', *Atmospheric Chemistry and Physics*, 14(20), pp. 10989–11010. doi: 10.5194/acp-14-10989-2014.
Wang, X. *et al.* (2016) 'Deriving brown carbon from multiwavelength absorption measurements: Method and application to AERONET and Aethalometer observations', *Atmospheric Chemistry and Physics*, 16(19), pp. 12733–12752. doi: 10.5194/acp-16-12733-2016.
Wang, X. *et al.* (2018) 'Exploring the observational constraints on the simulation of brown carbon', *Atmospheric Chemistry and Physics*, 18(2), pp. 635–653. doi: 10.5194/acp-18-635-2018.

Waquet, F. *et al.* (2013) 'Retrieval of aerosol microphysical and optical properties above liquid clouds from POLDER/PARASOL polarization measurements', *Atmospheric Measurement Techniques*, 6(4), pp. 991–1016. doi: 10.5194/amt-6-991-2013.
Weigum, N. M. *et al.* (2012) 'Scales of variability of black carbon plumes over the Pacific Ocean', *Geophysical Research Letters*, 39(15), pp. 1–5. doi: 10.1029/2012GL052127.
Weigum, N., Schutgens, N. and Stier, P. (2016) 'Effect of aerosol subgrid variability on aerosol optical depth and cloud condensation nuclei: Implications for global aerosol modelling', *Atmospheric Chemistry and Physics*, 16(21), pp. 13619–13639. doi: 10.5194/acp-16-13619-2016.
Weingartner, E. *et al.* (2003) 'Absorption of light by soot particles: Determination of the absorption coefficient by means of aethalometers', *Journal of Aerosol Science*, 34(10), pp. 1445–1463. doi: 10.1016/S0021-8502(03)00359-8.
van der Werf, G. R. *et al.* (2010) 'Global fire emissions and the contribution of deforestation, savanna, forest, agricultural, and peat fires (1997-2009)', *Atmospheric Chemistry and Physics*, 10(23), pp. 11707–11735. doi: 10.5194/acp-10-11707-2010.
van der Werf, G. R. *et al.* (2017) 'Global fire emissions estimates during 1997-2016', *Earth System Science Data*, 9(2), pp. 697–720. doi: 10.5194/essd-9-697-2017.
Werle, P., Miicke, R. and Slemr, F. (1993) 'The limits of signal averaging in atmospheric trace-gas monitoring by tunable diode-laser absorption spectroscopy (TDLAS)', *Applied Physics B*, 57(2), pp. 131–139. doi: 10.1007/BF00425997.
Westerling, A. L. *et al.* (2006) 'Warming and earlier spring increase Western U.S. forest wildfire activity', *Science*, 313(5789), pp. 940–943. doi: 10.1126/science.1128834.
Wheeler, M. D. *et al.* (1998) 'Cavity Ring-Down Spectroscopy', *Journal of the Chemical Society, Faraday Transactions*, 94(3), pp. 337–351. doi: 10.1039/A707686J.
Wiedensohler, A. (1988) 'An approximation of the bipolar charge distribution for particles in the submicron size range', *Journal of Aerosol Science*, 19(3), pp. 387–389. doi: 10.1016/0021-8502(88)90278-9.
Wiedensohler, A. *et al.* (2012) 'Mobility particle size spectrometers: Harmonization of technical standards and data structure to facilitate high quality long-term observations of atmospheric particle number size distributions', *Atmospheric Measurement Techniques*, 5(3), pp. 657–685. doi: 10.5194/amt-5-657-2012.
Williams, J. *et al.* (2002) 'and Physics Application of the variability-size relationship to atmospheric aerosol studies : estimating aerosol lifetimes and ages', pp. 133–145.
Winker, D. M. *et al.* (2013) 'The global 3-D distribution of tropospheric aerosols as characterized by CALIOP', *Atmospheric Chemistry and Physics*, 13(6), pp. 3345–3361. doi: 10.5194/acp-13-3345-2013.
Winker, D. M., Hunt, W. H. and McGill, M. J. (2007) 'Initial performance assessment of CALIOP', *Geophysical Research Letters*, 34(19), pp. 1–5. doi: 10.1029/2007GL030135.
World Health Organization (2006) 'WHO Air quality guidelines for particulate matter, ozone, nitrogen dioxide and sulfur dioxide: global update 2005: summary of risk assessment', *Geneva: World Health Organization*, pp. 1–

22. doi: 10.1016/0004-6981(88)90109-6.
Yang, M. *et al.* (2009) 'Attribution of aerosol light absorption to black carbon, brown carbon, and dust in China - Interpretations of atmospheric measurements during EAST-AIRE', *Atmospheric Chemistry and Physics*, 9(6), pp. 2035–2050. doi: 10.5194/acp-9-2035-2009.
Young, S. A. *et al.* (2013) 'The Retrieval of Profiles of Particulate Extinction from Cloud–Aerosol Lidar and Infrared Pathfinder Satellite Observations (CALIPSO) Data: Uncertainty and Error Sensitivity Analyses', *Journal of Atmospheric and Oceanic Technology*, 30(3), pp. 395–428. doi: 10.1175/JTECH-D-12-00046.1.
Yu, H. *et al.* (2006) 'A review of measurement-based assessments of the aerosol direct radiative effect and forcing', *Atmospheric Chemistry and Physics*, 6(3), pp. 613–666. doi: 10.5194/acp-6-613-2006.
Zalicki, P. and Zare, R. N. (1995) 'Cavity ring-down spectroscopy for quantitative absorption measurements', *Journal of Chemical Physics*, 102(7), pp. 2708–2717. doi: 10.1063/1.468647.
Zarzana, K. J., Cappa, C. D. and Tolbert, M. A. (2014) 'Sensitivity of aerosol refractive index retrievals using optical spectroscopy', *Aerosol Science and Technology*, 48(11), pp. 1133–1144. doi: 10.1080/02786826.2014.963498.
Zarzycki, C. M. and Bond, T. C. (2010) 'How much can the vertical distribution of black carbon affect its global direct radiative forcing?', *Geophysical Research Letters*, 37(20), pp. 1–6. doi: 10.1029/2010GL044555.
Zaveri, R. A. *et al.* (2010) 'Particle-resolved simulation of aerosol size, composition, mixing state, and the associated optical and cloud condensation nuclei activation properties in an evolving urban plume', *Journal of Geophysical Research Atmospheres*, 115(17), pp. 1–19. doi: 10.1029/2009JD013616.
Zaveri, R. A. *et al.* (2012) 'Overview of the 2010 Carbonaceous Aerosols and Radiative Effects Study (CARES)', *Atmospheric Chemistry and Physics*, 12(16), pp. 7647–7687. doi: 10.5194/acp-12-7647-2012.
Zdunkowski, W., Trautmann, T. and Bott, A. (2007) *Radiation in the Atmosphere: A Course in Theoretical Meteorology*. Cambridge: Cambridge University Press.
Zhang, Z. *et al.* (2016) 'Shortwave direct radiative effects of above-cloud aerosols over global oceans derived from 8 years of CALIOP and MODIS observations', *Atmospheric Chemistry and Physics*, 16(5), pp. 2877–2900. doi: 10.5194/acp-16-2877-2016.
Zhou, M. *et al.* (2005) 'A normalized description of the direct effect of key aerosol types on solar radiation as estimated from Aerosol Robotic Network aerosols and Moderate Resolution Imaging Spectroradiometer albedos', *Journal of Geophysical Research*, 110(D19), pp. 1–10. doi: 10.1029/2005JD005909.
Zhu, C.-S. *et al.* (2017) 'Spectral dependence of aerosol light absorption at an urban and a remote site over the Tibetan Plateau', *Science of the Total Environment*, 590–591(97), pp. 14–21. doi: 10.1016/j.scitotenv.2017.03.057.
Zuidema, P. *et al.* (2016) 'Smoke and clouds above the southeast Atlantic: Upcoming field campaigns probe absorbing aerosol's impact on climate', *Bulletin of the American Meteorological Society*, 97(7), pp. 1131–1135. doi: 10.1175/BAMS-D-15-00082.1.

Appendices

A) Detailed EXSCALABAR flow diagram.

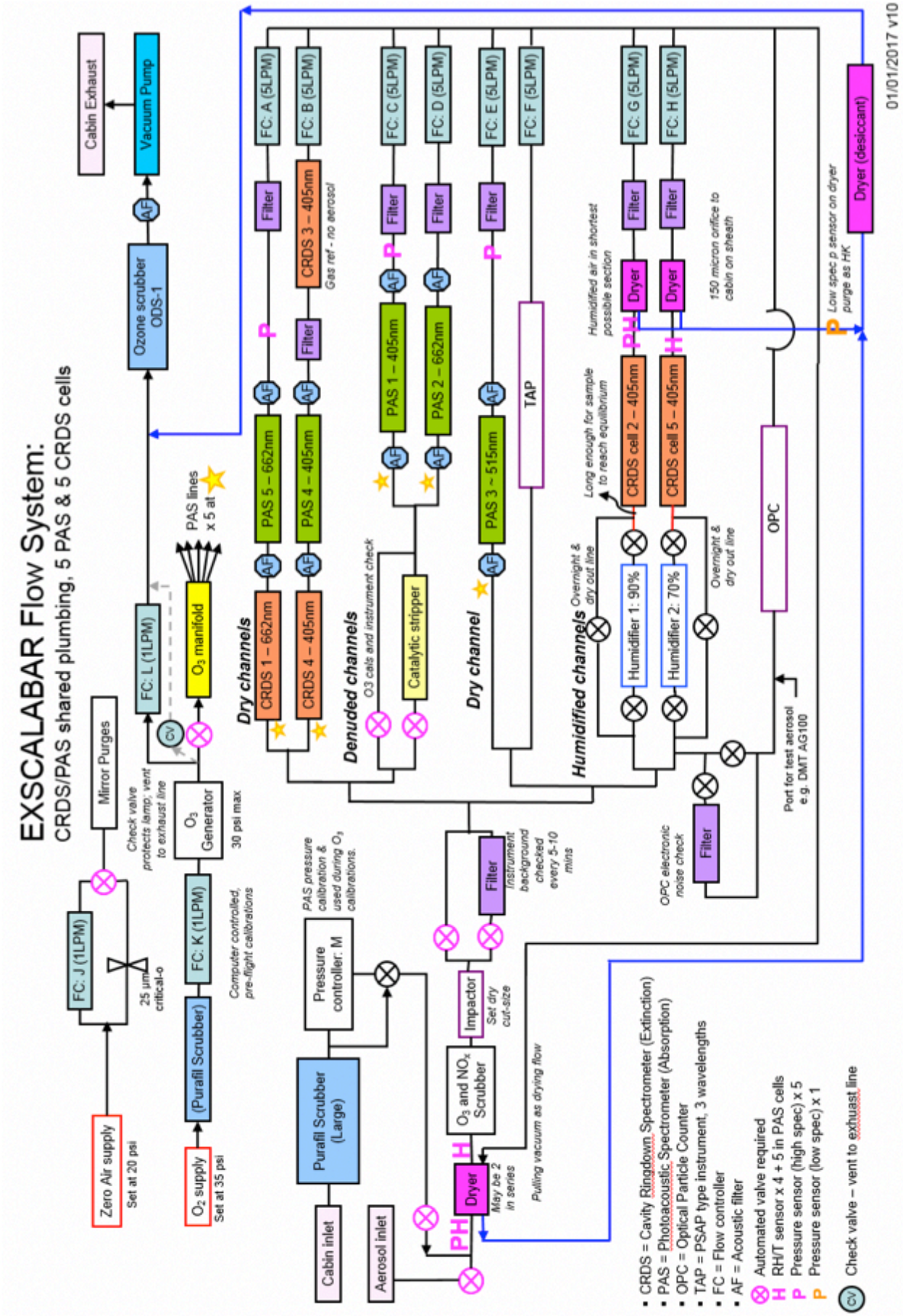

B) TAP biases as a function of organic aerosol concentration.

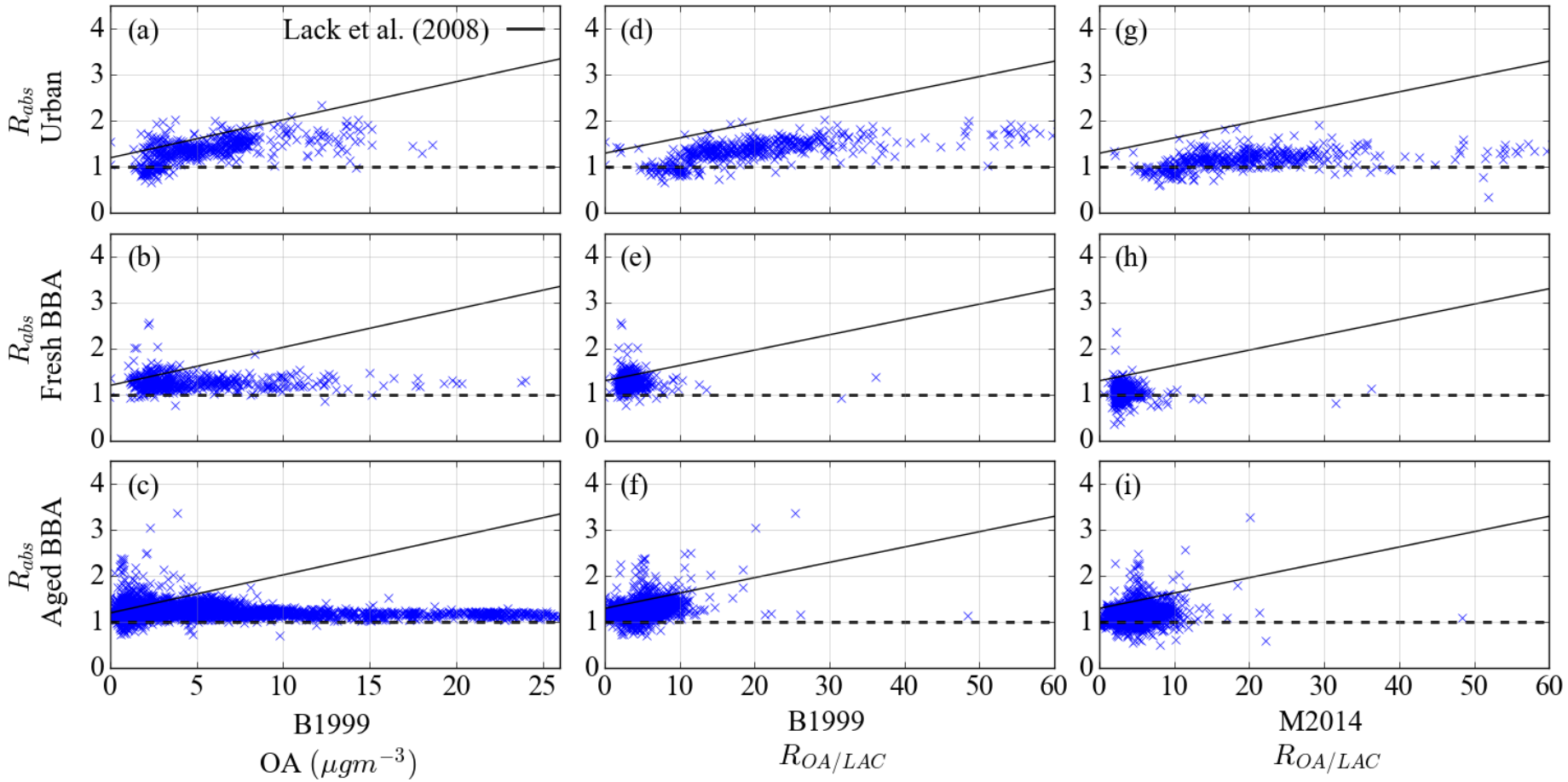

Figure B1: *The ratio of TAP to PAS absorption coefficients at 467 nm as a function of the organic aerosol mass concentration using the B1999 correction scheme (a-c) and as a function of the ratio of the organic aerosol to light-absorbing carbon mass concentrations when using the B1999 correction scheme (d-f) and using the M2014 correction scheme (g-i). All absorption coefficients correspond to > 1 Mm^{-1}.*

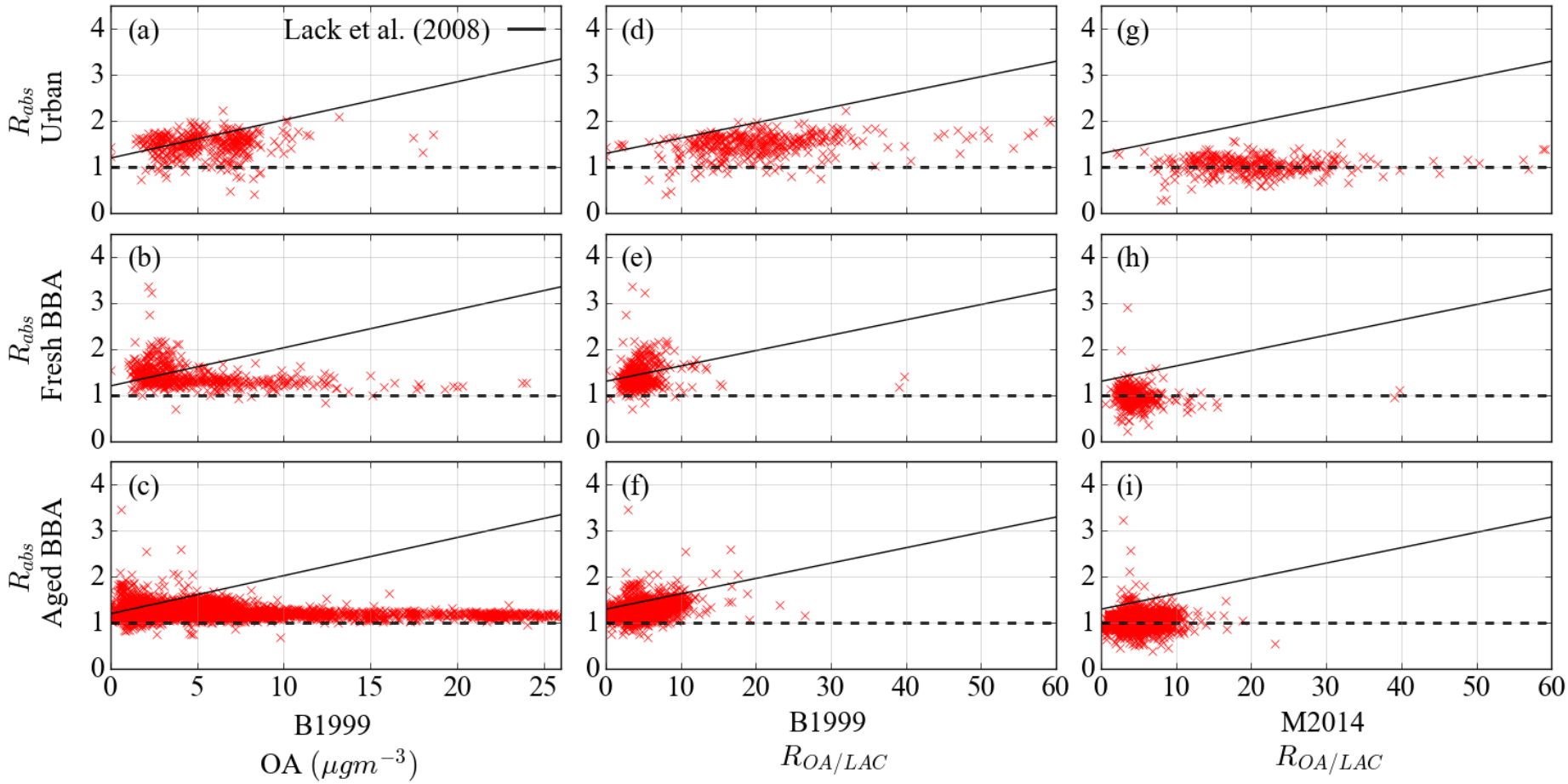

Figure B2: *The ratio of TAP to PAS absorption coefficients at 652 nm as a function of the organic aerosol mass concentration using the B1999 correction scheme (a-c) and as a function of the ratio of the organic aerosol to light-absorbing carbon mass concentrations when using the B1999 correction scheme (d-f) and using the M2014 correction scheme (g-i). All absorption coefficients correspond to > 1 Mm^{-1}.*

C) HadGEM3 simulations

Figures C1–C4 show the above cloud aerosol optical depth (ACAOD) derived using a cloud top height defined when the cloud liquid water content was greater than a pre-set threshold in the range 5×10^{-5} to 1×10^{-6} kg kg^{-1} for the N96 climate model simulations. Figures C5–C8 show the above cloud single scattering albedo (ACSSA) using the same cloud-top cloud liquid water content thresholds. This analysis was repeated using N216 climate model simulations, which are shown in figures C9–C12 and C13–C16 for the ACAOD and ACSSA, respectively. This analysis was also repeated using N512 climate model simulations, which are shown in figures C17–C20 and C21–C24 for the ACAOD and ACSSA, respectively.

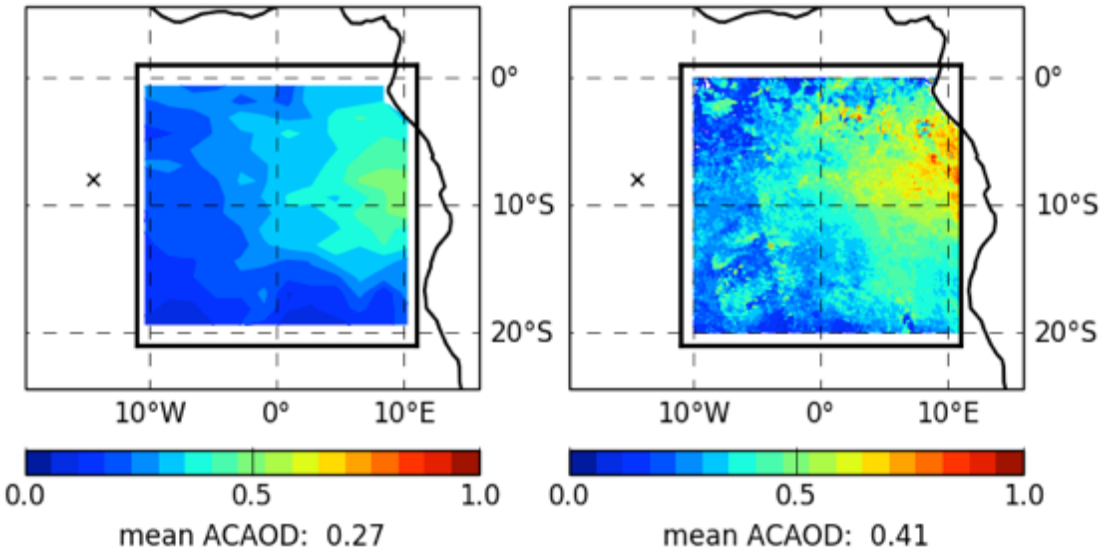

Figure C1: *Mean above cloud aerosol optical depth (ACAOD) for August and September 2006. HadGEM3 is on the left (N96), which was filtered according to Table 5.2. POLDER retrievals are on the right. The cloud top height diagnostic started at an altitude of 3500 m above ground level with a cloud liquid water content threshold of 5×10^{-5} kg kg^{-1}.*

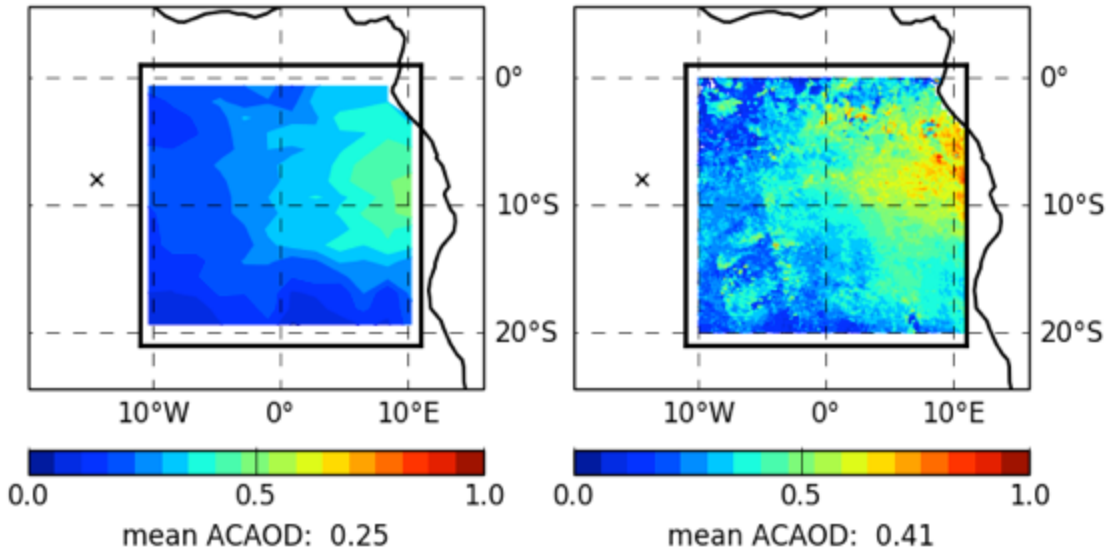

Figure C2: *As Figure C1 except that the cloud liquid water content threshold was 1×10^{-5} kg kg^{-1}.*

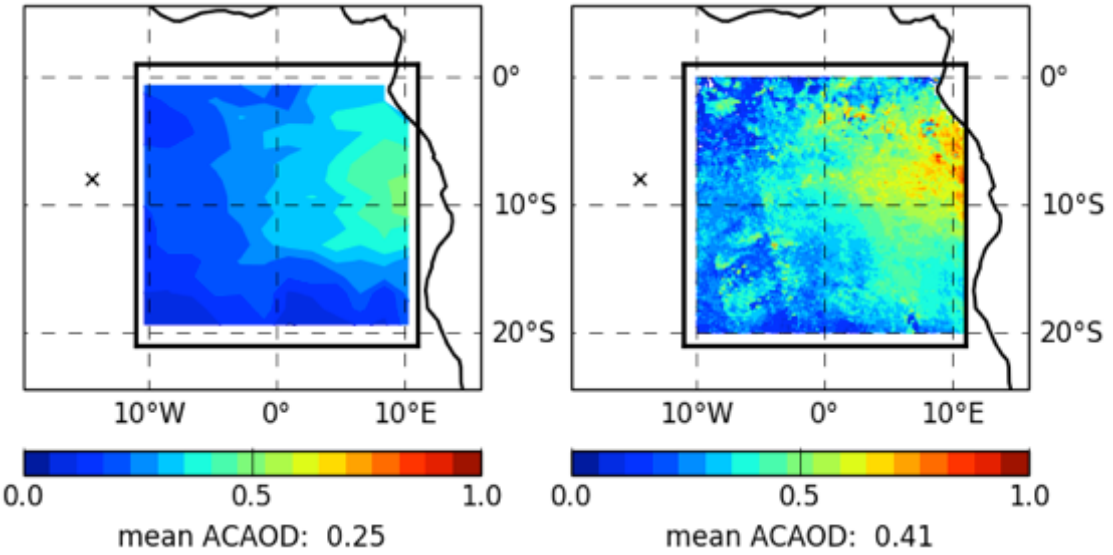

Figure C3: *As Figure C1 except that the cloud liquid water content threshold was 5×10^{-6} kg kg^{-1}.*

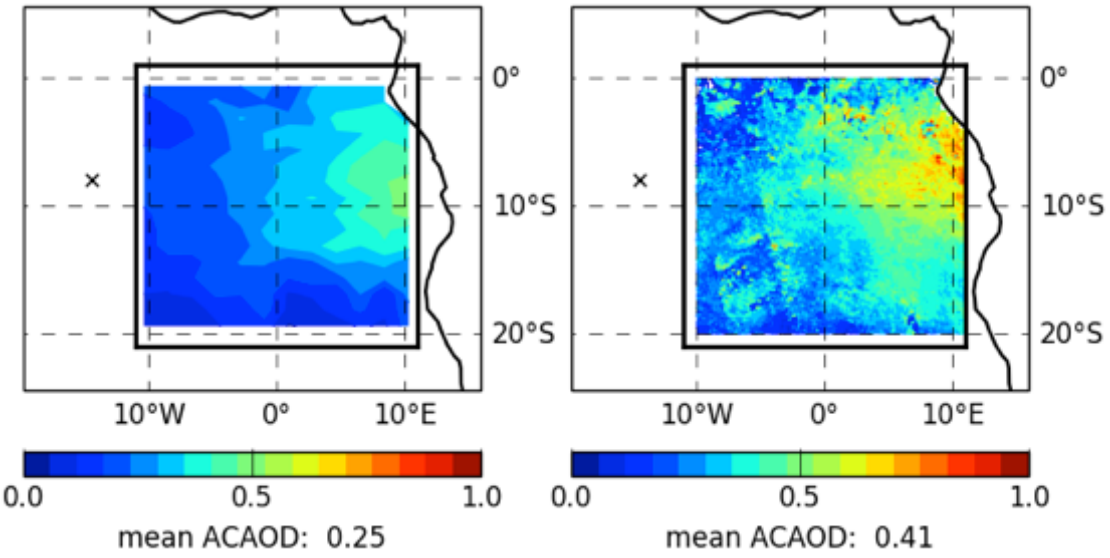

Figure C4: *As Figure C1 except that the cloud liquid water content threshold was 1×10^{-6} kg kg^{-1}.*

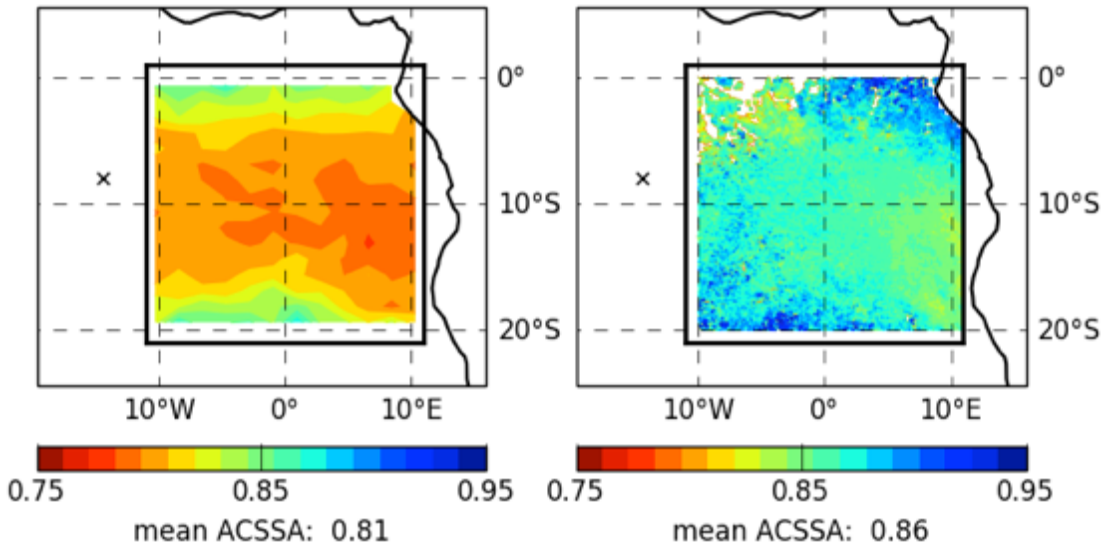

Figure C5: *Mean above cloud single scattering albedo (ACSSA) for August and September 2006. HadGEM3 is on the left (N96), which was filtered according to Table 5.2. POLDER retrievals are on the right. The cloud top height diagnostic started at an altitude of 3500 m above ground level with a cloud liquid water content threshold of 5×10^{-5} kg kg^{-1}.*

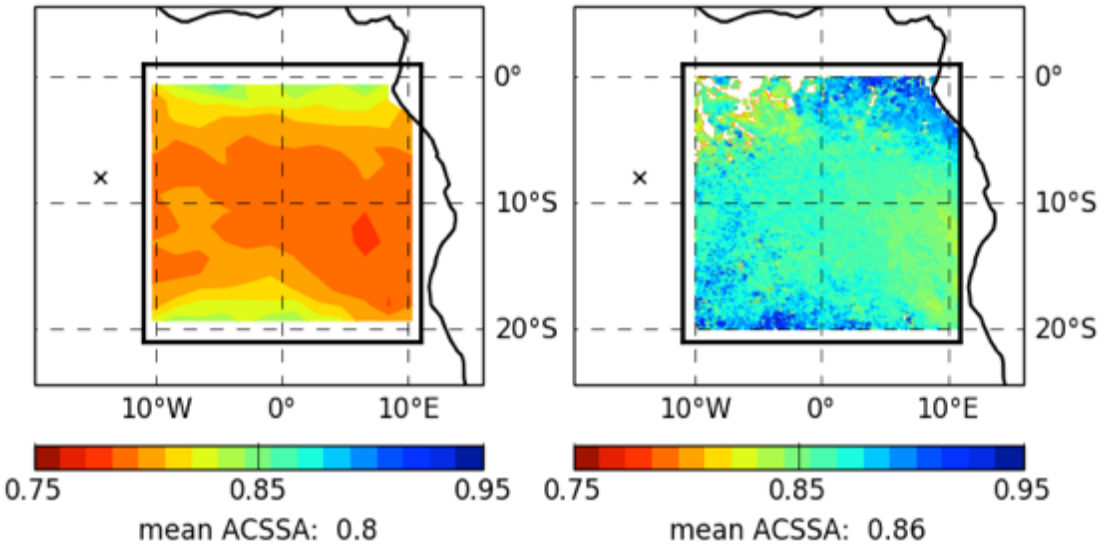

Figure C6: *As Figure C5 except that the cloud liquid water content threshold was 1×10^{-5} kg kg^{-1}.*

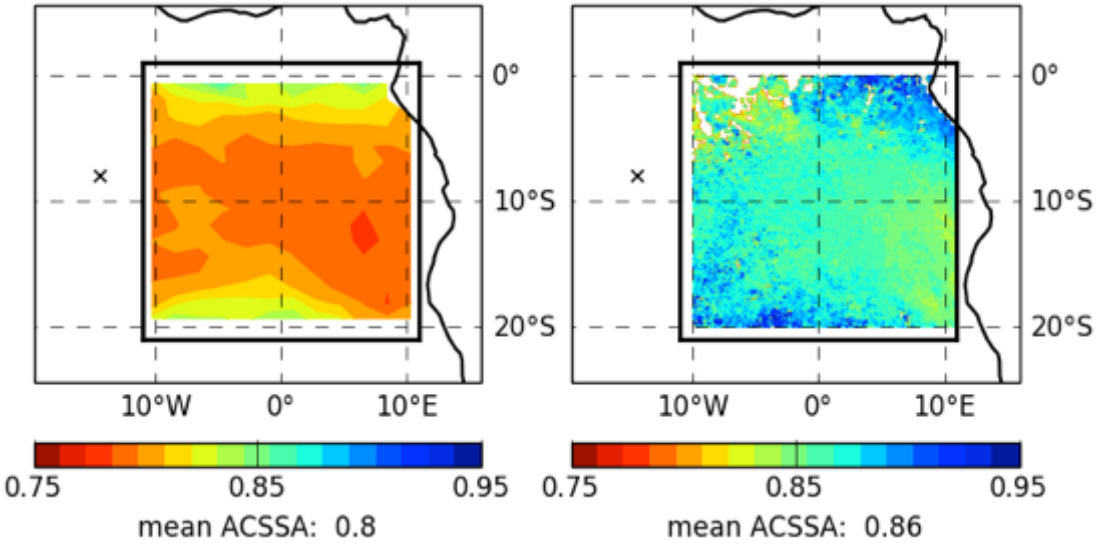

Figure C7: *As Figure C5 except that the cloud liquid water content threshold was 5×10^{-6} kg kg^{-1}.*

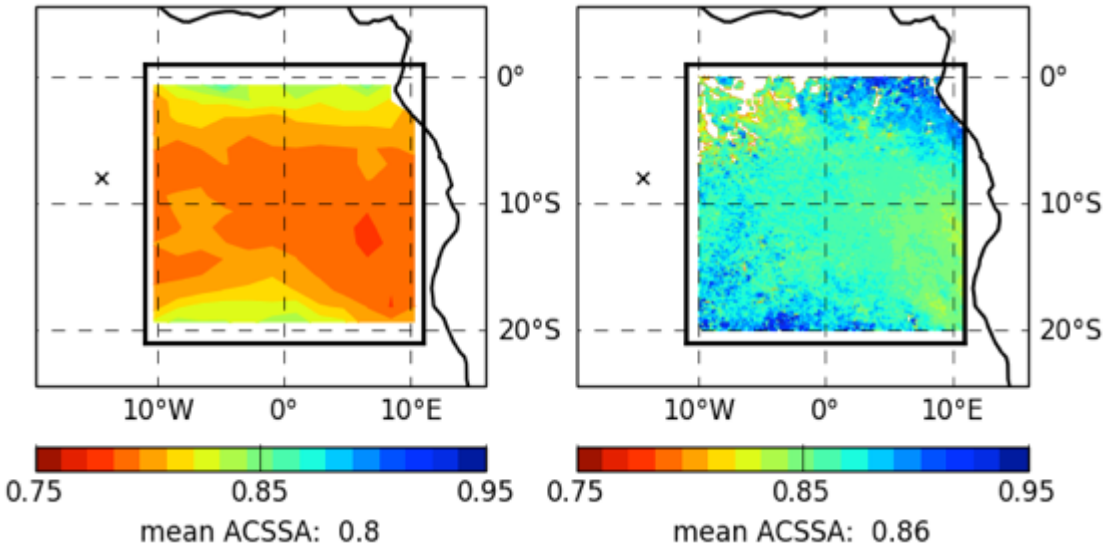

Figure C8: *As Figure C5 except that the cloud liquid water content threshold was 1×10^{-6} kg kg^{-1}.*

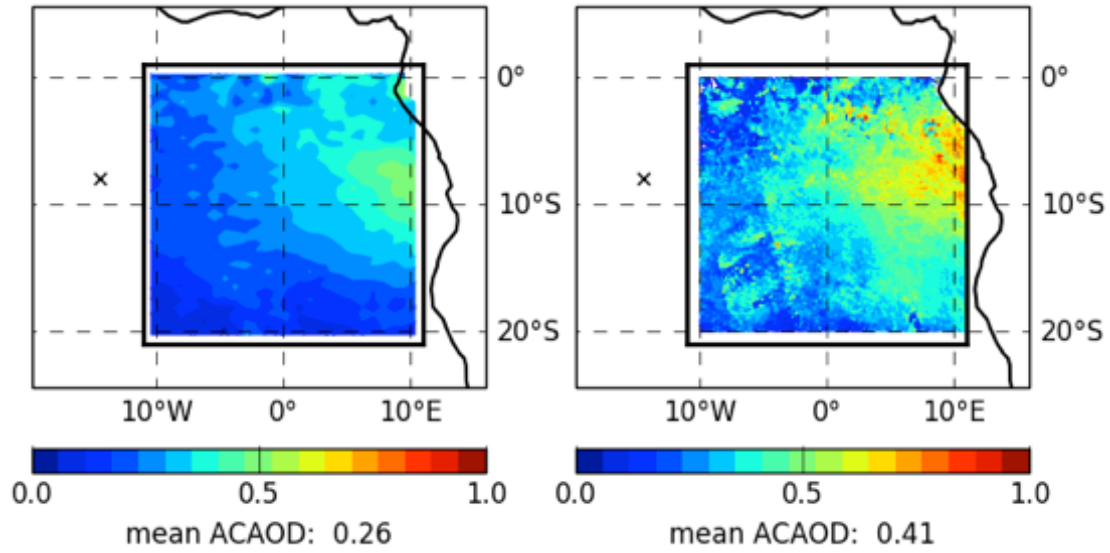

Figure C9: *Mean above cloud aerosol optical depth (ACAOD) for August and September 2006. HadGEM3 is on the left (N216), which was filtered according to Table 5.2. POLDER retrievals are on the right. The cloud top height diagnostic started at an altitude of 3500 m above ground level with a cloud liquid water content threshold of 5×10^{-5} kg kg^{-1}.*

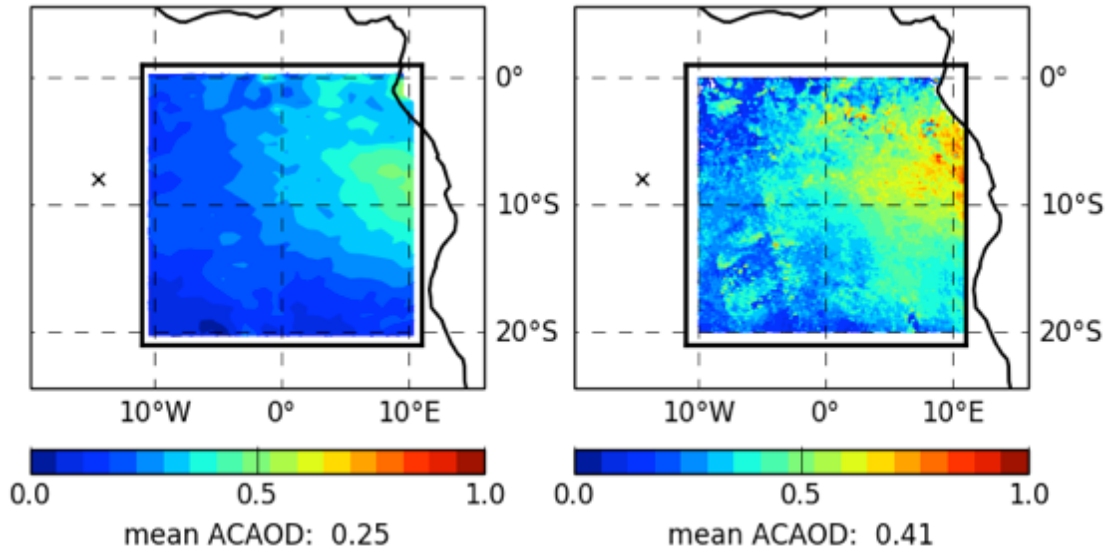

Figure C10: *As Figure C9 except that the cloud liquid water content threshold was 1×10^{-5} kg kg^{-1}.*

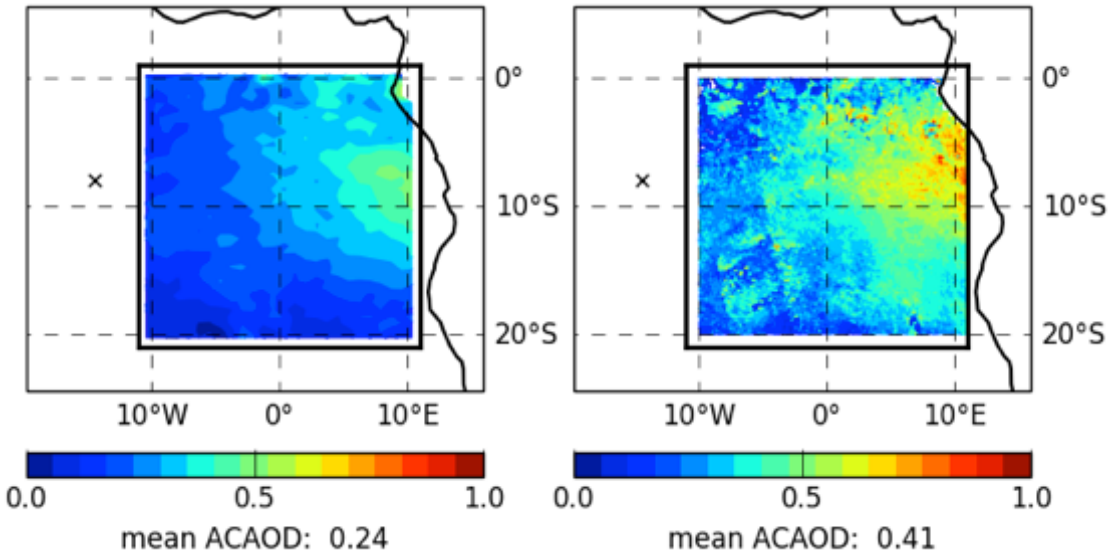

Figure C11: *As Figure C9 except that the cloud liquid water content threshold was 5×10^{-6} kg kg^{-1}.*

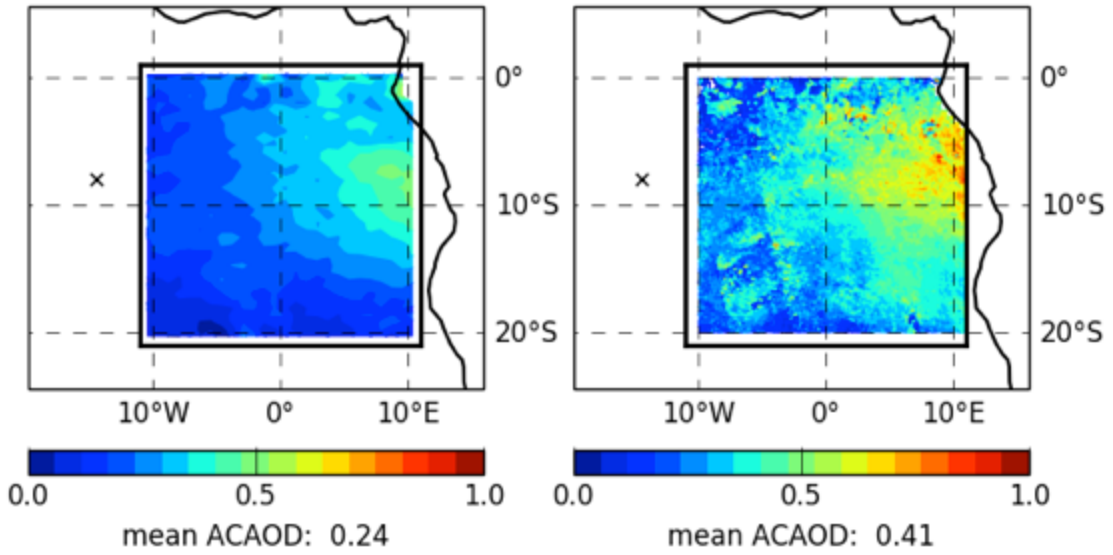

Figure C12: *As Figure C9 except that the cloud liquid water content threshold was 1×10^{-6} kg kg^{-1}.*

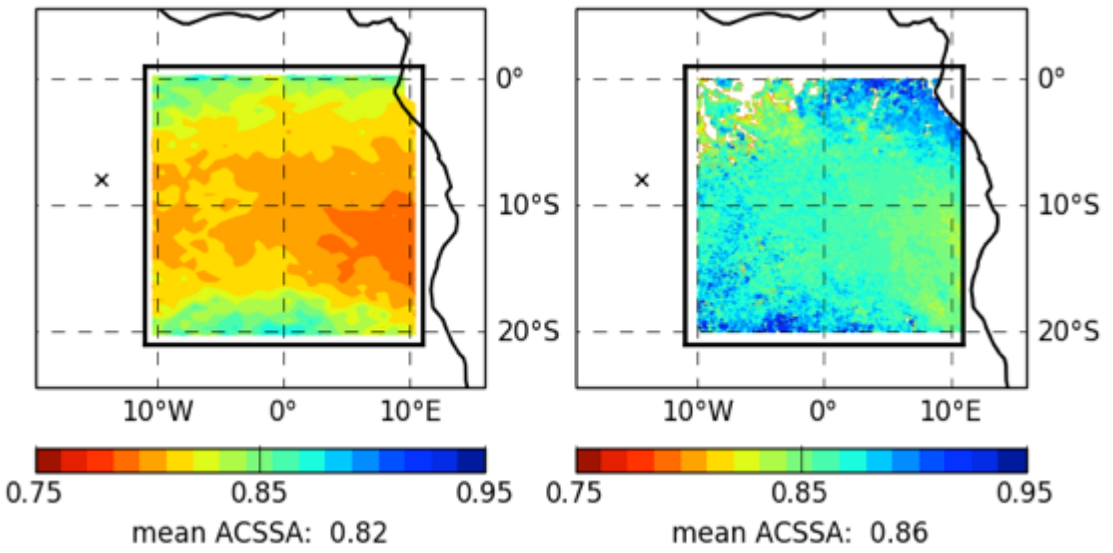

Figure C13: *Mean above cloud single scattering albedo (ACSSA) for August and September 2006. HadGEM3 is on the left (N216), which was filtered according to Table 5.2. POLDER retrievals are on the right. The cloud top height diagnostic started at an altitude of 3500 m above ground level with a cloud liquid water content threshold of 5×10^{-5} kg kg^{-1}.*

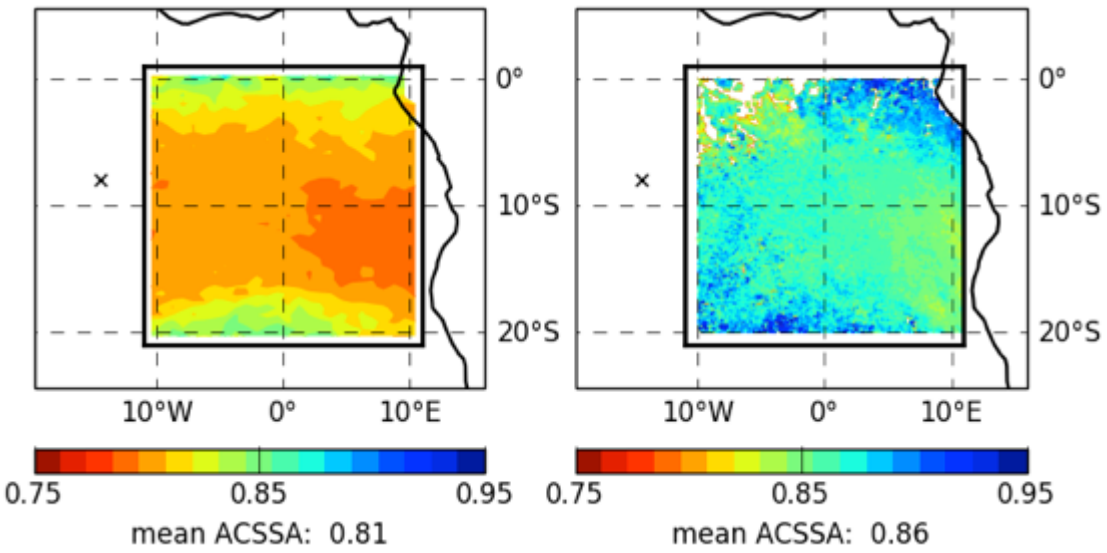

Figure C14: *As Figure C13 except that the cloud liquid water content threshold was 1×10^{-5} kg kg^{-1}.*

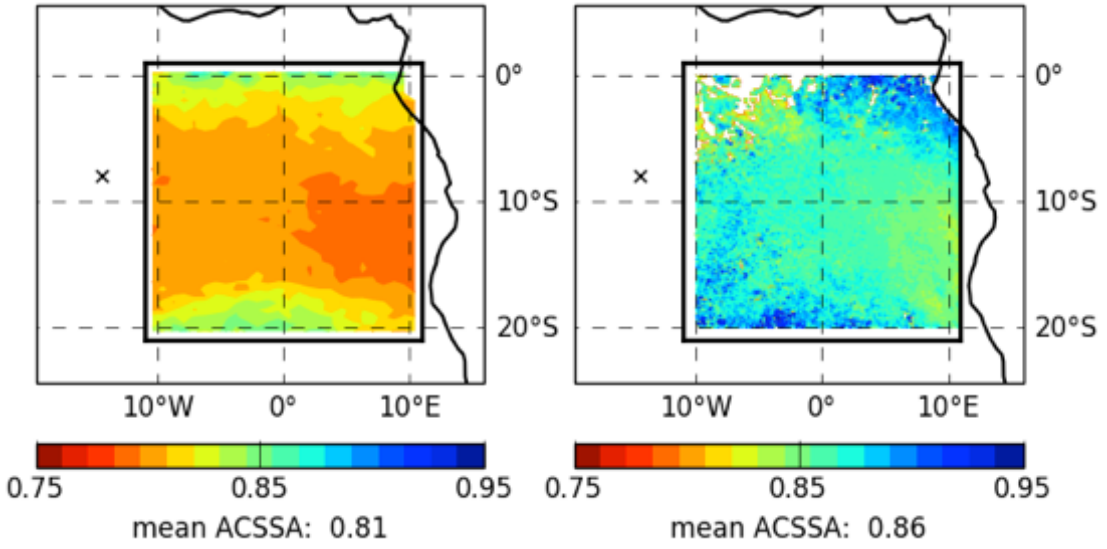

Figure C15: *As Figure C13 except that the cloud liquid water content threshold was 5×10^{-6} kg kg^{-1}.*

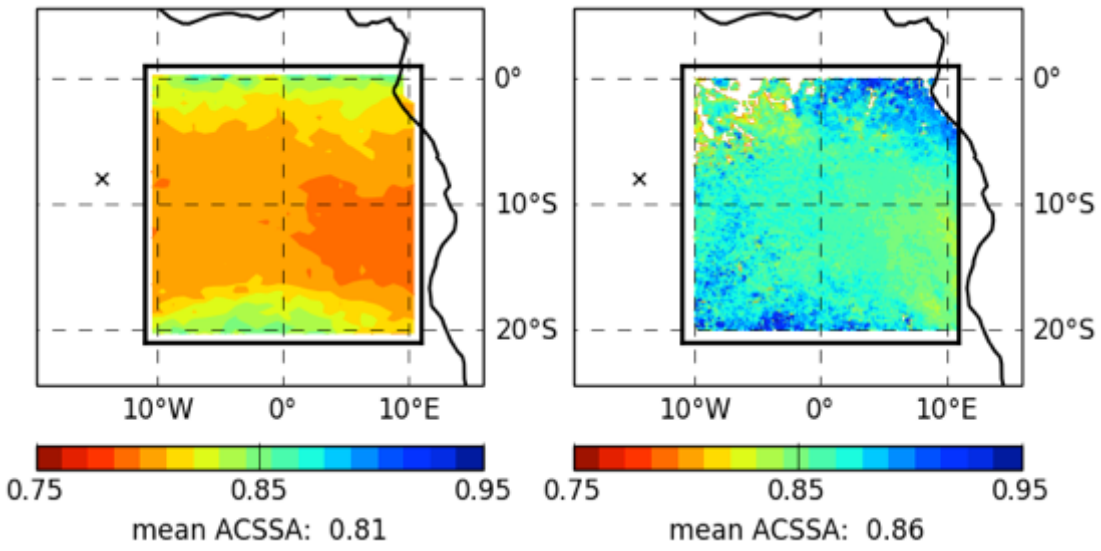

Figure C16: *As Figure C13 except that the cloud liquid water content threshold was 1×10^{-6} kg kg^{-1}.*

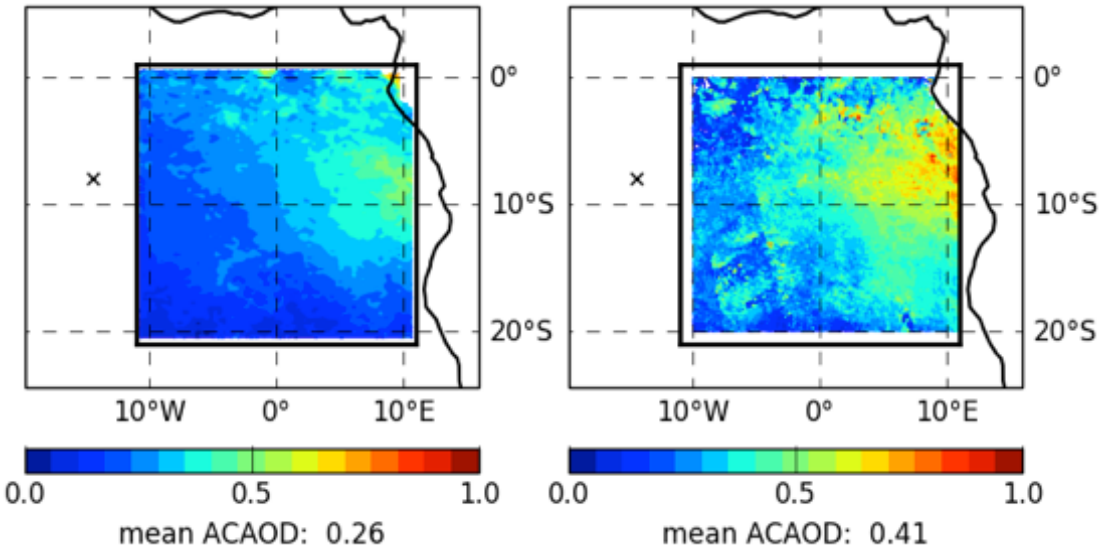

Figure C17: *Mean above cloud aerosol optical depth (ACAOD) for August and September 2006. HadGEM3 is on the left (N512), which was filtered according to Table 5.2. POLDER retrievals are on the right. The cloud top height diagnostic started at an altitude of 3500 m above ground level with a cloud liquid water content threshold of 5×10^{-5} kg kg^{-1}.*

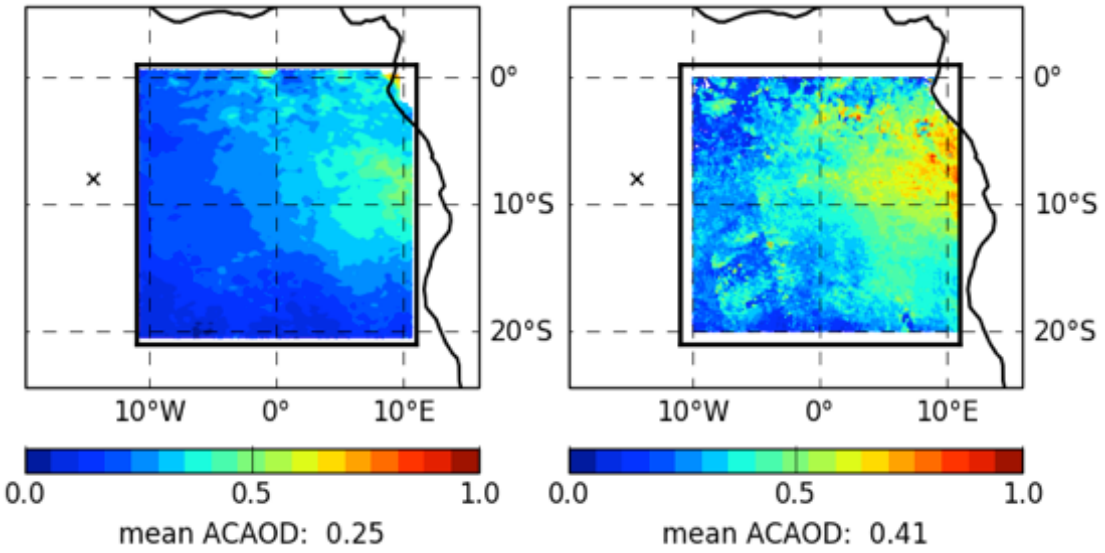

Figure C18: *As Figure C17 except that the cloud liquid water content threshold was 1×10^{-5} kg kg^{-1}.*

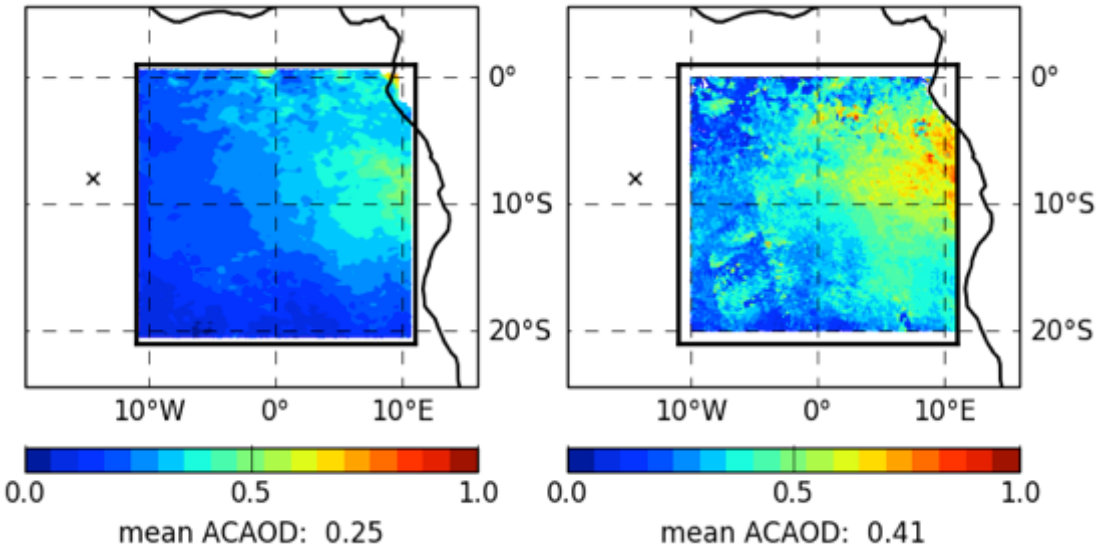

Figure C19: *As Figure C17 except that the cloud liquid water content threshold was 5×10^{-6} kg kg^{-1}.*

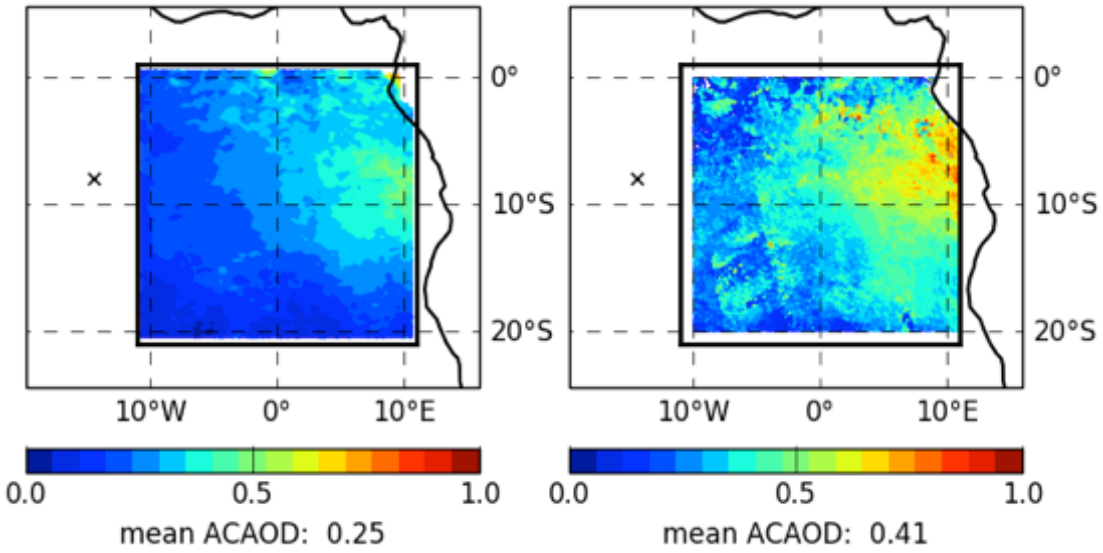

Figure C20: *As Figure C17 except that the cloud liquid water content threshold was 1×10^{-6} kg kg^{-1}.*

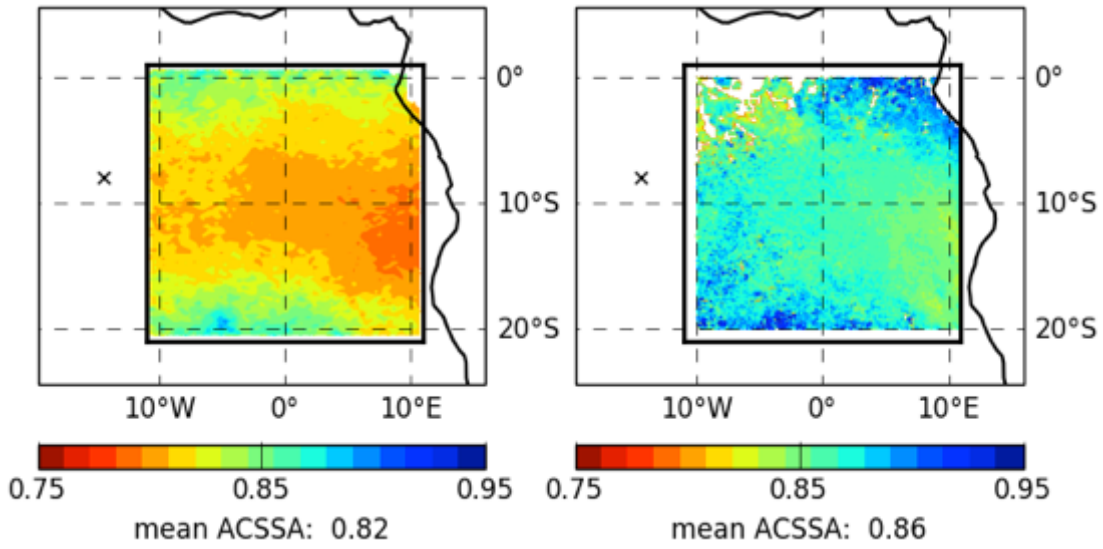

Figure C21: *Mean above cloud single scattering albedo (SSA) for August and September 2006. HadGEM3 is on the left (N512), which was filtered according to Table 5.2. POLDER retrievals are on the right. The cloud top height diagnostic started at an altitude of 3500 m above ground level with a cloud liquid water content threshold of 5×10^{-5} kg kg^{-1}.*

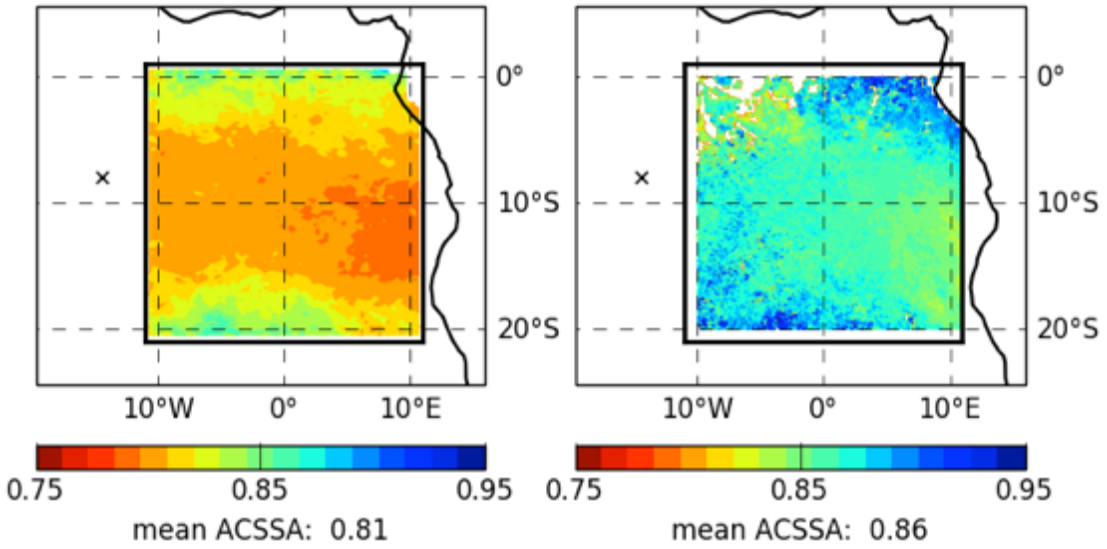

Figure C22: *As Figure C21 except that the cloud liquid water content threshold was 1×10^{-5} kg kg^{-1}.*

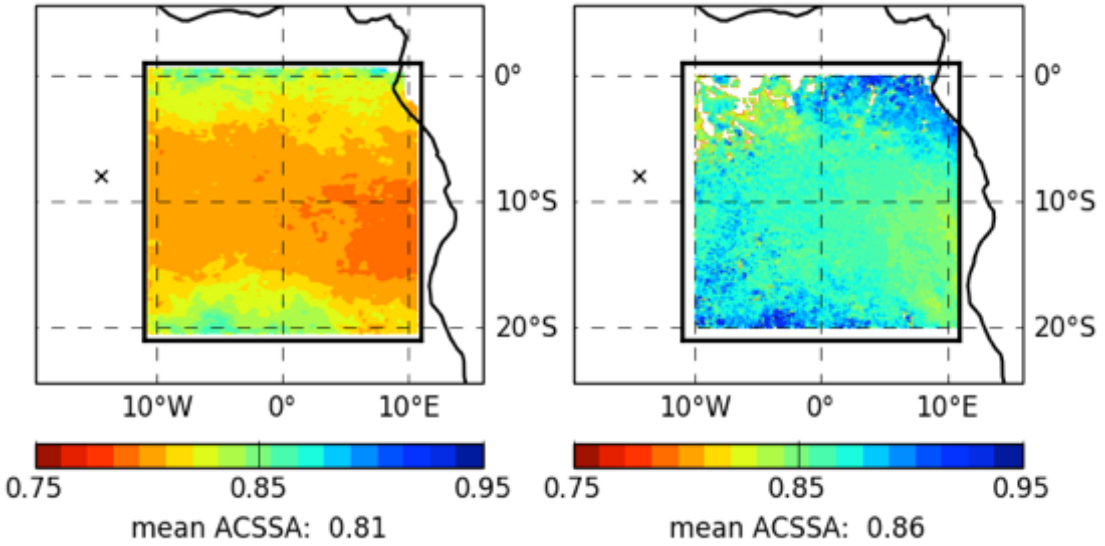

Figure C23: *As Figure C21 except that the cloud liquid water content threshold was 5×10^{-6} kg kg^{-1}.*

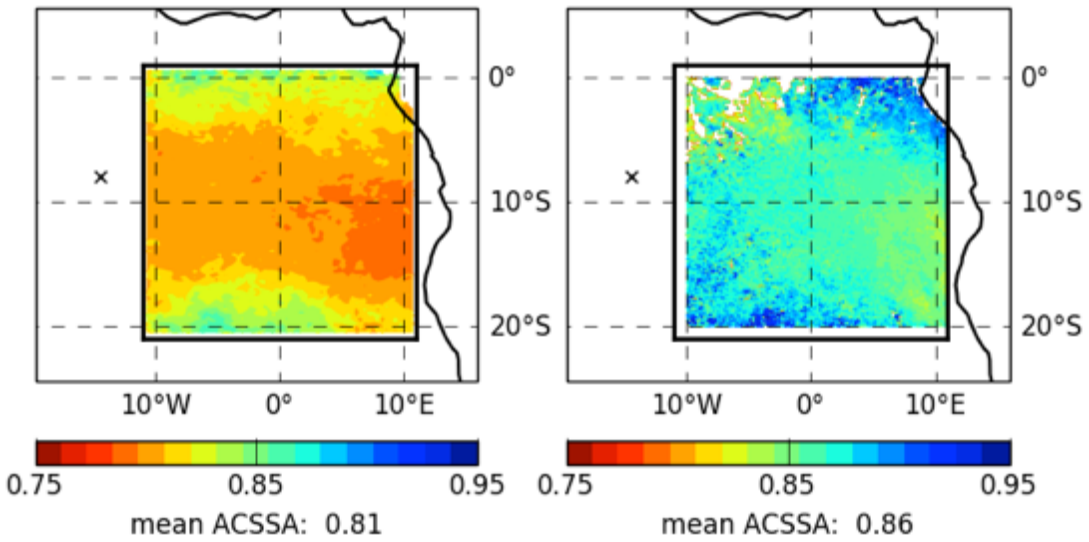

Figure C24: *As Figure C21 except that the cloud liquid water content threshold was 1×10^{-6} kg kg^{-1}.*

D) Davies, N. W. *et al.* (2018) 'On the accuracy of aerosol photoacoustic spectrometer calibrations using absorption by ozone', *Atmospheric Measurement Techniques*, 11(4), pp. 2313–2324. doi: 10.5194/amt-11-2313-2018.

Atmos. Meas. Tech., 11, 2313–2324, 2018
https://doi.org/10.5194/amt-11-2313-2018

Atmospheric Measurement Techniques
Open Access
EGU

On the accuracy of aerosol photoacoustic spectrometer calibrations using absorption by ozone

Nicholas W. Davies[1,2], **Michael I. Cotterell**[1,2], **Cathryn Fox**[2], **Kate Szpek**[2], **Jim M. Haywood**[1,3], **and Justin M. Langridge**[2]

[1]College of Engineering, Mathematics and Physical Sciences, University of Exeter, Exeter, EX4 4QF, UK
[2]Observation Based Research, Met Office, Exeter, EX1 3PB, UK
[3]Earth System and Mitigation Science, Met Office Hadley Centre, Exeter, EX1 3PB, UK

Correspondence: Justin M. Langridge (justin.langridge@metoffice.gov.uk)

Received: 30 November 2017 – Discussion started: 2 January 2018
Revised: 27 March 2018 – Accepted: 3 April 2018 – Published: 24 April 2018

Abstract. In recent years, photoacoustic spectroscopy has emerged as an invaluable tool for the accurate measurement of light absorption by atmospheric aerosol. Photoacoustic instruments require calibration, which can be achieved by measuring the photoacoustic signal generated by known quantities of gaseous ozone. Recent work has questioned the validity of this approach at short visible wavelengths (404 nm), indicating systematic calibration errors of the order of a factor of 2. We revisit this result and test the validity of the ozone calibration method using a suite of multipass photoacoustic cells operating at wavelengths 405, 514 and 658 nm. Using aerosolised nigrosin with mobility-selected diameters in the range 250–425 nm, we demonstrate excellent agreement between measured and modelled ensemble absorption cross sections at all wavelengths, thus demonstrating the validity of the ozone-based calibration method for aerosol photoacoustic spectroscopy at visible wavelengths.

1 Introduction

Uncertainty in the radiative forcing that drives climate change is dominated by the poorly constrained impact of aerosols on Earth's radiation budget, with aerosol–radiation interactions contributing a global mean effective radiative forcing of -0.45 (-0.95 to $+0.05$) W m^{-2} (Myhre et al., 2013; Stocker et al., 2013). Aerosol single-scattering albedo (the ratio of scattering efficiency to total extinction efficiency) is one of the key inputs used in radiative transfer models to represent aerosol optical behaviour and is amongst the largest contributors to uncertainty in direct radiative forcing (McComiskey et al., 2008). The accuracy of the single-scattering albedo is limited by knowledge of aerosol absorption properties (Boucher et al., 2013; Stier et al., 2013). Black carbon, a carbonaceous material formed by incomplete combustion, absorbs strongly at visible wavelengths and has been shown to have significant climate implications (e.g. Bond et al., 2013; Stocker et al., 2013). Evidence also shows that light-absorbing organic aerosols, commonly referred to as brown carbon, absorb strongly towards wavelengths in the ultraviolet (Andreae and Gelencsér, 2006). The optical properties of black and brown carbon are poorly captured in climate models owing in part to a lack of detailed measurements (Alexander et al., 2008; Bond et al., 2013; Cappa et al., 2012; Lack and Cappa, 2010; J. Liu et al., 2015; S. Liu et al., 2015; Myhre et al., 2013; Saleh et al., 2013; Wang et al., 2016).

Traditionally, aerosol absorption coefficients are retrieved via the difference method or by using filter-based absorption photometry. The difference method involves subtracting separate measurements of the scattering coefficient from the extinction coefficient, leading to large uncertainties in the calculated absorption arising from the quadrature combination of errors in the two measurements. These uncertainties in absorption are particularly high at single-scattering albedos corresponding to weakly absorbing aerosols (Bond et al., 1999; Lack et al., 2006; Strawa et al., 2003). Filter-based absorption measurements rely on determining the change in light transmittance across a particle-laden filter. This method is subject to biases and, although a range of correction schemes have been proposed (Arnott et al., 2005; Bond et al.,

1999; Collaud Coen et al., 2010; Müller et al., 2014; Schmid et al., 2006; Virkkula et al., 2005; Virkkula, 2010; Weingartner et al., 2003), aerosol absorption biases in the range of 20–200 % can remain (Backman et al., 2014; Cappa et al., 2008; Lack et al., 2008; Müller et al., 2014). Photoacoustic spectroscopy (PAS) is a state-of-the-art technique that measures absorption directly for particles in their natural suspended state (Arnott et al., 1999). It can be used to differentiate between the absorption enhancement due to the lensing effect of coated black carbon and the absorption contribution due to brown carbon by utilising thermally denuded channels (Lack et al., 2012b). For these reasons, it has become the technique of choice for measuring aerosol absorption.

The PAS principle relies on converting energy from a light source into sound. Light-absorbing media, such as aerosol, transfer intensity-modulated electromagnetic energy into thermal energy that heats the surrounding air. This gaseous heating generates a pressure wave that propagates radially away from the heated aerosol particle. The periodic heating driven by the modulated light beam is performed at the same frequency as a standing acoustic (pressure) wave eigenmode of the photoacoustic cell. Excitation of a PAS cell eigenmode over repeated heating cycles amplifies the photoacoustic pressure signal for detection by a microphone located within the PAS cell (Arnott et al., 1999; Miklós et al., 2001; Moosmüller et al., 2009). The amplitude of the microphone signal at the modulation frequency is related to the sample absorption coefficient through calibration. Multipass optics are commonly used to increase the circulating light intensity within the PAS cell, which provides increased sensitivity through increased sample heating. This approach is advantageous for aerosol studies compared to single-pass methods employing higher-powered lasers, as it increases sampling heating without exposing individual particles to large temperature changes which could lead to loss of semivolatile species through evaporation (Lack et al., 2006; McManus et al., 1995). Biases associated with PAS include a lack of proportionality between the photoacoustic signal and the aerosol absorption cross section for particles with radii greater than 0.7 µm (Cremer et al., 2017). This is not an issue for the current study, which uses an impactor to remove particles with radii > 0.5 µm; see Sect. 2.4.

There exist a number of options for calibrating photoacoustic spectrometers including use of nitrogen dioxide (Arnott et al., 2000; Nakayama et al., 2015), polydisperse kerosene soot (Nakayama et al., 2015), oxygen (Gillis et al., 2010; Tian et al., 2009) and ozone (Bluvshtein et al., 2017; Lack et al., 2006, 2012a). Ozone was chosen as the calibrant for our PAS cells, in part as nitrogen dioxide has been shown to introduce uncertainty in calibrations at 405 nm due to photolysis (Lack et al., 2012a) and generation of aerosol particles is challenging in the field. Gaseous ozone has been used successfully to calibrate photoacoustic spectrometers operating at laser wavelengths of 532 nm, with reported absorption accuracies of 1–5 % (Lack et al., 2006, 2012a). Demonstration of the validity of the ozone calibration approach involved the comparison of PAS measurements to model absorption calculations for laboratory-generated absorbing particles, such as nigrosin dye. Recently, Bluvshtein et al. (2017) performed similar experiments to probe the validity of the ozone calibration approach at 404 nm. They found a factor of ~ 2 discrepancy between the PAS response to ozone and nigrosin, which was attributed to an unspecified issue with ozone measurements at these wavelengths. This result has significant implications for photoacoustic spectrometer ozone calibrations at short visible wavelengths, suggesting that they would lead to an overestimation of aerosol absorption by a factor ~ 2. The focus of this study is to re-evaluate this result.

Given the importance of the Bluvshtein et al. (2017) work in motivating this study, we provide a brief overview of the experiments here. Ozone was generated from high-purity (99.999 %) oxygen using either a corona discharge ozone generator or, for lower concentrations, a UV lamp. Ozone concentrations in the range 250–1900 ppm were generated and diluted with dry nitrogen in the ratio 1 : 10 O_2-O_3 : N_2. Ozone absorption coefficients were measured using a cavity ring-down spectrometer (CRDS). CRDS measurements made in series versus those made in parallel to the PAS detection cell indicated little difference in ozone concentration and thus minimal loss through the PAS system. Nigrosin was atomised from a solution, dried to < 10 % relative humidity, size-selected using a differential mobility analyser (DMA) to yield mobility diameters in the range 250–325 nm and passed through an impactor to remove multiply charged particles. The aerosol stream flowed through a PAS cell at 0.6 L min^{-1}, which was then split evenly between the CRDS cell and a condensation particle counter (CPC). Particle concentrations in the range 200–1500 cm^{-3} were used. PAS-measured ensemble aerosol absorption coefficients were compared to modelled values computed using Mie–Debye–Lorenz theory (hereafter referred to as Mie theory) in combination with the size-selected particle diameters that were passed by the DMA and complex refractive indices determined via spectroscopic ellipsometry. Experiments were repeated for Pahokee peat fulvic acid and Suwannee River fulvic acid aerosol. The discrepancy between the PAS-measured ensemble absorption coefficients and absorption coefficients calculated using Mie theory differed by a factor of 2 for all three test aerosols. Several suggestions for the discrepancy were provided, including contamination by NO_2 and generation of light-scattering particles due to reaction of O_3 with the walls of the instrument. However, no evidence supporting these theories was provided. PAS measurements at wavelengths other than 404 nm were also not available, which prevented an independent check of the PAS responses to ozone and nigrosin at wavelengths that have been reported previously to be well calibrated using the ozone approach (e.g. Lack et al., 2006).

In this study, we use a suite of multi-wavelength PAS and CRDS measurements to evaluate the suitability of ozone as

a PAS calibrant gas. We follow the method described above whereby PAS-measured ensemble absorption cross sections for aerosolised nigrosin are compared to model calculations. Importantly, this comparison is evaluated for three visible wavelengths including the 405 nm wavelength pertinent to the work of Bluvshtein et al. (2017). In the following section, we provide a description of the experimental set-up including the photoacoustic and cavity ring-down spectrometers, ozone calibration apparatus, aerosol generation system and the method by which modelled ensemble aerosol absorption cross sections were calculated. Experimental results and discussion are presented in Sect. 3.

2 Methodology

2.1 Photoacoustic spectrometer

Photoacoustic detection cells based on the dual-resonator design of Lack et al. (2012a) were used. These cells were identical to those used by Bluvshtein et al. (2017) except that the planar windows were replaced with Brewster angle windows (Thorlabs, BW2502), which minimised reflection losses within the multipass optical system. Each PAS cell consisted of two cylindrical resonator cavities (a lower signal and upper reference resonator) coupled through buffer volumes on either side for noise suppression (Lack et al., 2006). The cells were manufactured from aluminium and had a total volume of 200 cm^3. Individual resonant cavities had dimensions of 110 mm length and 9.5 mm radius. The sample passed through both resonators but laser light passed only through the lower signal resonator. The cell was positioned within a multipass optical system formed by two cylindrical mirrors located outside of the PAS cell with mirror radii of curvature of 430 mm (front mirror, closest to laser) and 470 mm (back mirror). The concavities of the two mirrors were rotated 90° to each other. Each mirror was coated with a wavelength-specific dielectric coating to yield reflectivities exceeding 99.9 %. Toptica iBeam Smart (Toptica Photonics) lasers with wavelengths 405, 514 and 658 nm generated light with powers 300, 100 and 130 mW respectively. Laser wavelengths and line widths were measured using an Avantes spectrometer (CompactLine) for the blue and green wavelengths and a Hamamatsu spectrometer (C11697MB) for red wavelengths. Light was injected into each multipass system through a 2 mm hole in the centre of the first mirror. Light exiting the multipass system was measured using a photodiode (Thorlabs, S121C) positioned behind the second mirror. In an optimally aligned system, the laser would pass through the acoustic resonator 182 times (Lack et al., 2012a; Silver, 2005). However, no effort was made to achieve this limit in the current system. The alignment was conducted by visual inspection of the spot pattern only, which almost certainly resulted in a lower number of passes. Quantifying the number of passes through the resonator was not critical. Light exiting the resonator was measured using a photodiode, which allowed the PAS signal to be corrected for any laser power or alignment instability (Lack et al., 2012a). The acoustic signal was detected using microphones (Knowles Acoustics, EK-23132) positioned halfway along the lengths of each resonator to coincide with the pressure antinode corresponding to the lowest-order ($n = 1$) acoustic eigenmode of the photoacoustic cell. The responses from the two microphones were passed through a differential amplifier and Fourier transformed to the frequency domain. The photoacoustic response is defined as the magnitude of the frequency domain response at the $n = 1$ eigenfrequency and is referred to hereafter as the integrated area (IA). A speaker (Knowles Acoustics, ES-23127-000) was located in the reference resonator to enable periodic measurement of the cell resonant frequency and quality factor (Lack et al., 2012a). Following each speaker measurement, the laser modulation frequency was automatically adjusted to match the derived cell resonance frequency. Section 2.3 provides details regarding PAS corrections for cell resonance properties and laser power. Aerosol absorption coefficients (Mm^{-1}) measured by the photoacoustic spectrometers were converted to ensemble absorption cross sections (m^2) for comparison to theoretical calculations by dividing by the aerosol number concentrations reported by a CPC (see Sect. 2.4). The ensemble absorption cross section represents the mean of the absorption cross sections corresponding to a range of particles sizes, for example from multiply charged particles (see Sect. 2.5). The ensemble absorption cross section is hereafter referred to as the absorption cross section.

2.2 Cavity ring-down spectrometer

Cavity ring-down spectroscopy is a highly sensitive technique used for measuring the optical extinction coefficient of gases and particulate matter (O'Keefe and Deacon, 1988; Romanini et al., 1997). The CRDS system employed in this study was similar to that in Langridge et al. (2011) and only the differences will be highlighted here. All lasers (Toptica, iBeam Smart-S) were continuous-wave diode lasers, operated with square wave modulation at a frequency of 2000 Hz. Lasers were protected from back reflections using Faraday isolators (Thorlabs, IO-5-405-LP and IO-3D-660-VLP). A 658 nm laser (130 mW) pumped the red cell and a 405 nm laser (300 mW) pumped the blue cell. The laser spectral widths were > 100 GHz and much larger than the free spectral range of the optical cavities (∼ 350–400 MHz). This allowed passive coupling to occur rather than relying on an active mechanism to match the laser frequency to a cavity mode. The CRDS cells were made out of aluminium. Cavity mirrors were manufactured from fused silica with wavelength-specific coatings, 25 mm diameter, 1 m radii of curvature and reflectivities in excess of 99.99 % (Layertec GmbH, red 660 nm; CVI Laser Optics, blue 405 nm). A high-purity zero-air flow (BOC, 270028-L) set to 10 cm^3 min^{-1}

per mirror was introduced across the mirrors to prevent contamination. Photomultiplier tubes detected light exiting the cavity (Hamamatsu, H9433-201) and were protected from stray light using narrowband interference filters (Thorlabs, FB405-10 and FB660-10). Each time the laser turned off, the cavity output signal decayed exponentially. The signal was fitted to a single exponential function to extract the $1/e$ folding time, otherwise known as the cavity ring-down time. The extinction coefficient, α_{ext}, (Mm^{-1}) was calculated using

$$\alpha_{\mathrm{ext}} = \frac{R_{\mathrm{L}}}{c}\left(\frac{1}{\tau} - \frac{1}{\tau_0}\right), \quad (1)$$

where R_{L} is the ratio of the physical length of the cavity to the length over which sample was present, c is the speed of light and τ and τ_0 are the ring-down times for a cavity with and without scattering/absorbing species. The τ_0 times for both the 405 and 658 nm CRDS channels used in this study were measured before and after experiments in which aerosol was passed through the optical cavities. These τ_0 varied over time by only a small amount due to changes in cavity alignment, cleanliness and the sample pressure. However, typical representative times were 23.1 (405 nm) and 34.2 µs (658 nm). Cavity mirror-to-mirror lengths ranged from 371 to 423 mm, yielding geometric R_{L} factors in the range 1.150–1.173. The R_{L} factor appropriate for aerosol measurements was determined from the geometric dimensions of the detection cell. As highlighted by Fuchs et al. (2008), the R_{L} factor for detection of gaseous species can be different from this value due to the ability of gaseous samples to diffuse. We determined the gaseous R_{L} factors by measuring the change in the ring-down times for filtered air plus ozone (i) under standard operating conditions whereby ozone partially diffuses into the volume between the sample inlet and mirror and (ii) under non-standard operating conditions whereby ozone was fully mixed into the volume between the sample inlet and mirror by pulling the ozone-laden air out of the cavity through the mirror purge lines. This resulted in R_{L} factors of 1.05 (658 nm) and 1.04 (405 nm). The CRDS extinction measurement accuracy was evaluated by Langridge et al. (2011) to be better than 2 %. Extinction coefficients were converted to ensemble extinction cross sections (m^2) by dividing by the aerosol number concentrations measured using a CPC (see Sect. 2.4). The ensemble extinction cross section is hereafter referred to as the extinction cross section.

2.3 Ozone calibration

Gaseous ozone was generated using a coronal discharge ozone generator (Longevity Resources, EXT120-T) from high-purity oxygen (99.999 %, BOC, grade N5.0). The ozone-laden stream was split approximately evenly between the PAS and CRDS cells using a manifold equipped with 300 µm diameter orifices, as shown in Fig. 1. Teflon tubing was used throughout the flow system to minimise contamination and to reduce ozone losses.

The 405 and 658 nm CRDS cells quantified ozone concentrations for calibration of all five PAS cells. For PAS cells in series with the CRDS channels (PAS 4 and PAS 5), the CRDS-measured extinction coefficients were used directly to calibrate the corresponding in-line PAS channel measurements of IA. This calibration relation between sample extinction and IA was quantified at multiple values of ozone concentration, controlled by varying the discharge frequency on the coronal ozone generator. For PAS cells operated in parallel, it was necessary to accurately measure the relative ozone splitting ratio with respect to the CRDS flow paths. The following section details the method for characterising this ratio, which was based on monitoring the resonant frequency shift induced by changing the gas composition and hence speed of sound within the photoacoustic cells (Miklós et al., 2001).

At the start of each calibration cycle, pure oxygen was introduced into the PAS cells through the ozone manifold at a flow rate of $0.02\,\mathrm{L\,min^{-1}\,cell^{-1}}$, in addition to the $0.98\,\mathrm{L\,min^{-1}}$ filtered-air flow. Air was filtered using a particle filter (Headline Filters, DIF-LK40). The oxygen displaced a fraction of the filtered-air flow through each cell, changing the gas composition, speed of sound and thus cell resonant frequency, as shown in Fig. 2. The ozone flow splitting, $\Delta\nu$, between the two 658 nm PAS cells (PAS 2 and PAS 4 in Fig. 1) was calculated using

$$\Delta\nu = \frac{\left(F_{\mathrm{r}}^{\mathrm{air}} - F_{\mathrm{r}}^{\mathrm{air+O_2}}\right)_{\mathrm{PAS\,4}}}{\left(F_{\mathrm{r}}^{\mathrm{air}} - F_{\mathrm{r}}^{\mathrm{air+O_2}}\right)_{\mathrm{PAS\,2}}}, \quad (2)$$

where $F_{\mathrm{r}}^{\mathrm{air}}$ and $F_{\mathrm{r}}^{\mathrm{air+O_2}}$ are the PAS cell resonant frequencies of filtered ambient air and filtered ambient air plus oxygen, respectively, during the two highlighted periods in Fig. 2. Similarly, the ozone flow splitting between the 405 nm PAS cells was calculated using PAS 1 and PAS 5. The 514 nm PAS cell was calibrated using the 658 nm CRDS cell, and hence the ozone splitting ratio between PAS cells 3 and 4 was used. The ozone splitting ratio represents the fractional difference in the ozone concentrations within two PAS cells due to unequal flow splitting within the ozone manifold. The ozone splitting ratios, and therefore the ozone-laden flow rates, between two PAS cells located in parallel (for example, the PAS 2 and PAS 4 cells) were in the range 2–28 %. Measuring the ozone splitting between PAS cells using the resonant shift method compared extremely well to in-line mass flow measurements. The 1σ variability between ozone splitting corrections for eight repeat ozone calibrations was ± 1.3 %. A summary of the ozone splitting corrections can be found in the Supplement.

Following measurement of ozone splitting ratios, the ozone generator was powered and the main calibration was started. Calibrations involved the stepwise measurement of nine ozone concentration levels, where Fig. 3 shows the PAS and CRDS responses to ozone at 405 nm.

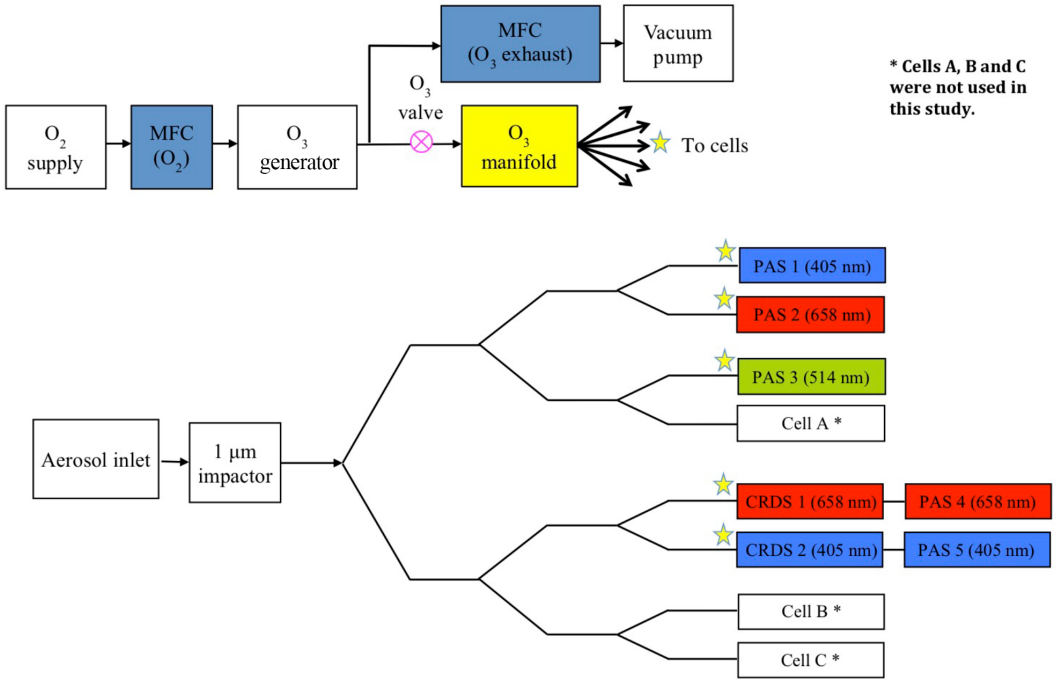

Figure 1. Schematic diagram of the PAS/CRDS experimental set-up including the ozone generation system and the relative positions of the PAS and CRDS cells. The stars indicate the ozone flow path, which entered the cells through different ports to the main aerosol flow. The PAS/CRDS wavelengths are centred at 405, 514 and 658 nm respectively. Abbreviations: MFC is mass flow controller.

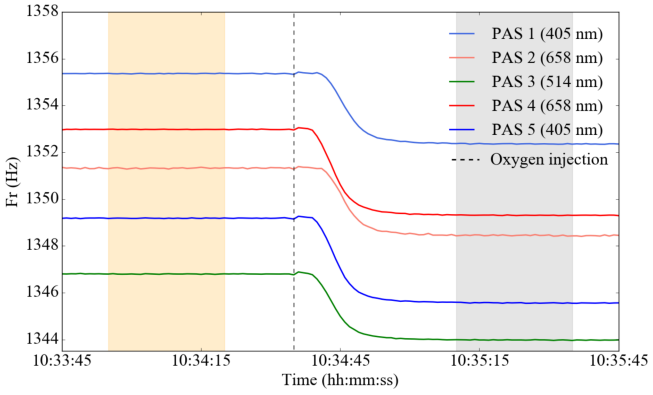

Figure 2. PAS cell resonant frequency as a function of time. Oxygen was introduced into the filtered-air flow at 10:34:35 (dotted line). Mean cell resonant frequencies before (orange highlighted region) and after (grey highlighted region) introducing oxygen were computed during the highlighted times.

At each ozone level, cell resonant frequencies and quality factors were quantified using the cell speakers. Subsequently, 90 s of data were collected, from which the mean and standard deviation of PAS IA and CRDS extinction were calculated. Using the minimum and maximum extinction coefficients for ozone in Fig. 3 (1.3 and 27.1 Mm^{-1}), an ozone absorption cross section of 1.62×10^{-23} cm^2 at the corresponding CRDS wavelength (405.03 nm) and assuming 2.46×10^{25} molecules air m^{-3} at the 405 nm CRDS cell temperature and pressure of 21.82 °C and 1001 mb, the ozone concentrations were in the range 33–680 ppmv (Serdyuchenko et al., 2014). Approximately the same levels of ozone were used in all cells. The ratios of ozone extinction coefficients measured in the 405 and 658 nm CRDS cells compared well to the ratio of the literature ozone absorption cross sections. After accounting for uneven ozone flow splitting between the cells, the ratio of the measured extinction coefficients at 658 and 405 nm agreed with the literature cross section ratio to within 2.0 %. This excellent agreement provides strong evidence that there were no issues with contamination by absorbing gaseous or aerosol species during ozone calibrations.

Analysis of calibration data involved the following steps. Firstly, corrections were applied to normalise the raw microphone IA, IA_{raw}, by the laser power and cell resonance properties so that the calibration could later be applied to measured data with different laser powers and resonance properties. The corrected photoacoustic response, IA_{norm}, was calculated by multiplying IA_{raw} by the correction factor shown in Eq. (3) (Arnott et al., 1999):

$$C = \frac{F_R}{Q P_L}, \tag{3}$$

where F_R is the cell resonance frequency, Q the cell quality factor and P_L the circulating laser power. P_L was measured

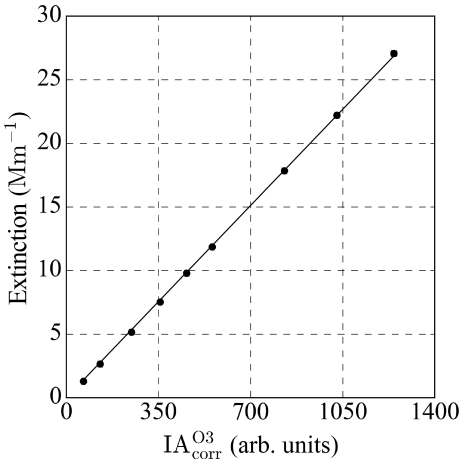

Figure 3. Photoacoustic spectrometer response (microphone integrated area; IA) and concurrent cavity ring-down spectrometer extinction coefficient for nine ozone concentrations at wavelength 405 nm. Each point is the mean of 90 s of 1 Hz data and error bars represent the 2σ precision of each measurement; these are not discernible by eye due to the excellent precision.

by the photodiode. PAS cell quality factors were in the range 87–93.

Secondly the background signal measured in the absence of ozone or particles, IA_{norm}^{bkg}, was characterised. This signal was subsequently subtracted from IA_{norm} to yield the background corrected microphone signal, $IA_{corr}^{O_3}$. A least squares linear fit of $IA_{corr}^{O_3}$ against CRDS-derived extinction was then performed to determine the PAS calibration coefficient. Figure 3 shows an example fit for a 405 nm PAS channel. Across all PAS cells, straight line gradients were typically in the range 0.02–0.32 and R^2 values were consistently > 0.999. All regressions relating to the calibrations were forced through zero. A summary of the calibration gradients and R^2 values can be found in the Supplement. The mean 1σ fitting uncertainty in the gradient of the linear ozone calibration gradients covering all cells was 0.15 %.

Since there was no green-wavelength CRDS cell available, the 514 nm PAS cell was calibrated by evaluating the 514 nm absorption coefficient using measurements from the 658 nm CRDS cell and Eq. (4):

$$\alpha_{abs\_514} = \frac{\alpha_{ext\_658}}{\sigma_{abs\_658}} \sigma_{abs\_514} \quad (4)$$

where $\sigma_{abs\_658} = 2.19 \times 10^{-21}$ and $\sigma_{abs\_514} = 1.62 \times 10^{-21}$ cm^2 are the ozone absorption cross sections at the wavelengths of interest (Gorshelev et al., 2014), α_{ext_658} is the extinction coefficient measured using the 658 nm CRDS channel and α_{abs_514} is the absorption measured by the 514 nm PAS channel. The 658 nm CRDS was used to calibrate the 514 nm PAS channel because it extended over a greater range of extinction coefficients (167–1506 Mm^{-1}) than the 405 nm CRDS (1–27 Mm^{-1}). This ensured that the 514 nm PAS calibration covered a range of absorption coefficients greater than that spanned by the nigrosin absorption coefficients. Calibrating the 405 nm channel using the 405 nm CRDS channel, as opposed to the 658 nm channel, would lead to absorption coefficients that were lower by 3.2 %. In the calculation of the extinction coefficient (see Eq. 1), the Rayleigh scattering term is common to both the τ and τ_0 measurements and therefore does not contribute to the extinction. Thus it is valid to scale the extinction coefficient measured with the CRDS at 658 nm (or 405 nm) by the literature absorption cross section ratio. What this analysis does not account for is any small difference in the Rayleigh scattering of air versus the Rayleigh scattering of air with a small ozone concentration (up to 680 ppm).

2.4 Aerosol generation and conditioning

Figure 4 shows a schematic diagram of the particle generation set-up. Water-soluble nigrosin, a strong light-absorbing dye at visible wavelengths, (Sigma Aldrich, CAS Number 8005-03-6, lot number MKBR1705V, product number 198285-100G) was dissolved into high-purity deionised water (VWR Chemicals) with a range of concentrations between 3.2 and 7.1 grams per litre (g L^{-1}). The solution was drawn into a TSI constant output atomiser (TSI, 3076), which used high-purity synthetic air (BOC, 270028-L) at a flow rate of approximately 2.5 L min^{-1}. The generated aerosol was dried to < 10% relative humidity using a silica gel diffusion drier (Topas, DDU-570) and passed through an electrical ioniser (MSP, 1090). After exiting the ioniser, the aerosol stream was split between a differential mobility analyser (DMA) column (TSI, 3081) and mass flow controller. Flow rates through the mass flow controller were set to regulate the flow through the DMA such that the sample-to-sheath flow ratio was at least 1 : 10 with a sample flow rate in the range 0.3–0.4 L min^{-1} and sheath flow rate in the range 3.5–4.0 L min^{-1}. This ensured that the flow through the ioniser was sufficiently high for a Fuch's charging distribution to be applied to the particles, while ensuring that the DMA could output particle diameters between 10 and 532 nm. The flow rate through the DMA decreased as its impactor removed particles with diameter > 1 µm, which impeded the flow and thus altered the flow splitting between the mass flow controller (MFC) and DMA column. This varied by < 5 % over the course of a test. Section 2.5 provides details of the sensitivity of modelled optical properties of nigrosin to DMA flow rates. The DMA was coupled to a CPC (TSI, 3776) to operate as a scanning mobility particle sizer (SMPS, path A in Fig. 4). This was used to characterise the atomiser output for periods at the start and end of each experiment, thus enabling quantification of any drift. To obtain a quasi-monodisperse aerosol size distribution for optical measurements, the DMA was operated at a fixed voltage (path B in Fig. 4).

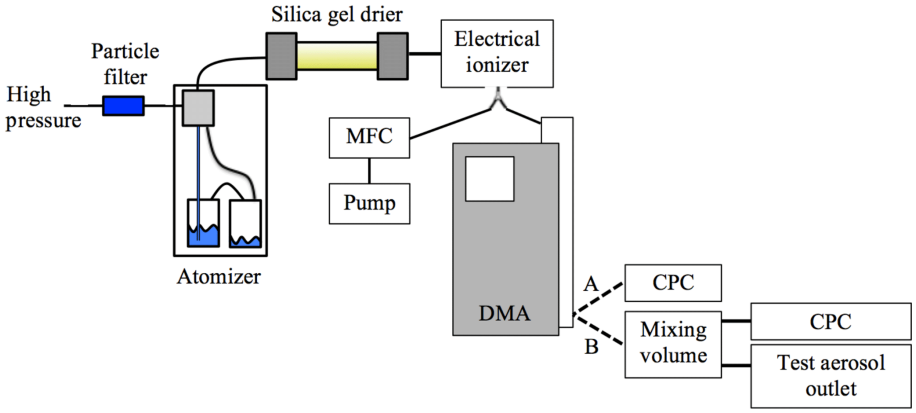

Figure 4. Experimental set-up for generating nigrosin aerosol. The dashed lines labelled A and B represent two independent flow lines (changed manually) used for scanning mode (line A) or fixed voltage size-selection mode (line B). Abbreviations: MFC is mass flow controller, DMA is differential mobility analyser and CPC is condensation particle counter.

For optical measurements, aerosolised nigrosin was mobility-selected with central diameters in the range 250–425 nm in 25 nm steps. The aerosol flow was split between optical cells using a series of Y-flow splitters (Brechtel, 1110 and 1104). All PAS cells were operated in parallel, with two of these cells also having CRDS channels in series as shown previously in Fig. 1. The flow rate through each cell was $1\,\mathrm{L\,min^{-1}}$ and was controlled using mass flow controllers (Alicat, MC Series). This resulted in a plug-flow residence time within each PAS cell of approximately 12 s. To measure the particle number concentration, the mass flow controller on the output of the 514 nm PAS cell was replaced with a second CPC (TSI, 3010), which used a critical orifice to control the flow rate to $1\,\mathrm{L\,min^{-1}}$. Aerosol number concentrations during experiments ranged from 40 to $575\,\mathrm{cm^{-3}}$.

The aerosol flow splitting between cells was evaluated to test whether the CPC-measured number count in the 514 nm PAS cell was representative of the other PAS cells. The aerosol number concentration within the mixing volume and at the outlet of each PAS cell was in turn measured using the two CPCs simultaneously. This allowed the particle transmission efficiency through each PAS cell to be determined independently of variations in particle generation stability. Differences between particle transmission through the 514 nm PAS cell and other PAS cells ranged from 1.1 to 4.5 %. Particle concentrations were adjusted to account for these variations.

2.5 Modelling ensemble absorption cross sections

It is well established that the use of differential mobility analysis for aerosol size selection leads to the generation of a size distribution with polydispersity arising, in part, from the multiple charging of particles (e.g. Wiedensohler et al., 2012). To correctly model the optical properties of the size-selected sample, the multiplet contributions must be taken into account. Transfer function theory predicts the aerosol size distribution exiting the DMA (Knutson and Whitby, 1975). Mie theory (Bohren and Huffman, 1998) can then be applied to calculate single-particle optical cross sections at each diameter in the ensemble. By combining the two theories, the ensemble optical cross sections (hereafter referred to as the cross section) for quasi-monodisperse mobility-size-selected aerosol can be calculated. The following section describes how this was implemented.

Firstly, we measured the polydisperse input aerosol size distribution to the DMA (Fig. 5a) using the SMPS. The accuracy of SMPS sizing was confirmed using monodisperse polystyrene latex spheres (ThermoFisher Scientific, 3000 Series Nanosphere Size Standard). Bimodal log-normal distributions were fitted to the SMPS-measured particle size distributions over the diameter range 71–532 nm. A summary of the best-fit parameters can be found in the Supplement. We measured size distributions before and after running mobility-selected nigrosin through the PAS and CRDS cells to characterise the variability in the particle size distribution. The impact that this variability had on the size distribution exiting the DMA and consequently on the modelled optical cross sections was evaluated by propagating each measured size distribution through the Mie closure routine (described below). In summary, variability in the aerosol source stability led to a mean standard deviation in the modelled absorption cross sections of 4.3 % for all wavelengths and size-selected diameters.

The DMA transfer function describes the probability of a particle of given diameter exiting the DMA. It is used to derive the quasi-monodisperse size distribution at the DMA outlet when operated at a fixed voltage (Knutson and Whitby, 1975). Figure 5b describes the diffusional transfer function for a particle with a 250 nm mobility diameter calculated using the equations presented by Stolzenburg (1988). The transfer function was evaluated for the DMA geometry and aerosol/sheath flow rates used in this study. We verified our

calculations of the transfer function in several ways. The width of the transfer function in the absence of diffusional broadening was verified using the expression presented by Stolzenburg and McMurry (2008). The diffusional broadening parameters used in the transfer function model were also evaluated against the values presented in Stolzenburg (1988), namely the G_{DMA} and $\widetilde{D}$ factors, which agreed to better than 1 %. Finally, the diffusional transfer function was verified quantitatively against the Hagwood et al. (1999) simulations, which used the same Stolzenburg (1988) formulation as used in this work.

To model the quasi-monodisperse aerosol size distribution at the DMA outlet when operated at a fixed voltage, the particle charging efficiencies for the range of particle diameters in the polydisperse input size distribution were calculated using Fuch's charging theory (Wiedensohler, 1988). Aerosol charging efficiencies were calculated for positive ions with up to six elementary charges (Fig. 5c). This was found to be a good approximation of particle charging efficiencies for the experimental set-up described in Fig. 1. We verified that the modelled ratios of singly to doubly charged particles exiting the DMA agreed with experimentally measured ratios using polydisperse size distributions from a Passive Cavity Aerosol Spectrometer Probe (DMT, PCASP-100X). Modelled and measured charge fractions agreed to within 6 % for particles with diameter ≥ 250 nm, with this uncertainty in part due to the resolution of the PCASP diameter bins. Propagating this uncertainty through the Mie closure routine (described below) led to a mean uncertainty of ± 0.93 % in the modelled absorption cross sections for all wavelengths and mobility-selected diameters.

The quasi-monodisperse aerosol size distribution, i.e. the size distribution exiting the DMA, was calculated by multiplying the polydisperse aerosol size distribution at the DMA input by the DMA diffusional transfer function and the aerosol charging efficiencies for corresponding particle diameters (Fig. 5d).

From the calculated size distribution exiting the DMA, the absorption and extinction cross sections were calculated using Mie theory (Bohren and Huffman, 1998) for each particle diameter in the size distribution, the PAS wavelengths and nigrosin refractive indices from Bluvshtein et al. (2017) (Fig. 5e). Mie theory assumes that a particle interacting with radiation is spherical, which is a reasonable assumption for nigrosin particles based on previous studies (e.g. Lack et al., 2006). We chose to use the refractive index values reported by Bluvshtein et al. (2017) to facilitate direct comparison between the two sets of results. The refractive indices used in this analysis were $1.624 \pm 0.0063 + (0.1541 \pm 0.0081)\,i$ for 405 nm, $1.622 \pm 0.0085 + (0.2594 \pm 0.011)\,i$ for 514 nm and $1.811 \pm 0.007 + (0.2476 \pm 0.0031)\,i$ for 658 nm. Sensitivity of the modelled absorption cross section to the imaginary part of the refractive index was quantified using the values and uncertainties presented in Bluvshtein et al. (2017), resulting in a mean uncertainty for all wavelengths and mobility-selected diameters of 1.15 %. Similarly, uncertainty in the modelled absorption cross sections due to a ± 5 % change in the DMA aerosol flow rate was 0.21 %.

Finally, the ensemble absorption and extinction cross sections were calculated by weighting the Mie cross sections by the relative number of each size particle exiting the DMA, calculated using

$$\overline{\sigma_{\mathrm{abs}}} = \sum\nolimits_i \sigma_i^{\mathrm{abs}} N_i, \tag{5}$$

where σ_i^{abs} is the Mie absorption cross section at diameter D_i and N_i is the component of the normalised size distribution at diameter D_i, i.e. the distribution that was assumed to enter the PAS and CRDS cells, such that $\sum N_i = 1$. A similar expression was used to calculate $\overline{\sigma_{\mathrm{ext}}}$, where σ_{abs} was replaced by σ_{ext}. The cumulative absorption cross section for 250 nm mobility-selected nigrosin is plotted in Fig. 5f. This highlights the relative importance of the absorption contribution from multiply charged particles. Although this contribution was lower for larger mobility-selected diameter particles, it can still significantly contribute to absorption as shown by the dashed green line in Fig. 5f for 400 nm diameter particles.

3 Results and discussion

Initially, we verified the accuracies of the cavity ring-down spectrometers, as they form an integral part of the photoacoustic spectrometer calibrations. The ensemble extinction cross sections (hereafter referred to as extinction cross section) for nigrosin with mobility-selected diameters in the range 250–425 nm were measured using CRDS and modelled using Mie theory, as outlined in Sect. 2.5. The mean gradient between the modelled and CRDS-measured extinction cross sections was 0.98 ± 0.01 (2σ fitting uncertainty) as shown in Fig. 6. Gradients for the 658 and 405 nm wavelengths were 0.96 and 1.00 respectively.

The mean gradient between the modelled and PAS-measured absorption cross sections for nigrosin for all five ozone-calibrated PAS cells was 1.08 ± 0.01 (2σ fitting uncertainty) as shown in Fig. 7. Gradients for the 405, 514 and 658 nm wavelengths were 1.08, 1.07 and 1.09 respectively. These data encompass multiple experimental runs using three independent ozone calibrations.

The uncertainties in the measured optical cross sections for nigrosin shown by the error bars in Figs. 6 and 7 represent the standard deviations for each 90 s cross section measurement, encompassing the precision in both the associated PAS absorption coefficient and CPC measurements. Modelled optical cross sections may be subject to an additional 5 % bias due to uncertainty in the CPC accuracy (Fletcher et al., 2009). Similarly, uncertainties in the modelled cross sections were calculated by combining the uncertainties due to variability in the size distribution, charging distribution and imaginary part of the refractive index in quadrature.

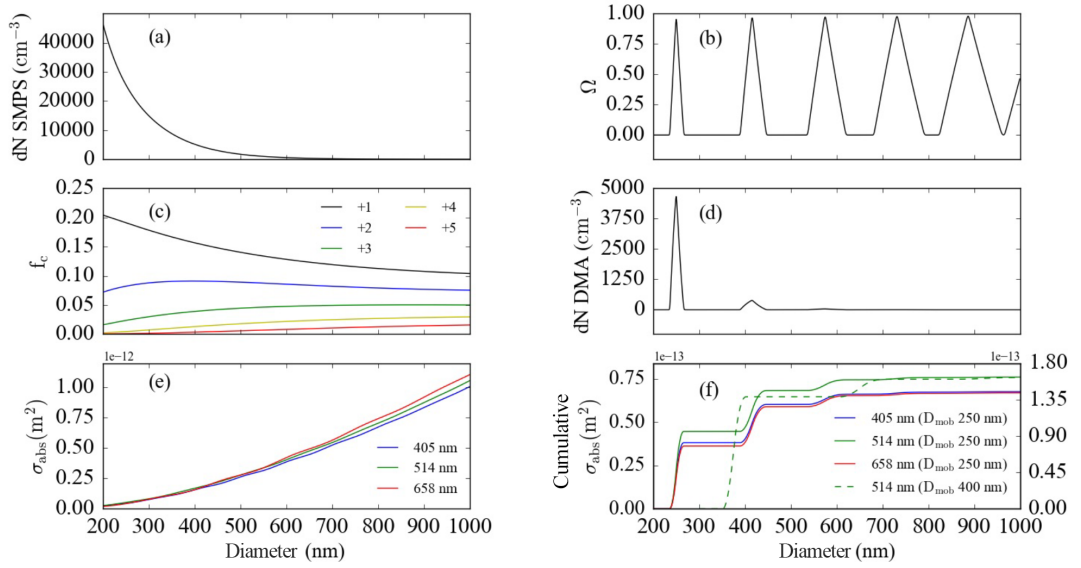

Figure 5. An overview of steps involved in modelling the absorption cross section. **(a)** SMPS-measured particle size distribution. **(b)** DMA diffusional transfer function for a fixed DMA voltage corresponding to a mobility-selected diameter of 250 nm. **(c)** Fuch's charging probabilities for positively charged particles. The figure legend indicates the magnitude of the positive charge. **(d)** Modelled size distribution exiting the DMA column when operated at a fixed voltage for a mobility diameter of 250 nm. **(e)** Absorption cross sections calculated using Mie theory for three visible wavelengths of light, as indicated in the figure legend. **(f)** Cumulative absorption cross sections for nigrosin with a mobility-selected diameter of 250 nm. The dashed green line represents the absorption cross section at wavelength 514 nm corresponding to a 400 nm mobility-selected diameter nigrosin particle using the scale on the right.

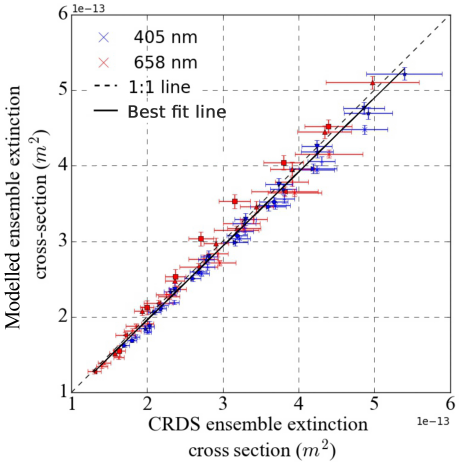

Figure 6. Modelled versus CRDS-measured extinction cross sections for nigrosin aerosol at 405 and 658 nm wavelengths.

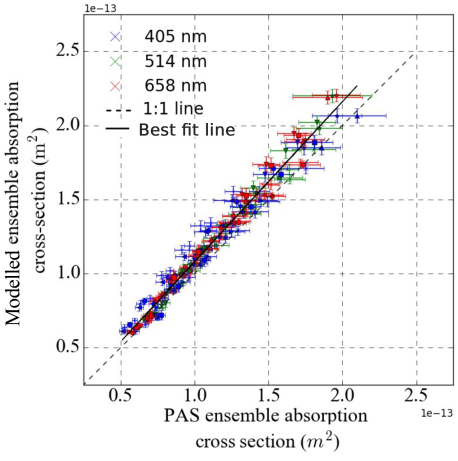

Figure 7. Modelled versus PAS-measured absorption cross sections for nigrosin aerosol at 405, 514 and 658 nm wavelengths.

The key result of this work is the demonstration that photoacoustic spectrometers can be accurately calibrated using ozone at short wavelengths (405 nm), which contrasts with the recent results of Bluvshtein et al. (2017). A thorough evaluation of model uncertainties has shown that this result is robust, despite uncertainties in the imaginary part of the nigrosin refractive index and variability in the measured polydisperse aerosol size distribution used to calculate model absorption properties. It is unclear as to the underlying cause of discrepancy between the results presented here and those in Bluvshtein et al. (2017). Possible reasons include measurement contamination or differences in methods used for the calculation of model optical cross sections. In particular, we have demonstrated the importance of accurately modelling the contribution of multiply charged particles to capture the optical behaviour of the quasi-monodisperse distributions used in these experiments.

4 Conclusions

This study has shown that the ozone calibration method can be used to accurately calibrate photoacoustic instruments operating at short visible wavelengths. This alleviates concerns based on previously published results, which have shown a large discrepancy at 404 nm. Using nigrosin aerosol with mobility-selected diameters in the range 250–425 nm, we verified that the measured absorption cross sections using photoacoustic spectroscopy agreed with modelled values to within 8 %. Our result is robust for optical wavelengths 405, 514 and 658 nm.

Data availability. For data related to this paper please contact Justin Langridge (justin.langridge@metoffice.gov.uk).

The Supplement related to this article is available online at https://doi.org/10.5194/amt-11-2313-2018-supplement.

Competing interests. The authors declare that they have no conflict of interest.

Acknowledgements. This work was funded by the Met Office. In addition, Nicholas W. Davies was supported by a NERC/Met Office Industrial Case studentship (ref 640052003). Michael I. Cotterell was supported by a Tom West Analytical Chemistry Trust Fund Fellowship. Michael I. Cotterell and Jim M. Haywood were supported by the CLARIFY-2017 Natural Environment Research Council funded proposal (NE/L013797/1). We thank Andrew Orr-Ewing and Philip Coulter of the University of Bristol for their help with measurements of the spectrum of the laser sources used in this work.

Edited by: Hendrik Fuchs
Reviewed by: two anonymous referees

References

Alexander, D. T. L., Crozier, P. A., and Anderson, J. R.: Brown Carbon Spheres in East Asian Outflow and Their Optical Properties, Science, 321, 833–836, https://doi.org/10.1126/science.1155296, 2008.

Andreae, M. O. and Gelencsér, A.: Black carbon or brown carbon? The nature of light-absorbing carbonaceous aerosols, Atmos. Chem. Phys., 6, 3131–3148, https://doi.org/10.5194/acp-6-3131-2006, 2006.

Arnott, W. P., Moosmüller, H., Rogers, C. F., Jin, T., and Bruch, R.: Photoacoustic spectrometer for measuring light absorption by aerosol: Instrument description, Atmos. Environ., 33, 2845–2852, https://doi.org/10.1016/S1352-2310(98)00361-6, 1999.

Arnott, W. P., Moosmüller, H., and Walker, J. W.: Nitrogen dioxide and kerosene-flame soot calibration of photoacoustic instruments for measurement of light absorption by aerosols, Rev. Sci. Instrum., 71, 4545–4552, https://doi.org/10.1063/1.1322585, 2000.

Arnott, W. P., Hamasha, K., Moosmüller, H., Sheridan, P. J., and Ogren, J. A.: Towards aerosol light-absorption measurements with a 7-wavelength aethalometer: Evaluation with a photoacoustic instrument and 3-wavelength nephelometer, Aerosol Sci. Tech., 39, 17–29, https://doi.org/10.1080/027868290901972, 2005.

Backman, J., Virkkula, A., Vakkari, V., Beukes, J. P., Van Zyl, P. G., Josipovic, M., Piketh, S., Tiitta, P., Chiloane, K., Petäjä, T., Kulmala, M., and Laakso, L.: Differences in aerosol absorption Ångström exponents between correction algorithms for a particle soot absorption photometer measured on the South African Highveld, Atmos. Meas. Tech., 7, 4285–4298, https://doi.org/10.5194/amt-7-4285-2014, 2014.

Bluvshtein, N., Flores, J. M., He, Q., Segre, E., Segev, L., Hong, N., Donohue, A., Hilfiker, J. N., and Rudich, Y.: Calibration of a multi-pass photoacoustic spectrometer cell using light-absorbing aerosols, Atmos. Meas. Tech., 10, 1203–1213, https://doi.org/10.5194/amt-10-1203-2017, 2017.

Bohren, C. F. and Huffman, D. R.: Absorption and Scattering of Light by Small Particles, Wiley, New York, https://doi.org/10.1002/9783527618156 1998.

Bond, T. C., Anderson, T. L., and Campbell, D.: Calibration and Intercomparison of Filter-Based Measurements of Visible Light Absorption by Aerosols, Aerosol Sci. Tech., 30, 582–600, https://doi.org/10.1080/027868299304435, 1999.

Bond, T. C., Doherty, S. J., Fahey, D. W., Forster, P. M., Berntsen, T., Deangelo, B. J., Flanner, M. G., Ghan, S., Kärcher, B., Koch, D., Kinne, S., Kondo, Y., Quinn, P. K., Sarofim, M. C., Schultz, M. G., Schulz, M., Venkataraman, C., Zhang, H., Zhang, S., Bellouin, N., Guttikunda, S. K., Hopke, P. K., Jacobson, M. Z., Kaiser, J. W., Klimont, Z., Lohmann, U., Schwarz, J. P., Shindell, D., Storelvmo, T., Warren, S. G., and Zender, C. S.: Bounding the role of black carbon in the climate system: A scientific assessment, J. Geophys. Res.-Atmos., 118, 5380–5552, https://doi.org/10.1002/jgrd.50171, 2013.

Boucher, O., Randall, D., Artaxo, P., Bretherton, C., Feingold, G., Forster, P., Kerminen, V.-M., Kondo, Y., Liao, H., Lohmann, U., Rasch, P., Satheesh, S. K., Sherwood, S., Stevens, B., and Zhang, X.-Y.: Clouds and Aerosols, in: Climate Change 2013 – The Physical Science Basis, Contribution of Working Group I to the Fifth Assessment Report of the Intergovernmental Panel on Climate Change, edited by: Stocker, T. F., Qin, D., Plattner, G.-K., Tignor, M., Allen, S. K., Boschung, J., Nauels, A., Xia, Y., Bex, V., and Midgley, P. M., Cambridge University Press, Cambridge, United Kingdom and New York, NY, USA, 571–658, 2013.

Cappa, C. D., Lack, D. A., Burkholder, J. B., and Ravishankara, A. R.: Bias in filter-based aerosol light absorption measurements due to organic aerosol loading: Evidence from laboratory measurements, Aerosol Sci. Tech., 42, 1022–1032, https://doi.org/10.1080/02786820802389285, 2008.

Cappa, C. D., Onasch, T. B., Massoli, P., Worsnop, D. R., Bates, T. S., Cross, E. S., Davidovits, P., Hakala, J., Hayden, K. L., Jobson, B. T., Kolesar, K. R., Lack, D. A., Lerner, B. M., Li, S.-M., Mellon, D., Nuaaman, I., Olfert, J. S., Petaja, T., Quinn, P. K., Song, C., Subramanian, R., Williams, E. J., and Zaveri, R. A.: Radiative Absorption Enhancements Due to the Mixing

State of Atmospheric Black Carbon, Science, 337, 1078–1081, https://doi.org/10.1126/science.1223447, 2012.

Collaud Coen, M., Weingartner, E., Apituley, A., Ceburnis, D., Fierz-Schmidhauser, R., Flentje, H., Henzing, J. S., Jennings, S. G., Moerman, M., Petzold, A., Schmid, O., and Baltensperger, U.: Minimizing light absorption measurement artifacts of the Aethalometer: evaluation of five correction algorithms, Atmos. Meas. Tech., 3, 457–474, https://doi.org/10.5194/amt-3-457-2010, 2010.

Cremer, J. W., Covert, P. A., Parmentier, E. A., and Signorell, R.: Direct Measurement of Photoacoustic Signal Sensitivity to Aerosol Particle Size, J. Phys. Chem. Lett., 8, 3398–3403, https://doi.org/10.1021/acs.jpclett.7b01288, 2017.

Fletcher, R. A., Mulholland, G. W., Winchester, M. R., King, R. L., and Klinedinst, D. B.: Calibration of a condensation particle counter using a NIST traceable method, Aerosol Sci. Tech., 43, 425–441, https://doi.org/10.1080/02786820802716735, 2009.

Fuchs, H., Dube, W. P., Cicioira, S. J., and Brown, S. S.: Determination of Inlet Transmission and Conversion Efficiencies for in Situ Measurements of the Nocturnal Nitrogen Oxides, NO_3, N_2O_5 and NO_2, via Pulsed Cavity Ring-Down Spectroscopy, Anal. Chem., 80, 6010–6017, https://doi.org/10.1021/ac8007253, 2008.

Gillis, K. A., Havey, D. K., and Hodges, J. T.: Standard photoacoustic spectrometer: Model and validation using O2 A-band spectra, Rev. Sci. Instrum., 81, 064902-1–064902-13, https://doi.org/10.1063/1.3436660, 2010.

Gorshelev, V., Serdyuchenko, A., Weber, M., Chehade, W., and Burrows, J. P.: High spectral resolution ozone absorption cross-sections – Part 1: Measurements, data analysis and comparison with previous measurements around 293 K, Atmos. Meas. Tech., 7, 609–624, https://doi.org/10.5194/amt-7-609-2014, 2014.

Hagwood, C., Sivathanu, Y., and Mulholland, G.: The DMA Transfer Function with Brownian Motion a Trajectory/Monte-carlo Approach, Aerosol Sci. Tech., 30, 40–61, https://doi.org/10.1080/027868299304877, 1999.

Knutson, E. O. and Whitby, K. T.: Aerosol classification by electric mobility: apparatus, theory, and applications, J. Aerosol Sci., 6, 443–451, https://doi.org/10.1016/0021-8502(75)90060-9, 1975.

Lack, D. A. and Cappa, C. D.: Impact of brown and clear carbon on light absorption enhancement, single scatter albedo and absorption wavelength dependence of black carbon, Atmos. Chem. Phys., 10, 4207–4220, https://doi.org/10.5194/acp-10-4207-2010, 2010.

Lack, D. A., Lovejoy, E. R., Baynard, T., Pettersson, A., and Ravishankara, A. R.: Aerosol Absorption Measurement using Photoacoustic Spectroscopy: Sensitivity, Calibration, and Uncertainty Developments, Aerosol Sci. Tech., 40, 697–708, https://doi.org/10.1080/02786820600803917, 2006.

Lack, D. A., Cappa, C. D., Covert, D. S., Baynard, T., Massoli, P., Sierau, B., Bates, T. S., Quinn, P. K., Lovejoy, E. R., and Ravishankara, A. R.: Bias in Filter-Based Aerosol Light Absorption Measurements Due to Organic Aerosol Loading: Evidence from Ambient Measurements, Aerosol Sci. Tech., 42, 1033–1041, https://doi.org/10.1080/02786820802389277, 2008.

Lack, D. A., Richardson, M. S., Law, D., Langridge, J. M., Cappa, C. D., McLaughlin, R. J., and Murphy, D. M.: Aircraft Instrument for Comprehensive Characterization of Aerosol Optical Properties, Part 2: Black and Brown Carbon Absorption and Absorption Enhancement Measured with Photo Acoustic Spectroscopy, Aerosol Sci. Tech., 46, 555–568, https://doi.org/10.1080/02786826.2011.645955, 2012a.

Lack, D. A., Langridge, J. M., Bahreini, R., Cappa, C. D., Middlebrook, A. M., and Schwarz, J. P.: Brown carbon and internal mixing in biomass burning particles, P. Natl. Acad. Sci. USA, 109, 14802–14807, https://doi.org/10.1073/pnas.1206575109, 2012b.

Langridge, J. M., Richardson, M. S., Lack, D. A., Law, D., and Murphy, D. M.: Aircraft Instrument for Comprehensive Characterization of Aerosol Optical Properties, Part I: Wavelength-Dependent Optical Extinction and Its Relative Humidity Dependence Measured Using Cavity Ringdown Spectroscopy, Aerosol Sci. Tech., 45, 1305–1318, https://doi.org/10.1080/02786826.2011.592745, 2011.

Liu, J., Scheuer, E., Dibb, J., Diskin, G. S., Ziemba, L. D., Thornhill, K. L., Anderson, B. E., Wisthaler, A., Mikoviny, T., Devi, J. J., Bergin, M., Perring, A. E., Markovic, M. Z., Schwarz, J. P., Campuzano-Jost, P., Day, D. A., Jimenez, J. L., and Weber, R. J.: Brown carbon aerosol in the North American continental troposphere: sources, abundance, and radiative forcing, Atmos. Chem. Phys., 15, 7841–7858, https://doi.org/10.5194/acp-15-7841-2015, 2015.

Liu, S., Aiken, A. C., Gorkowski, K., Dubey, M. K., Cappa, C. D., Williams, L. R., Herndon, S. C., Massoli, P., Fortner, E. C., Chhabra, P. S., Brooks, W. A., Onasch, T. B., Jayne, J. T., Worsnop, D. R., China, S., Sharma, N., Mazzoleni, C., Xu, L., Ng, N. L., Liu, D., Allan, J. D., Lee, J. D., Fleming, Z. L., Mohr, C., Zotter, P., Szidat, S., and Prévôt, A. S. H.: Enhanced light absorption by mixed source black and brown carbon particles in UK winter, Nat. Commun., 6, 1–10, https://doi.org/10.1038/ncomms9435, 2015.

McComiskey, A., Schwartz, S. E., Schmid, B., Guan, H., Lewis, E. R., Ricchiazzi, P., and Ogren, J. A.: Direct aerosol forcing: Calculation from observables and sensitivities to inputs, J. Geophys. Res.-Atmos., 113, 1–16, https://doi.org/10.1029/2007JD009170, 2008.

McManus, J. B., Kebabian, P. L., and Zahniser, M. S.: Astigmatic mirror multipass absorption cells for long-path-length spectroscopy, Appl. Opt., 34, 3336–3348, https://doi.org/10.1364/AO.34.003336, 1995.

Miklós, A., Hess, P., and Bozóki, Z.: Application of acoustic resonators in photoacoustic trace gas analysis and metrology, Rev. Sci. Instrum., 72, 1937–1955, https://doi.org/10.1063/1.1353198, 2001.

Moosmüller, H., Chakrabarty, R. K., and Arnott, W. P.: Aerosol light absorption and its measurement: A review, J. Quant. Spectrosc. Ra., 110, 844–878, https://doi.org/10.1016/j.jqsrt.2009.02.035, 2009.

Müller, T., Virkkula, A., and Ogren, J. A.: Constrained two-stream algorithm for calculating aerosol light absorption coefficient from the Particle Soot Absorption Photometer, Atmos. Meas. Tech., 7, 4049–4070, https://doi.org/10.5194/amt-7-4049-2014, 2014.

Myhre, G., Samset, B. H., Schulz, M., Balkanski, Y., Bauer, S., Berntsen, T. K., Bian, H., Bellouin, N., Chin, M., Diehl, T., Easter, R. C., Feichter, J., Ghan, S. J., Hauglustaine, D., Iversen, T., Kinne, S., Kirkevåg, A., Lamarque, J.-F., Lin, G., Liu, X., Lund, M. T., Luo, G., Ma, X., van Noije, T., Penner, J. E., Rasch, P. J., Ruiz, A., Seland, Ø., Skeie, R. B., Stier, P., Takemura, T.,

Tsigaridis, K., Wang, P., Wang, Z., Xu, L., Yu, H., Yu, F., Yoon, J.-H., Zhang, K., Zhang, H., and Zhou, C.: Radiative forcing of the direct aerosol effect from AeroCom Phase II simulations, Atmos. Chem. Phys., 13, 1853–1877, https://doi.org/10.5194/acp-13-1853-2013, 2013.

Nakayama, T., Suzuki, H., Kagamitani, S., Ikeda, Y., Uchiyama, A., and Matsumi, Y.: Characterization of a Three Wavelength Photoacoustic Soot Spectrometer (PASS-3) and a Photoacoustic Extinctiometer (PAX), J. Meteorol. Soc. Jpn., 93, 285–308, https://doi.org/10.2151/jmsj.2015-016, 2015.

O'Keefe, A. and Deacon, D. A. G.: Cavity ring-down optical spectrometer for absorption measurements using pulsed laser sources, Rev. Sci. Instrum., 59, 2544–2551, https://doi.org/10.1063/1.1139895, 1988.

Romanini, D., Kachanov, A. A., and Stoeckel, E.: Cavity ringdown spectroscopy: broad band absolute absorption measurements, Chem. Phys. Lett., 270, 546–550, https://doi.org/10.1016/S0009-2614(97)00407-7, 1997.

Saleh, R., Hennigan, C. J., McMeeking, G. R., Chuang, W. K., Robinson, E. S., Coe, H., Donahue, N. M., and Robinson, A. L.: Absorptivity of brown carbon in fresh and photo-chemically aged biomass-burning emissions, Atmos. Chem. Phys., 13, 7683–7693, https://doi.org/10.5194/acp-13-7683-2013, 2013.

Schmid, O., Artaxo, P., Arnott, W. P., Chand, D., Gatti, L. V., Frank, G. P., Hoffer, A., Schnaiter, M., and Andreae, M. O.: Spectral light absorption by ambient aerosols influenced by biomass burning in the Amazon Basin. I: Comparison and field calibration of absorption measurement techniques, Atmos. Chem. Phys., 6, 3443–3462, https://doi.org/10.5194/acp-6-3443-2006, 2006.

Serdyuchenko, A., Gorshelev, V., Weber, M., Chehade, W., and Burrows, J. P.: High spectral resolution ozone absorption cross-sections – Part 2: Temperature dependence, Atmos. Meas. Tech., 7, 625–636, https://doi.org/10.5194/amt-7-625-2014, 2014.

Silver, J. A.: Simple dense-pattern optical multipass cells, Appl. Opt., 44, 6545–6556, https://doi.org/10.1364/AO.44.006545, 2005.

Stier, P., Schutgens, N. A. J., Bellouin, N., Bian, H., Boucher, O., Chin, M., Ghan, S., Huneeus, N., Kinne, S., Lin, G., Ma, X., Myhre, G., Penner, J. E., Randles, C. A., Samset, B., Schulz, M., Takemura, T., Yu, F., Yu, H., and Zhou, C.: Host model uncertainties in aerosol radiative forcing estimates: results from the AeroCom Prescribed intercomparison study, Atmos. Chem. Phys., 13, 3245–3270, https://doi.org/10.5194/acp-13-3245-2013, 2013.

Stocker, T. F., Qin, D., Plattner, G.-K., Alexander, L. V, Allen, S. K., Bindoff, N. L., Bréon, F.-M., Church, J. A., Cubasch, U., Emori, S., Forster, P., Friedlingstein, P., Gillett, N., Gregory, J. M., Hartmann, D. L., Jansen, E., Kirtman, B., Knutti, R., Krishna Kumar, K., Lemke, P., Marotzke, J., Masson-Delmotte, V., Meehl, G. A., Mokhov, I. I., Piao, S., Ramaswamy, V., Randall, D., Rhein, M., Rojas, M., Sabine, C., Shindell, D., Talley, L. D., Vaughan, D. G., and Xie, S.-P.: Technical Summary, in: Climate Change 2013 – The Physical Science Basis, Contribution of Working Group I to the Fifth Assessment Report of the Intergovernmental Panel on Climate Change edited by: Stocker, T. F., Qin, D., Plattner, G.-K., Tignor, M., Allen, S. K., Boschung, J., Nauels, A., Xia, Y., Bex, V., and Midgley, P. M., Cambridge, United Kingdom and New York, NY, USA, 33–115, 2013.

Stolzenburg, M.: An ultrafine aerosol size distribution measuring system, available at: https://www.researchgate.net/publication/230691922_An_Ultrafine_Aerosol_Size_Distribution_System (last access: 18 April 2018), 1988.

Stolzenburg, M. R. and McMurry, P. H.: Equations Governing Single and Tandem DMA Configurations and a New Lognormal Approximation to the Transfer Function, Aerosol Sci. Tech., 42, 421–432, https://doi.org/10.1080/02786820802157823, 2008.

Strawa, A. W., Castaneda, R., Owano, T., Baer, D. S., and Paldus, B. A.: The Measurement of Aerosol Optical Properties Using Continuous Wave Cavity Ring-Down Techniques, J. Atmos. Ocean. Tech., 20, 454–465, https://doi.org/10.1175/1520-0426(2003)20<454:TMOAOP>2.0.CO;2, 2003.

Tian, G., Moosmüller, H., and Arnott, W. P.: Simultaneous photoacoustic spectroscopy of aerosol and oxygen A-band absorption for the calibration of aerosol light absorption measurements, Aerosol Sci. Tech., 43, 1084–1090, https://doi.org/10.1080/02786820903170972, 2009.

Virkkula, A.: Correction of the Calibration of the 3-wavelength Particle Soot Absorption Photometer (3λ PSAP), Aerosol Sci. Tech., 44, 706–712, https://doi.org/10.1080/02786826.2010.482110, 2010.

Virkkula, A., Ahlquist, N. C., Covert, D. S., Sheridan, P. J., Arnott, W. P., and Ogren, J. A.: A Three-Wavelength Optical Extinction Cell for Measuring Aerosol Light Extinction and Its Application to Determining Light Absorption Coefficient, Aerosol Sci. Tech., 39, 52–67, https://doi.org/10.1080/027868290901918, 2005.

Wang, X., Heald, C. L., Sedlacek, A. J., de Sá, S. S., Martin, S. T., Alexander, M. L., Watson, T. B., Aiken, A. C., Springston, S. R., and Artaxo, P.: Deriving brown carbon from multiwavelength absorption measurements: method and application to AERONET and Aethalometer observations, Atmos. Chem. Phys., 16, 12733–12752, https://doi.org/10.5194/acp-16-12733-2016, 2016.

Weingartner, E., Saathoff, H., Schnaiter, M., Streit, N., Bitnar, B., and Baltensperger, U.: Absorption of light by soot particles: Determination of the absorption coefficient by means of aethalometers, J. Aerosol Sci., 34, 1445–1463, https://doi.org/10.1016/S0021-8502(03)00359-8, 2003.

Wiedensohler, A.: An approximation of the bipolar charge distribution for particles in the submicron size range, J. Aerosol Sci., 19, 387–389, https://doi.org/10.1016/0021-8502(88)90278-9, 1988.

Wiedensohler, A., Birmili, W., Nowak, A., Sonntag, A., Weinhold, K., Merkel, M., Wehner, B., Tuch, T., Pfeifer, S., Fiebig, M., Fjäraa, A. M., Asmi, E., Sellegri, K., Depuy, R., Venzac, H., Villani, P., Laj, P., Aalto, P., Ogren, J. A., Swietlicki, E., Williams, P., Roldin, P., Quincey, P., Hüglin, C., Fierz-Schmidhauser, R., Gysel, M., Weingartner, E., Riccobono, F., Santos, S., Grüning, C., Faloon, K., Beddows, D., Harrison, R., Monahan, C., Jennings, S. G., O'Dowd, C. D., Marinoni, A., Horn, H.-G., Keck, L., Jiang, J., Scheckman, J., McMurry, P. H., Deng, Z., Zhao, C. S., Moerman, M., Henzing, B., de Leeuw, G., Löschau, G., and Bastian, S.: Mobility particle size spectrometers: harmonization of technical standards and data structure to facilitate high quality long-term observations of atmospheric particle number size distributions, Atmos. Meas. Tech., 5, 657–685, https://doi.org/10.5194/amt-5-657-2012, 2012.